Modeling and Estimation of Cardiorespiratory Function, with Application to Mechanical Ventilation

Nikolaos Karamolegkos

Submitted in partial fulfillment of the
requirements for the degree of
Doctor of Philosophy
in the Graduate School of Arts and Sciences

COLUMBIA UNIVERSITY

2018

© 2018
Nikolaos Karamolegkos
All rights reserved

ABSTRACT

Modeling and Estimation of Cardiorespiratory Function, with Application to Mechanical Ventilation

Nikolaos Karamolegkos

Evidence-based medicine is at the heart of current medical practice where clinical decisions are driven by research data. However, most current therapy recommendations follow generalized protocols and guidelines that are based on epidemiological (population) studies and thus not suited for the individual patient's demands. *Patient-tailored* therapies are considered, hence, an unmet clinical need. We believe that mathematical models of the physiology can attend to such a clinical need, because they can be tuned to the individual patient. Such models provide a sound mathematical framework for personalized clinical decisions. In particular, physiological models in medicine can serve the following two purposes: 1) They can be an efficient tool to quantify cardiopulmonary dynamics, conduct virtual clinical/physiological experiments, and investigate the effects of specific treatments. 2) Model-based *estimation* techniques can assess physiological parameters or variables, which are otherwise impractical or dangerous to measure; they can effectively tune a generic model to become patient-specific, able to mimic the behavior of a particular patient.

In this thesis, we propose a series of modifications to a previously developed cardiopulmonary model (CP Model) in order to better replicate heart-lung interaction phenomena that are typically observed under mechanical ventilation, hence allowing for a more accurate analysis of ventilation-induced changes in cardiac function. The response of this modified model is validated with experimental data collected during mechanical ventilation conditions.

Further, as an industrial application of mathematical models, we present a patient emulator system that comprises the modified CP Model, a physical ventilator, and a piston-cylinder arrangement that serves as an electrical-to-hydraulic transducer. The modified CP Model then serves as the virtual patient that is being ventilated, where disease conditions can be

instilled. Such a system is designed to offer a well-controlled experimental environment for ventilator manufacturers to efficaciously test and compare ventilation modalities and therapies, thereby enhancing their verification and validation manufacturing processes.

Finally, we develop a model-based approach to estimate (noninvasively) the function of the cardiovascular system, in terms of cardiac performance (i.e., cardiac output) and the dynamics of the systemic arterial tree (i.e., time constant). With this technique, we envision to provide continuous and real-time bedside monitoring of changes in cardiovascular function, such as those induced by changes in ventilator settings.

Contents

List of figures **iv**

List of tables **xviii**

Acknowledgements **xix**

1 Introduction **1**

1.1 Motivation 1

1.2 Thesis organization 8

2 Modeling the heart-lung interactions during mechanical ventilation **10**

2.1 Introduction 10

2.2 The original cardiopulmonary model 14

2.3 Model modifications 15

2.3.1 Pericardial membrane 18

2.3.2 Interventricular septum 18

2.3.3 Pulmonary peripheral vessels 22

2.4 Comparison between modified and original models 26

2.4.1 Normoxia 27

2.4.2 Hypercapnia & Hypoxia 30

2.4.3 Hemodynamic effects of respiration 36

2.5 Validation of modified model 38

2.5.1 Comparison with experimental data 41

2.5.2 Physiological heart-lung interaction phenomena 49

2.6 Sensitivity analysis 63

2.7 Model limitations 67

2.8 Conclusion 70

3 Cardiopulmonary model-based patient emulator 72

3.1 Introduction 72

3.2 State-of-art testing devices 73

3.3 The patient emulator system 76

3.3.1 Software-hardware interface 80

3.3.2 Graphical user interface 84

3.4 System validation 86

3.4.1 Standardized tests 86

3.4.2 Comparison with experimental data 88

3.5 Potential applications 96

3.6 Conclusion 96

4 Cardiovascular system identification 98

4.1 Introduction 98

4.1.1 System identification and parameter estimation 102

4.2 The cardiovascular system 104

4.2.1 The heart as a source 104

4.2.2 The systemic circulation as a dynamic system 106

4.3 Mathematical models of systemic circulation 109

4.3.1 Lumped-parameter models 110

4.3.2 Distributed-parameter models 114

4.4 Cardiac output assessment 118

4.4.1 Current clinical methods 120
4.4.2 Model-based estimation methods 125
4.5 Proposed approach 138
4.5.1 A feasibility study with central venous pressure 138
4.5.2 Proposed estimation algorithm 147
4.6 Algorithm validation 153
4.6.1 Simulation studies on Windkessel-type models 154
4.6.2 Simulation studies on a distributed systemic arterial model 163
4.7 Conclusion and future work 172

5 Summary and future research **176**
5.1 Future research 178

Bibliography **185**

Appendix **199**

List of figures

1.1 A high-level schematic representation of the motivation behind the work presented in this thesis (*green* boxes). System ID, system identification; CDS, clinical decision support. 8

2.1 High-level block diagram of the cardiopulmonary model. CNS, central nervous system; $P_{a_{O_2}}$ and $P_{a_{CO_2}}$, oxygen (O_2) and carbon dioxide (CO_2) arterial blood partial pressures, respectively; $C_{a_{O_2}}$ and $C_{a_{CO_2}}$, O_2 and CO_2 gas concentrations in the arterial blood, respectively; $C_{v_{O_2}}$ and $C_{v_{CO_2}}$, O_2 and CO_2 gas concentrations in the venous blood, respectively; P_{sa}, systemic arterial blood pressure; P_{pl}, pleural (intrathoracic) pressure; P_{mus}, respiratory muscle pressure; V_T, tidal volume. 16

2.2 Schematic block diagram of the cardiovascular system of the modified CP Model. P_{sa} and P_{pa}, systemic and pulmonary arterial blood pressures; P_{ra} and P_{la}, right and left atrial pressures; P_{rv} and P_{lv}, right and left ventricular pressures; P_{pal}, pulmonary arteriolar pressure; P_{pc}, pulmonary capillary pressure; P_{pv}, pulmonary venous pressure; P_{peri}, pericardial pressure; P_{pl}, pleural (intrathoracic) pressure; P_A, alveolar pressure; V_{ra} and V_{la}, right and left atrial volumes; V_{rv} and V_{lv}, right and left ventricular volumes; V_{spt}, septal volume; V_{peri}, pericardial volume; V_A, alveolar volume; $Q_{rv,o}$ and $Q_{lv,o}$, right and left ventricular output blood flows; Q_{pa}, pulmonary arterial blood flow; Q_{pal}, pulmonary arteriolar blood flow; Q_{pc}, pulmonary capillary blood flow; Q_{ps}, pulmonary shunt blood flow; MV, mitral valve; AV, aortic valve; TV, tricuspid valve; PV, pulmonary valve; H, imaginary plane defining the volumes of the septum and of the right and left ventricular free walls. 17

2.3 Electrical diagram of the pulmonary circulation model of the modified CP Model. P, pressure; Q, blood flow; R, resistance; L, inertance; C, compliance. Subscripts: *pa*, pulmonary arteries; *pal*, pulmonary arterioles; *pc*, pulmonary capillaries; *pv*, pulmonary veins; *la*, left atrium; *ps*, pulmonary shunt; *pl*, pleural space; A, alveolar space. The variable resistances P_{pal}, R_{pc}, and P_{ps} are indicated by diagonal arrows. 23

2.4 Comparison of left (*left* plot) and right (*right* plot) ventricular pressure-volume loops between original (*black* line) and modified (*gray* dashed line) models. P_{lv} and V_{lv}, left ventricular pressure and volume, respectively; P_{rv} and V_{rv}, right ventricular pressure and volume, respectively. 31

2.5 Comparison of the respiratory responses of the original (*left* column) and modified (*right* column) models to a 25-minute 7% CO_2 hypercapnic stimulus. From *top* to *bottom*: tidal volume (V_T), respiratory rate (RR), minute ventilation (V_e), alveolar partial pressure of CO_2 ($P_{A_{CO_2}}$), and alveolar partial pressure of O_2 ($P_{A_{O_2}}$). The coefficient of variations (CV) of the root mean squared deviation (RMSD) between each of the simulated variables from the original model and those from the modified model are shown on the top right. The arrows on the time axis represent the time instance at which the stimulus is administered and subsequently withdrawn. 32

2.6 Comparison of the respiratory responses of the original (*left* column) and modified (*right* column) models to a 10-minute 7% O_2 hypoxic stimulus. From *top* to *bottom*: tidal volume (V_T), respiratory rate (RR), minute ventilation (V_e), alveolar partial pressure of CO_2 ($P_{A_{CO_2}}$), and alveolar partial pressure of O_2 ($P_{A_{O_2}}$). The coefficient of variations (CV) of the root mean squared deviations (RMSD) between each of the simulated variables from the original model and those from the modified model are shown on the top right. The arrows on the time axis represent the time instance at which the stimulus is administered and subsequently withdrawn. 33

2.7 Mechanical effects of respiration on cardiovascular variables. From *top* to *bottom*: pleural pressure (P_{pl}), pericardial pressure (P_{peri}), venous return (VR), right ventricular output blood flow ($Q_{rv,o}$), right ventricular stroke volume (SV_{rv}), left ventricular output blood flow ($Q_{lv,o}$), left ventricular stroke volume (SV_{lv}). 37

2.8 Cardiovascular response to step changes in the level of positive pressure ventilation (PPV). Literature data (*black* points and error bars are means and standard errors of the means respectively) are collected during a human study with 18 healthy, spontaneously breathing, subjects and are published by Kyhl et al. [1]. Both model-simulated (*gray* points) and experimental data are assessed from end-expiratory heart beats at the end of each 30-minute PPV period. LV, left ventricular; RV, right ventricular; CO, cardiac output; HR, heart rate (bpm, beats per minute); SV, stroke volume; EDV, end-diastolic volume; ESV, end-systolic volume. 43

2.9 Cyclic intra-breath changes in left (*left* column) and right (*right* column) ventricular functions during positive pressure ventilation. Literature data (*black* squares and error bars are means and standard errors of the means respectively) are taken from Vieillard-Baron et al. [2], who studied 31 fully sedated patients under mechanical ventilation support. Both model (*gray* circles) and experimental data are with reference to the left vertical axes in each subfigure. Note that Vieillard-Baron et al. [2] does not report measurements for RV $EDVI$ and $ESVI$. LV, left ventricular; RV, right ventricular; SVI, stroke volume index; $EDVI$, end-diastolic volume index; $ESVI$, end-systolic volume index; P_{ao} (right vertical axes), airway opening pressure. 48

2.10 Model-simulated Frank-Starling relationships between cardiac index (CI) and end-diastolic volume index ($EDVI$) for the left (LV, *black* curve) and the right (RV, *gray* curve) ventricles. Filled circles are evaluated as PEEP was increased from 0 cmH$_2$O to 20 cmH$_2$O (respectively PEEP$_0$ and PEEP$_{20}$ in Table 2.8). Hollow circles represent the state with PEEP$_{20}$ and volume expansion (PEEP$_{20}$ + VE in Table 2.8). 51

2.11 Cardiovascular response to step changes in the level of positive end-expiratory pressure (PEEP) of a virtual patient with either pulmonary ARDS ($\mathrm{ARDS_p}$, *black* squares) or extra-pulmonary ARDS ($\mathrm{ARDS_{exp}}$, *gray* circles). Each PEEP level is applied for a period of 20 minutes and simulation results are averaged over the last 10 minutes of each PEEP segment. LV, left ventricular; RV, right ventricular; SVI, stroke volume index; $EDVI$, end-diastolic volume index; $ESVI$, end-systolic volume index. 55

2.12 Model-predicted movement of the interventricular septum over sixteen cardiac and two respiratory cycles in positive pressure ventilation. Septal volume (V_{spt}, left vertical axis) models the position of the septum with respect to a vertical imaginary plane H (see Fig. 2.2). Cardiac cycles are indicated by the end-diastolic (gray stars) and end-systolic (gray crosshairs) marks. Respiratory cycles are represented by the pleural pressure (P_{pl}, right vertical axis) waveform that increases with each positive pressure inspiration. 57

2.13 Hemodynamic effects of mechanical ventilation in relation to changes in airway opening pressure (gray waveform). *White* dashed boxes indicate changes in respiratory system variables, whereas *light* and *dark gray* boxes respectively refer to changes in right (RV) and left (LV) ventricular functions. Transpulmonary pressure is defined as the difference between alveolar and pleural pressures. The figure is adapted from [3]. 59

2.14 Percent change (left vertical axes) in left (*left* plot) and right (*right* plot) ventricular preload (*black* bars), afterload (*gray* bars), and ejection fraction (*white* bars) with reference to a ventilatory event represented by the airway opening pressure waveform ($\mathrm{P_{ao}}$, right vertical axes). Ventricular function indices have been computed based on the simulation results in Fig. 2.9. The gray horizontal dotted line indicates the zero percent level of the change in preload, afterload, or ejection fraction. 60

2.15 Cyclic changes in left (LV) and right (RV) ventricular stroke volume indices (SVI) during positive pressure ventilation for selective introduction of each of the proposed model additions, i.e., pericardial membrane (pericardium), interventricular septum, and modified pulmonary circulation. *Top* plots show, beat-by-beat, the values for LV and RV SVI from the original CP Model (*black* bars, original model), the CP Model when only the pericardium has been included in the cardiac model (*dark gray* bars, pericardium-only model), the CP Model when only the septum has been included in the cardiac model (*gray* bars, septum-only model), and the modified CP Model (*light gray* bars, modified model) that includes all three model additions. A single respiratory cycle is represented by the airway pressure waveform (P_{ao}, right vertical axis). Literature data (*white* bats) from Vieillard-Baron et al. [2] are also presented for reference. *Bottom* plot displays the corresponding percent change (ΔSVI) in LV and RV SVI values for the data presented in the top graphs. 65

2.16 Comparison of the effects of positive end-expiratory pressure (PEEP, *left* plot) and pleural pressure (P_{pl}, *right* plot) on cardiac index (CI) between model-predicted (*gray* circles) and experimental (*black* squares) data. Literature data are taken from Dhainaut et al. [4] and are reported with their mean and standard error of the mean values. Notice that each P_{pl} point represents the average pleural pressure (or esophageal pressure—a surrogate of pleural pressure—for the human study) at each respective PEEP level of the left plot. 68

3.1 Passive mechanical simulators of the respiratory mechanics. 74

3.2 State-of-art model-based breathing simulators. 77

3.3 A schematic illustration of the advantages of the proposed patient emulator system for testing mechanical ventilation therapies in comparison to the current practice. 78

3.4 The patient emulator system (CP Model and ASL 5000 Breathing Simulator) connected to a mechanical ventilator. Image courtesy of Philips Respironics. 79

3.5 A high-level block diagram of the patient emulator system. AIN, analog input port of the ASL 5000 Breathing Simulator; A/D and D/A, analog-to-digital and digital-to-analog converters of the dedicated computer, respectively; GUI, graphical user interface for interacting with the CP Model (virtual patient). 80

3.6 Pressure transducers. 82

3.7 Comparison of Honeywell TruStability® and Omega PX140 pressure transducers. 83

3.8 Sample screenshots of the patient emulator's GUI depicting the different physiological system tabs. 85

3.9 Sample screenshot of the plot window of the patient emulator's GUI. 86

3.10 Muscle pressure (P_{mus}, *left* axis) and work of breathing (WOB, *right* axis) of the virtual patient in response to step changes of the supplied PSV level (cmH_2O) as reflected in the measured airway opening pressure (P_{ao}, *left* axis). 91

3.11 Effect of a PSV step change (from 10 cmH_2O to 20 cmH_2O, *top right* plot) on the duration of inspiration (*left* plot) and on the amplitude of P_{mus} ($P_{mus,max}$, *bottom right* plot) as a result of the Hering-Breuer reflex and the chemoreceptors' feedback (slow decay of $P_{mus,max}$ in the *right* plot). Airway opening pressure P_{ao} is also included in the left plot for reference to the P_{mus} profile. 92

3.12 Comparison between patient emulator (*red* bars, mean values) and experimental data from a human study involving 33 patients and reported by Vande-Graaff et al. [5] (*blue* bars, mean±standard error of the mean values). WOB, work of breathing; V_T, tidal volume; RR, respiratory rate; V_e, minute ventilation; $P_{a_{O_2}}$ and $P_{a_{CO_2}}$, arterial oxygen and carbon dioxide partial pressures respectively. 93

3.13 Patient emulator-predicted data based on the human study protocol reported by Dhainaut et al. [4]. Each PEEP level is applied for a period of 20 minutes. $\mathrm{PEEP_x}$, PEEP at x $\mathrm{cmH_2O}$ where x = {0, 5, 10, 15, 20}; $\mathrm{PEEP_{20}}$ + VE, PEEP at 20 $\mathrm{cmH_2O}$ and blood volume expansion with 625±72 ml of plasma expanders; CI, cardiac index; HR, heart rate (bpm, beats per minute); SVI, stroke volume index. See Section 2.5 and Table 2.8 for more information. . . 95

4.1 A schematic block diagram of a dynamic system that is excited by input $u(t)$ and generates output $y(t)$. 99

4.2 A schematic diagram of a state-space identification technique. $u[k]$, input sequence; $y[k]$, output sequence; A_d, B_d, C_d, and D_d, matrices of discrete-time state-space model. 103

4.3 A schematic representation of the human cardiovascular system. Red lines indicate vessels that transfer oxygenated blood (e.g., arteries and arterioles), whereas blue lines are vessels with deoxygenated blood (e.g., veins). Magenta areas represent the vascular beds involved in either alveolar or tissue gas exchange (capillaries). Image distributed under a CC BY-SA 3.0 license. . . 105

4.4 Pressure and flow waveforms simulated by the CP Model over three cardiac cycles. P_{lv}, left ventricular pressure (*top* plot, *black* line); P_{sa}, systemic aortic pressure (*top* plot, *red* line); $Q_{lv,o}$, left ventricular output blood flow (*bottom* plot, *red* line). 107

4.5 Representations of the systemic circulation. The coloring scheme in Fig. 4.5a follows that of Fig. 4.3. Note that Fig. 4.5a follows the clinically accepted convention for the arterial compartment (i.e., input) being on the right-hand side, whereas Fig. 4.5b adheres to the engineering community's approach where the input is placed on the left-hand side of the schematic. P_{sa}, systemic aortic pressure; $Q_{lv,o}$, left ventricular output blood flow; P_{ra}, right atrial pressure (or central venous pressure). 109

4.6 Electrical analog of the two-element Windkessel model of the systemic circulation. P, arterial pressure; Q, arterial blood flow; C_t, total arterial compliance; R_t, peripheral (or terminal) resistance. 111

4.7 Electrical analogs of Windkessel-type models. P, systemic arterial pressure; Q, blood flow; R_c, characteristic resistance; L_c, characteristic inertance; C_t, total arterial compliance; R_t, peripheral (or terminal) resistance. 114

4.8 Schematic representations of two distributed-element models of the systemic arterial tree. 116

4.9 Sample pressure and flow waveforms simulated from the distributed arterial model by Stergiopulos et al. [6] over three cardiac cycles. Q_{asc} (*left* plot, left vertical axis) and P_{asc} (*right* plot, left vertical axis) are the ascending aortic blood flow and pressure, respectively. Q_{fem} (*left* plot, right vertical axis) and P_{fem} (*right* plot, right vertical axis) are the femoral blood flow and pressure, respectively. Note that the two axes in the left plot are on different scales, whereas the ones in the right plot have the same limits. 117

4.10 Sample pressure and flow waveforms simulated from a two-element Windkessel model over three cardiac cycles. $Q_{lv,o}$, left ventricular output blood flow (*left* plot); P_{sa}, systemic arterial pressure (*right* plot). 127

4.11 A schematic representation of the estimation method proposed by Mukkamala et al. [7]. u, impulse train input; P, systemic arterial pressure (system's output); $\hat{a}_i$ and $\hat{b}_j$, estimates of the optimal ARX model; $\hat{\tau}$, estimated time constant. 134

4.12 Electrical diagram of the simplified fourth-order model of the systemic circulation system. ABP, arterial blood pressure; CVP, central venous pressure; P, pressure; Q, blood flow; R, resistance; L, inertance; C, compliance. Subscripts: sa, systemic arteries; sp, systemic peripheral circulation; sv, systemic veins; ra, right atrium. P_{atm} is the atmospheric pressure which is assumed equal to zero. 139

4.13 Sample ABP (*left* plot) and CVP (*right* plot) waveforms simulated under noise-free conditions from the fourth-order model presented in Fig. 4.12 and described in (4.20). 143

4.14 Singular value plot of OKID/DP for the noise-free ($\sigma_{\%} = 0$) and noisy data with levels of noise standard deviation $\sigma_{\%} = 1, 5, 10, 20$. Notice that the number of non-zero—with reference to the noise level corrupting the data—singular values indicates the order of the model. 144

4.15 Sample pressure and flow waveforms simulated from the distributed arterial model by Stergiopulos et al. [6] over three cardiac cycles. Q_{asc} (*top left* plot) and P_{asc} (*top right* plot) are the ascending aortic blood flow and pressure, respectively. Q_{fem} (*bottom left* plot) and P_{fem} (*bottom right* plot) are the femoral blood flow and pressure, respectively. The yellow and purple vertical lines respectively indicate the systolic and diastolic portions of the second cardiac cycle. 148

4.16 Sample ascending aortic (Q_{asc}, *left* plot) and femoral (Q_{fem}, *right* plot) flow waveforms simulated from the distributed arterial model by Stergiopulos et al. [6] over a single cardiac cycle. The black dashed lines on both plots represent piecewise quadratic profiles derived from parametrization of the corresponding flow waveforms during systole. Notice that the time axis is normalized with respect to the beginning of the heart beat. t_o, t_p, and t_r are the onset, peak, and return time instances of the piecewise quadratic functions respectively and t_e represents the end of the heart beat. 150

4.17 Schematic diagram of the proposed estimation algorithm. u, piecewise quadratic input based on the selected onset (t_o), peak (t_p), and return (t_r) time instances; P, systemic arterial pressure (system's output); $\bar{a}_i$ and $\bar{b}_j$, estimates of ARX model for each flow profile; $\hat{a}_i$ and $\hat{b}_j$, estimates of the optimal ARX model (with minimum SSR); $\hat{\tau}$, estimated time constant of optimal ARX model; LS, least squares; SSR, sum of squared residuals. 152

4.18 Sample flow (Q, *top* plot) and pressure (P, *bottom* plot) waveforms generated by the two-element Windkessel model. Q is used as input to the model and P is the corresponding simulated output. 156

4.19 Pressure features and model parameters of the dataset used for the simulation studies on a two-element Windkessel model. $\bar{P}$ and PP (*upper* plot), beat-by-beat mean and pulse pressures, respectively; R_t and C_t (*middle* plot), peripheral resistance and total arterial compliance of the two-element Windkessel model, respectively; τ (*lower* plot), time constant (equal to $R_t\,C_t$). . . 157

4.20 Comparison of the estimated time constant values from *noise-free* data simulated by the two-element Windkessel model. τ_{true}, true time constant value; $\hat{\tau}_{prop}$, estimated time constant from the proposed algorithm; $\hat{\tau}_{muk}$, estimated time constant from the algorithm by Mukkamala et al. [7]. 158

4.21 A sample segment of three cardiac cycles showing the *noise-free* pressure waveform (P, *left* plot), the true flow signal (Q, *blue* line in *right* plot), and the optimal piecewise quadratic function (Q_{prop}, *red* dashed line in *right* plot) found by the proposed estimation algorithm. Notice that the flow waveforms are normalized with respect to their maximum values. 159

4.22 Comparison of the estimated time constant values from simulated pressure data corrupted by different levels of gaussian distributed white *noise*. Missing entries have abnormally high values. See Fig. 4.20 legend for explanation of symbols. 161

4.23 A sample segment of three cardiac cycles showing the optimal piecewise quadratic function (Q_{prop}, *right* plot) found by the proposed estimation algorithm on simulated pressure data corrupted by different levels of gaussian distributed white *noise*. See Fig. 4.21 legend for explanation of symbols. . . 162

4.24 Ascending aortic flow (Q_{asc}, *upper* plot) and pressure (P_{asc}, *middle* plot) waveforms simulated from the distributed-parameter model by Stergiopulos et al. [6]. $\bar{P}$ and PP (*lower* plot), beat-by-beat mean and pulse pressures, respectively. 164

4.25 Exponential fitting on the diastolic part of the ascending aortic pressure (P_{asc}) simulated from the distributed-parameter model by Stergiopulos et al. [6]. P_f, exponential fitting function; P_0, initial value of exponential function (not meaningful in this case). 166

4.26 Comparison of the estimated time constant values from *ascending aortic* synthetic data with different levels of additive white noise. τ_{true} (*blank* dots), true time constant value; $\hat{\tau}_{prop}$ (*crosshairs* in left column), estimated time constant from the proposed algorithm; $\hat{\tau}_{muk}$ (*stars* in right column), estimated time constant from the algorithm by Mukkamala et al. [7]; σ, standard deviation (in mmHg) of additive gaussian zero-mean white noise. Dashed encircled estimates indicate segments containing data generated from different model parameters, i.e., different time constants. 168

4.27 A sample segment of three cardiac cycles showing the optimal piecewise quadratic function (Q_{prop}, *right* plot) found by the proposed estimation algorithm on synthetic *ascending aortic* pressure data corrupted by different levels of gaussian distributed white noise. $P = P_{asc}$ (*left* column), ascending aortic pressure; Q (*right* column), normalized ascending aortic flow. 169

4.28 Sample deep femoral flow ($Q_{deep,fem}$, *top* plot) and pressure ($P_{deep,fem}$, *bottom* plot) waveforms generated from the distributed model by Stergiopulos et al. [6]. 171

4.29 Pressure features ($\bar{P}$ and PP, beat-by-beat mean and pulse pressures, respectively) and time constant ($\tau = R_t\, C_t$, *lower* plot) of the terminal three-element Windkessel model at the terminal node of the *deep femoral* arterial segment of the distributed model by Stergiopulos et al. [6]. 172

4.30 Comparison of the estimated time constant values from *deep femoral* synthetic data with different levels of additive white noise. τ_{true} (*blank* dots), true time constant value; $\hat{\tau}_{prop}$ (*crosshairs* in left column), estimated time constant from the proposed algorithm; $\hat{\tau}_{muk}$ (*stars* in right column), estimated time constant from the algorithm by Mukkamala et al. [7]; σ, standard deviation (in mmHg) of additive gaussian zero-mean white noise. 174

4.31 A sample segment of three cardiac cycles showing the optimal piecewise quadratic function (Q_{prop}, *right* plot) found by the proposed estimation algorithm on synthetic *deep femoral* pressure data corrupted by different levels of gaussian distributed white noise. $P = P_{deep,fem}$ (*left* column), deep femoral pressure; Q (*right* column), normalized deep femoral flow. 175

5.1 A high-level schematic representation of potential future research based on the work presented in this thesis (*green* boxes). System ID, system identification; CDS, clinical decision support. 180

List of tables

2.1 Parameters of the heart model in basal conditions (Eqs. 2.1–2.5 and 2.8) . . 19
2.2 Parameters of the septal elastance reflex effector model (Eqs. 2.6 and 2.7) . . 22
2.3 Parameters of the pulmonary circulatory system (Eqs. A1–A21) 26
2.4 Static values of main hemodynamic variables in normoxic conditions 28
2.5 Comparison of the steady-state respiratory and cardiovascular responses of the original and modified models to a 25-minute 3, 5, and 7% CO_2 hypercapnic stimulus 34
2.6 Comparison of the steady-state respiratory and cardiovascular responses of the original and modified models to a 10-minute 9, 8, and 7% O_2 hypoxic stimulus 35
2.7 Hemodynamic effects of respiration 39
2.8 Cardiovascular response to step changes in positive end-expiratory pressure (PEEP) and blood volume expansion (VE) in ARDS subjects 45

3.1 ISO standardized tests for pressure-controlled breaths 87
3.2 Comparison between patient emulator (PE) and literature data (Lit.) reported in [5] 94

4.1 Eigenvalue comparison between true and identified A matrices 146

Acknowledgements

I now take this opportunity to acknowledge all those who made this journey not only possible but also an exciting and transformative experience.

This adventure began with me deciding to speak with my later-to-become supervisor, Dr. Nicolas W. Chbat, after taking his physiological control systems course. His apparent passion to the subject stimulated my interest in the work he was doing at the time at Philips Research North America and, naturally, I approached him hoping to become part of his team. Since then, Dr. Chbat has been my main advisor and mentor and has provided me with invaluable guidance throughout my PhD. I, therefore, would like to express my deepest gratitude toward Dr. Chbat for granting me this opportunity and for being a reliable source of support.

I would like to extend my gratitude toward my academic advisor at Columbia University, Professor Andrew Laine. This unique experience could not have been possible without him facilitating the logistical and technical aspects of this academia-industry partnership.

I am at most thankful for being part of a great team, the Cardiopulmonary Group at Philips Research, and particularly Antonio, Francesco, and Roberto, with whom I worked very closely throughout my research studies. Antonio's experience in physiological modeling tremendously helped me in the development and evaluation of the modeling work of Chapter 2. Francesco, on the other hand, enthusiastically offered his knowledge, insights, and great intuition on the various aspects of system identification and helped me formulate the general framework of the estimation algorithm presented in Chapter 4. Last but not least, Roberto contributed to establishing the software-hardware interface of the patient emulator of Chapter 3. Besides our scientific endeavors, unforgettable will be the highly enjoyable but also ponderous moments during our regular espresso breaks, sharing our deepest thoughts about work, life, sports, and...tiramisu! Many thanks to the rest of my colleagues at Philips Research—Srini, Miriam, Reza, Dong, Limei, Syed—and, especially, my friends at Quadrus Technologies—Caitlyn, Jiayao, and Ben—who have been very supportive in times where support was much needed.

I would like to thank Philips Research North America for supporting my research studies through granting me the Van der Pol Fellowship and providing me access to their facilities. Also, I would like to express my gratitude toward Dr. Adam Seiver, from Philips Healthcare Therapeutic Care business unit, for supporting this work and providing his valuable feedback from the business perspective. Further, I have to acknowledge Quadrus Technologies for providing the necessary financial support during the last months of my PhD that allowed me to finalize my research work.

My warmest remarks go to my fiancèe, Neveen, who has been my partner and most significant other throughout the course of my PhD. I feel particularly grateful for having Neveen in my life as her wholehearted support, care, encouragement, and love proved to be the necessary elements to make me feel complete and joyful as a person, while being passionate and productive at work. Her sincere understanding of the challenges and commitments during my studies allowed me to deeply enjoy our relationship and have the ideal work-life balance.

Finally, I am extremely thankful to my parents, Kalliopi and Panagiotis, for their unconditional love, support, and all the sacrifices they made throughout their lives to provide me with the best education possible.

Chapter 1

Introduction

1.1 Motivation

Recent advances in computing and sensor technologies have significantly enhanced the standard of care by enabling the measurement and continuous monitoring of physiological variables, like the electrocardiogram (ECG), the arterial blood pressure (ABP), and the saturation of oxygen in the arterial blood (S_{pO_2}). Until recently, only a few medical specialists, like cardiologists in the operating room, were using sophisticated monitoring devices. However, the advent of technological solutions enabled the collection and interpretation of clinical data in all departments within medicine. This, in turn, spurred the interest of the medical community to the paradigm of evidence-based medicine, where therapies are articulated according to data-driven research work. Although more and more therapeutic trajectories have been formulated based on scientific evidence, it became apparent that most therapy recommendations were largely based on average population features and generalized protocols dictated by the subject's medical history, chronic and acute disease states. Population-based guidelines have indeed improved clinical standards; they have, though, suffered from the lack of specificity regarding the *individual* patient's characteristics and demands. However, it is well known, and even intuitive, that personalized therapies have a great potential to surpass therapy recommendations that follow general guidelines. While the latter are developed based on epidemiological (population) studies, *patient-tailored* therapies take into consideration the health status and pathophysiology of the specific patient.

For instance, general clinical protocols suggest institution of positive end-expiratory pressure (PEEP) as a ventilation therapy to patients with chronic obstructive pulmonary disease (COPD) who are under mechanical ventilation support. COPD is a common condition that causes expiratory airflow limitation due to airway obstruction, thereby leading to lung inflation and increased static alveolar pressure. Consequently, patients with COPD suffer from increased and prolonged diaphragmatic muscle drive. This muscular activity is necessary to initiate the inspiratory flow and also essential for the patient to fully exhale the volume of air that contains the waste products of tissue metabolic activity. Accordingly, PEEP application has become the recommended means to treat such patients. The externally applied PEEP aims to balance the increased alveolar pressure, prompting better ventilation and a decrease in the patient's work of breathing. However, it is also well known that elevated pressure in the lungs developed, for instance, due to high values of PEEP can adversely affect cardiac output. Therefore, any potential ventilatory intervention on COPD patients would need to be specifically tailored to the individual patient's cardiac function.

Another example of the necessity of patient-tailored ventilation therapy pertains to weaning from the mechanical ventilator. During periods of ventilation, PEEP and the level of pressure support both contribute to elevate the intrathoracic and pericardial pressures. In addition, it is well documented that ventricular wall stress is determined by the balance between intra- and extra-ventricular (i.e., pericardial) pressures. As a result, an increase in pericardial pressure yields a reduction in ventricular wall stress. This, in turn, allows the heart to pump blood easier, thus improving cardiac function. Such a cardiac function augmentation can significantly help congestive heart failure (CHF) patients who suffer from reduced cardiac contractility. On the other hand, the weaning phase (i.e., liberation from the mechanical ventilator), which is currently performed with a progressive reduction of pressure support and ultimately with spontaneous breathing trials, has the opposite effects on cardiac activity. It reduces the intrathoracic pressure, thereby increasing the wall stress and adding excessive load on the already impaired heart. If not treated appropriately, with the use of inotropic drugs, reduction of pressure support during the weaning phase may eventually lead to a complete heart failure.

The aforementioned cases demonstrate the benefits of a personalized treatment over generalized protocols when it comes to the effects of ventilation therapy on cardiac function. Such conditions arise due to the mechanical interaction phenomena between heart and lungs. Even though such cardiorespiratory interactions are pronounced in mechanically ventilated patients, they are often overlooked in clinical settings when physicians select ventilator settings and ventilation modalities. Furthermore, clinical decision-making usually relies on personal experience, intuition, generalized protocols, and trial and error strategies. Clearly, decisions made under such conditions lead to suboptimal ventilator settings affecting both respiratory and cardiovascular systems. For example, the level of pressure support, which is one of the ventilator settings under pressure support ventilation (PSV), directly affects respiratory drive and determines the degree of unloading of the respiratory muscles. An appropriate degree of respiratory muscle unloading is required to prevent muscle atrophy and fatigue and thus it is a key determinant of successful weaning and liberation from the ventilator. At the same time, the level of pressure support indirectly affects the intrathoracic pressure through the mechanical properties of the lungs and chest wall. Choosing, then, a value for the ventilator's PSV setting without considering the characteristics of the respiratory system may not only lead to ventilator-induced lung injury, but also to the development of excess pressure within the thoracic cavity. This, in turn, may compromise cardiac performance. In particular, excess pressure in the thorax could potentially compress the venae cavae, thus limiting the blood flow returning back to the heart (venous return). The loading capacity of the heart would then be decreased, resulting in a reduction, according to the Frank-Starling mechanism, of cardiac stroke volume.

Undoubtedly, the existence of a methodical and rigorous approach to selecting the appropriate settings and therapies is a clear unmet clinical need. This is of particular significance in intensive care units (ICUs) that are indispensable components of contemporary medical centers. Solely in the United States, there exist more than 6,000 ICU rooms, admitting about 5 million patients per year [8], the majority of whom are diagnosed with either a cardiovascular (e.g., CHF) or a respiratory (e.g., COPD) disorder [9]. Among them, about 30% (1.5 million patients), require the institution of mechanical ventilation as a form of life support [10]; a number that is undoubtedly set to increase as a result of the high prevalence of COPD, for instance. High occupancy of the ICUs [10] adds additional burden to the attending physicians, further contributing to suboptimal choices in therapeutic decisions. For example, a study [11] showed that standardized protocols provided optimal, patient-tailored, ventilator settings during only 12% of the time. Additionally, not only does hospitalization in an ICU room cost more than double of a hospital stay without critical care services (ranging up to about $3,500 per day [12, 13]), but also it is more likely for an ICU patient to experience major complications, like ventilator-induced lung injury and heart failure. In addition, prolonged institution of mechanical ventilation, either due to the patient's own clinical condition or to ventilation-associated complications, leads to higher costs for palliative care [14] and higher mortality rates in post-ICU days [15]. It is therefore clear that selecting the optimal ventilation therapy and/or cardiovascular intervention can dramatically reduce the length of ICU stay, bringing about significant short- and long-term health benefits to the patients and economic advantages to the clinical institutions.

Under this scheme, we believe that physiology-based mathematical models will have a profound impact on clinical practice because they allow a mechanistic understanding of the complex interaction phenomena that occur in the human cardiopulmonary system in both health and disease. Multiple neural, humoral, and mechanical mechanisms interact to generate a life-sustaining response under different diseased conditions and external interventions (e.g., institution of mechanical ventilation, fluid and drug administration). For instance, chemoreceptors control the partial pressures of oxygen and carbon dioxide in the arterial blood by regulating the depth and frequency of the breathing efforts, i.e., minute ventilation. At the same time though, the chemoreflex affects the sympathetic and vagal cardiac and systemic innervations, thereby modulating cardiac activity and the vasculature's mechanical properties. External ventilatory support, on the other hand, although utilized as a means to sustain adequate ventilation and gas exchange on patients who are unable to breath on their own, affects the respiratory system's dynamics. More importantly, it accentuates the mechanical heart-lung interactions, which are often ignored or misinterpreted in critical care settings. As such, a holistic view of the entire system's function is critical for deciding and selecting patient-tailored critical care services, such as mechanical ventilation support, fluid resuscitation, and drug administration. Large-scale integrated models offer a deterministic description of the cardiopulmonary's system inherent dynamics and can potentially assist physicians in assessing and understanding the effect of specific therapies and interventions on the patient's clinical condition.

Essentially, physiological models explain the time response of the cardiorespiratory system's components via differential equations. These equations are formulated according to "first principles" and represent the physics of physiological mechanisms and their dynamics. To this end, such equations include physiological state variables and their derivatives along with parameters that represent the physical attributes of each organ (e.g., material properties and geometry). For example, the circulatory system is typically described as a series of fluid reservoirs (capacitors) interconnected via rigid tubes (resistors). The combination of all cardiopulmonary system's components then forms an interconnected network of physiological subsystems that continuously interact in a complex and nonlinear way via gas exchange, tissue metabolism, mechanical linkages and several neural control mechanisms. In that capacity, large-scale integrated models lend themselves to the possibility in creating in-silico virtual patients that can replicate physiological responses observed under different respiratory and cardiovascular interventions. By using such virtual patients, physicians can then adjust key model parameters and recreate the physiological dynamics indicative of a patient class of interest, such as a COPD or a CHF patient. In turn, this customized class-specific model will allow physicians to perform "what-if" scenarios to assess the effectiveness of specific treatments with respect to the virtual patient health progression. Models can also provide a framework to quantitatively compare the results from such test case scenarios, enabling the selection of the optimal intervention (e.g., change in ventilator settings) in accordance to a desired therapeutic trajectory and clinical goal.

Besides contributing to the improvement of clinical care standards, model-based virtual patients can be transformed into high-fidelity emulators on which ventilators can be tested and evaluated. Physiological models, in the form of patient emulators, can then enhance and accelerate the design of new and advanced ventilators. This is particularly important for medical device companies which are keen to develop fully automated ventilation modes, in an effort to seize any opportunity presented in an expansive ventilator market that could exceed $5 billion by 2020, according to a recent study [16]. Model-based patient emulators can create a highly controllable experimental environment, enabling in such a way the quantitative comparison of different ventilation modes that takes into consideration multiple factors, such as virtual patient outcomes, patient-ventilator interactions, operator's engagement time, and hospitalization costs [11, 17]. As a consequence, such patient emulator systems can reduce or even eliminate animal or human experimentation, thereby saving time and money—typically spent on formulating the experimental protocol, on taking approval from the institutional review board committee, and on patient recruitment—during the design and development phases of mechanical ventilators.

It is thus evident that mathematical models can form a strong basis for understanding physiological mechanisms and allow the development of physiology-based virtual patients and patient emulators. Further, models can play a major role in the estimation of key cardiovascular parameters. Evaluation of the patient's condition and therapeutic decision making usually rely on only a few measurements that are readily available at the bedside, like the

ABP signal. Complementary to these, model-based parameter estimation, or system identification, techniques can enhance the clinical practice by providing physiological parameters or variables that are otherwise impractical or dangerous to obtain. One example is the cardiac output, an index of cardiac performance, which describes the amount of blood ejected by the heart. Currently, one way to measure cardiac output involves a highly invasive procedure, namely the thermodilution method, that requires the insertion of a triple-lumen catheter in the pulmonary artery. Another noninvasive, but rather expensive, way to measure cardiac output is via the Doppler ultrasound technique. The thermodilution technique is still considered the gold standard approach for measuring cardiac output, but its use has waned due to the cardiovascular complications associated with it. Furthermore, both methods provide only intermittent values and require expert personnel for the placement of the catheter or the ultrasound probe. Clearly, a noninvasive model-based technique to estimate cardiac output, or any other cardiovascular quantity, is highly desirable in the medical community. These model-based techniques can provide a continual assessment of cardiac performance via the estimation of cardiac output, which can be subsequently utilized to evaluate the circulatory system's health status.

In summary, Fig. 1.1 shows a high-level schematic representation of the motivation behind the work in this thesis which aims to improve the current standard of care in clinical settings. In particular, continual monitoring of the patient's clinical condition via medical instruments leads to a set of measured physiological variables, with one of them, for instance, being the ABP signal. These, in turn, are fed into parameter estimation, or system identification, techniques that estimate parameters or variables that are otherwise impractical or dangerous to measure (e.g., cardiac output). Practically, such techniques can fine tune a generic physiological model to the particular patient under study, thus turning the generic model into a patient specific one. The estimated parameters/variables can then complement the measured quantities for a more accurate assessment of the patient's health status, thereby offering a personalized clinical decision support (CDS) to the attending physicians and contributing to the articulation of optimal control strategies on medical devices, such as automatic selection of ventilator settings according to a therapeutic target.

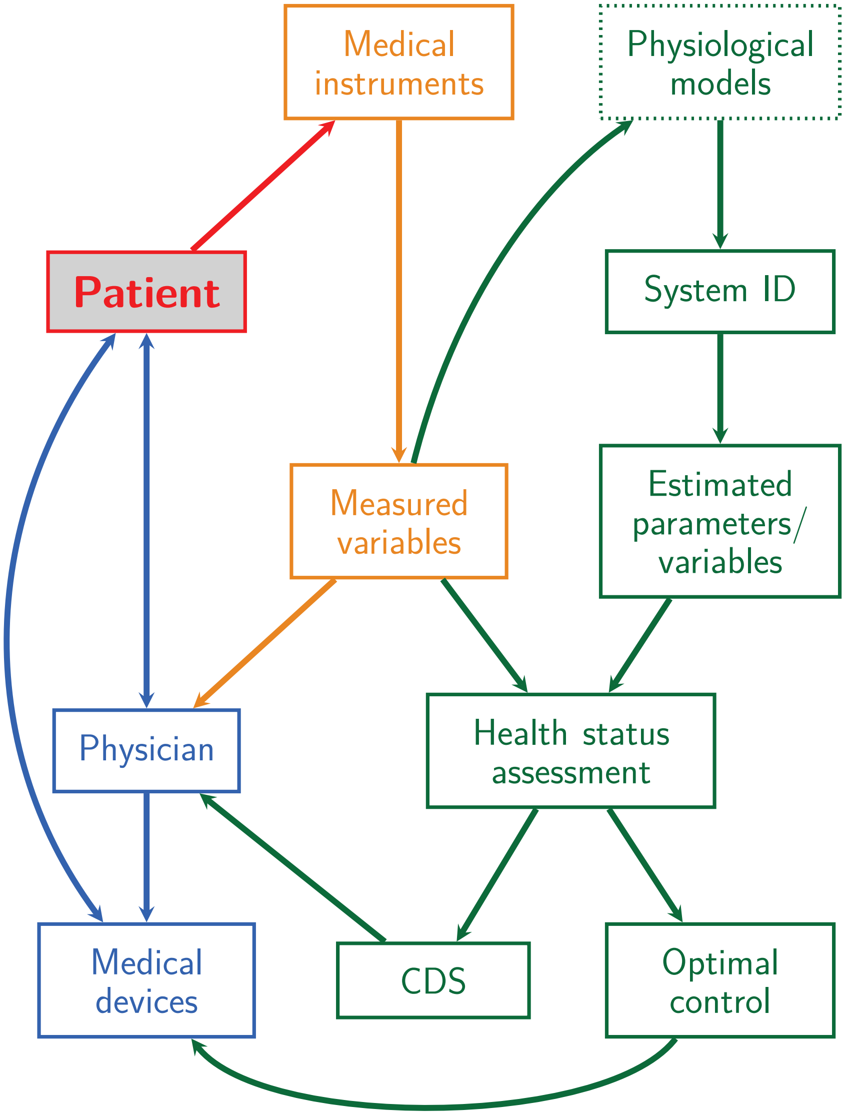
Medical instruments
Physiological models
Patient
System ID
Measured variables
Estimated parameters/ variables
Physician
Health status assessment
Medical devices
CDS
Optimal control

Fig. 1.1. A high-level schematic representation of the motivation behind the work presented in this thesis (*green* boxes). System ID, system identification; CDS, clinical decision support.

1.2 Thesis organization

This thesis outlines a plan to use physiological models as a key component for developing tools to improve testing of mechanical ventilation therapies and to estimate important cardiovascular parameters and variables. It is thus structured based on the logical progression toward the materialization of such a plan. In *Chapter 2*, we propose a series of modifications (i.e., pericardial membrane, interventricular septum, modified pulmonary circulation) to a previously developed cardiopulmonary model [18, 19] in order to better replicate the heart-lung interaction phenomena typically observed in mechanical ventilation conditions. We also describe simulation studies to validate the response of such a modified model and highlight its limitations. Then, in *Chapter 3*, we present the patient emulator, a novel system that can be used as a platform for in-silico testing of mechanical ventilation therapies. The system is based on the proposed large-scale mathematical model of the human cardiopulmonary system of Chapter 1, interfaced with a physical ventilator via a controlled piston-cylinder configuration. The performance of the proposed patient emulator is demonstrated by simulating a realistic pressure support ventilation step protocol. Finally, in *Chapter 4*, we introduce a model-based approach to estimate cardiac output from arterial blood pressure measurements. Our approach is articulated after a comprehensive analysis of the systemic circulation's dynamic characteristics and a detailed evaluation of the limitations of current estimation techniques. Validation of the proposed algorithm is carried out on synthetic data simulated from either a lumped- or a distributed-parameter model of the arterial tree.

Chapter 2

Modeling the heart-lung interactions during mechanical ventilation

2.1 Introduction

The human body is a complex dynamic system with sophisticated regulatory processes to maintain the proper function of body organs. Physiological homeostasis, defined as the body's ability to keep vital physiological variables within normal ranges, is dependent on interactions between the cardiopulmonary system and the neurohumoral control mechanisms that regulate the system's function via short- and long-term pathways. For instance, adequate oxygen (O_2) delivery to, and carbon dioxide (CO_2) removal from, the body organs are the result of neural feedback mechanisms acting on the cardiorespiratory system via inputs from different sensors. Chemoreceptors and baroreceptors, for example, respectively monitor the gas contents in blood and the level of blood pressure in the systemic arterial circulation, while chemoreflex and baroreflex signals induce changes to efferent neural activities, modulating cardiovascular and respiratory functions.

Neural pathways clearly have a major contribution to regulating the function of the cardiopulmonary system. However, direct mechanical cardiorespiratory interactions also exist.

These arise due to the location of the heart being inside the thoracic cavity. Despite its role as a natural protective medium to the heart, the thorax also forms a mechanical linkage between the heart and lungs that significantly affects cardiac activity. Lung inflation due to respiratory activity causes cyclic variations in the intrathoracic (pleural) pressure, which, in turn, affect all cardiovascular components within the thoracic cavity, such as thoracic veins, heart, pulmonary circulation, and aorta. Not only do the respiratory-induced variations in cardiac function appear under normal breathing conditions, giving rise to the well-known phenomenon of “pulsus paradoxus” [20], but they are also prevalent in mechanically ventilated subjects—though reciprocal in nature (reversed pulsus paradoxus) [21].

Mechanical ventilation is a life support procedure. It is typically instituted when a patient is unable to maintain adequate ventilation and gas exchange on their own. Positive pressure ventilation, a ubiquitous form of mechanical ventilation, delivers air at the patient’s airway opening and expands the lungs by increasing the transpulmonary pressure, the difference between alveolar and pleural pressures. Such ventilatory events induce positive swings in pleural pressure, which represents the external pressure for the thoracic veins. Consequently, downstream pressure of the systemic venous return is increased, resulting in a decrease in the flow of blood into the right atrium and right ventricle [22]. In addition, inflation of the lung alveoli compresses the pulmonary peripheral vessels, hence raising the pulmonary circulation’s impedance to blood flow [23]. Increase in right ventricular afterload in addition to preload reduction during inhalation, respectively due to the increased pulmonary impedance and decreased systemic venous return, limit the stroke volume ejected by the right ventricle. Besides right ventricular activity, inspiratory events during positive pressure ventilation also influence the function of the left ventricle. Compression of the pulmonary capillaries due to alveolar inflation reduces the blood volume in the pulmonary circulation and increases the flow of blood into the left atrium (pulmonary venous return) [24]. Thus, left ventricular filling is raised during the inspiratory heart beats, thereby leading to a higher ventricular output (stroke volume) according to the Frank-Starling mechanism.

Despite such cyclic changes in left and right ventricular functions due to breathing, the autonomic nervous system (ANS) is capable of adequately regulating the activity of the heart [25]. However, erroneous ventilator settings (e.g., high pressure support level) or sustained ventilation patterns, like in the case of positive end-expiratory pressure (PEEP), can potentially compromise cardiac performance (PEEP is a constant pressure delivered to the patient to prevent alveolar collapse). For instance, general clinical protocols [26] suggest institution of PEEP to patients with acute respiratory distress syndrome (ARDS) who are under mechanical ventilation support. ARDS is a common inflammatory condition that causes increased permeability of the pulmonary vascular wall [27]. This allows fluid to seep into the alveolar compartments, leading to a decreased lung compliance. Inevitably, patients with ARDS suffer from poor gas exchange and could eventually develop arterial hypoxemia if their condition is left untreated. Tachypnea is another typical manifestation of ARDS. It is perceived to be a response of the ANS to counterbalance the impaired gas exchange by increasing minute ventilation and permitting more oxygen-rich air to enter the lungs. Accordingly, PEEP application has become the recommended method to treat such patients [26] in an effort to expand the fluid-filled alveoli and reduce the edema. With alveolar recruitment, gas exchange is expected to improve, thereby prompting better blood oxygenation [28]. However, it is also well known that elevated pressure in the lungs, developed due to high PEEP, can adversely affect cardiac output through a reduction in systemic venous return. Therefore, any ventilatory intervention on ARDS patients would need to be appropriately selected by taking into consideration potential detrimental effects on the cardiovascular system.

It is apparent that determining the most effective therapy, like a treatment for an ARDS patient, requires a systematic understanding of the inter-connections between the different components of the human cardiopulmonary system. Mathematical models of the cardiopulmonary physiology lend themselves to such an understanding. They establish a mechanistic description of the complex cardiorespiratory interactions and demonstrate their cause-effect relationships. As a result, model-based computer simulations can provide an efficient quantitative tool to analyze cardiopulmonary dynamics. Using such simulations, medical personnel can conduct virtual physiological experiments, investigate different clinical scenarios, and assess the outcomes of specific treatments based on a virtual patient health progression.

Over the past few years, several investigators [29, 30], besides our group [18, 19], have proposed mathematical models of the combined cardiorespiratory physiology. However, most of the earlier work was not tailored to simulate mechanical ventilation scenarios. This would, in fact, require a model that includes both neural and mechanical cardiorespiratory inter-connections, since both mechanisms are necessary to reproduce the cardiopulmonary dynamics that occur under mechanical ventilation conditions (e.g., patient's response to changes in ventilator settings). Specifically, the model proposed by Cheng et al. [29], although quite comprehensive, is primarily focused on the ANS response during sleep, like simulation of Cheyne-Stokes respiration and sleep apnea. The model from Lu et al. [30], on the other hand, has more rigor in describing the dynamics associated with the mechanical heart-lung interactions. However, this model is less detailed in the description of the short-term neural mechanisms involved in the cardiovascular and respiratory control systems. The integrated cardiopulmonary model (CP Model) that was recently introduced by our group [18, 19] features cardiorespiratory control mechanisms, cardiovascular circulation, respiratory mechanics, alveolar and tissue gas exchange, as well as gas transport. It is, to our opinion, a truly comprehensive model and hence suitable to simulate cardiopulmonary dynamics in mechanically ventilated subjects. However, despite its rigorous representation of the neural pathways, the CP Model presented certain limitations, especially with regard to the mechanisms that contribute to the mechanical heart-lung interactions, as highlighted by Albanese et al. [18].

In fact, experimental studies [31] have indicated that the cyclic changes in cardiac activity induced by respiratory events are predominantly attributed to four elements: the thoracic cavity, the pericardial membrane (pericardium), the interventricular septum, and the pulmonary peripheral vessels whose resistance to blood flow changes as a function of alveolar volume. Of these elements, the CP Model proposed by Albanese et al. [18] incorporated only the thoracic cavity. As such, the purpose of this work is to better model the mechanical cardiorespiratory interactions by 1) adding the interventricular septum and the pericardium to the cardiac model of the integrated CP Model and 2) introducing a modified pulmonary circulation model that includes a varying pulmonary peripheral resistance as a function of alveolar volume. Additionally, with the current study, we aim to validate the "modified CP Model", which includes the pericardium, the septum, and the varying pulmonary peripheral resistance, by comparing the model-predicted cardiorespiratory variables with experimental human data taken from literature. Such experimental datasets represent ventilatory interventions and strategies typically considered by medical personnel.

2.2 The original cardiopulmonary model

The cardiopulmonary model (CP Model) was first proposed by Albanese et al. [18] and was based on experimental evidence of the cardiopulmonary dynamics observed in healthy, spontaneously breathing, individuals. The parameters of the model were assigned in reference to a generic 70-kg subject so that the model's dynamic response illustrates features typical to such average population data. The model was also validated with experimental data under hypoxia and hypercapnia [19]. Subsequently, as part of our work for the development of the patient emulator system of Chapter 3, we introduced certain modifications in order to improve the model's clinical interpretability and its response in mechanically ventilated conditions[1]. In particular, we proposed an extension to the ventilatory control module by including a simple model of the Hering-Breuer (HB) reflex. The HB mechanism affects respiratory muscle activity in order to prevent lung over-inflation and it is of paramount importance in spontaneously breathing subjects under mechanical ventilation support. Such a reflex was modeled via a tidal volume threshold-based logic that adapts according to the partial pressures of O_2 and CO_2 in the arterial blood. This logic determines the duration of each inspiratory breathing cycle and forces the model's respiratory muscle pressure generator to switch into the expiratory phase as soon as the tidal volume threshold has been reached. Besides the ventilatory control module, we also introduced a series of changes in the systemic circulation and respiratory mechanics models. Specifically, the four-compartment lung mechanics model was replaced by a first-order single-compartment model [32] due to its widespread use in the respiratory community. Further, the five-compartment systemic arterial circulation was reduced to a dynamically equivalent two-compartment model, as in the model proposed by Ursino [33], where the muscular, coronary, and cerebral components were lumped into the extrasplanchnic element. This choice was dictated by the fact that the analysis was not focused on studying the response of the different systemic vascular compartments, but rather on analyzing the overall cardiovascular response to physiological events induced by mechanical ventilation. Fig. 2.1 shows the high-level block diagram of the CP Model after the aforementioned adaptations. It serves as the basis for the work presented herein and will be referred to as the "original CP Model" in the following sections.

---

[1] As we will analyze in further detail in Chapter 3, the patient emulator system presents an industrial application of the modified CP Model. The model then serves as the virtual patient that is being ventilated by a real physical ventilator, where disease conditions can be instilled. Such a system was designed to offer a well-controlled experimental environment for comparison of mechanical ventilation therapies.

2.3 Model modifications

As mentioned in Section 2.1, a series of modifications are introduced to the cardiovascular component of the original CP Model in the attempt to improve its capability to reproduce heart-lung interaction mechanisms that are typically observed during mechanical ventilation. These modifications are the inclusions of the pericardium, the interventricular septum, and the modified pulmonary peripheral circulation and are all three depicted in the block diagram of Fig. 2.2. The modified pulmonary circulation model includes the following connection between alveolar space and pulmonary peripheral vessels, as schematically shown in Fig. 2.2:

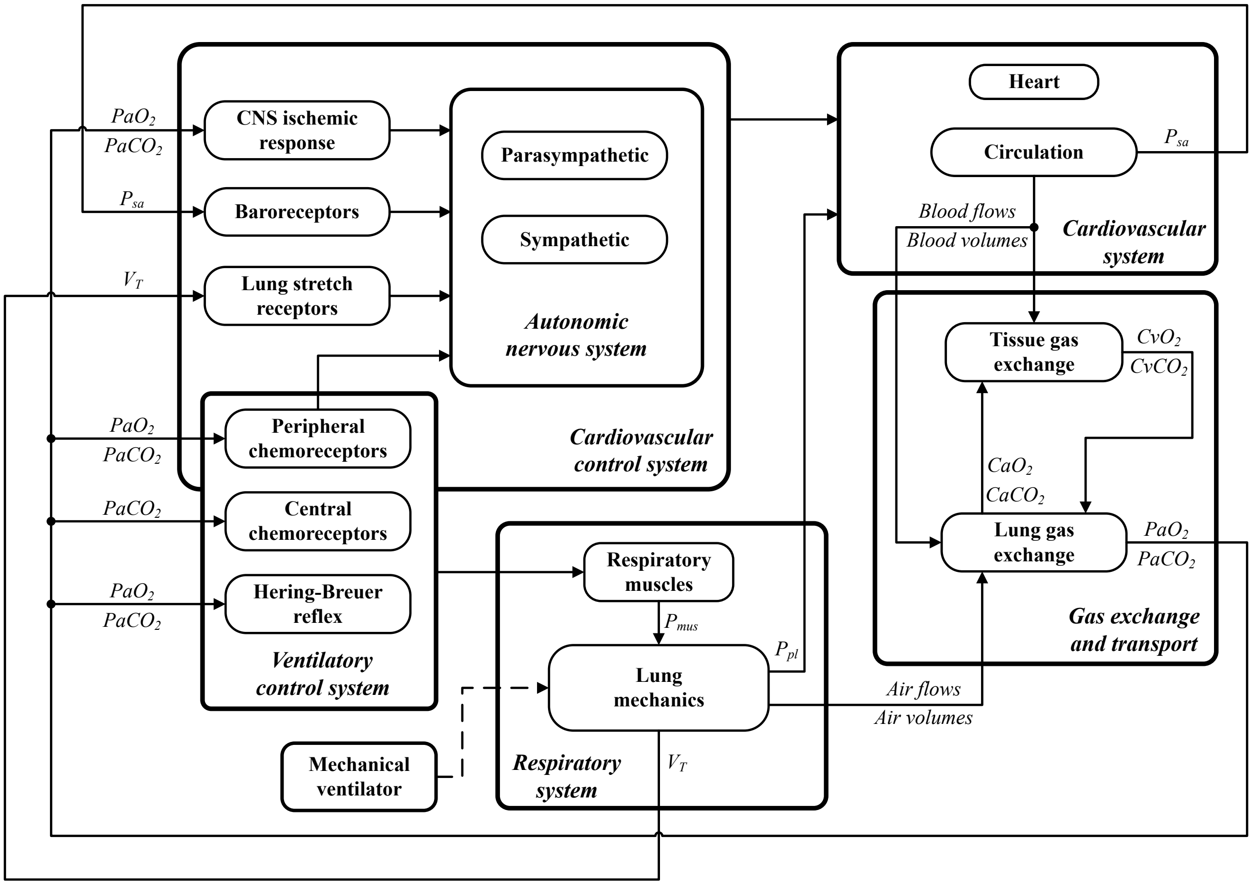
PaO2
PaCO2
CNS ischemic response
Psa
Baroreceptors
VT
Lung stretch receptors
Parasympathetic
Sympathetic
Autonomic nervous system
PaO2
PaCO2
Peripheral chemoreceptors
PaCO2
Central chemoreceptors
PaO2
PaCO2
Hering-Breuer reflex
Ventilatory control system
Cardiovascular control system
Mechanical ventilator
Respiratory muscles
Pmus
Lung mechanics
Ppl
Respiratory system
VT
Heart
Circulation
Psa
Blood flows
Blood volumes
Cardiovascular system
Tissue gas exchange
CvO2
CvCO2
CaO2
CaCO2
Lung gas exchange
PaO2
PaCO2
Gas exchange and transport
Air flows
Air volumes

Fig. 2.1. High-level block diagram of the cardiopulmonary model. CNS, central nervous system; Pa_{O_2} and Pa_{CO_2}, oxygen (O_2) and carbon dioxide (CO_2) arterial blood partial pressures, respectively; Ca_{O_2} and Ca_{CO_2}, O_2 and CO_2 gas concentrations in the arterial blood, respectively; Cv_{O_2} and Cv_{CO_2}, O_2 and CO_2 gas concentrations in the venous blood, respectively; P_{sa}, systemic arterial blood pressure; P_{pl}, pleural (intrathoracic) pressure; P_{mus}, respiratory muscle pressure; V_T, tidal volume.

1) alveolar pressure (P_A) acting as the extravascular pressure of the pulmonary capillaries, and 2) alveolar volume (V_A) affecting the flow of blood into the capillaries via a V_A-dependent resistance. In what follows are the detailed descriptions of the three aforementioned model additions.

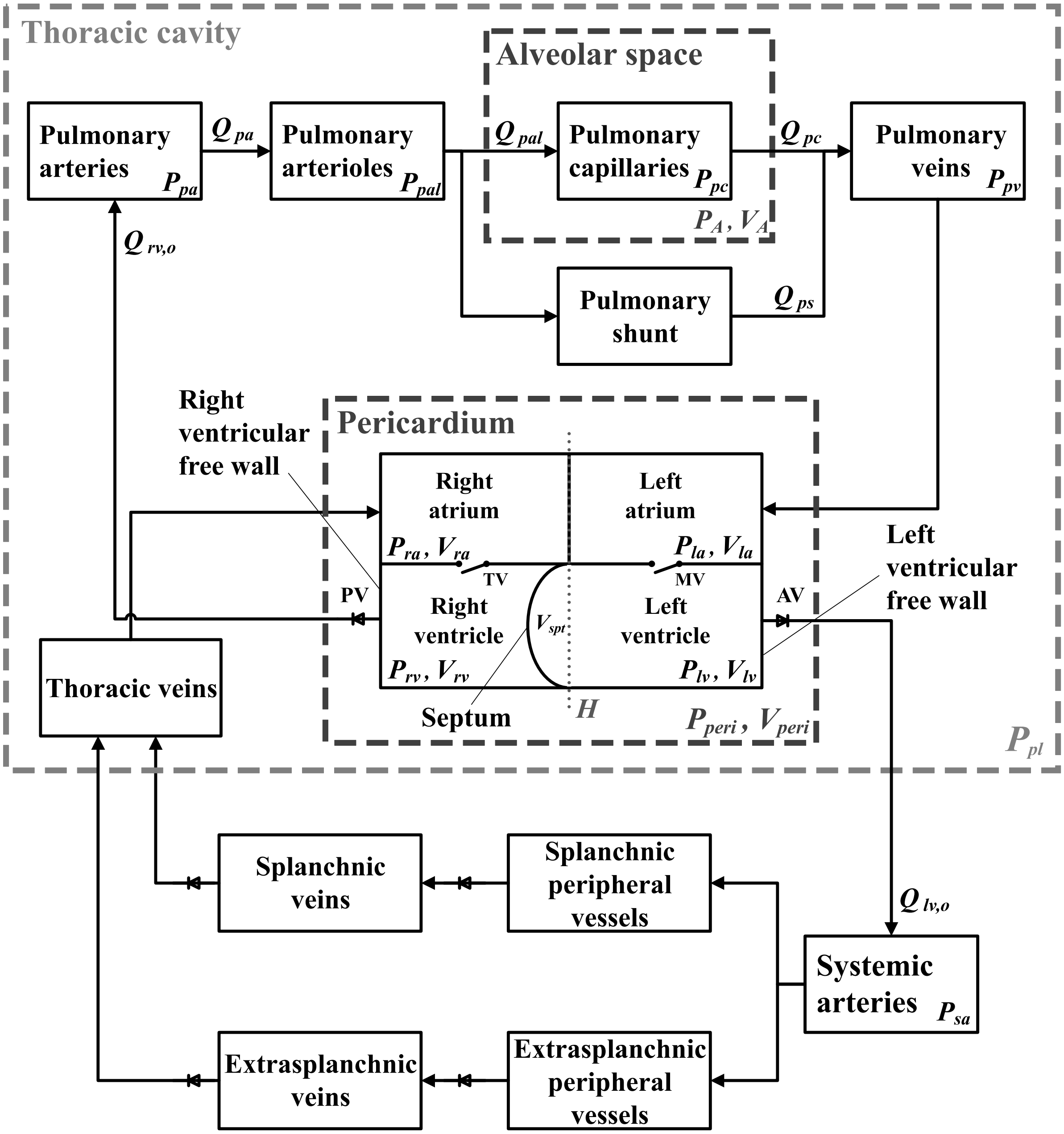
Thoracic cavity
Alveolar space
Pulmonary arteries P_{pa}
Q_{pa}
Pulmonary arterioles P_{pal}
Q_{pal}
Pulmonary capillaries P_{pc}
Q_{pc}
Pulmonary veins P_{pv}
P_A, V_A
$Q_{rv,o}$
Pulmonary shunt
Q_{ps}
Right ventricular free wall
Pericardium
Right atrium
Left atrium
P_{ra}, V_{ra}
P_{la}, V_{la}
TV
MV
PV
AV
Right ventricle
Left ventricle
V_{spt}
P_{rv}, V_{rv}
P_{lv}, V_{lv}
Left ventricular free wall
Thoracic veins
Septum
H
P_{peri}, V_{peri}
P_{pl}
Splanchnic veins
Splanchnic peripheral vessels
$Q_{lv,o}$
Systemic arteries P_{sa}
Extrasplanchnic veins
Extrasplanchnic peripheral vessels

Fig. 2.2. Schematic block diagram of the cardiovascular system of the modified CP Model. P_{sa} and P_{pa}, systemic and pulmonary arterial blood pressures; P_{ra} and P_{la}, right and left atrial pressures; P_{rv} and P_{lv}, right and left ventricular pressures; P_{pal}, pulmonary arteriolar pressure; P_{pc}, pulmonary capillary pressure; P_{pv}, pulmonary venous pressure; P_{peri}, pericardial pressure; P_{pl}, pleural (intrathoracic) pressure; P_A, alveolar pressure; V_{ra} and V_{la}, right and left atrial volumes; V_{rv} and V_{lv}, right and left ventricular volumes; V_{spt}, septal volume; V_{peri}, pericardial volume; V_A, alveolar volume; $Q_{rv,o}$ and $Q_{lv,o}$, right and left ventricular output blood flows; Q_{pa}, pulmonary arterial blood flow; Q_{pal}, pulmonary arteriolar blood flow; Q_{pc}, pulmonary capillary blood flow; Q_{ps}, pulmonary shunt blood flow; MV, mitral valve; AV, aortic valve; TV, tricuspid valve; PV, pulmonary valve; H, imaginary plane defining the volumes of the septum and of the right and left ventricular free walls.

2.3.1 Pericardial membrane

The pericardium is a membrane that envelops the heart and serves as the connective medium, inside the thoracic cavity, between the heart and the chest wall. Its behavior resembles that of a passive fluid chamber with nonlinear elastic properties. To describe the pericardial pressure-volume characteristics, we have used the exponential function proposed by Chung et al. [34]. Such a function relates the transmular pressure across the pericardium (P_{pcd})—the difference between the pressure inside the pericardial membrane (P_{peri}) and the pleural pressure outside of the pericardium (P_{pl})—with the total blood volume enclosed by it (V_{tot}),

$$P_{pcd}(V_{tot}) = P_{0,pcd} \cdot \left(e^{k_{E,pcd} \cdot (V_{tot} - V_{u,pcd})} - 1 \right). \tag{2.1}$$

$P_{0,pcd}$ is a scaling factor, $k_{E,pcd}$ is an elastance coefficient, and $V_{u,pcd}$ is the volume enclosed by the pericardium when the transmular pressure P_{pcd} is zero (unstressed volume). The values of these parameters have been taken from [30] and are reported in Table 2.1. Notice that the total volume V_{tot} is composed of the volumes of all four heart chambers, the volume of fluid within the pericardial space (V_{peri} = 40 ml [35]), in addition to the volumes of the myocardial tissue and coronary circulation, which are, however, neglected in the modified CP Model.

2.3.2 Interventricular septum

The original CP Model featured four mechanically independent heart chambers. In the modified cardiopulmonary model, we modify the original cardiac model to include only the interventricular septum, while we maintain the assumption of a rigid interatrial wall. That is, we assume that atrial interference has a minimal contribution to the overall cardiovascular hemodynamics despite the fact that such an interference could influence cardiac function [38], particularly in patients with heart defects.

To model the interventricular septum, we follow the approach suggested by Chung et

Table 2.1. Parameters of the heart model in basal conditions (Eqs. 2.1–2.5 and 2.8)

Parameter	RV free wall	LV free wall	Pericardium	Septum
$k_{E,(\cdot)}$ (ml^{-1})	0.011 [33]	0.014 [33]	0.005 [30]	0.175[36]
$P_{0,(\cdot)}$ (mmHg)	1.5 [33]	1.5 [33]	0.5 [30]	1.11 [36]
$V_{u,(\cdot)}$ (ml)	35.904 [18]	14.758 [18]	200 [30]	0 [36]
$E_{max,(\cdot)0}$ (mmHg/ml)	1.412 [37]	2.392 [37]	—	32.4

Note that the subscript $(\cdot)$ is used as a placeholder to indicate the respective compartment, that is rvf and lvf for the right (RV) and left ventricular (LV) free walls respectively, *pcd* for the pericardium, and *spt* for the septum. The subscript 0 indicates the basal value of the parameter E_{max}, which is subject to changes by the autonomic nervous system. k_E, elastance coefficient; P_0, scaling factor; V_u, unstressed volume; E_{max}, wall elastance at the maximum contraction point (end-systole).

al. [34] who extensively validated their proposed model with echocardiographic images. According to that work, the expansion of the original heart model to include the septum is accomplished by splitting the total ventricular space via an imaginary plane H into three compartments (Fig. 2.2). This separation creates three functional volumes: the right and left ventricular free wall volumes (V_{rvf} and V_{lvf}, respectively) and the septal volume (V_{spt}). V_{rvf} (or V_{lvf}) represents the blood volume that is bounded between the right (left) ventricular free wall and the plane H in Fig. 2.2. Similarly, V_{spt} characterizes the volume of blood between the septal wall and H. Further, due to the natural position of the interventricular wall protruding into the right ventricle, a septal curvature towards the right ventricular free wall (Fig. 2.2) designates a positive V_{spt}. As a consequence, right and left ventricular volumes are respectively defined as $V_{rv} = V_{rvf} - V_{spt}$ and $V_{lv} = V_{lvf} + V_{spt}$.

Heart contraction is simulated by the activation of the three walls, i.e., the right and left ventricular free walls and the interventricular septum. Modeling the ventricular walls and septum as active contractile elements originates from the physiologic behavior of the myocardium to contract as the electrical stimulus progresses via the right and left bundle branches (septal myocardium) into the Purkinje fiber system (ventricular myocardium) [39].

Moreover, such an electrical activation is known to induce the septum's paradoxical movement *against* its transmular pressure gradient [40], since left ventricular pressure (P_{lv}) is always larger than right ventricular pressure (P_{rv}) under normal physiological conditions.

The contractile activity of the three walls is modeled by means of a variable-elastance model such that the pressure-volume relationship varies between end-systolic and end-diastolic states. The transition between these two states is governed by a half-sine activation function $\phi(t)$ whose period is equal to the heart period [18]. The pressure-volume relationships of the two ventricular free walls remain unchanged as compared to the ones in [18]. For instance, the maximal isometric transmular pressure across the left ventricular free wall ($P_{max,lvf}$) is defined as a function of V_{lvf} according to the equation

$$P_{max,lvf}(t) = \phi(t) \cdot P_{max,lvf}(V_{lvf})|_{ES} + (1 - \phi(t)) \cdot P_{max,lvf}(V_{lvf})|_{ED}. \tag{2.2}$$

$P_{max,lvf}(V_{lvf})|_{ES} = E_{max,lvf} \cdot (V_{lvf} - V_{u,lvf})$ and $P_{max,lvf}(V_{lvf})|_{ED} = P_{0,lvf} \cdot (e^{k_{E,lvf} \cdot V_{lvf}} - 1)$ respectively are the end-systolic (ES) and end-diastolic (ED) components that determine the elastic behavior of the free wall during a cardiac cycle. $E_{max,lvf}$ is the wall elastance at the maximum contraction point (end-systole), $V_{u,lvf}$ is the unstressed volume of the ventricular wall, and $P_{0,lvf}$, $k_{E,lvf}$ are the parameters that characterize the end-diastolic exponential function. Subsequently, the maximal pressure of the left ventricle (prior to any viscous losses due to blood flow over the aortic valve) can be computed by taking into account that P_{peri} acts as the external (reference) pressure of the ventricular free wall. Hence, $P_{max,lv} = P_{max,lvf} + P_{peri}$. For the sake of brevity, the equations that are necessary to simulate the complete ventricular function, including ventricular filling, valve operation, and ventricular ejection, are omitted from this section. A detailed description of these elements can be found in [33].

As for the elastic properties of the right ventricular free wall and septum, an analogous approach is considered. The right ventricular free wall adheres to the same formulation of the biphasic pressure-volume relationship as in (2.2). On the other hand, the behavior of the septal wall is modeled in the inverse way. Specifically, Chung et al. [34] suggests a variable-elastance model that predicts the instantaneous septal volume V_{spt} as a function of the pressure gradient across the septum, $P_{spt} = P_{lv} - P_{rv}$:

$$V_{spt}(t) = \phi(t) \cdot V_{spt}(P_{spt})|_{ES} + (1 - \phi(t)) \cdot V_{spt}(P_{spt})|_{ED}, \tag{2.3}$$

where

$$V_{spt}(P_{spt})|_{ES} = \frac{1}{E_{max,spt}} \cdot P_{spt} + V_{u,spt} \quad \text{and} \tag{2.4}$$

$$V_{spt}(P_{spt})|_{ED} = \begin{cases} \dfrac{1}{k_{E,spt}} \cdot \log\left(\dfrac{P_{spt}}{P_{0,spt}} + 1\right) + V_{u,spt}, & P_{spt} \geq 0 \\ -\dfrac{1}{k_{E,spt}} \cdot \log\left(-\dfrac{P_{spt}}{P_{0,spt}} + 1\right) + V_{u,spt}, & P_{spt} < 0 \end{cases} \tag{2.5}$$

for end-systole (ES) and end-diastole (ED), respectively. The parameters $E_{max,spt}$, $V_{u,spt}$, $k_{E,spt}$, and $P_{0,spt}$ have the same meaning as those of the left ventricular free wall in (2.2). The values of the parameters that characterize the elastic properties of all three cardiac walls are reported in Table 2.1, along with the corresponding reference source.

It is important to note that the difference between $E_{max,(\cdot)0}$ in Table 2.1 and $E_{max,(\cdot)}$ used in (2.2–2.5) is attributed to the effect of the autonomic nervous system. The ANS efferent sympathetic pathway regulates the magnitude of cardiac contraction by controlling the elastance values of the two ventricular free walls and of the septum. $E_{max,(\cdot)0}$ then indicates the basal elastance value that is subject to modulation by the ANS, whereas $E_{max,(\cdot)}$ is the resultant value after the action of the ANS. The equations describing the regulatory mechanisms for the ventricular free wall elastances are kept the same as the ones in the original CP Model [18], which were taken from Ursino and Magosso [37]. We then need to introduce the model for the septal elastance effector response to the ANS sympathetic activity. This model follows the same approach suggested by Ursino and Magosso [37] for the ventricular free wall elastances; that is, it includes a logarithmic function to describe the effector's static response, a pure delay, and a low-pass first-order filter for simulating its dynamic behavior. Specifically, the maximal elastance of the septum ($E_{max,spt}$) changes with respect to the frequency of the sympathetic efferent fibers (f_{sh}) according to the following equations:

$$\sigma_{E_{max,spt}} = \begin{cases} G_{E_{max,spt}} \cdot \ln\left(f_{sh} \cdot (t - D_{E_{max,spt}}) - f_{es,min} + 1\right), & \text{if } f_{sh} \geq f_{es,min} \\ 0, & \text{if } f_{sh} < f_{es,min} \end{cases}, \tag{2.6}$$

$$\frac{d\Delta E_{max,spt}}{dt} = \frac{1}{\tau_{E_{max,spt}}} \cdot (-\Delta E_{max,spt} + \sigma_{E_{max,spt}}), \text{ and} \tag{2.7}$$

$$E_{max,spt}(t) = \Delta E_{max,spt}(t) + E_{max,spt0}. \tag{2.8}$$

$\sigma_{E_{max,spt}}$ is the output of the logarithmic static function in (2.6), $G_{E_{max,spt}}$ is a gain factor, $D_{E_{max,spt}}$ is the latency in the static response, $\tau_{E_{max,spt}}$ is the time constant of the first-order filter, and $f_{es,min}$ is a threshold for sympathetic stimulation. Following the method by Ursino and Magosso [37], $G_{E_{max,spt}}$ and $E_{max,spt0}$ are respectively set to 16.1% and 81% of the original septal elastance value reported in [36]. The parameter values, besides $E_{max,spt0}$ (see Table 2.1), of this reflex regulatory mechanism are reported in Table 2.2.

Table 2.2. Parameters of the septal elastance reflex effector model (Eqs. 2.6 and 2.7)

$D_{E_{max,spt}} = 2$ s [37]	$\tau_{E_{max,spt}} = 8$ s [37]
$G_{E_{max,spt}} = 6.44$ mmHg·ml^{-1}·(spikes/s)$^{-1}$	$f_{es,min} = 2.66$ spikes/s [37]

See text for explanation of symbols.

2.3.3 Pulmonary peripheral vessels

The location of the pulmonary circulation within the lung interstitium, the space between the alveoli and the visceral pleura, dictates that the external pressure of most of the pulmonary vessels, like the pulmonary arteries and veins, is equal (on average) to pleural pressure. However, the capillaries that participate in gas exchange are in direct contact with the alveoli. This, in fact, allows the diffusion of gases, like O_2 and CO_2, to take place. Consequently, it is reasonable to conclude that the extravascular pressure of these capillaries more closely resembles an average alveolar pressure rather than the pleural pressure [31]. This consideration is also supported by the "waterfall phenomenon" that has been observed between pulmonary capillary and venous vasculatures [41]. Additionally, the close proximity of the capillaries to the alveolar space contributes to the compression of the intra-capillary lumen as alveolar volume increases [42]. Such a phenomenon is the primary factor in the increase of pulmonary impedance and thus of right ventricular afterload, typically observed during inspiration in positive pressure ventilation [23]. Reducing the vascular lumen inevitably leads to a reduction of the blood flow toward the pulmonary capillaries, an event that can be represented by an increased hydraulic resistance of the conduit preceding the capillary compartment.

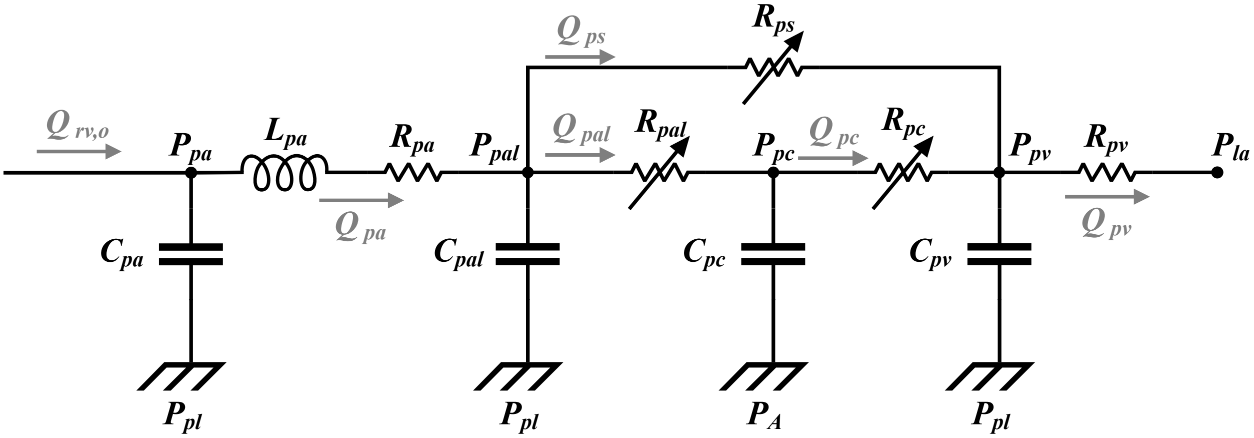

Fig. 2.3. Electrical diagram of the pulmonary circulation model of the modified CP Model. P, pressure; Q, blood flow; R, resistance; L, inertance; C, compliance. Subscripts: pa, pulmonary arteries; pal, pulmonary arterioles; pc, pulmonary capillaries; pv, pulmonary veins; la, left atrium; ps, pulmonary shunt; pl, pleural space; A, alveolar space. The variable resistances P_{pal}, R_{pc}, and P_{ps} are indicated by diagonal arrows.

Accordingly, Fig. 2.3 shows the modified pulmonary circulation model that is developed based on the work by Lu et al. [30]. The model consists of four pressure nodes—pulmonary arteries (P_{pa}), pulmonary arterioles (P_{pal}), pulmonary capillaries (P_{pc}), and pulmonary veins (P_{pv})—, a pulmonary shunt compartment, and three variable resistances—pulmonary arteriolar (or pre-capillary) resistance (R_{pal}), pulmonary shunt resistance (R_{ps}), and pulmonary post-capillary resistance (R_{pc}). In comparison with the original CP Model, the following modifications have been introduced. 1) The single pulmonary peripheral compartment in the original model [18] has been replaced by two nodes: the pulmonary arterioles and the pulmonary capillaries. With this approach, we attain an explicit separation of the extra-alveolar peripheral vessels from the capillary level that is in close proximity to the alveoli. Pleural pressure (P_{pl}) can then be set as the external pressure of the pulmonary arterioles, while the pressure at the pulmonary capillaries is referenced to alveolar pressure (P_A). These two distinct pressure nodes also allow for a more accurate representation of the pulmonary shunt. Anatomically, the shunt is located between pulmonary arteries and pulmonary veins and comprises the pulmonary peripheral vessels that do not participate in gas exchange. Hence, it is more reasonable, from an anatomical point of view, to model the shunt as a compartment, parallel to the pulmonary capillaries, that originates from the arteriolar pressure node and thus it is not subjected to the same transmular pressure as the capillaries (see Fig. 2.3). 2) The effects of the compression of the pulmonary capillaries due to lung expansion have been modeled via a variable resistance (R_{pal}) that is function of alveolar volume (V_A). According to Lu et al. [30],

$$R_{pal}(V_A) = R_{pal,0} \cdot \left(\frac{V_A}{V_{A,max}} \right)^2, \tag{2.9}$$

where $R_{pal,0}$ is a constant value that represents the arteriolar resistance when alveolar volume has reached its maximum value, $V_{A,max}$. Alveolar inflation hence yields a quadratic increase in R_{pal}, thereby inducing a reduction of the blood flow toward the pulmonary capillaries. Clearly, (2.9) is a function solely of V_A. However, retaining such a relationship with no additional modifications invalidates our modeling scheme, which includes a pulmonary shunt component (see Figs. 2.2 and 2.3) to simulate the amount of blood that does not contribute to gas exchange. Modeling the effects of anatomical shunting is accomplished by adjusting the resistance values of shunted and non-shunted pulmonary peripheral compartments, i.e., R_{ps}, and R_{pal} and R_{pc} respectively, such that the distribution of blood between the two segments matches the selected shunt fraction (sh). For example, in normal physiological conditions sh is equal to 1.7%. This indicates that 1.7% of blood flow coming out of the pulmonary arteries does not participate in gas exchange (shunted blood flow). As a result, not only does the arteriolar resistance need to depend on V_A but on sh as well. Hence, (2.9) is modified as follows:

$$R_{pal}(V_A, sh) = \frac{R_{pp,tot}}{2 \cdot (1 - sh)} \cdot \left(\frac{V_A}{FRC_{nom}} \right)^2 , \tag{2.10}$$

where $R_{pp,tot}$ is the total resistance of the pulmonary peripheral circulation at steady-state conditions and at a nominal functional residual capacity (FRC_{nom}),

$$R_{pp,tot} = \frac{R_{ps} \cdot (R_{pc} + P_{pal}(V_A = FRC_{nom}))}{R_{ps} + R_{pc} + P_{pal}(V_A = FRC_{nom})}. \tag{2.11}$$

The value of FRC_{nom} is selected equal to 2.25 liters as the model-predicted functional residual capacity for a nominal set of respiratory system parameters, i.e., an airway resistance of 1.7459 $cmH_2O \cdot s/l$, and lung and chest wall compliances of 0.2 l/cmH_2O and 0.2445 l/cmH_2O, respectively. The complete set of equations that describe the pulmonary circulation model is presented in the Appendix.

Table 2.3 presents the parameters of the pulmonary circulation model of Fig. 2.3 along with the reference sources where the parameter values were taken from. Notice that the compliance and unstressed volume values of the pulmonary arterioles and pulmonary capillaries (C_{pal} and $V_{u,pal}$, and C_{pc} and $V_{u,pc}$, respectively) have been computed such that their parallel arrangement (in zero-flow conditions) provides values equivalent to those published in [18] and [37]. In particular, the unstressed volume of the pulmonary peripheral circulation in the original CP Model [18] is 108.24 ml, while Ursino and Magosso [37] report a value of 5.8 ml/mmHg for the compliance of the peripheral compartments. To complete the calculation, we follow the convention used by Lu et al. [30] where $C_{pc} = 2 \cdot C_{pal}$ and $V_{u,pc} = {}^{3}\!/_{2} \cdot V_{u,pal}$.

Table 2.3. Parameters of the pulmonary circulatory system (Eqs. A1–A21)

Compliance (ml/mmHg)	Unstressed volume (ml)	Resistance (mmHg·s/ml)	Inertance (mmHg·s^2/ml)
$C_{pa} = 0.76$ [18]	$V_{u,pa} = 0$ [18]	$R_{pa} = 0.023$ [18]	$L_{pa} = 1.8 \cdot 10^{-4}$ [18]
$C_{pal} = 1.93$	$V_{u,pal} = 43.30$	$R_{pp,tot} = 0.0894$ [37]	
$C_{pc} = 3.87$	$V_{u,pc} = 64.94$		
$C_{pv} = 25.37$ [18]	$V_{u,pv} = 105.6$ [18]	$R_{pv} = 0.0056$ [18]	

See text and Fig. 2.3 legend for explanation of symbols.

2.4 Comparison between modified and original models

In this section, we compare the response of the modified CP Model with the original model under normal breathing conditions. The dynamic equations of the modified CP Model, including those that describe the pericardium, the interventricular septum, and the modified pulmonary circulation, were programmed in Simulink® (MathWorks, Natick, MA). Simulink® is a computational environment specialized for high-accuracy numerical integration of ordinary differential equations. In our implementation, simulation of the cardiopulmonary system's dynamic response was attained by solving the model's differential equations via the fourth-order Runge-Kutta method with a fixed-size integration step of 0.0005 seconds (2 kHz rate).

Comparison of the response of the modified CP Model with the original model serves two primary purposes. 1) First, we intend to illustrate that the original and modified models are dynamically equivalent, both in normal resting conditions (normoxia) and under external perturbations, namely hypercapnia and hypoxia. These scenarios were selected in line with previous work by our group [18, 19], where model-predicted respiratory and cardiovascular variables were compared against experimental data collected from healthy human subjects. Demonstrating the equivalence of the responses from the two models effectively provides a verification that any validation performed by Cheng et al. [19] would also hold for the modified CP Model. 2) Second, we want to illustrate the differences between the two models with regard to the mechanical effects of respiration (normal breathing) on cardiovascular function. This serves as a first demonstration of the improvements presented by the three newly introduced model components toward a better representation of the heart-lung interactions. A more rigorous analysis is presented in Section 2.5, where we validate the modified CP model with experimental data, and in Section 2.6, where we evaluate the individual contribution of the three new model components to the overall model response in mechanical ventilation scenarios.

2.4.1 Normoxia

Table 2.4 includes the static values (at end-expiration) of main hemodynamic variables predicted by the modified CP Model in normoxic conditions. That is, we simulate the response of a healthy individual who is breathing spontaneously from room air ($F_{I_{O_2}} = 21.038\%$ and $F_{I_{CO_2}} = 0.0421\%$). The predictions of the original CP Model under the same normoxic conditions are also reported in Table 2.4, along with the normal ranges observed in the general population. All model-predicted variables attain static values within their expected physiological ranges. We notice no significant difference in the variability between the two models and we can therefore conclude that the overall hemodynamic responses of the two models are practically equivalent.

In detail, both end-systolic and end-diastolic left ventricular volumes (V_{lv}) of the modified CP Model show a notable increase compared to those predicted by the original model. On the other hand, right ventricular volumes (V_{rv}) are reduced relatively to their original values.

Table 2.4. Static values of main hemodynamic variables in normoxic conditions

Variable	Original model	Modified model	Normal range
Systemic arterial pressure, P_{sa} (mmHg)			
Mean	89.39	89.39	70–105 [18]
Systolic	121.83	121.85	100–140 [18]
Diastolic	76.66	76.77	60–90 [18]
Left ventricular pressure, P_{lv} (mmHg)			
Systolic	121.83	121.85	90–140 [18]
End-diastolic	4.68	4.65	4–12 [18]
Left ventricular volume, V_{lv} (ml)			
End-systolic	52.64	55.98	37–57 [43]
End-diastolic	133.24	136.07	121–163 [43]
Left atrial pressure, P_{la} (mmHg)			
Mean	4.55	4.35	4–12 [44]
Pulmonary arterial pressure, P_{pa} (mmHg)			
Mean	15.10	14.35	9–18 [44]
Systolic	24.25	26.86	15–28 [18]
Diastolic	9.47	7.11	5–16 [18]
Right ventricular pressure, P_{rv} (mmHg)			
Systolic	24.25	26.86	15–28 [18]
End-diastolic	1.25	1.91	0–8 [18]
Right ventricular volume, V_{rv} (ml)			
End-systolic	52.21	49.31	36–64 [45]
End-diastolic	129.94	127.05	121–167 [45]
Right atrial pressure, P_{ra} (mmHg)			
Mean	1.30	1.71	2–6 [18]

The model-predicted values are taken from the end-expiratory heart beat after a 2,000-second simulation.

Such volumetric changes are attributed to the inclusion of the interventricular septum whose natural position toward the right ventricular free wall (see Section 2.3) inevitably prompts a decrease in right ventricular volume and a concomitant increase in the volume of the left ventricle. As for the ventricular pressures, we anticipate that an increase (or decrease) in the end-diastolic volume induces a decrease (increase) in the corresponding end-diastolic pressure. For instance, a reduction in the end-diastolic left ventricular pressure (4.68 mmHg in the original model versus 4.65 mmHg in the modified model) is observed following the increase in the end-diastolic V_{lv} (133.24 ml versus 136.07 ml, respectively). It is worth noticing though that the magnitudes of change in end-diastolic left and right ventricular pressures (P_{lv} and P_{rv}, respectively) between original and modified models are significantly different; namely, P_{rv} increases by 0.66 mmHg whereas P_{lv} is reduced by just 0.03 mmHg. This phenomenon is associated with the compound effects of septum and pericardium on each ventricle. On one hand, the septum-induced changes in ventricular volumes, and thus pressures, are opposite in direction between left and right ventricles, i.e., decrease in P_{lv} and increase in P_{rv} (secondary to the septum-induced increase in V_{lv} and decrease in V_{rv}). On the other hand, the pericardium's compressive forces tend to increase the pressures of both ventricles, especially at the higher end-diastolic volumes. Hence, the magnitude of change in end-diastolic P_{lv} and P_{rv} is practically determined by the net balance between septal and pericardial forces, which can act either toward the same or the opposite direction. Ventricular volumes influence mean atrial pressures as well. For instance, the increased left ventricular volume (modified model) requires a larger blood flow out of the left atrium, thereby inducing a reduction in left atrial pressure (P_{la}). On the other hand, right atrial pressure (P_{ra}) is elevated due to lower V_{rv} values. Finally, we notice that systemic and pulmonary arterial pressures (P_{sa} and P_{pa}, respectively) of the modified model exhibit a disparate behavior with respect to the values of the original model. Mean, systolic, and diastolic P_{sa} exhibit a negligible change owing to the effects of the cardiovascular control mechanisms (e.g., baroreceptors). Systemic pulse pressure, the difference between systolic and diastolic pressures, is slightly reduced (45.17 mmHg in the original CP Model versus 45.08 mmHg in the modified model) due to the small decrease in the left ventricular stroke volume (80.59 ml versus 80.09 ml, respectively). However, P_{pa} is particularly affected by the proposed model additions. Specifically, mean P_{pa} is reduced, whereas pulse pressure is increased (9.15 mmHg originally versus 12.51 mmHg in the modified model). These observations lead us to conclude that although we tried to maintain the same hemodynamic behavior of the modified pulmonary circulation with respect to its original implementation (see Section 2.3), the pulmonary system impedance in the modified CP Model was slightly altered, thereby leading to the aforementioned changes in P_{pa}. The same conclusion can also be drawn by Fig. 2.4, where we compare the left (left plot) and right (right plot) ventricular pressure-volume loops from the two models. Even though the shape of the modified model's left ventricular pressure-volume loop remain the same as that of the original model (i.e., same systemic impedance), the pressure-volume loop of the right ventricle in the modified model shows a significant change due to the change in pulmonary impedance.

2.4.2 Hypercapnia & Hypoxia

Hypercapnic conditions are simulated by controlling the fraction of inspired CO_2 ($F_{I_{CO_2}}$) while keeping the fraction of inspired O_2 ($F_{I_{O_2}}$) at a normal room air level (21.038%). On the other hand, hypoxia is attained by controlling $F_{I_{O_2}}$ while maintaining $F_{I_{CO_2}}$ at its normal level (0.0421%). In the current study, we replicate the scenarios used by Cheng et al. [46]: 1) In the hypercapnic experiments, $F_{I_{CO_2}}$ is adjusted from its baseline value in room air to the desired hypercapnia level and subsequently reverted to baseline after a 25-minute period. 2) For the hypoxia case, we first lower $F_{I_{O_2}}$ from 21.038% to the desired level and then, after 10 minutes, we change it back to room air level. For example, Figs. 2.5 and 2.6 display the dynamic respiratory responses of the original and modified CP Models during a 7% CO_2 hypercapnic stimulus and a 7% O_2 hypoxic stimulus, respectively. Both figures include the time profiles of tidal volume (V_T), respiratory rate (RR), minute ventilation

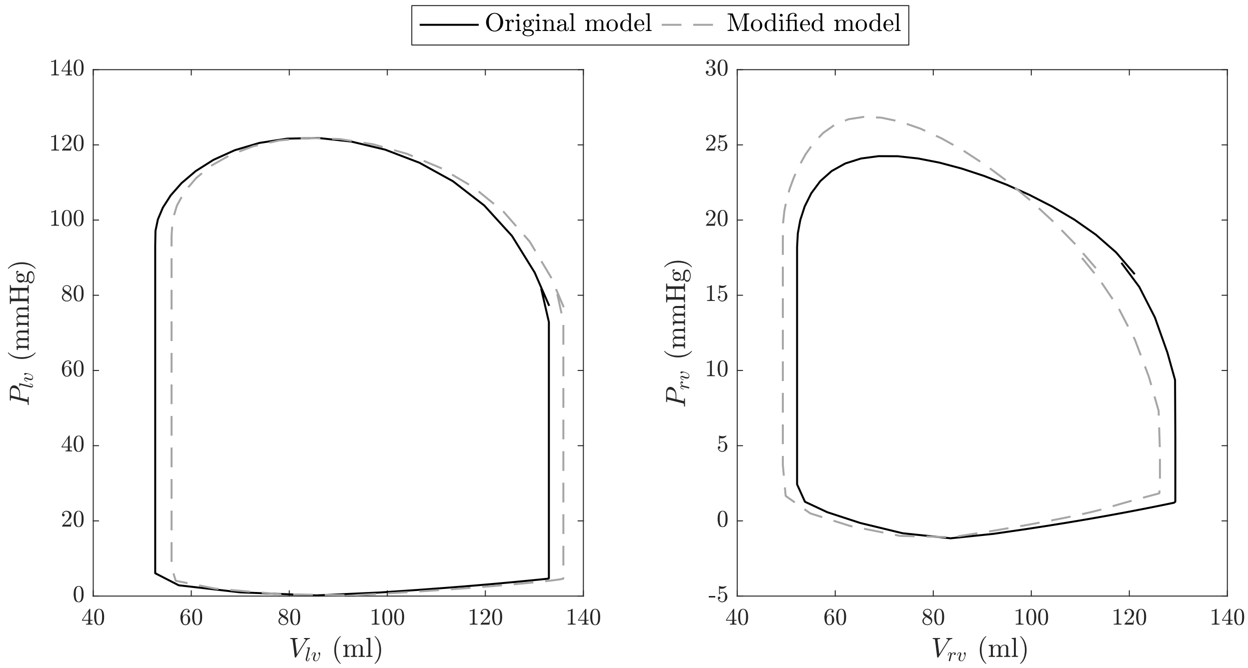

Fig. 2.4. Comparison of left (*left* plot) and right (*right* plot) ventricular pressure-volume loops between original (*black* line) and modified (*gray* dashed line) models. P_{lv} and V_{lv}, left ventricular pressure and volume, respectively; P_{rv} and V_{rv}, right ventricular pressure and volume, respectively.

(V_e), and alveolar CO_2 and O_2 partial pressures ($P_{A_{CO_2}}$ and $P_{A_{O_2}}$, respectively). To obtain a quantitative assessment of the difference between the predicted signal trajectories from the two models (modified versus original), we compute the coefficient of variations (CV) of the root mean squared deviations (RMSD),

$$\mathrm{CV(RMSD)} = \frac{\mathrm{RMSD}}{\bar{x}_o} = \frac{\sqrt{\dfrac{\sum_{i=1}^{N} \left(x_o(i) - x_m(i)\right)^2}{N}}}{\bar{x}_o}, \tag{2.12}$$

where x_o represents V_T, RR, V_e, $P_{A_{CO_2}}$, or $P_{A_{O_2}}$ in the original CP Model ($\bar{x}_o$ is the corresponding mean value over the duration of the simulation), x_m represents the same variables in the modified CP Model, N is the total number of samples in the dataset, and i represents the i-th sample of the dataset. Low CV(RMSD) values for all five respiratory variables in both hypercapnia and hypoxia experiments (see Figs. 2.5 and 2.6 respectively) indicate that the modified CP Model can be considered equivalent to the original model.

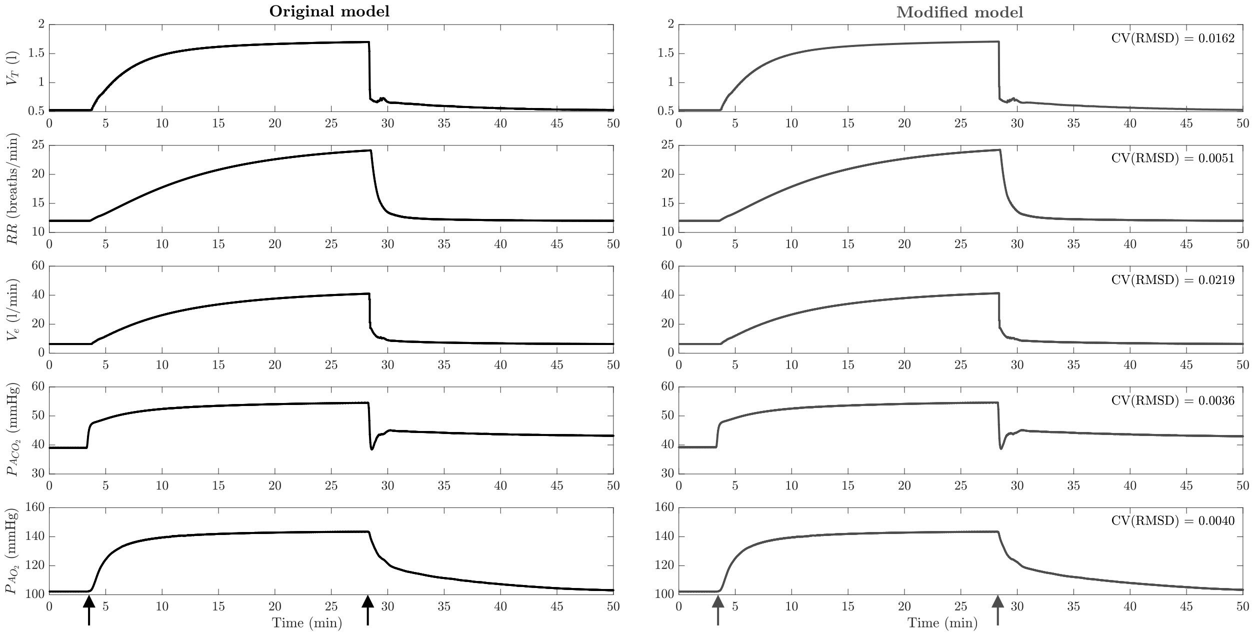

Fig. 2.5. Comparison of the respiratory responses of the original (*left* column) and modified (*right* column) models to a 25-minute 7% CO_2 hypercapnic stimulus. From *top* to *bottom*: tidal volume (V_T), respiratory rate (RR), minute ventilation (V_e), alveolar partial pressure of CO_2 ($P_{A_{CO_2}}$), and alveolar partial pressure of O_2 ($P_{A_{O_2}}$). The coefficient of variations (CV) of the root mean squared deviation (RMSD) between each of the simulated variables from the original model and those from the modified model are shown on the top right. The arrows on the time axis represent the time instance at which the stimulus is administered and subsequently withdrawn.

A comparison of the steady-state responses of the two models for different hypercapnic (3, 5, and 7% $F_{I_{CO_2}}$) and hypoxic (9, 8, and 7% $F_{I_{O_2}}$) stimuli is shown in Tables 2.5 and 2.6 respectively. These tables report the steady-state values of V_T, RR, V_e, $P_{A_{CO_2}}$, $P_{A_{O_2}}$, cardiac output (CO), heart rate (HR), and systolic, mean, and diastolic arterial blood pressures (SBP, MBP, and DBP respectively) immediately before the administration (values inside the parentheses in Tables 2.5 and 2.6) and the withdrawal of the stimulus. Notice that because we ran the simulations with the same nominal parameter set (representing a healthy individual), the steady-state response is always the same prior to the perturbation in the inspired gas fractions. As anticipated after examining the dynamic responses in Figs. 2.5 and 2.6, the steady-state response of the modified CP Model exhibits minimal variation with

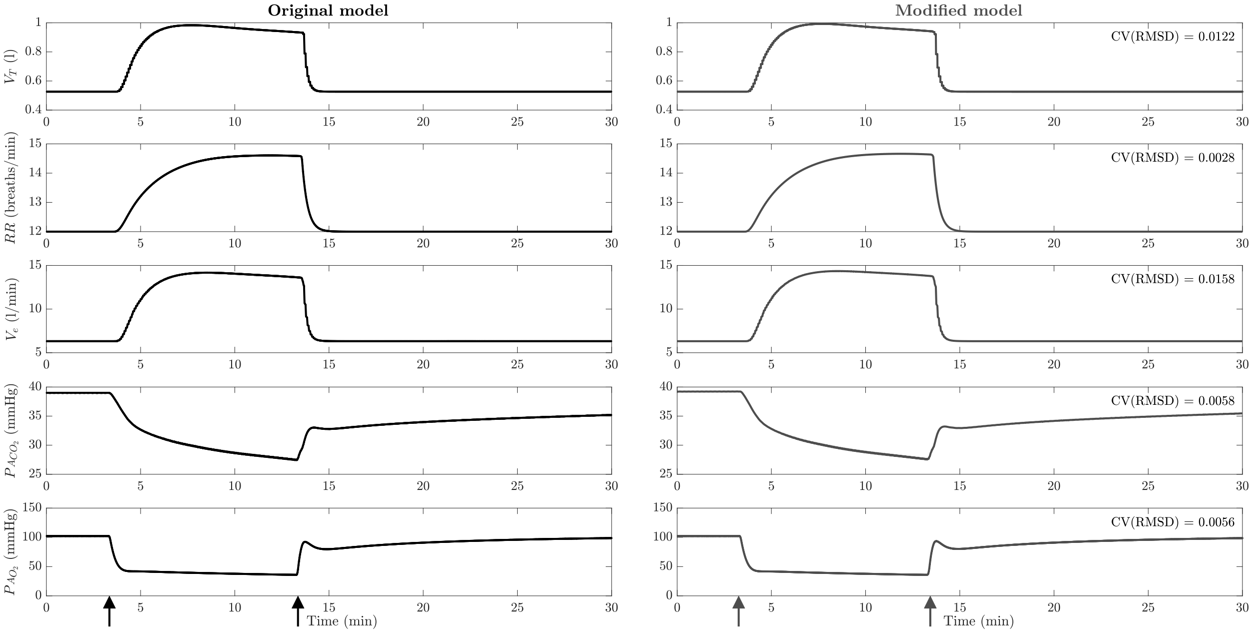

Fig. 2.6. Comparison of the respiratory responses of the original (*left* column) and modified (*right* column) models to a 10-minute 7% O_2 hypoxic stimulus. From *top* to *bottom*: tidal volume (V_T), respiratory rate (RR), minute ventilation (V_e), alveolar partial pressure of CO_2 ($P_{A_{CO_2}}$), and alveolar partial pressure of O_2 ($P_{A_{O_2}}$). The coefficient of variations (CV) of the root mean squared deviations (RMSD) between each of the simulated variables from the original model and those from the modified model are shown on the top right. The arrows on the time axis represent the time instance at which the stimulus is administered and subsequently withdrawn.

respect to that of the original model under all conditions, whether normoxic (prestimulus), hypercapnic, or hypoxic.

Table 2.5. Comparison of the steady-state respiratory and cardiovascular responses of the original and modified models to a 25-minute 3, 5, and 7% CO_2 hypercapnic stimulus

Variable	$F_{I_{CO_2}}$ (%)	Original model	Modified model
V_T (l)	3	0.71 (0.53)	0.72 (0.53)
	5	1.09 (0.53)	1.10 (0.53)
	7	1.70 (0.53)	1.71 (0.53)
RR (breaths/min)	3	12.71 (12.00)	12.75 (12.00)
	5	17.53 (12.00)	17.64 (12.00)
	7	24.11 (12.00)	24.20 (12.00)
V_e (l/min)	3	9.05 (6.32)	9.13 (6.32)
	5	19.05 (6.32)	19.38 (6.32)
	7	40.99 (6.32)	41.31 (6.32)
$P_{A_{CO_2}}$ (mmHg)	3	45.58 (39.00)	45.68 (39.22)
	5	46.62 (39.00)	46.77 (39.22)
	7	54.54 (39.00)	54.64 (39.22)
$P_{A_{O_2}}$ (mmHg)	3	118.38 (102.20)	118.67 (102.18)
	5	135.82 (102.20)	135.85 (102.18)
	7	143.41 (102.20)	143.40 (102.18)
CO (l/min)	3	5.25 (5.41)	5.19 (5.34)
	5	5.41 (5.41)	5.35 (5.34)
	7	5.45 (5.41)	5.40 (5.34)
HR (beats/min)	3	68.35 (67.59)	68.53 (67.72)
	5	72.19 (67.59)	72.40 (67.72)
	7	75.68 (67.59)	75.78 (67.72)
SBP (mmHg)	3	125.79 (121.95)	125.69 (121.63)
	5	126.16 (121.95)	126.22 (121.63)
	7	131.74 (121.95)	131.84 (121.63)
MBP (mmHg)	3	94.08 (89.39)	93.95 (89.19)
	5	94.94 (89.39)	94.84 (89.19)
	7	101.10 (89.39)	100.98 (89.19)
DBP (mmHg)	3	81.40 (76.18)	81.35 (76.23)
	5	82.53 (76.18)	82.42 (76.23)
	7	88.85 (76.18)	88.82 (76.23)

The values shown in the table are evaluated at the end of a 25-minute hypercapnic stimulus. The values inside the parentheses indicate the steady-state normoxic response right before the application of the stimulus and are the same across the CO_2 stimuli range, because all simulations are performed with the same nominal parameter set. V_T, tidal volume; RR, respiratory rate; V_e, minute ventilation; $P_{A_{CO_2}}$, alveolar partial pressure of CO_2; $P_{A_{O_2}}$, alveolar partial pressure of O_2; CO, cardiac output; HR, heart rate; SBP, systolic arterial blood pressure; MBP, mean arterial blood pressure; DBP, diastolic arterial blood pressure.

Table 2.6. Comparison of the steady-state respiratory and cardiovascular responses of the original and modified models to a 10-minute 9, 8, and 7% O_2 hypoxic stimulus

Variable	$F_{I_{O_2}}$ (%)	Original model	Modified model
V_T (l)	9	0.84 (0.53)	0.85 (0.53)
	8	0.89 (0.53)	0.89 (0.53)
	7	0.94 (0.53)	0.94 (0.53)
RR (breaths/min)	9	13.95 (12.00)	13.99 (12.00)
	8	14.27 (12.00)	14.31 (12.00)
	7	14.59 (12.00)	14.64 (12.00)
V_e (l/min)	9	11.68 (6.32)	11.82 (6.32)
	8	12.64 (6.32)	12.79 (6.32)
	7	13.65 (6.32)	13.83 (6.32)
$P_{A_{CO_2}}$ (mmHg)	9	29.68 (39.00)	29.85 (39.22)
	8	28.60 (39.00)	28.63 (39.22)
	7	27.46 (39.00)	27.65 (39.22)
$P_{A_{O_2}}$ (mmHg)	9	44.33 (102.20)	44.33 (102.18)
	8	40.05 (102.20)	40.10 (102.18)
	7	35.91 (102.20)	35.84 (102.18)
CO (l/min)	9	6.44 (5.41)	6.37 (5.34)
	8	6.72 (5.41)	6.67 (5.34)
	7	6.91 (5.41)	6.88 (5.34)
HR (beats/min)	9	76.95 (67.59)	77.16 (67.72)
	8	81.20 (67.59)	81.36 (67.72)
	7	83.87 (67.59)	84.05 (67.72)
SBP (mmHg)	9	126.63 (121.95)	126.29 (121.63)
	8	128.39 (121.95)	128.24 (121.63)
	7	129.77 (121.95)	129.64 (121.63)
MBP (mmHg)	9	91.87 (89.39)	91.72 (89.19)
	8	93.47 (89.39)	93.43 (89.19)
	7	94.60 (89.39)	94.60 (89.19)
DBP (mmHg)	9	77.54 (76.18)	77.51 (76.23)
	8	79.04 (76.18)	79.05 (76.23)
	7	80.05 (76.18)	80.06 (76.23)

The values shown in the table are evaluated at the end of a 10-minute hypoxic stimulus. The values inside the parentheses indicate the steady-state normoxic response right before the application of the stimulus and are the same across the O_2 stimuli range, because all simulations are performed with the same nominal parameter set. V_T, tidal volume; RR, respiratory rate; V_e, minute ventilation; $P_{A_{CO_2}}$, alveolar partial pressure of CO_2; $P_{A_{O_2}}$, alveolar partial pressure of O_2; CO, cardiac output; HR, heart rate; SBP, systolic arterial blood pressure; MBP, mean arterial blood pressure; DBP, diastolic arterial blood pressure.

2.4.3 Hemodynamic effects of respiration

Heart-lung interactions during normal breathing are evaluated in terms of the magnitude of change in the right and left ventricular stroke volumes. Fig. 2.7 depicts the effects of respiration on pericardial pressure (P_{peri}), venous return (VR), right and left ventricular output flows ($Q_{rv,o}$ and $Q_{lv,o}$ respectively) and stroke volumes (SV_{rv} and SV_{lv} respectively). Negative swings in pleural pressure (P_{pl}) indicate the inspiratory portion of each breath. Pericardial pressure exhibits swings similar to the ones in P_{pl} superposed with deflections due to cardiac activity. As the heart chambers expand in volume during the diastolic phase, the pericardial space is compressed and thus P_{peri} increases. Moreover, negative deflections of pleural pressure during inspiration decrease the pressure inside the thoracic veins, resulting in a larger pressure gradient for the blood that returns back to the heart (higher venous return). Consequently, right ventricular output flow and stroke volume increase and reach their maximum values at the end of inhalation. Simultaneously, during inspiration, the negative swings in pleural pressure enhance the loading capacity of the pulmonary vessels and more blood is retained in the pulmonary circulation. Blood flow in the left atrium and left ventricular preload are both expected to decrease, leading to a reduction of the left ventricular output flow and stroke volume according to the Frank-Starling mechanism.

It is important to note that this phenomenon, known to as “pulsus paradoxus”, is observed in both original and modified models. However, the addition of the three newly proposed model components accentuates these effects (see bottom plot in Fig. 2.7 and Table 2.7) and allows the model to reproduce the literature data more accurately. More specifically, the septum has a major contribution to the diastolic ventricular interdependence, where an inspiratory increase in the right ventricular end-diastolic volume induces a change in left ventricular pressure-volume relationship. Nevertheless, in the modified CP Model, we assume that during inhalation the diastolic ventricular elastance remains constant and we only consider the reduction in left ventricular volume that is caused by the leftward movement of the septum. Moreover, the pericardium enhances even accentuates the effects of respiration

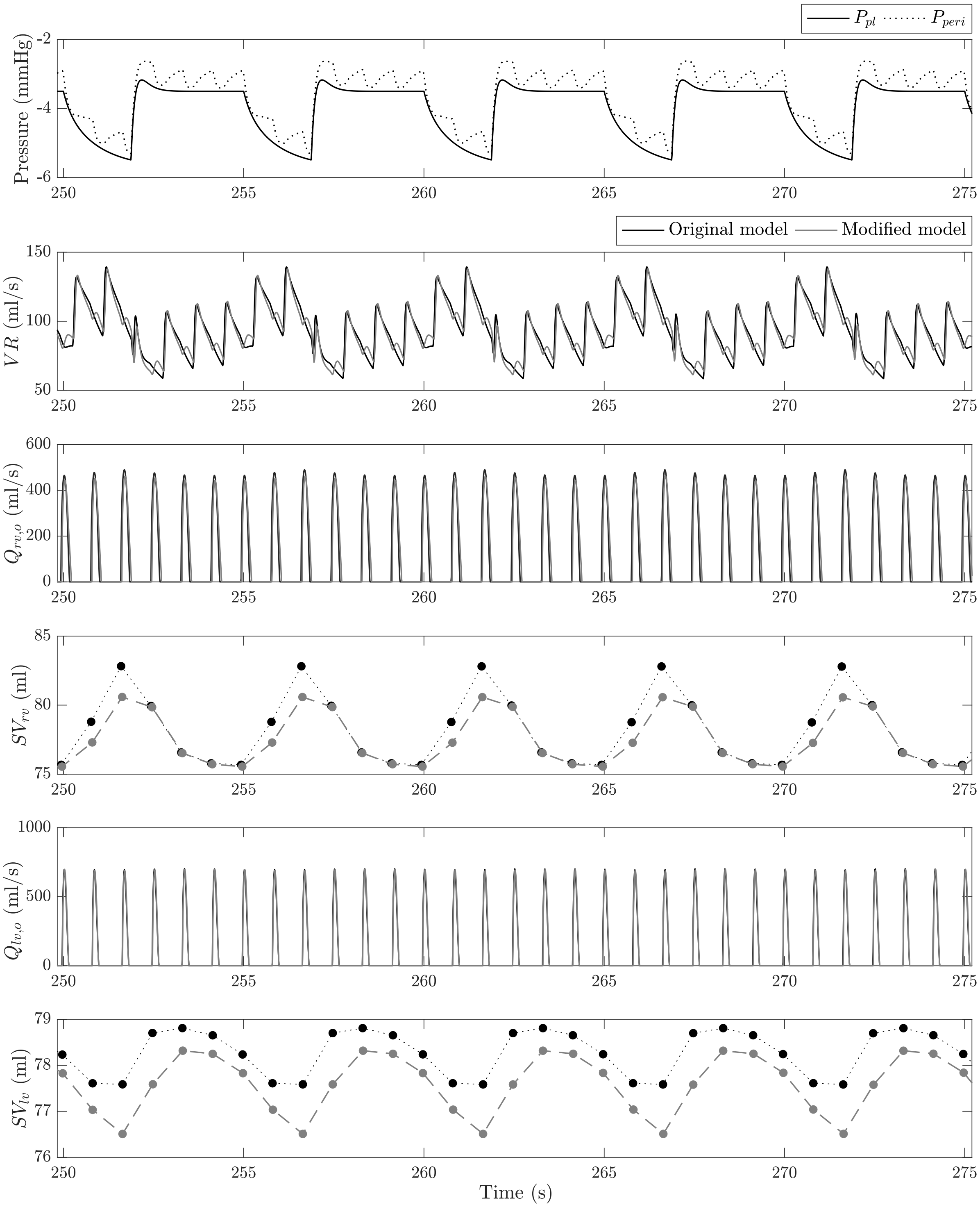

Fig. 2.7. Mechanical effects of respiration on cardiovascular variables. From *top* to *bottom*: pleural pressure (P_{pl}), pericardial pressure (P_{peri}), venous return (VR), right ventricular output blood flow ($Q_{rv,o}$), right ventricular stroke volume (SV_{rv}), left ventricular output blood flow ($Q_{lv,o}$), left ventricular stroke volume (SV_{lv}).

on cardiac function. Inspiratory reduction of left ventricular preload yields a lower than normal (at static conditions) left ventricular diastolic pressure. In addition, pericardial pressure is on average higher than pleural pressure (see top plot in Fig. 2.7). As a result, during inhalation, left ventricular diastolic transmular pressure is lower than that of the original model (without pericardium), a phenomenon that leads to an additional decrease of the left ventricular end-diastolic volume and thus stroke volume.

Lastly, similar to the study by Ruskin et al. [47], Table 2.7 categorizes the heart beats according to their location within the breathing cycle into end-expiratory, peak-inspiratory and early/mid-expiratory beats. Although the maximum variation in the left ventricular stroke volume of the modified model (1.81 ml) increased compared to that of the original model (1.23 ml), it still deviates from the experimental data in [47] (5±2 ml). Nevertheless, the direction of change is in good agreement with the human study; the left ventricle at peak-inspiration ejects blood with the lowest stroke volume which, in turn, attains its highest value at the early/mid-expiratory beat. The pulse pressure is directly proportional to the change in the stroke volume apart from a small discrepancy between the end- and early/mid-expiratory beats of the modified CP Model, which could be the result of numerical errors. As aforementioned, right ventricular stroke volume reaches its highest value at the peak-inspiratory beat and then progressively decreases through early/mid- and end-expiration.

2.5 Validation of modified model

Model validation is an indispensable part of the development of any mathematical model and a crucial step for the model's adoption by the research community. However, the highly interconnected and complex nature of physiological systems poses significant challenges to model validation. It is therefore not surprising that there has not been an established technique that provides a systematic and comprehensive evaluation of a model's response

Table 2.7. Hemodynamic effects of respiration

Variable	Original model	Modified model
Left ventricular stroke volume, SV_{lv} (ml)		
End-expiration	78.65	78.25
Peak-inspiration	77.58	76.51
Early/mid-expiration	78.81	78.32
Maximum variation	**1.23**	**1.81**
Pulse pressure (systolic minus diastolic), PP (mmHg)		
End-expiration	45.17	45.08
Peak-inspiration	44.75	44.54
Early/mid-expiration	45.34	44.95
Maximum variation	**0.59**	**0.54**
Right ventricular stroke volume, SV_{rv} (ml)		
End-expiration	75.79	75.55
Peak-inspiration	82.80	80.57
Early/mid-expiration	76.58	76.54
Maximum variation	**7.01**	**5.02**

with respect to experimental data [48, 49]. Nevertheless, validation of the modified CP Model has been conducted based on the criteria proposed by Summers et al. [49] and adopted by our group for validating the original CP Model [19]. According to these criteria, the model-predicted response is considered to be in good agreement with experimental data when the simulated outputs 1) are directionally appropriate in a qualitative manner, 2) attain steady-state values that closely match the experimental data, and 3) are fairly accurate during the transient dynamic state of the system's response.

We hence validate the modified CP Model based on these criteria, by comparing its response during simulated mechanical ventilation conditions against literature data collected on mechanically ventilated subjects. Since our goal is to demonstrate the model's capability to describe the main heart-lung interaction mechanisms typically observed during mechanical ventilation, we therefore focus our attention on changes in cardiac activity during PEEP application and on the cyclic variations in left and right ventricular functions induced by respiratory events. In particular, we compare the model predictions with data from human studies under the three following scenarios: 1) changes in positive pressure ventilation (PPV) on spontaneously breathing healthy subjects [1], 2) step changes in positive end-expiratory pressure on sedated patients [4], and 3) constant ventilatory support on sedated patients [2]. In addition, we use simulations from the modified CP Model to analyze heart-lung interaction phenomena and to provide a physiological explanation to a few contradicting experimental results so that we give further credence to the capability of the model in describing the underlying mechanisms of cardiorespiratory interactions.

As far as the model validation is concerned, it is important to point out that the nature of the human data used in this study require a validation process different than the one followed in earlier work by our group. Cheng et al. [19] evaluated the original model's response with data obtained from groups of healthy individuals. Model parameters were hence maintained at their nominal values (reported in [18]), corresponding to a general 70-kg healthy subject. On the contrary, the validation process presented below is based on experimental data collected from patients with either a respiratory (e.g., ARDS) or a cardiovascular (e.g., sepsis) pathological condition. Accordingly, a subset of parameters, pertaining to the clinical case under investigation, was modified ad hoc such that the model outputs match the average basal values reported in the literature for each particular patient group. For instance, a respiratory failure prompted the adjustment of parameters in the lung mechanics model, such as the compliances and unstressed volumes of the lungs and the chest wall, whereas a cardiovascular disease required the cardiac model parameters, like the ventricular end-systolic and end-diastolic pressure-volume relationships, to be altered. Note that eventually we envision the use of estimation techniques, like the one presented in Chapter 4, to tailor the model, or parts of it, for simulation of individual patients. Instead of adjusting the parameter values in an ad hoc manner to match average population data, fine-tuning using optimization techniques of the same subset of parameters can result in a patient-specific model. Such a model can then be used to conduct virtual physiological experiments, predict the response of the specific subject to therapeutic interventions, and provide a patient-tailored therapy planning.

2.5.1 Comparison with experimental data

As mentioned above, for the simulation studies presented herein, a few key parameters of the modified CP Model were modified with respect to their nominal values reported in [18]. Of major importance are the parameters of the heart model (see Table 2.1) that determine the end-diastolic (k_E and P_0) and end-systolic ($E_{max,0}$) pressure-volume relationships. They were adjusted in an ad hoc manner such that we achieve basal values (before the initiation of the experimental protocol) of the left and right ventricular end-diastolic and end-systolic volumes close to those reported in the literature data. Ideally, if the experimental data were within the normal physiological ranges (see Table 2.4), we would not have to change the parameter values in the model. However, the literature-reported cardiac volumes deviate considerably from their normal physiological ranges based on which the nominal parameter set of the original CP Model had been selected. We hypothesize that this discrepancy in cardiac volumes may be attributed either to cardiac complications in the study population or to the administration of drugs prior to the study. In addition to the above mentioned parameters characterizing cardiac function, few parameters related to the respiratory mechanics and the ventilatory control system were also modified. For example, lung and chest wall compliances (C_L and C_{cw}, respectively) and unstressed volumes ($V_{u,L}$ and $V_{u,cw}$, respectively) were reduced as compared with their original values. The objective for such parameter changes was threefold: 1) match the average tidal volume in the experimental data, 2) reach a basal mean value of pleural pressure similar to that reported by the study investigators, and 3) achieve an equal, on average, magnitude of change in P_{pl} for each step change in ventilator settings (e.g., pressure support level or PEEP). Further, if the response of a sedated subject was to be simulated, we set the sensitivities of the central and peripheral chemoreflex mechanisms, which regulate the amplitude and frequency of breathing, as well as the basal breathing amplitude to zero. Finally, we should emphasize that the aforementioned parameter changes were performed at the beginning of each simulation study and parameter values were subsequently maintained constant for the entire duration of the experimental protocol.

The first study considered in our validation procedure is the one by Kyhl et al. [1]. This study involves 18 healthy volunteers who were asked to breath spontaneously, at the beginning in atmospheric conditions (PPV_0) and then under positive pressure ventilation with pressure support level of 3 $\mathrm{cmH_2O}$ and positive end-expiratory pressures (PEEP) of 9 and 19 $\mathrm{cmH_2O}$ (labeled PPV_{10} and PPV_{20} respectively). Each of the three periods lasted 30 minutes. Cardiac magnetic resonance imaging was used to assess the volumes of the heart chambers during short end-expiratory pauses at the end of each PPV period. Fig. 2.8 includes the mean and standard error of the mean values from the human study (literature data) for CO, HR, left (LV) and right (RV) ventricular stroke (SV), end-diastolic (EDV), and end-systolic (ESV) volumes. In addition, Fig. 2.8 reports the corresponding model-predicted outputs (model data) as mean values calculated over end-expiratory heart beats at the end of each simulated PPV period. In order to attain the basal values (at PPV_0) of the stroke and end-diastolic volumes reported in the study, we set $E_{max,lvf0}$, $E_{max,rvf0}$, $k_{E,lvf}$, and $k_{E,rvf}$ respectively to 3.05 mmHg/ml, 0.8 mmHg/ml, 0.008 $\mathrm{ml^{-1}}$, and 0.007 $\mathrm{ml^{-1}}$.

The simulation results in Fig. 2.8 show that the model is able to mimic the effects of positive pressure ventilation on cardiac activity as ventilator settings are adjusted from baseline (PPV_0) to PPV_{10} and then to PPV_{20}—that is, during an increase in PEEP from 0 to 9 and then to 19 $\mathrm{cmH_2O}$ respectively. In particular, all experimental and model-predicted cardiac volumes are reduced during positive pressure ventilation (see PPV_{10} and PPV_{20}), while heart rate increases. Despite the increase in HR, there is a marked drop in LV stoke volume as PEEP is increased, thus leading to a reduction in cardiac output. Such a drop in CO is attributed to reduced systemic venous return caused by elevation in pleural pressure.

In addition, notice that the model predictions, besides RV ESV, are within one standard deviation of the sampling distribution (standard error) of the subjects in the study for all PPV levels. Although RV ESV maintains its directionality as compared with the study data, the absolute magnitude of the change is small, especially at PPV_{20}.

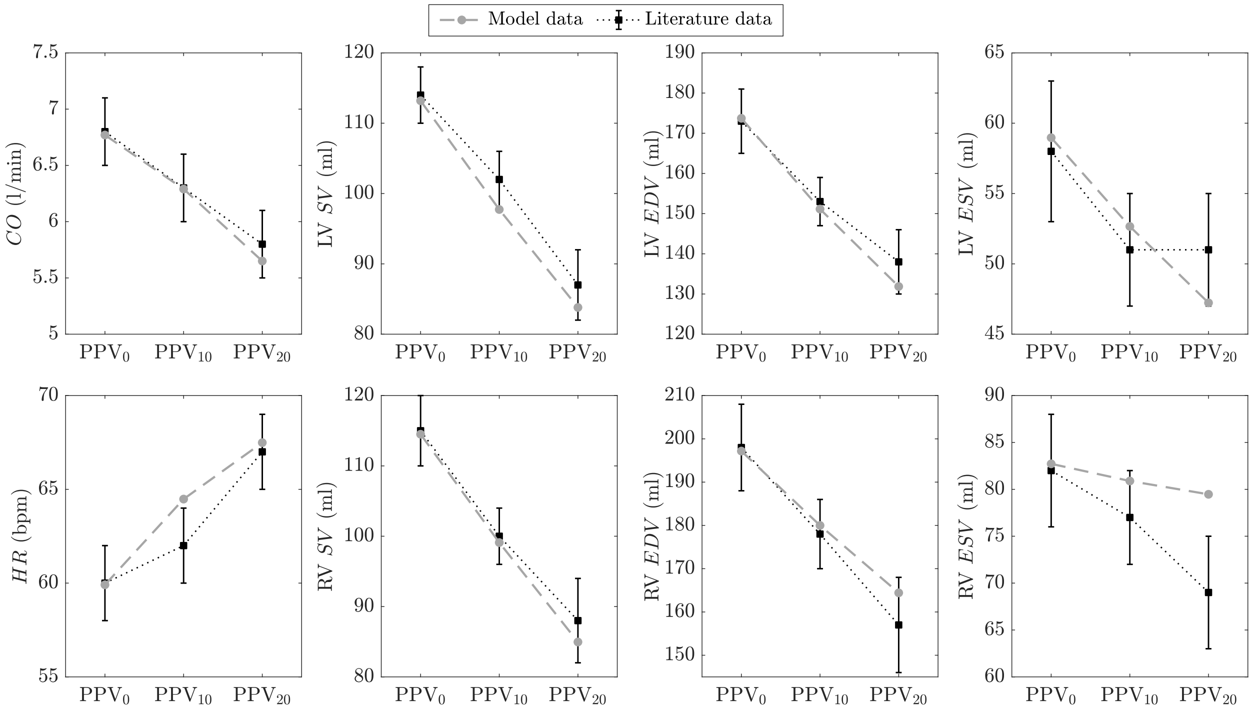

Fig. 2.8. Cardiovascular response to step changes in the level of positive pressure ventilation (PPV). Literature data (*black* points and error bars are means and standard errors of the means respectively) are collected during a human study with 18 healthy, spontaneously breathing, subjects and are published by Kyhl et al. [1]. Both model-simulated (*gray* points) and experimental data are assessed from end-expiratory heart beats at the end of each 30-minute PPV period. LV, left ventricular; RV, right ventricular; CO, cardiac output; HR, heart rate (bpm, beats per minute); SV, stroke volume; EDV, end-diastolic volume; ESV, end-systolic volume.

Then, we analyze the cardiovascular response to step changes in the level of PEEP and subsequently to blood infusion (volume expansion) via Table 2.8. Literature data are reported by Dhainaut et al. [4] and are assessed from a group of 21 sedated ARDS patients. The experimental data include mean and standard error values for cardiac index (CI), HR, stroke volume index (SVI), LV and RV end-diastolic ($EDVI$) and end-systolic ($ESVI$) volume indices, and ejection fractions (EF); all volumetric indices are calculated by normalizing the raw volume data with respect to the body surface area (BSA). According to the experimental protocol, the PEEP level is adjusted in increments of 5 cmH$_2$O, covering a range of [0–20] cmH$_2$O (PEEP$_0$, PEEP$_5$, PEEP$_{10}$, PEEP$_{15}$, and PEEP$_{20}$ respectively). Such a process is known as "PEEP titration" and is typically used on ARDS subjects for determining the optimal level of PEEP that promotes lung recruitment and facilitates arterial blood oxygenation [50]. All other ventilator settings (e.g., tidal volume equal to 10–14 ml/kg of body weight and $F_{I_{O_2}} = 0.5$) were kept unchanged and no medications were administered throughout the experimental study. Each ventilatory period lasted 20 minutes and the hemodynamic measurements of Table 2.8 were collected within the last 10 minutes of each interval. After the application of PEEP$_{20}$, volume expansion (VE) with plasma expanders (i.e., fluid resuscitation) was used; its purpose was to normalize the cardiac index at a level similar to baseline at PEEP$_0$. For our simulation study, the basal values of end-diastolic and end-systolic ventricular volume indices were obtained by setting $E_{max,lvf0}$, $E_{max,rvf0}$, $k_{E,lvf}$, and $k_{E,rvf}$ to 4 mmHg/ml, 0.4 mmHg/ml, 0.007 ml^{-1}, and 0.0065 ml^{-1} respectively. Additionally, to match the elevated heart rate observed in the study's ARDS population, the basal heart period was adjusted from its nominal value of 0.58 seconds [18, 33] to 0.27 seconds. As for the respiratory system, we adjusted the lung and chest wall mechanical properties as follows: $C_L = 0.065$ l/cmH$_2$O, $C_{cw} = 0.1$ l/cmH$_2$O, $V_{u,L} = 0.4$ l, and $V_{u,cw} = 1$ l. Such changes allowed us to achieve a tidal volume of about 0.75 liters (about 11 ml/kg of body weight) and a basal mean P_{pl} value of -1.07 cmH$_2$O, compared to 0±1.6 cmH$_2$O in [4]. As commonly observed in ARDS patients, venous admixture (pulmonary shunt fraction) and $F_{I_{O_2}}$ were higher than normal and respectively set to 0.35 (35%) and 50%.

The cardiovascular response of the modified CP Model to the aforementioned PEEP titration scenario is also presented in Table 2.8. The model-predicted outputs are in good agreement with experimental data. Namely, left and right ventricular $EDVI$ are reduced as PEEP is progressively increased, thereby leading to a decrease in cardiac index in line with physiological understanding and the Frank-Starling relationship. Moreover, left ventricular

Table 2.8. Cardiovascular response to step changes in positive end-expiratory pressure (PEEP) and blood volume expansion (VE) in ARDS subjects

	PEEP$_0$		**PEEP$_5$**		**PEEP$_{10}$**		**PEEP$_{15}$**		**PEEP$_{20}$**		**PEEP$_{20}$ + VE**	
Variable	Model	Liter.	Model	Liter.	Model	Liter.	Model	Liter.	Model	Liter.	Model	Liter.
CI (l/min/m^2)	4.50	4.47±0.7	4.33	4.41±0.7	4.12	4.15±0.64	3.88	3.81±0.61	3.64	3.37±0.53	4.51	4.5±0.69
HR (bpm)	113.54	109±12	116.18	110±12	118.19	112±13	119.98	112±13	122.05	113±13	114.37	110±12
SVI (ml/m^2)	39.65	41±2.7	37.31	40±2.6	34.87	37.1±2.5	32.39	34±2.3	29.87	29.8±2	39.45	40.9±2.7
Left ventricle												
$EDVI$ (ml/m^2)	58.47	61.2±4.7	55.03	59.7±4.7	51.61	54.4±4.5	48.35	50±4.2	45.16	43.8±3.9	56.65	59.7±4.8
$ESVI$ (ml/m^2)	18.81	20.2±3.5	17.72	19.7±3.5	16.74	17.3±3.4	15.96	16±3.4	15.29	14±3.3	17.20	18.8±3.5
EF (%)	67.78	67±6	67.75	67±6	67.52	68±6	66.93	68±6	66.07	68±6	69.61	67±6
Right ventricle												
$EDVI$ (ml/m^2)	99.24	97.6±7.2	96.48	93±7	93.25	88.1±6.7	89.29	82.9±6.5	84.75	74.5±6	119.13	99.8±7.3
$ESVI$ (ml/m^2)	59.58	56.6±5.1	59.18	53±5.1	58.39	51±5	56.91	48.9±5	54.89	44.7±4.7	79.69	58.9±5.2
EF (%)	39.96	42±5	38.65	43±5	37.36	42±5	36.22	41±5	35.17	40±5	33.09	41±5

Literature (Liter.) data (mean±standard error of the mean) are reported by Dhainaut et al. [4] based on a human study involving 21 ARDS patients. Each PEEP level is applied for a period of 20 minutes. Both model-simulated and experimental data are assumed from end-expiratory heart beats during the last 10 minutes of each PEEP segment. The model's volumetric indices were calculated by assuming a nominal body surface area of 1.9 m^2. PEEP$_x$, PEEP at x cmH$_2$O where x = {0, 5, 10, 15, 20}; PEEP$_{20}$ + VE, PEEP at 20 cmH$_2$O and blood volume expansion with 625±72 ml of plasma expanders; CI, cardiac index; HR, heart rate (bpm, beats per minute); SVI, stroke volume index; $EDVI$, end-diastolic volume index; $ESVI$, end-systolic volume index; EF, ejection fraction.

ejection fraction is relatively constant across the entire PEEP range, indicating that LV afterload is not significantly affected by PEEP application. On the contrary, right ventricular EF is lower at high PEEP values in both experimental and simulation results. This effectively demonstrates an elevated pulmonary impedance owing to the compression of the pulmonary capillaries by the PEEP-induced lung expansion. Model outputs, however, differ from the study data when infusion of blood is instituted (PEEP_{20} + VE). On one hand, simulated left ventricular function, including cardiac and stroke volume indices, return to basal conditions (PEEP_0) after volume expansion, in agreement with the experimental evidence. On the other hand, model-predicted right ventricular $EDVI$ and $ESVI$ increase beyond their baseline values. This outcome contradicts the data from Dhainaut et al. [4], which show a complete return of right ventricular volumes to baseline after volume expansion. According to the investigators in [4], such a phenomenon suggests that the effect of PEEP application on the study's population right ventricular function is primarily manifested by a decrease in right ventricular preload (venous return). Based on this conclusion, we conjecture that model simulations instead indicate right ventricular overload due to the collapse of the pulmonary capillaries when PEEP is increased. This hypothesis is also supported by an earlier study from Dhainaut et al. [51], which demonstrated that application of high PEEP levels caused a marked increase in right ventricular afterload and hence RV $EDVI$. Such contradicting outcomes with respect to the effect of PEEP on right ventricular activity will be analyzed in more detail in the next section.

Finally, we examine the cyclic variations in left and right ventricular functions caused by respiratory events during positive pressure ventilation. Fig. 2.9 compares the model-simulated left (left column) and right (right column) ventricular volume indices, i.e., SVI, $EDVI$, and $ESVI$, with those published by Vieillard-Baron et al. [2]. Experimental data were collected from a group of 31 sedated patients on mechanical ventilation support. A pressure-control mode with tidal volume of 7–9 ml/kg, respiratory rate of 15 breaths/minute, an end-inspiratory pause of 0.5 seconds, and PEEP of 5 cmH_2O were selected. The study investigators acquired hemodynamic measurements via a transesophageal echocardiographic transducer and focused on the following four heart beats based on their location within a breathing cycle: 1) an end-expiratory beat, right before the inspiratory portion of a breath, 2) a beat toward the end of lung inflation, 3) an end-inspiratory beat (at the end of the end-inspiratory pause), and 4) a beat during the early phase of expiration. Data collected from these four heart cycles are shown sequentially in the subplots of Fig. 2.9 (black squares). As mentioned earlier, the experimental conditions were simulated in the modified CP Model by adjusting the parameters of the cardiovascular and respiratory systems so that we attain baseline values close to those observed in the patient study population [2]. Namely, we set $C_L = 0.06$ l/cmH$_2$O, $C_{cw} = 0.11$ l/cmH$_2$O, $V_{u,L} = 0.4$ l, and $V_{u,cw} = 1$ l in order to get a total respiratory system compliance of 0.039 l/cmH$_2$O (the compliance of the study group was 0.038±0.007 l/cmH$_2$O), a tidal volume of about 0.6 liters (about 8.5 ml/kg of body weight, compared with 7–9 ml/kg in [2]) and a pleural pressure value of -1.75 cmH$_2$O at the end of expiration ($P_{pl} = -2.04 \pm 0.14$ cmH$_2$O in [2]). In the cardiovascular component, we modified the following parameters: $E_{max,lvf0}$, $k_{E,lvf}$, $k_{E,rvf}$, $P_{0,lvf}$, and $P_{0,rvf}$ to 1.9 mmHg/ml, 0.016 ml^{-1}, 0.011 ml^{-1}, 0.8 mmHg, and 1.5 mmHg respectively.

The results shown in Fig. 2.9 demonstrate that the model-predicted outputs follow the trends in the experimental data for both left and right ventricular volume indices. In particular, left ventricular SVI attains its minimum value at end-expiration, while it reaches the maximum level at the end of inhalation. Similar trend is also displayed by LV $EDVI$, a behavior that is physiologically attributed to the Frank-Starling mechanism. According to the mechanism, an increase in end-diastolic volume, which indicates a change in preload, induces a direct increase in stroke volume. Hence, we expect that under most circumstances (apart from cases of ventricular failure) a change in end-diastolic volume will always be accompanied by a proportional change in stroke volume. The increase in left ventricular $EDVI$ with inhalation is ascribed to the compression of the pulmonary peripheral vessels that promotes more blood into the left atrium, thereby increasing left ventricular filling.

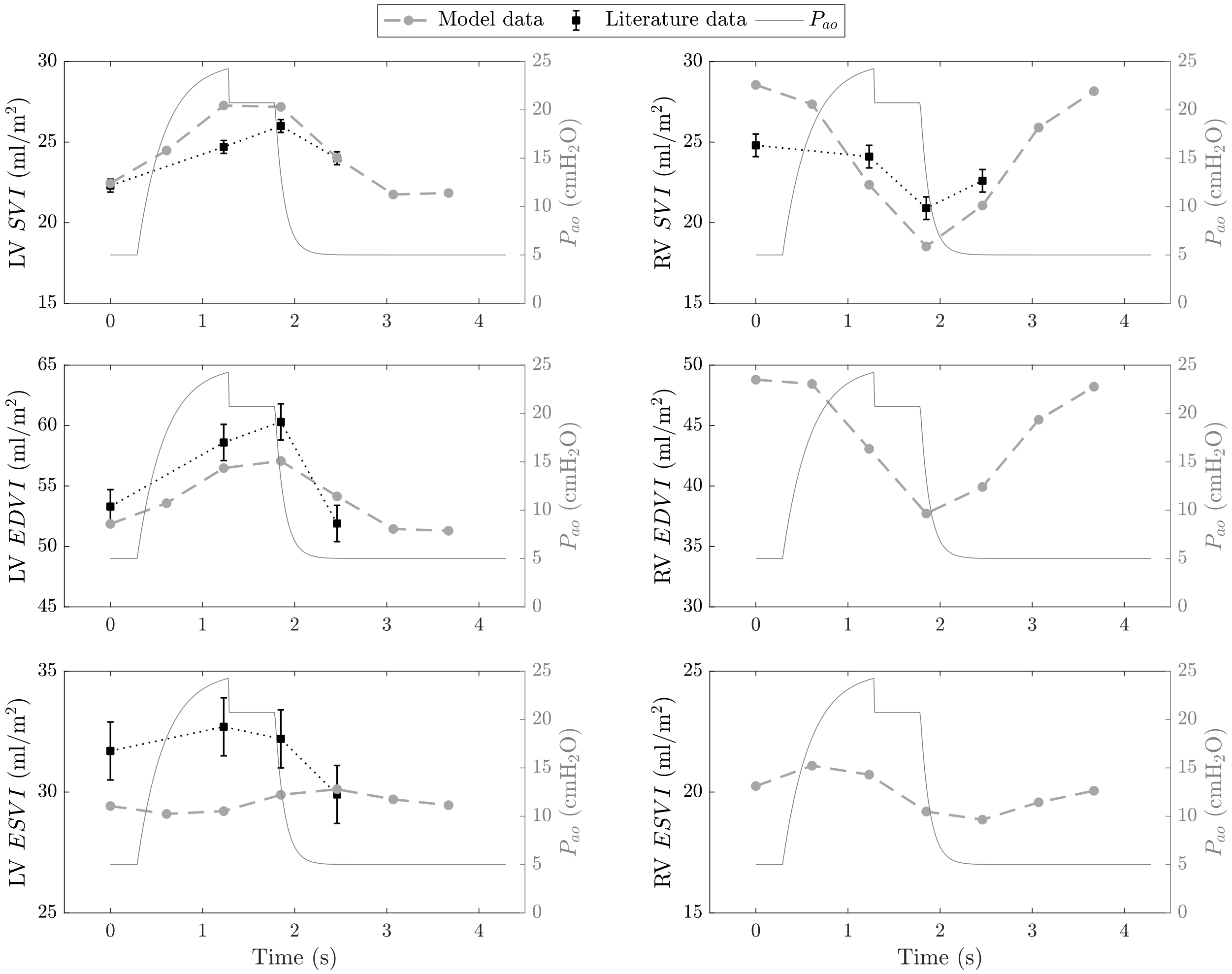

Fig. 2.9. Cyclic intra-breath changes in left (*left* column) and right (*right* column) ventricular functions during positive pressure ventilation. Literature data (*black* squares and error bars are means and standard errors of the means respectively) are taken from Vieillard-Baron et al. [2], who studied 31 fully sedated patients under mechanical ventilation support. Both model (*gray* circles) and experimental data are with reference to the left vertical axes in each subfigure. Note that Vieillard-Baron et al. [2] does not report measurements for RV $EDVI$ and $ESVI$. LV, left ventricular; RV, right ventricular; SVI, stroke volume index; $EDVI$, end-diastolic volume index; $ESVI$, end-systolic volume index; P_{ao} (right vertical axes), airway opening pressure.

With regard to the left ventricular end-systolic volume, Vieillard-Baron et al. [2] report that there is a statistically insignificant change in $ESVI$ during the breathing cycle. Although the model-predicted variations in $ESVI$ are not directionally appropriate with respect to the experimental data, we notice that their magnitude is considerably smaller compared to changes in $EDVI$ and SVI. The inspiratory decrease in LV $ESVI$ predicted by the modified

CP Model is nevertheless supported by other investigators [3] and will be further analyzed in the next section.

The right ventricle, on the other hand, is primarily affected by the increase in pleural pressure, a direct consequence of the increase in transpulmonary pressure during positive pressure ventilation. Elevation of pleural pressure during inhalation sequentially decreases systemic venous return, right ventricular filling (end-diastolic volume), and hence right ventricular stroke volume. RV SVI attains its minimum value during the end-inspiratory pause and then increases back to baseline during exhalation, which is also linked to the withdrawal of pressure support. Model predictions of right ventricular SVI are directionally appropriate to the literature data, although the simulated beat-to-beat changes are more pronounced in magnitude. Unfortunately, such a discrepancy cannot be sufficiently explained due to the lack of data reported by Vieillard-Baron et al. [2] regarding RV $EDVI$ and $ESVI$. Notice, however, that in line with previous studies [52], the model-predicted intra-breath variation in right ventricular SVI is larger than that of the left ventricle, a phenomenon that is ascribed to the damping effect of the pulmonary circulation (i.e., pulmonary impedance). Namely, at every breath, for any given respiratory-induced increase in RV stroke volume, the corresponding increase in LV stroke volume is of smaller amplitude. This is because the pulmonary circulation effectively accommodates for part of the blood volume ejected from the right ventricle before it reaches the left heart [53].

2.5.2 Physiological heart-lung interaction phenomena

Complementary to the simulation data and figures in the previous section, some additional aspects of the model-predicted changes in cardiovascular function during mechanical ventilation are worthy of further discussion. Of particular substance are simulation studies from the modified CP Model that aim to explain a few contradicting experimental findings regarding different heart-lung interaction phenomena, like the effect of PEEP on right ventricular performance.

As shown by Kyhl et al. [1] and Dhainaut et al. [4] and demonstrated by the modified CP Model as well (Fig. 2.8 and Table 2.8 respectively), cardiac activity is greatly affected by changes in the level of PEEP. The evident drop in cardiac output as a result of a step increase in PEEP is primarily attributed to a reduction in ventricular filling (preload), determined by the volume of blood within the ventricle at the end of diastole. This behavior in ventricular function is considered to be driven by the well-known Frank-Starling mechanism that governs the length-tension relationship in cardiac myocytes. To illustrate the consistency of the modified CP Model to replicate such a mechanism, we plot, using the data from Table 2.8, the cardiac index as a function of the corresponding $EDVI$ (Fig. 2.10). Clearly, the Frank-Starling law is well reproduced by the model outputs for both left and right ventricular functions. As indicated in the previous section, volume expansion (i.e., fluid resuscitation) entirely reversed the output of both ventricles. However, right ventricular $EDVI$ after such a volume expansion (VE) was higher than its basal value at PEEP_0, an indication of right ventricular overload. This phenomenon resulted in the obvious deviation of the "PEEP_{20} + VE" point from the right ventricular function curve in Fig. 2.10. Fig. 2.10 also reveals that the inotropic states of the two ventricles remain relatively unchanged with PEEP application since all respective points fall close to a quadratic ventricular function curve—note that in case of an increase in ventricular inotropy, the Frank-Starling curve would shift upward and to the left. As demonstrated by Huemer et al. [54] and Jardin et al. [55], despite some compensatory sympathetic activation due to the decrease in cardiac output (especially at high PEEP levels), changes in PEEP have moderate effects on the end-systolic left and right ventricular contractilities (i.e., inotropic state). End-systolic ventricular contractility is expected to be independent of ventricular preload and constant over a wide range of afterload [54, 55]. Besides the preliminary evidence of a minimal inotropic change with PEEP provided by the simulated ventricular function curves in Fig. 2.10, the model-predicted maximal ventricular elastances ($E_{max,lvf}$ and $E_{max,rvf}$) provide further proof of such a phenomenon. Both neural-modulated elastances attain values close to their basal conditions (at PEEP_0)

for all PEEP levels. Namely, $E_{max,lvf} = 4.544$, 4.540, 4.542, 4.554, and 4.577 mmHg/ml and $E_{max,rvf} = 0.723$, 0.721, 0.722, 0.729, and 0.742 mmHg/ml for PEEP_0, PEEP_5, PEEP_{10}, PEEP_{15}, and PEEP_{20} respectively.

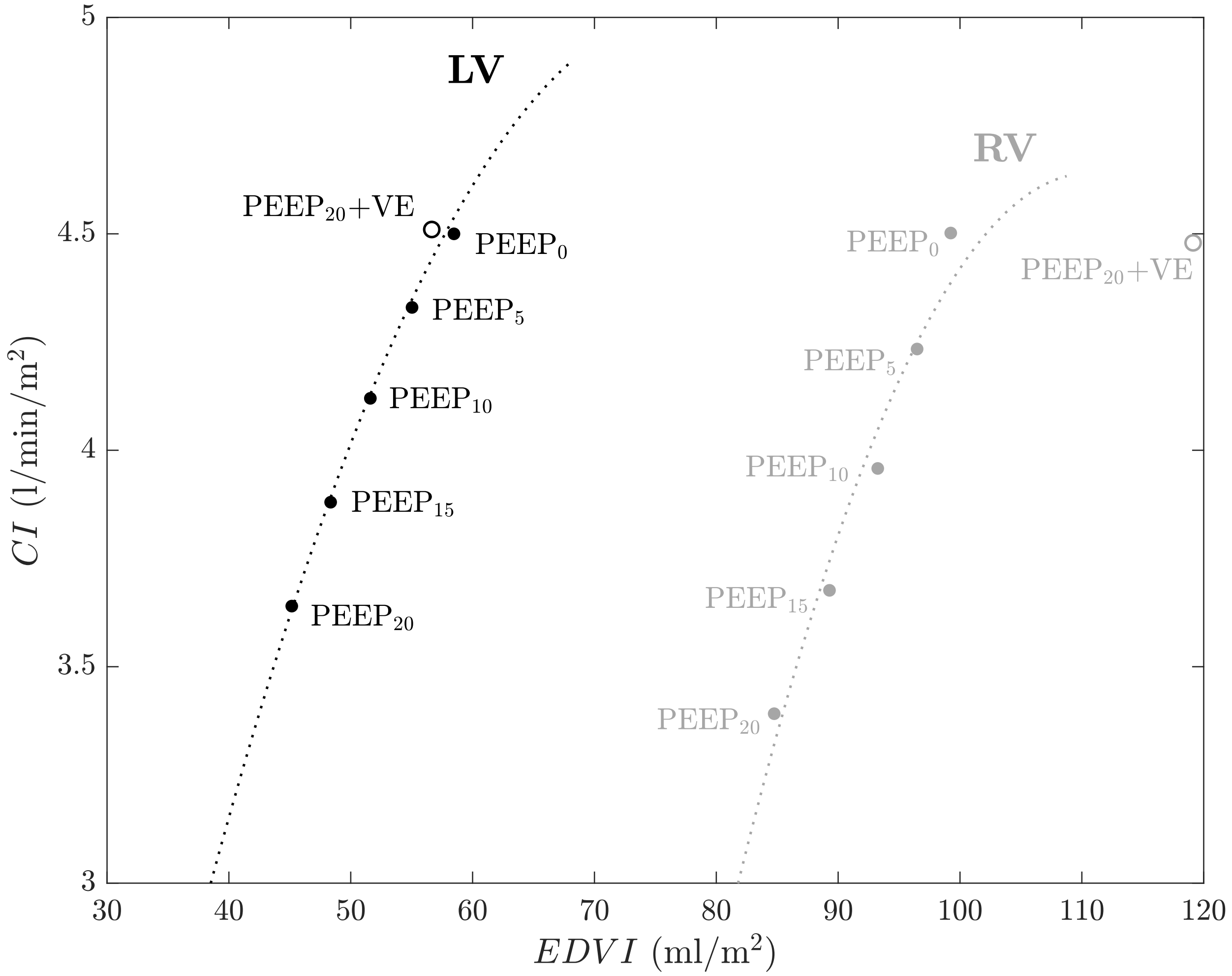

Fig. 2.10. Model-simulated Frank-Starling relationships between cardiac index (CI) and end-diastolic volume index ($EDVI$) for the left (LV, *black* curve) and the right (RV, *gray* curve) ventricles. Filled circles are evaluated as PEEP was increased from 0 cmH_2O to 20 cmH_2O (respectively PEEP_0 and PEEP_{20} in Table 2.8). Hollow circles represent the state with PEEP_{20} and volume expansion (PEEP_{20} + VE in Table 2.8).

According to Kyhl et al. [1], PEEP application also contributes to a shift in blood volume from the thoracic cardiovascular components (central blood volume), i.e., the volume of blood in heart, pulmonary circulation, and thoracic arteries and veins, to the extra-thoracic systemic circulation. Similar blood volume shift is also predicted by the modified CP Model.

For instance, simulating the experimental protocol in [1] (see Fig. 2.8), the central blood volume decreases from 891.57 ml to 773.46 ml and finally to 670.22 ml in response to step increases in PEEP from 0 to 9 and then to 19 cmH_2O respectively. Perschau et al. [56] described the same phenomenon and reported a decrease of about 10.1%±7.5% in blood volume after a change of PEEP from 0 to 10 cmH_2O. Such experimental observation supports the model predictions, which show a decrease of about 13.3% for the same step increase in the level of PEEP.

As explained in the Section 2.1, institution of PEEP is routinely recommended to patients who suffer from ARDS. Although ARDS is typically manifested as fluid accumulation in the lungs, the root cause of the edema can be attributed to either a pulmonary disease ($\mathrm{ARDS_p}$), like pneumonia, or an extra-pulmonary disease ($\mathrm{ARDS_{exp}}$), like peritonitis [57]. Furthermore, the specific underlying pathology of ARDS leads to alteration of the mechanical properties of the respiratory system. For instance, Gattinoni et al. [57] reported a marked difference in lung elastance (E_L) and chest wall elastance (E_{cw}) values between the two groups ($\mathrm{ARDS_p}$ and $\mathrm{ARDS_{exp}}$), while the total respiratory system elastance (E_{rs}) was relatively the same in the two populations. The $\mathrm{ARDS_p}$ group had $E_L = 20.23$ l/cmH_2O and $E_{cw} = 5.31$ l/cmH_2O, whereas the $\mathrm{ARDS_{exp}}$ group had $E_L = 15.95$ l/cmH_2O and $E_{cw} = 15.88$ l/cmH_2O (all values are at zero PEEP). Such disparate values in lung and chest wall elastances are expected to affect how an increase in airway opening pressure is transmitted into the pleural cavity [58]. For example, a high lung compliance coupled with a low compliance value of the chest wall, like in the case of $\mathrm{ARDS_{exp}}$, would induce a significant increase in P_{pl} as a response to an increase in airway opening pressure. High lung compliance values favor a relatively easy alveolar expansion, while the stiff chest wall (low chest wall compliance value) does not allow the parietal pleura to enlarge at the same level as the visceral pleura. It is important to note, however, that the tidal volume delivered to the patient depends on total respiratory system compliance rather than the individual lung and chest wall compliance values. As we illustrated in previous sections, right ventricular preload is influenced by pleural pressure via changes in systemic venous return, whereas right ventricular afterload depends on the pulmonary system's impedance that varies due to the compression of the pulmonary capillaries from lung inflation. Hence, we can conjecture that the distribution of E_{rs} between E_L and E_{cw} can potentially alter the effect of PEEP on both right ventricular preload and afterload and it may be the reason behind some contradictory experimental results regarding right ventricular performance. For instance, Dhainaut et al. [4] showed that PEEP increments change right ventricular function via a decrease in systemic venous return. This inevitably leads to reduced right ventricular volumes ($EDVI$ and $ESVI$ in Table 2.8). On the contrary, an earlier study by Dhainaut et al. [51] as well as experimental data by Jardin et al. [53] demonstrated an augmentation in the size of the right ventricle when PEEP is instituted. Such a phenomenon was ascribed to the increase in pulmonary system impedance (right ventricular afterload), thereby leading the investigators to suggest that PEEP application induces right ventricular overloading.

Given these sometimes contradicting experimental observations, it seemed natural to investigate if the proposed modified CP Model would be able to elucidate the mechanisms by which the mechanical properties of the respiratory system can alter the effect of PEEP on right ventricular function. To this end, we set up the model to replicate the two ARDS groups mentioned by Gattinoni et al. [57]. With these simulations, we wanted to assess the degree and direction of change in the activity of the right ventricle as PEEP is increased from 0 to 20 cmH_2O in steps of 5 cmH_2O. Fig. 2.11 compares the model-simulated cardiovascular response (LV and RV SVI, $EDVI$, and $ESVI$) for a pulmonary ARDS ($\mathrm{ARDS_p}$, black squares) and an extra-pulmonary ARDS ($\mathrm{ARDS_{exp}}$, gray circles) condition. As anticipated, for any given increase in PEEP, the overall decrease in systemic venous return causes a reduction in left and right ventricular stroke volumes for both $\mathrm{ARDS_p}$ and $\mathrm{ARDS_{exp}}$ simulations. However, the loading status of the right ventricle, as reflected by the direction of change in $ESVI$, highly differs between the two groups. Particularly, in the $\mathrm{ARDS_{exp}}$ case, right ventricular $ESVI$ significantly decreases in response to the marked drop in $EDVI$, which is, in turn, due to the reduction in venous return associated with the increasing PEEP levels. On the contrary, in the $\mathrm{ARDS_p}$ case, the increase in PEEP generates a concomitant increase in right ventricular end-systolic volume. This is a direct consequence of 1) the increased right ventricular afterload (pulmonary impedance) caused by the compression of the pulmonary peripheral vessels and 2) the moderate decrease in RV preload ($EDVI$). Such a small decrease in $EDVI$ is attributed to the low transmission of the airway opening pressure to the pleural space as a result of the stiff lungs (low lung compliance). Clearly, this response suggests that institution of PEEP on a patient with $\mathrm{ARDS_p}$ may lead to right ventricular overloading, potentially causing ventricular failure [59], despite the overall decrease in systemic venous return.

Conflicting experimental findings have also been reported regarding the movement of the septum in response to changes in PEEP and the associated septal influence on left ventricular performance. Some researchers, like Jardin et al. [53, 55], demonstrated that PEEP induces an increase in septal curvature (an indication of the position of the septum inside the heart) by shifting the interventricular septum leftwards. Such a septal movement effectively constricts the left ventricle, thereby reducing left ventricular filling and its ejection capacity. On the contrary, studies by Dhainaut et al. [51] and Huemer et al. [54] showed negligible ventricular interdependence with a minimal change in the radius of the septal curvature. Similar to the approach used earlier, one could use the proposed modified CP Model to generate physiological hypotheses regarding the potential root causes of such contradicting experimental results. For instance, the simulation results from the $\mathrm{ARDS_p}$ and $\mathrm{ARDS_{exp}}$ cases discussed above might provide a plausible explanation. In fact, the increased right ventricular afterload on the $\mathrm{ARDS_p}$ virtual patient pushes the septum toward the left ventricular free wall by reducing the model-predicted septal volume. Namely, $\bar{V}_{spt} = 2.16$, 2.12, 2.06, 1.99, and 1.93 ml respectively for PEEP = 0, 5, 10, 15, and 20 $\mathrm{cmH_2O}$ ($\bar{V}_{spt}$ is calculated by averaging the septal volume waveform over a 10-minute period at the end of each PEEP segment). On the contrary, the $\mathrm{ARDS_{exp}}$ simulation predicts an increase in septal volume

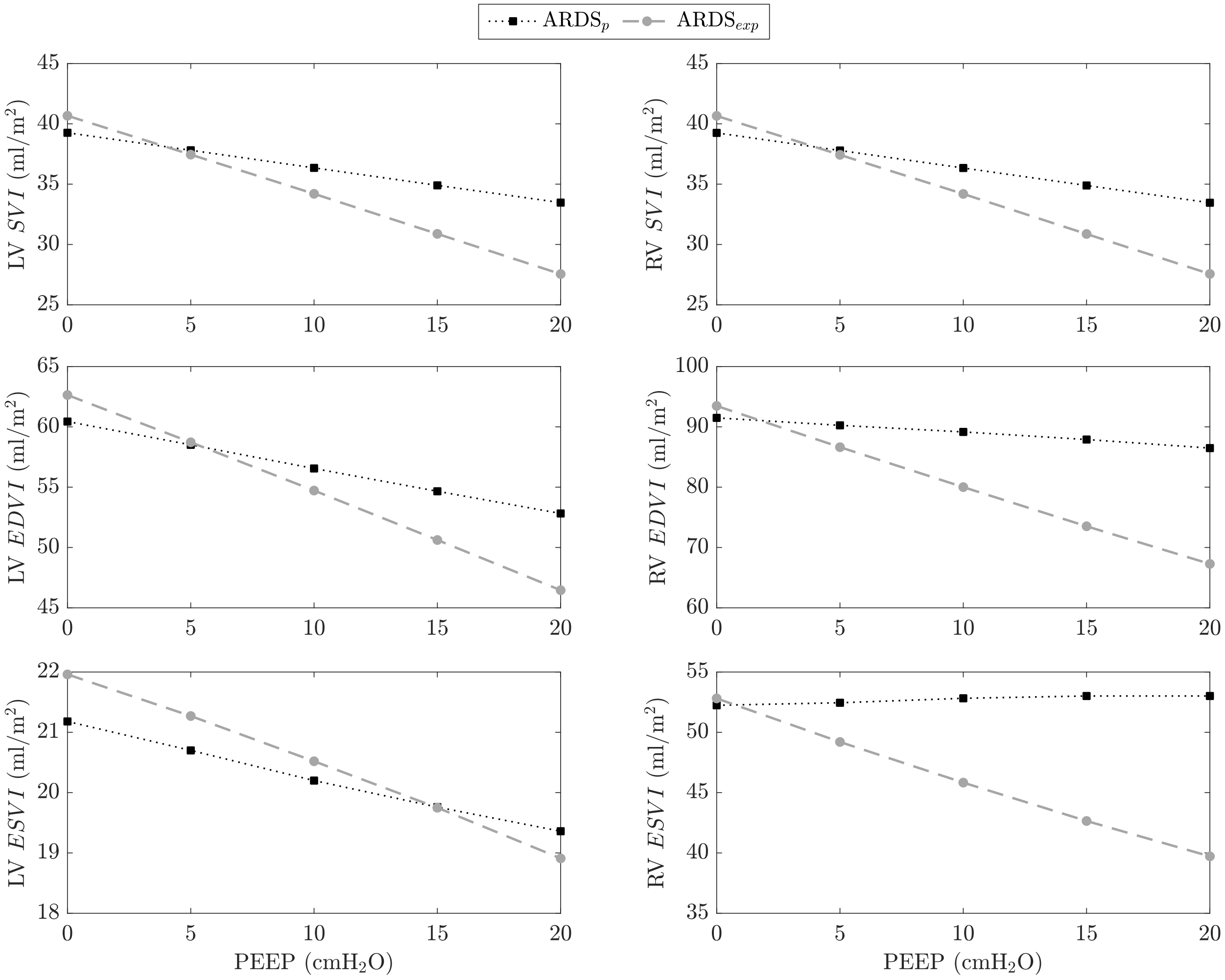

Fig. 2.11. Cardiovascular response to step changes in the level of positive end-expiratory pressure (PEEP) of a virtual patient with either pulmonary ARDS (ARDS$_\mathrm{p}$, *black* squares) or extra-pulmonary ARDS (ARDS$_\mathrm{exp}$, *gray* circles). Each PEEP level is applied for a period of 20 minutes and simulation results are averaged over the last 10 minutes of each PEEP segment. LV, left ventricular; RV, right ventricular; SVI, stroke volume index; $EDVI$, end-diastolic volume index; $ESVI$, end-systolic volume index.

from 2 ml at PEEP$_0$ to 2.37 ml at PEEP$_{20}$. This indicates a septal movement toward the right ventricular free wall, ascribed to the marked reduction in the right ventricular $EDVI$ (see Fig. 2.11).

Furthermore, it is worth noting that the simulated movement of the septum within a heart beat as well as over a respiratory cycle shows similar behavior in both ARDS cases and it is in good agreement with experimental observations. In particular, Jardin et al. [53] reported an early diastolic septal flattening (i.e., leftward movement) owing to the fact that the tricuspid valve opens before the mitral valve. Additionally, Mitchell et al. [60] found an increased transseptal pressure gradient (the difference between left and right ventricular pressures) following the inspiratory reduction in venous return. With this drop in the pressure gradient across the septum, a rightward septal shift was observed during inhalation. Fig. 2.12 displays the model-predicted septal movement (represented by the septal volume waveform, V_{spt}) for a series of cardiac and respiratory cycles from the aforementioned $\mathrm{ARDS}_{\mathrm{exp}}$ case. Septal flattening in early diastole is evident by the low V_{spt} value after the end-systolic marks (gray crosshairs). Further, the experimentally observed rightward movement of the septum during inhalation is shown in the simulation results by the overall increase in V_{spt} at the peak-inspiratory heart beats (see, for example, around the 2-second time instance).

Ventricular interference during mechanical ventilation is primarily linked to the presence of the interventricular septum [60]. However, as we will see in the next section, sensitivity analysis on the newly introduced model modifications highlighted the contribution of the pericardial membrane and the pulmonary circulation to the interdependence between left and right ventricular functions. This contribution has indeed been suggested by multiple studies [31] and may play an important role in explaining the physiological changes in ventricular functions that are typically observed during mechanical ventilation. Ventricular activity is usually described by three indices: preload, afterload, and ejection fraction. Preload is defined as the level of stretching of the cardiac myocytes immediately before contraction. Afterload, on the other hand, is the maximal stress applied on the ventricular wall during contraction and is associated to the load that the ventricle needs to overcome in order to eject blood. Finally, ejection fraction is the proportion of blood, relative to its the maximal volume, pumped by a ventricle per heart beat and depends on both preload and afterload conditions. Positive pressure ventilation is known to affect all three indices. For instance, Fig. 2.13 qualitatively summarizes, based on experimental evidence by Michard and Teboul [3], the changes induced by mechanical ventilation in left and right ventricular function indices. Analogously, but in more quantitative terms, Fig. 2.14 depicts the

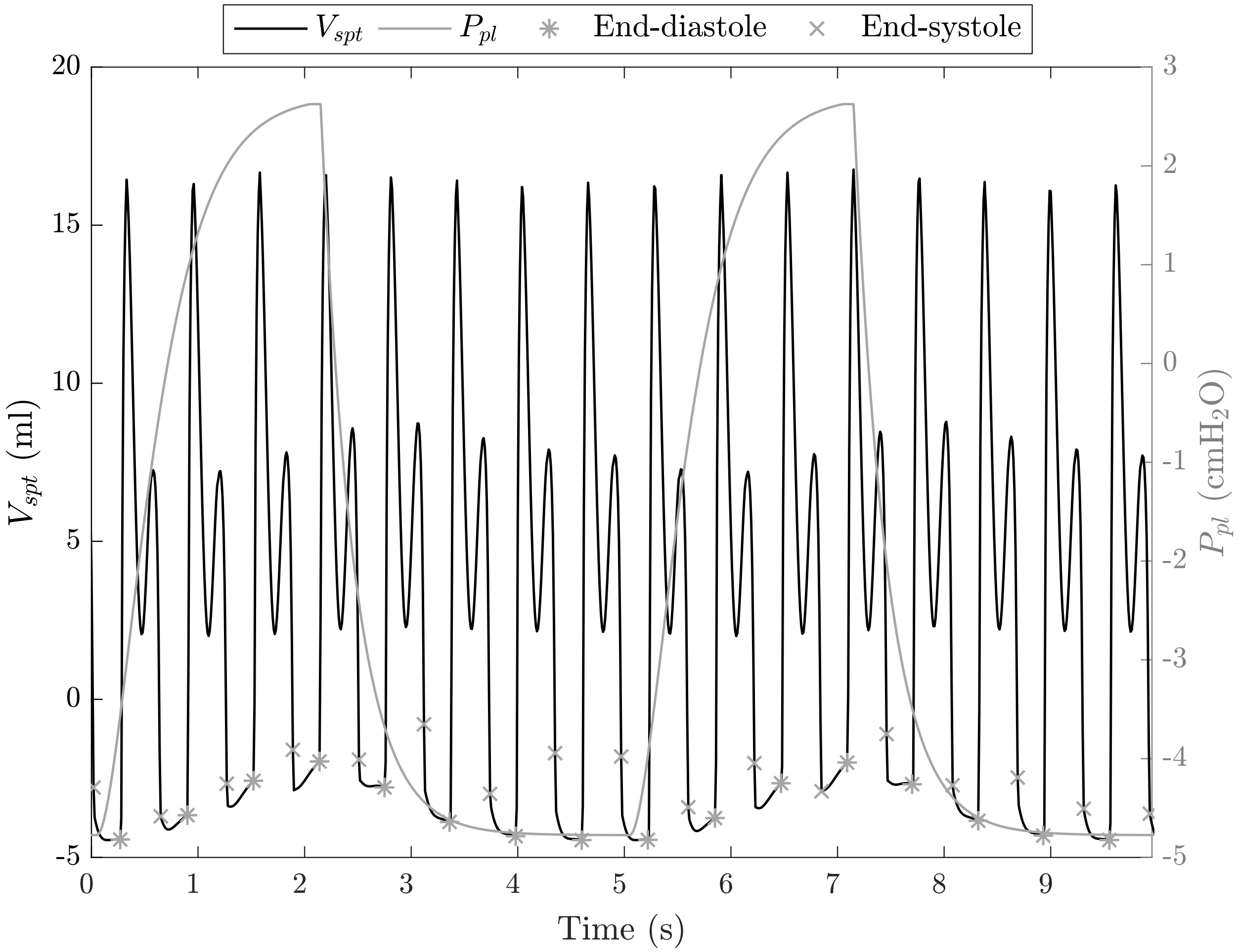

Fig. 2.12. Model-predicted movement of the interventricular septum over sixteen cardiac and two respiratory cycles in positive pressure ventilation. Septal volume (V_{spt}, left vertical axis) models the position of the septum with respect to a vertical imaginary plane H (see Fig. 2.2). Cardiac cycles are indicated by the end-diastolic (gray stars) and end-systolic (gray crosshairs) marks. Respiratory cycles are represented by the pleural pressure (P_{pl}, right vertical axis) waveform that increases with each positive pressure inspiration.

model-predicted beat-to-beat changes in preload, afterload, and ejection fraction computed from the simulation data in Fig. 2.9. Preload is assumed equal to ventricular volume at end-diastole ($EDVI$). Afterload, on the other hand, is assessed based on the Laplace equation. Particularly, assuming that the ventricle is a spherical compartment of radius r with a thin—relative to its radius—wall of thickness h, the wall stress σ can be computed as: $\sigma = (P \cdot r)/(2 \cdot h)$, where P is the maximal transmular pressure across the wall [61]. Notice, however, that the modified CP Model simulates ventricular pressures and volumes without explicitly accounting for the radius and wall thickness of each ventricle. Thus, we cannot directly use the Laplace formula. To overcome such a modeling limitation in computing stress, we proceed as follows: 1) we first assume that the volume of the ventricle is spherical, $V = {}^4\!/_3 \cdot \pi \cdot r^3$ and then 2) we calculate a quantity σ_p that is proportional to the actual wall stress; namely, $\sigma_p = P \cdot \sqrt[3]{V} \propto \sigma$, where P is the end-systolic transmular pressure and V is the corresponding end-systolic volume [54]. σ_p is expressed in mmHg·cm, or alternatively in dynes/cm, and it can be considered as the linear force applied across the ventricular wall per unit length of the wall. Lastly, the ejection fraction is defined as the ratio of stroke volume to end-diastolic volume, i.e., $EF = SVI/EDVI$. It is evident that the model-generated data in Fig. 2.14 are in good agreement with the qualitative representation of the ventilation-induced changes in left and right ventricular functions in Fig. 2.13. In particular, positive pressure inhalation induces lung expansion by increasing transpulmonary and, consequently, pleural pressures. As mentioned in previous sections, positive swings in pleural pressure reduce systemic venous return and hence right ventricular preload (see Fig. 2.13 and black bars in right plot of Fig. 2.14). Such pleural pressure swings also increase pericardial pressure, which, in turn, prompts a decrease in left ventricular transmular pressure. Since afterload depends on the pressure across the ventricular wall, a reduction in transmular systolic pressure is anticipated to lower the afterload of the left ventricle (see Fig. 2.13 and gray bars in left plot of Fig. 2.14). At the same time, inspiratory elevation of alveolar pressure and compression of the pulmonary peripheral vessels due to lung inflation have two consequences. 1) First, they increase the pulmonary system impedance and hence the afterload of the right ventricle (see Fig. 2.13 and gray bars in right plot of Fig. 2.14). This is clearly indicated by the model simulation shown in Fig. 2.14, which predicts an increase in RV afterload of about 17% during the first heart beat right after the beginning of the positive pressure inhalation phase. Note that subsequent transient drop in right ventricular afterload, following the first inspiratory heart beat, can be attributed to the decrease in right ventricular filling since afterload depends on both pressure and volume. 2) Second, they promote blood flow into the left ventricle, thereby increasing left ventricular preload (see Fig. 2.13 and black bars in left plot of Fig. 2.14). The decrease in right ventricular preload during inhalation, along with the concomitant increase in right ventricular afterload, in turn, generate a reduction in right ventricular ejection fraction (see Fig. 2.13 and white bars in Fig. 2.14). Analogously, the increased preload of the left ventricle, accompanied by a decrease of its afterload, generate a transient increase in LV ejection fraction toward the end of inhalation. During exhalation, due to the inspiratory reduction in right ventricular ejection that lowers the filling of the left ventricle, LV stroke volume is reduced according to the Frank-Starling mechanism.

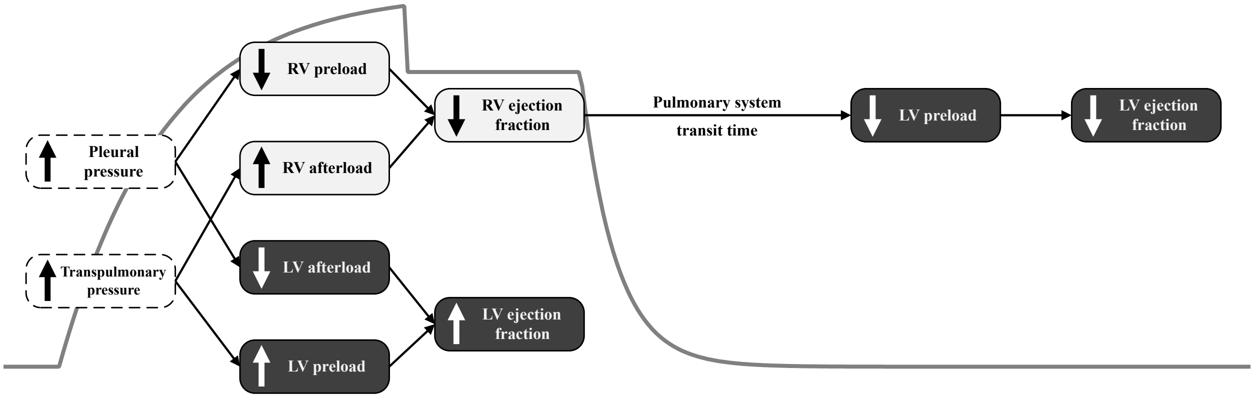

Fig. 2.13. Hemodynamic effects of mechanical ventilation in relation to changes in airway opening pressure (gray waveform). *White* dashed boxes indicate changes in respiratory system variables, whereas *light* and *dark gray* boxes respectively refer to changes in right (RV) and left (LV) ventricular functions. Transpulmonary pressure is defined as the difference between alveolar and pleural pressures. The figure is adapted from [3].

Changes in cardiac function, such as those induced by mechanical ventilation and summarized in Figs. 2.13 and 2.14, are usually observed through variations in left ventricular stroke volume, which is undoubtedly the primary indicator of cardiac performance. Such variations are propagated into the systemic circulation, causing changes to the arterial pulse pressure, the difference between systolic and diastolic pressures. Respiratory-related changes in stroke volume as well as in pulse pressure can then be directly associated to the interactions between heart and lungs in mechanically ventilated conditions. As a result, intra-breath variability in stroke volume and primarily in pulse pressure, thanks to its less invasive nature, have recently been proposed as dynamic predictors of a patient's response to two clinical

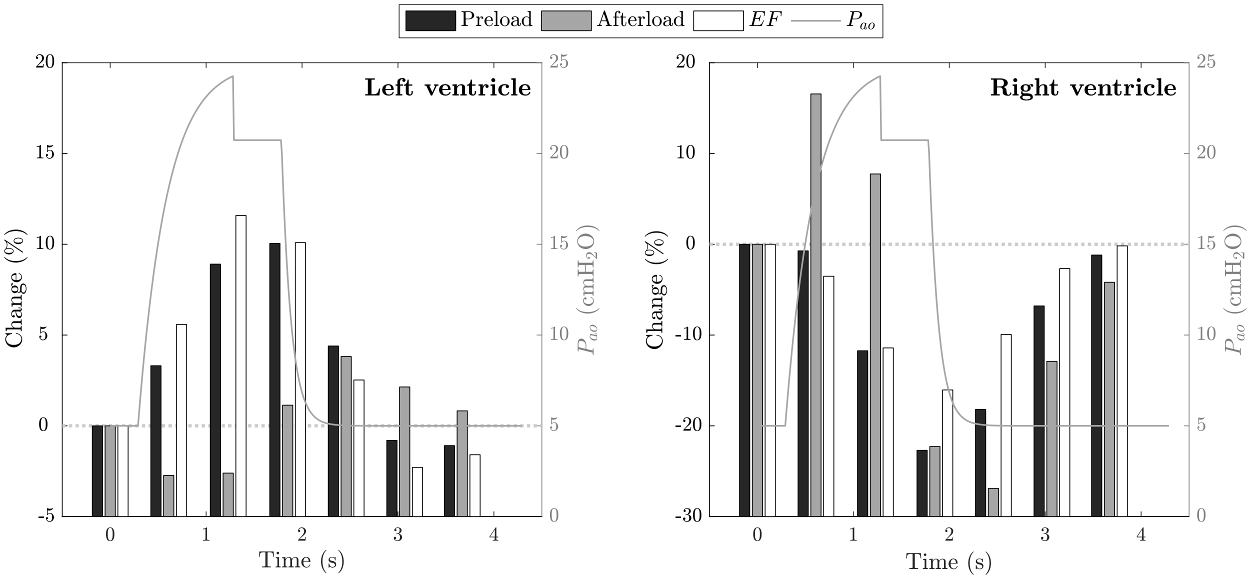

Fig. 2.14. Percent change (left vertical axes) in left (*left* plot) and right (*right* plot) ventricular preload (*black* bars), afterload (*gray* bars), and ejection fraction (*white* bars) with reference to a ventilatory event represented by the airway opening pressure waveform (P_{ao}, right vertical axes). Ventricular function indices have been computed based on the simulation results in Fig. 2.9. The gray horizontal dotted line indicates the zero percent level of the change in preload, afterload, or ejection fraction.

interventions: PEEP application [62] and fluid resuscitation (or volume expansion) [63, 64]. As previously mentioned, the detrimental hemodynamic effects of PEEP are of profound significance, especially in ARDS patients who require institution of high PEEP levels. It is thus crucial that these effects are assessed prior to PEEP application. Volume expansion, on the other hand, is considered a means to restore cardiac output in patients with reduced blood volume (hypovolemic). Since direct assessment of volume status is not possible with current technology, physicians typically rely on hypotension as a clinical manifestation of hypovolemia. Hypotension, however, is a common clinical symptom that can be attributed not only to the presence of an underlying hypovolemic condition, but also to many other pathological conditions, including sepsis and cardiac failure. As a result, a significant number of hypotensive patients, who are suspected of also having hypovolemia, are administered with fluids with the hope that their cardiac output will increase. However, volume expansion is beneficial only to those patients who are truly in a hypovolemic state, whereas it can have detrimental effects in those who are not hypovolemic, potentially causing congestive heart failure and ultimately pulmonary edema. Hence, prediction of fluid responsiveness has the potential to prevent the adverse consequences induced by volume expansion in patients with hypotension that is not caused by an underlying hypovolemic condition.

Given the clinical relevance of PEEP and volume expansion therapies, as well as the popularity of recent technologies that monitor ventilation-induced variations in stroke volume and pulse pressure as a way to assess the patient's response to these therapies, we evaluate the capability of the modified CP Model to reproduce the ventilation-induced pulse pressure variations. To this end, we simulate both PEEP and VE therapies and measure the percent change in pulse pressure over a breathing cycle as originally proposed by Michard et al. [62, 64]:

$$\Delta PP = \frac{PP_{max} - PP_{min}}{(PP_{max} + PP_{min})/2} \cdot 100, \tag{2.13}$$

where PP_{max} and PP_{min} are the maximum and minimum pulse pressure values within a breathing cycle respectively. Pulse pressure is known to be directly proportional to stroke volume. Thus, based on our previous analysis (see Fig. 2.14) and assuming a constant arterial compliance, PP_{max} is expected to occur at peak inspiration, while PP_{min} is observed on heart beats during exhalation. For both PEEP and volume expansion scenarios, we simulated two patient groups: one with low blood volume (hypovolemia) and one with low systemic vascular resistance (sepsis). The model parameters were selected such that the two groups have the same—low—mean arterial blood pressure, at basal conditions, in spite of the differences in the underlying clinical case (i.e., low blood volume or low resistance). The simulation results demonstrated a good agreement with the experimental findings from literature studies [62, 64]. Namely, a high ΔPP value, prior to intervention, is indicative of a hypovolemic subject whose cardiac performance is significantly affected by institution of PEEP or volume expansion. For instance, the hypovolemic virtual patient in the first scenario (PEEP application) had a ΔPP of about 15.5% with an average cardiac index of 3.15 $l/min/m^2$ at zero PEEP. On the other hand, for the septic case, ΔPP was initially

9.5% and CI was 4.15 l/min/m^2. When PEEP of 10 cmH$_2$O was applied, the hypovolemic subject showed a decrease in CI of about 10% to 2.83 l/min/m^2 (ΔPP was increased to 19.2%), while the cardiac index of the septic virtual patient was reduced by only 2.6% to 4.04 l/min/m^2 (ΔPP was increased to just 9.9%). Obviously, there is a clear correlation between the ΔPP at zero PEEP and the magnitude of change in cardiac index with PEEP application. This is in agreement with what was observed in [62]; namely, the level of ΔPP at zero PEEP was directly related to the magnitude of drop in CI after PEEP was increased (i.e., the higher the ΔPP at zero PEEP, the larger the drop in CI). It is worth noting that the model-predicted increase in ΔPP with PEEP application for both cases is in agreement with the experimental observations reported by Michard et al. [62] and Kubitz et al. [65]. Such an increase is ascribed to the fact PEEP reduces cardiac volumes, effectively forcing the heart to work on a steeper portion of the Frank-Starling curve (see Fig. 2.10, for example). Under these conditions, a change in left ventricular filling (preload) will induce a much larger change in stroke volume, and thus pulse pressure, compared to that at zero PEEP [24]. Similar conclusions with regard to the ΔPP prediction capability can also be drawn in reference to the fluid resuscitation scenario. In particular, for the hypovolemic case, ΔPP and CI were initially 18.2% and 2.93 l/min/m^2 respectively. After volume expansion, ΔPP was reduced to 11.7%, while CI was increased to 3.41 l/min/m^2, a 16.4% increase. On the contrary, the septic virtual patient showed much smaller changes in both ΔPP and CI; ΔPP was initially 9.8% and then reduced to 7.5%, while cardiac index increased by only 9.2%, from 4.1 to 4.48 l/min/m^2. We can therefore conclude that the model predictions adhere to the 13% threshold in the ΔPP value before volume expansion that allowed Michard et al. [62] to discriminate between responders (increase in CI after blood infusion greater than 15%) and non-responders with a sensitivity of 94% and a specificity of 96%.

2.6 Sensitivity analysis

The introductions of the pericardial membrane, the interventricular septum, and the modified pulmonary circulation to the original CP Model—as per Section 2.3—were based on experimental evidence that these three elements have a significant contribution to the interactions between the heart and the lungs, especially during mechanical ventilation [31]. Indeed, comparison with human studies from literature demonstrated that the modified CP Model can adequately replicate the effects of positive pressure ventilation on cardiac function. However, despite the physiological basis for introducing these three elements and the evident agreement of the model predictions with experimental data, it is nevertheless of great importance to analyze their individual contribution to the overall cardiovascular model response during mechanical ventilation. To this end, we replicated the scenario described by Vieillard-Baron et al. [2] using the following models: 1) the original CP Model, which does not include the pericardium, the septum, nor the V_A-dependent pulmonary peripheral resistance (original model), 2) the original CP Model with the addition of the pericardium only (pericardium-only model), 3) the original CP Model with the addition of the septum only (septum-only model), and 4) the modified CP Model. Fig. 2.15 shows left and right ventricular stroke volume indices (SVI) from the aforementioned four models during one breathing cycle. The breathing cycle is represented by the airway opening pressure (P_{ao}) on the right vertical axis scale. The experimental data reported in [2] and shown in Fig. 2.9 are also included in Fig. 2.15 for reference. Additionally, Fig. 2.15 displays the percent change (ΔSVI) in left and right ventricular SVI over a breathing cycle. ΔSVI is computed as

$$\Delta SVI = \frac{SVI_{max} - SVI_{min}}{SVI_{min}} \cdot 100, \tag{2.14}$$

where SVI_{max} and SVI_{min} represent the maximum and minimum SVI values within a breathing cycle respectively. Focusing primarily on the ΔSVI values, we observe that each individual model component (i.e., pericardium, septum, modified pulmonary circulation) improves the response of the original CP Model with respect to the experimentally observed left ventricular ΔSVI. Specifically, the simulated ΔSVI values are 8.2%, 9.0%, 11.5%, and 21% respectively for the aforementioned four models as compared with the experimental ΔSVI of 16.7%±4%. Right ventricular ΔSVI, on the other hand, displays a minor change with respect to the proposed model additions. This can be ascribed to the fact that the respiratory-induced changes in right ventricular stroke volume are primarily driven by the cyclic variations in venous return that are secondary to the intrathoracic pressure swings associated with breathing. Since the original CP model already incorporates the effect of intrathoracic pressure on systemic venous return, it is not surprising then that none of the three additions (i.e., pericardium, septum, modified pulmonary circulation) affect right ventricular ΔSVI substantially.

Few additional observations about the effects of the newly introduced model elements on left ventricular ΔSVI can be demonstrated. 1) In the simulation scenario presented in Fig. 2.15, the effect of the septum on ΔSVI is considerably higher than that of the pericardium. When only the pericardium is added to the original model, ΔSVI is increased from 8.2% to 9.0%, while the corresponding increase in ΔSVI for the septum-only model is about 3.3% (from 8.2% to 11.5%). Such an observation is supported by human studies that have demonstrated the septum's predominant role in affecting left ventricular performance via the direct ventricular interdependence phenomenon [31]. However, the relative contributions of septum and pericardium on LV ΔSVI are notably altered in cases of excessive cardiac volumes (e.g., hypervolemia). Under such pathological conditions, the heart operates on a less steep part of the Frank-Starling curve (rightward shift); namely, any given change in preload will induce a smaller change in stroke volume compared to that under normovolemia. Hence, since the septum affects left ventricular preload through the ventricular interdependence, the septal influence on LV stroke volume will be attenuated when cardiac volumes are increased. At the same time, the elevated cardiac volumes cause a considerable increase in the amplitude of the restraining forces that the pericardium exerts on the

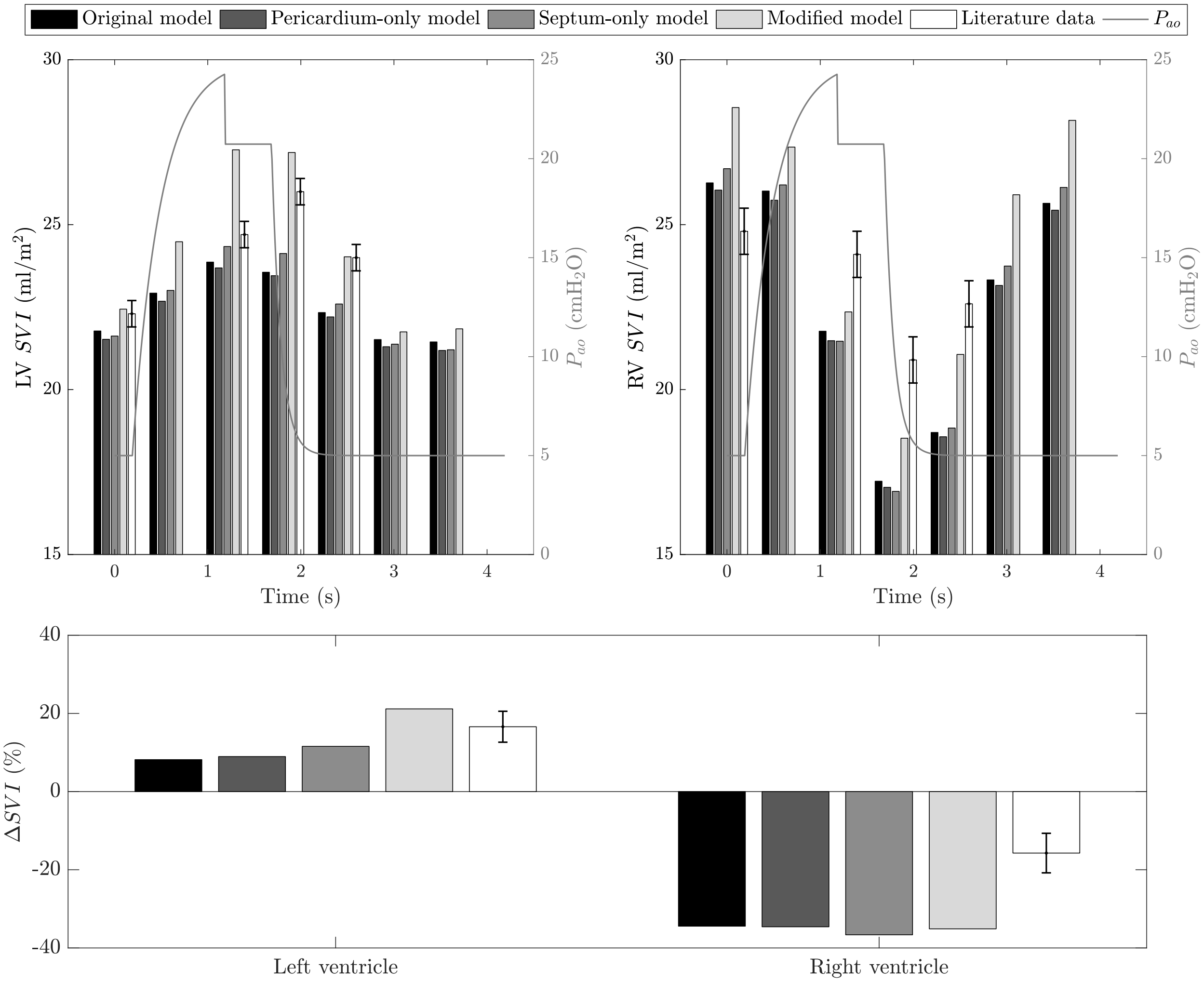

Fig. 2.15. Cyclic changes in left (LV) and right (RV) ventricular stroke volume indices (SVI) during positive pressure ventilation for selective introduction of each of the proposed model additions, i.e., pericardial membrane (pericardium), interventricular septum, and modified pulmonary circulation. *Top* plots show, beat-by-beat, the values for LV and RV SVI from the original CP Model (*black* bars, original model), the CP Model when only the pericardium has been included in the cardiac model (*dark gray* bars, pericardium-only model), the CP Model when only the septum has been included in the cardiac model (*gray* bars, septum-only model), and the modified CP Model (*light gray* bars, modified model) that includes all three model additions. A single respiratory cycle is represented by the airway pressure waveform (P_{ao}, right vertical axis). Literature data (*white* bats) from Vieillard-Baron et al. [2] are also presented for reference. *Bottom* plot displays the corresponding percent change (ΔSVI) in LV and RV SVI values for the data presented in the top graphs.

heart to prevent cardiac over-dilatation [35]. Consequently, pericardial pressure is increased, leading to a reduction in LV afterload (pericardial pressure is the external pressure for the ventricles) and hence to improved left ventricular output. It is then apparent that in hypervolemic conditions, septal contribution on left ventricular ΔSVI will be lower than that of the pericardium. This physiological phenomenon is also observed in simulation studies with the modified CP Model. Simulating, for instance, a volume overload condition by administering 1.5 liters of fluid to the virtual patients that produced the results in Fig. 2.15 has the following outcome: the ΔSVI from the septum-only model is 1.4%, whereas the pericardium-only model predicts a higher value that is equal to 1.8%. As previously explained, the ΔSVI values from these two models (septum-only and pericardium-only) remain higher compared with that from the original CP Model (0.6%). Nevertheless, notice that the absolute ΔSVI values from all model simulations are markedly lower in comparison to those in Fig. 2.15, a result that is attributed to the heart's different operating point on the Frank-Starling curve (rightward shift). 2) Multiple studies [66, 67] have shown that a closed pericardium accentuates the interference between left and right ventricles. Simulation results from the modified CP Model confirm this experimental observation. As mentioned earlier, the inclusion of only the pericardium contributes to a 0.8% increase in ΔSVI (from 8.2% of the original model to 9.0% of the pericardium-only model). However, a CP Model that includes both septum and pericardium predicts a ΔSVI value of 12.6%, a 1.1% increase relative to the ΔSVI of the septum-only model. Such a 1.1% increase in ΔSVI is higher than the corresponding ΔSVI increase (0.8%) when only the pericardium was included into the original model, thus indicating that the pericardium does accentuate the septum-induced ventricular interdependence. 3) Fig. 2.15 clearly shows that in order to reproduce a ΔSVI of similar magnitude as that reported in the experimental data by Vieillard-Baron et al. [2], it is necessary to include all three model components (i.e., pericardium, septum, modified pulmonary circulation). Particularly, since the magnitude of ΔSVI attained by the pericardium-only and septum-only models are substantially smaller than that reported in [2], the inclusion of the V_A-dependent pulmonary peripheral resistance seems to play a major role.

2.7 Model limitations

Despite the proven capability, based on the analyses in previous sections, of the proposed modified CP Model in describing heart-lung interaction mechanisms, it is necessary to point out some of its limitations. These can also serve as a basis for future work.

First, the modified CP Model does not consider the effects of PEEP on alveolar recruitment and gas exchange. For instance, it is well known that institution of PEEP on ARDS patients is recommended as a way to improve gas exchange and increase arterial P_{O_2}. This is achieved because PEEP aims to inflate the collapsed alveoli and reduce the edema and the intrapulmonary shunt [68]. Alveolar recruitment is typically represented via a respiratory mechanics nonlinear pressure-volume relationship [69], whereby lung compliance is expected to increase as the collapsed lung regions are being recruited with PEEP application. As a consequence, the recruited alveoli can participate in gas exchange, effectively prompting a reduction in the intrapulmonary shunt. However, the modified CP Model assumes a linear pressure-volume relationship (linear lung compliance) and a constant value for the shunt fraction, the proportion of blood that does not participate in gas exchange. If, for example, the PEEP-induced alveolar recruitment was to be modeled via a nonlinear compliance and a varying shunt fraction, the increased tidal volumes (for the same level of pressure support) due to the higher compliance value along with the reduction in shunt would allow more oxygen-rich air to participate in gas exchange, thereby leading to better blood oxygenation and higher model-simulated $P_{a_{O_2}}$ values. Besides gas exchange, having a constant lung compliance also has disadvantages with respect to the mechanism that describes the effects of PEEP on cardiac output (see Fig. 2.16). Specifically, Dhainaut et al. [4] found a curvilinear relationship between PEEP values and cardiac index (black squares in left plot of Fig. 2.16), whereas the modified CP Model predicted a linear relationship between the two (gray circles in left plot of Fig. 2.16). At the same time, CI and pleural pressure were linearly related for both simulated and experimental data (right plot in Fig. 2.16). Noticeable is, however, the effect of PEEP on pleural pressure. Each step increase in PEEP resulted in a constant step increment of pleural pressure in the modified CP Model, whereas the experimental data showed larger step increments at higher PEEP levels (compare the x-axis increments in the right hand-side plot of Fig. 2.16). Similar to the conclusion by Dhainaut et al. [4], we conjecture that the varying levels of change in pleural pressure with PEEP are attributed to the nonlinear lung compliance. The increased compliance at higher PEEP levels allows for a larger lung expansion. This, in turn, leads to a more profound compression of the pleural space, a fact that is translated to a larger increase in P_{pl} compared to that at low PEEP values. We can therefore conclude that since pleural pressure directly affects venous return, the varying step increments in P_{pl} due to the nonlinear lung compliance are responsible for the curvilinear relationship between CI and PEEP reported in literature [4].

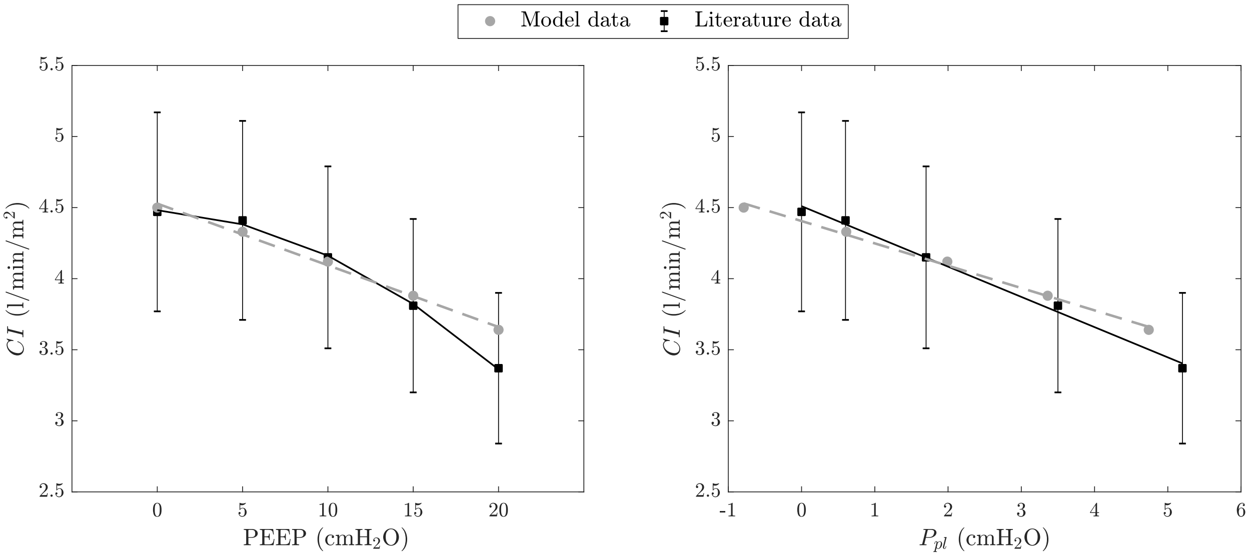

Fig. 2.16. Comparison of the effects of positive end-expiratory pressure (PEEP, *left* plot) and pleural pressure (P_{pl}, *right* plot) on cardiac index (CI) between model-predicted (*gray* circles) and experimental (*black* squares) data. Literature data are taken from Dhainaut et al. [4] and are reported with their mean and standard error of the mean values. Notice that each P_{pl} point represents the average pleural pressure (or esophageal pressure—a surrogate of pleural pressure—for the human study) at each respective PEEP level of the left plot.

Second, certain limitations also exist in the heart model. 1) As indicated in Section 2.3, the modified CP Model does not account for any mechanical interdependence between the two atria [38]. 2) Furthermore, a constant left ventricular diastolic pressure-volume relationship is used. Although some studies [40, 53] have shown that right ventricular overload may lead to a decrease in left ventricular diastolic elastance, the current model implementation only considers the leftward movement of the septum as the sole reason for right-to-left ventricular interference that causes a decrease in left ventricular volume. 3) Finally, activation of the left and right ventricular free walls is assumed to happen simultaneously. Such a choice is based on the ambiguity in experimental evidence with regard to the temporal relationship between left and right ventricular contractions in healthy individuals [70, 71, 72]. Nevertheless, attention has been taken so that simulation of contraction delays due to pathological conditions, such as left or right bundle branch blocks, can be readily performed.

Lastly, there exist a few additional mechanisms that could contribute to the hemodynamic effects of ventilation and are not included in the modified CP Model. For instance, systemic venous return depends on the gradient between the pressure in the extra-thoracic veins (upstream pressure) and that in the venae cavae inside the thorax (downstream pressure). These two pressure points are, in turn, affected by abdominal and pleural pressures respectively. While mechanical ventilation induces positive swings in pleural pressure, it also causes the diaphragm to descend, thereby raising abdominal pressure [73, 74]. Pleural pressure swings are considered the primary determinants in decreasing venous return. However, the concomitant increase in abdominal pressure is expected to minimize the effect of P_{pl} in reducing venous return. In the modified CP Model though, we assume that abdominal pressure is equal to atmospheric pressure (zero), and thus the model-predicted changes in venous return depend solely on changes in the pleural pressure. This assumption could result in a model-predicted venous return that is larger than in real clinical scenarios, particularly if diaphragmatic descent is significant. Two more physiological mechanisms are not considered in the modified CP Model. 1) We did not model the effects of spontaneous ventilation on metabolic activity. Spontaneous ventilation is perceived as exercise, especially in lung disease states [75]. In such pathological conditions, the patient's work of breathing as well as their O_2 metabolic demands are drastically increased. Albeit the absence of such a mechanism in the modified CP Model, we do not expect that it would have a major impact in the simulation results presented herein. With the exception of the study by Kyhl et al. [1] who analyzed healthy individuals, all other subjects were completely sedated. 2) As presented in Section 2.3, we assumed that the pulmonary vascular resistance of the modified CP Model is a function of alveolar volume only. However, Madden et al. [76] showed that the resistance of the pulmonary circulation is also affected by the level of alveolar P_{O_2}. It was demonstrated that such a phenomenon, referred to as hypoxic pulmonary vasoconstriction [75], causes a decrease in the blood flow through the pulmonary vascular bed (i.e., increased vascular resistance) once $P_{A_{O_2}}$ falls below 60 mmHg.

2.8 Conclusion

In conclusion, in this chapter, we presented a modified CP Model where we appended the pericardial membrane and the interventricular septum to the cardiac component of a previously developed and validated cardiopulmonary model [18, 19]. In addition, we modified the original pulmonary circulation model to account for the compression of the pulmonary peripheral vessels due to lung inflation. Such modifications were adopted in an effort to better model the heart-lung interactions that are of profound importance, especially in mechanical ventilation conditions. The introduction of the pericardium was also intended to allow for simulation of cardiac disease states, such as pericarditis and cardiac tamponade. We then verified the consistency of this modified CP Model with respect to its original version. Comparison of the outputs from the modified CP Model with experimental data in reference to the ventilation-induced changes in cardiac function showed promising results, both in transient (intra-breath) and steady-state conditions (PEEP application). Moreover, simulations from the proposed modified model were able to provide physiologic explanations to a few contradicting experimental observations, thus providing credence to the benefits of using such a model. We therefore believe that this modified CP Model can serve as an effective tool to study, analyze, and evaluate the effects of mechanical ventilation therapy on cardiac performance.

Chapter 3

Cardiopulmonary model-based patient emulator

3.1 Introduction

Mechanical ventilation (MV) is a commonly used life-saving procedure in intensive care units. It is required when a patient is not able to breathe on their own. Positive-pressure ventilation, a form of MV, has been available for more than a century [17] and has become the standard practice for mechanically ventilated patients in the clinical setting. Despite the existence of many modes of MV being offered by ventilator manufacturers [77], new ventilation modes are constantly being proposed in an attempt to reduce operator's time, favor patient-ventilator interactions and synchrony, and ultimately improve patient outcomes. These ventilation modes differ from one another in the way they control the flow and/or pressure of the air delivered to the patient. In an effort to demonstrate the effects of each mode on patient outcomes, extensive clinical trials have been performed comparing all the available ventilation modes together. However, the results of these clinical trials have often been inconclusive [78, 79]. One of the major limitations of human clinical trials is the difficulty of creating controlled experimental conditions and isolating the effects of the ventilation mode under investigation from other possible factors that could affect patients' responses and clinical outcomes. Thus, there is a clear unmet need for devices that would allow standardized testing as well as comparison between existing and new ventilation modes, possibly leading to reducing the number of human and animal trials. In this chapter, we will first provide a brief description of the devices currently available in the market for testing ventilation modes and highlight their limitations. Then, we will present our developed patient emulator system, a novel system for in-silico ventilation therapy testing, that is based on the cardiopulmonary model (CP Model) presented in Chapter 1 interfaced with a physical ventilator via a controlled piston-cylinder actuator.

3.2 State-of-art testing devices

Until recently, preclinical testing of ventilation modes has been primarily based on passive mechanical devices trying to mimic the inflation of a patient's lungs. These devices are available in two configurations: 1) bag-style test lungs, and 2) bellows-type systems. On one hand, bag-style test lungs, like the Linear Test Lung (Fig. 3.1a) from IngMar Medical, Ltd. (Pittsburgh, PA), offer easy portability and simple usage. They operate by means of inflation of a fixed elastic balloon placed within a plastic encasing. Thus, their testing capabilities are limited to the specific range of pressure-volume relationships describing the balloon's elastic properties, which cannot be configured in a precise way. In other words, they are able to replicate the respiratory mechanics within an approximated and limited range of the respiratory system's elastance[1]. On the other hand, bellows-type systems, like the Dual Adult Test Lung Simulator (Fig. 3.1b) by Michigan Instruments, Inc. (Grand Rapids, MI), are equipped with a bellows configuration for simulating the human respiratory mechanics. Compared to bag-style test lungs, bellows-type simulators offer a wider range of operation in terms of the simulated respiratory system compliance and tidal volumes. The desired compliance value can be accurately set by a steel alloy spring, whose position (along the device's length) determines the extension to which the bellows are inflated (i.e., compliance) and hence the inspired tidal volumes. Even though bellows-type systems are not portable, they are quite versatile as they provide additional gas and pressure sensor ports for monitoring the oxygen content and pressures inside the bellows[2]. As for the respiratory system resistance[3], both bag-style and bellows-type systems use fixed-orifice flow restrictors placed at the entry point of either system. Such restrictors can then be readily interchanged according to the desired testing procedure. For instance, obstructive diseases, like asthma, can be simulated by applying a restrictor with a smaller orifice and thus higher resistance to air flow.

---

[1] Respiratory system elastance comprises the lung and chest wall elastic mechanical properties. The elasticity of the lungs is attributed to pulmonary tissue's elastic properties and to lung's surface tension, whereas chest wall elastance is ascribed to the structure and properties of the rib cage. Practically, the combination of lungs and chest wall engenders the elastic recoil pressures that must be overcome for breathing to occur.

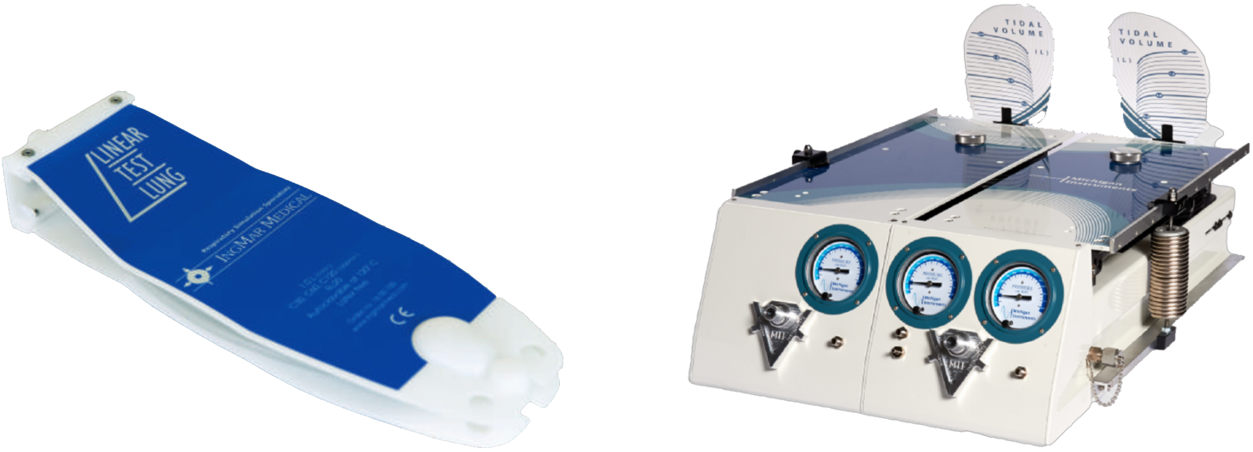

(a) Linear Test Lung. Image courtesy of IngMar Medical, Ltd.

(b) Dual Adult Test Lung Simulator. Image courtesy of Michigan Instruments, Inc.

Fig. 3.1. Passive mechanical simulators of the respiratory mechanics.

The aforementioned devices present great advantages in testing and verifying the accuracy of the ventilator under examination in delivering the prescribed levels of pressure and volumes[4]. However, it is evident that they lack the ability to simulate spontaneously breathing patients under mechanical ventilation support[5]. Such patients are able to initiate breathing events and inflate the lungs, but not fully capable to sustain their breathing efforts for a prolonged period of time. Hence, external ventilation support via a mechanical ventilator is necessary. The ventilator essentially shares the work performed on the respiratory system to expand the lungs with the patient. One way to simulate spontaneously breathing patients and the ensuing patient-ventilator interactions is via physiology-based mathematical models, like the one presented in Chapter 1. The comprehensiveness of such models allows the development of virtual patients that replicate a wide range of clinically observed patient-ventilator interaction phenomena. Accordingly, the software-implemented virtual patient can interface with a mechanical ventilator via a computer-controlled hardware apparatus.

---

[2] Notice that the volume of air inside the bellows approximates the volume in the alveolar space

[3] Respiratory system resistance is typically ascribed to the resistive properties of the upper airways as well as to the viscosity of the pulmonary tissues.

Currently, there are few high-fidelity simulators that use physiological models of the combined cardio-respiratory system and respond to external ventilatory input. One particular example is the Human Patient Simulator (Fig. 3.2a) from CAE Healthcare, CAE Inc. (Sarasota, FL). It is a sophisticated simulation platform designed to support anesthesia and medical gases, interface with real clinical monitors and ventilators, and even respond to the administration of drugs and anesthetic gases. However, it is expensive and typically reserved for training of clinical personnel within dedicated simulation centers of specialized hospitals. As a consequence, ventilator manufacturers are using simpler breathing simulators that only consider the respiratory mechanics as their mathematical model engine. The ASL 5000 Breathing Simulator, developed by IngMar Medical, Inc. (Pittsburgh, PA), (Fig. 3.2b) is probably the most popular one and is extensively used for testing ventilation therapies. The main drawback of such breathing simulators is that they do not account for gas exchange or the interactions between the respiratory and cardiovascular systems. For instance, it is well known that elevated pressure in the lungs, which is typically developed when high values of positive end-expiratory pressure (PEEP) are used, can negatively affect cardiac output. Furthermore, the level of pressure support, which is one of the ventilator settings when pressure support ventilation is used, directly affects respiratory drive and determines the degree of unloading of the respiratory muscles. An appropriate degree of respiratory muscle unloading is required to prevent muscle atrophy and fatigue and thus it is a key determinant of successful weaning and liberation from the ventilator. Hence, all these physiological interactions cannot be demonstrated by simple breathing simulators without gas exchange, neural feedback, and cardiovascular components. For this reason, we leveraged the power of the cardiopulmonary model of Chapter 2 to describe physiological cardio-respiratory dynamics and developed our patient emulator system.

---

[4] Pressure and volume levels are determined based on the mechanical properties of the patient's respiratory system. Such properties are, in turn, defined as the system's resistance and compliance.

[5] Michigan Instruments, Inc. do offer a module to transform the Dual Adult Test Lung Simulator into a spontaneously breathing system. However, this system is not very intuitive to use and has limited features in regard to simulating spontaneous breathing events.

3.3 The patient emulator system

The current state of affairs for ventilator testing relies on extensive human and animal trials. These experimental studies are costly, time-consuming, and cause discomfort to the in-vivo subjects. Patient emulators, which are based on large-scale integrated mathematical models of the human cardiopulmonary system, can then provide a more efficacious design and testing of ventilation therapies. In particular, the physiological models within such emulator systems can be considered as virtual patients on which ventilation modes can be tested and evaluated. Not only will this permit testing and comparison to be performed in a highly controllable environment and without requiring animal or human experimentation, but it will also save time and money during the development phase. Additionally, the use of a patient emulator system can lead to the formulation of new and improved standardized testing protocols. The advantages offered by this system are essentially attributed to the comprehensiveness of the physiological model in use. It is then necessary for the system's model-engine to accurately

(a) Human Patient Simulator. Image courtesy of CAE Healthcare, CAE, Inc.

(b) ASL 5000 Breathing Simulator.
Image courtesy of IngMar Medical, Ltd.

Fig. 3.2. State-of-art model-based breathing simulators.

describe the dynamics of the cardiovascular and pulmonary systems, tissue and alveolar gas exchange, as well as the main mechanical and short-term neural control mechanisms between the cardiovascular and respiratory functions. To this end, our proposed patient emulator system is based on the comprehensive multi-compartment CP Model presented in Chapter 2. An overview of the advantages of using our patient emulator for testing ventilation therapies as compared to the current practice, summarized in the previous section, is presented in Fig. 3.3. Fig. 3.3 schematically shows that testing ventilation therapies using such an emulator system can potentially shorten the duration of testing by reducing the time spent on human and animal trials.

Fig. 3.4 displays the patient emulator system connected to a mechanical ventilator. Fun-

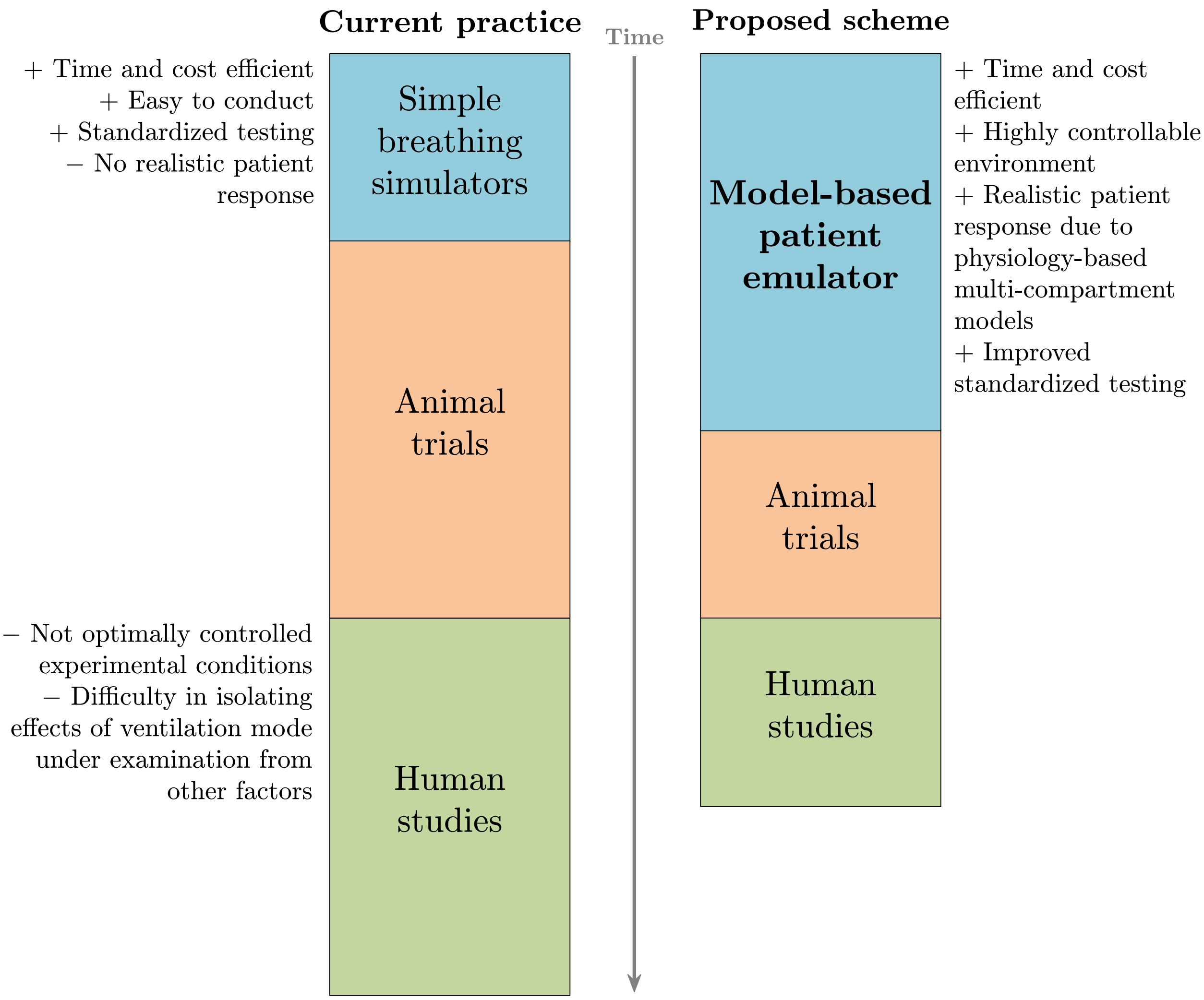
Current practice
Time
Proposed scheme
+ Time and cost efficient
+ Easy to conduct
+ Standardized testing
– No realistic patient response
Simple breathing simulators
Animal trials
– Not optimally controlled experimental conditions
– Difficulty in isolating effects of ventilation mode under examination from other factors
Human studies
Model-based patient emulator
+ Time and cost efficient
+ Highly controllable environment
+ Realistic patient response due to physiology-based multi-compartment models
+ Improved standardized testing
Animal trials
Human studies

Fig. 3.3. A schematic illustration of the advantages of the proposed patient emulator system for testing mechanical ventilation therapies in comparison to the current practice.

damentally, the system comprises two main components: 1) a mathematical model engine, namely the modified CP Model proposed in Chapter 2 (see Fig. 2.2), with its graphical user interface and 2) a piston-cylinder arrangement (ASL 5000 Breathing Simulator, IngMar Medical, Ltd., Pittsburgh, PA) that serves as a two-way electrical-to-hydraulic transducer and allows the CP Model to communicate with a physical mechanical ventilator.

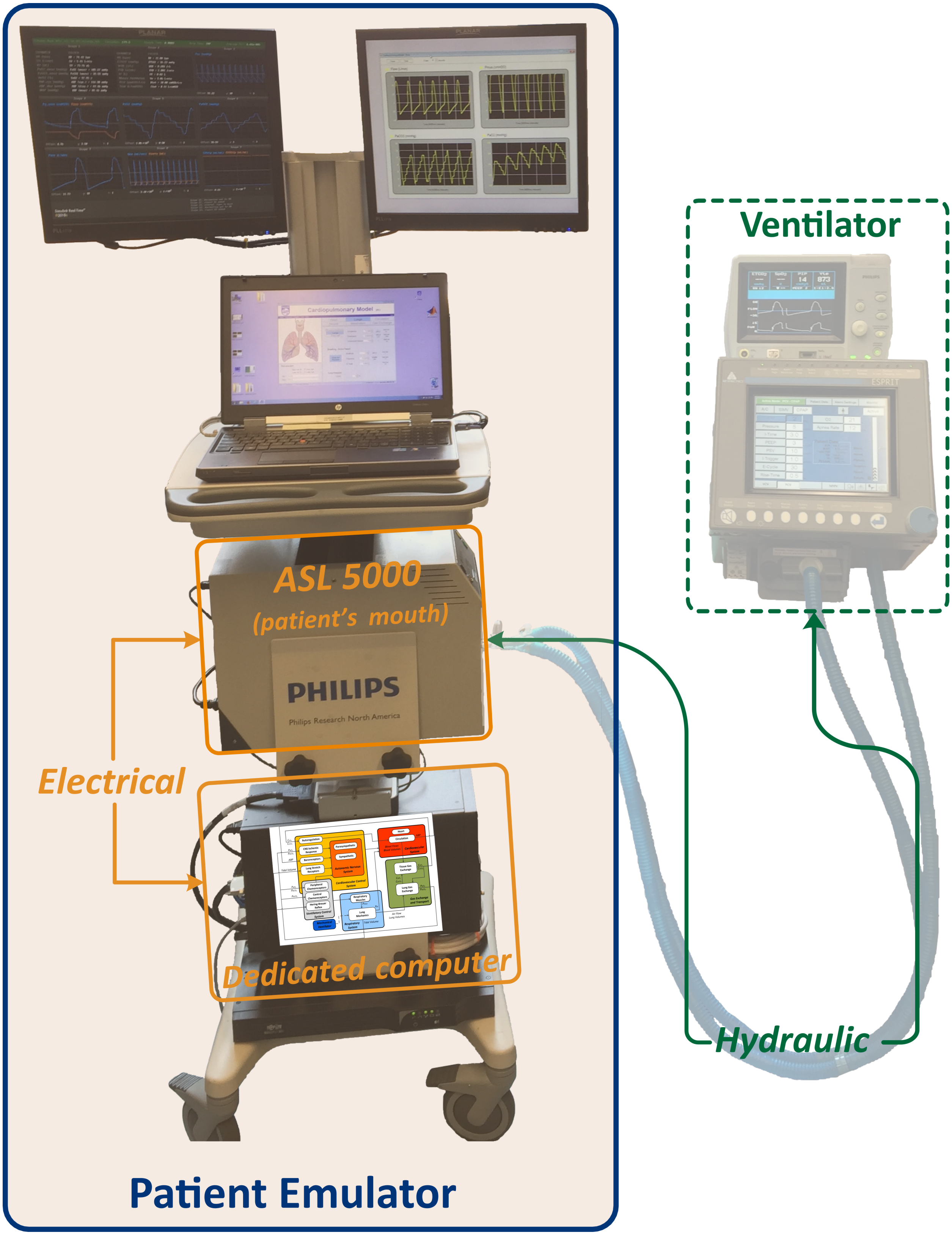
Ventilator
ASL 5000
(patient's mouth)
PHILIPS
Philips Research North America
Electrical
Dedicated computer
Hydraulic
Patient Emulator

Fig. 3.4. The patient emulator system (CP Model and ASL 5000 Breathing Simulator) connected to a mechanical ventilator. Image courtesy of Philips Respironics.

3.3.1 Software-hardware interface

In more detail, Fig. 3.5 shows a high-level block diagram of the patient emulator, including the system's main hardware components: 1) a dedicated computer that runs the Simulink® Real-Time environment (The MathWorks, Inc., Natick, MA), 2) an ASL 5000 Breathing Simulator, and 3) a pressure transducer.

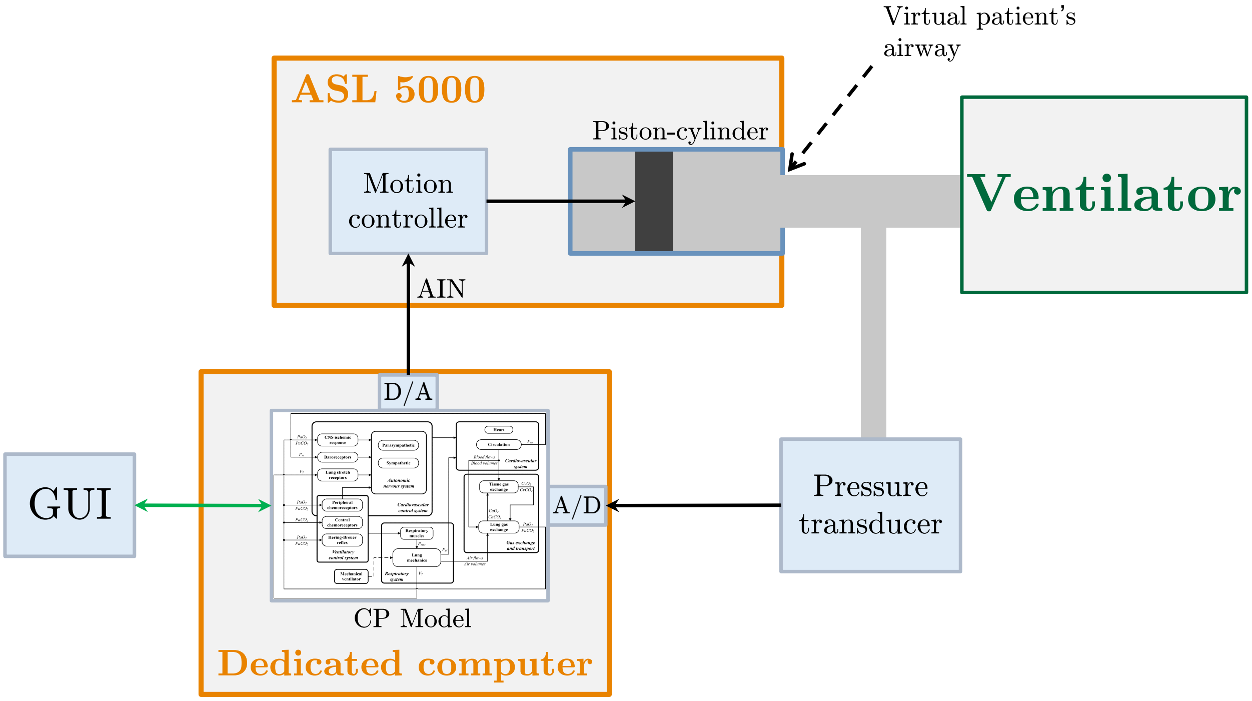
Virtual patient's airway
ASL 5000
Piston-cylinder
Motion controller
Ventilator
AIN
D/A
GUI
A/D
Pressure transducer
CP Model
Dedicated computer

Fig. 3.5. A high-level block diagram of the patient emulator system. AIN, analog input port of the ASL 5000 Breathing Simulator; A/D and D/A, analog-to-digital and digital-to-analog converters of the dedicated computer, respectively; GUI, graphical user interface for interacting with the CP Model (virtual patient).

The primary purpose of the dedicated computer is to provide a computing framework for the Simulink® Real-Time environment to run the modified CP Model (virtual patient) in real-time at a pre-defined step size. As mentioned in Chapter 2, Simulink® is a computational software specialized in high-accuracy numerical integration of ordinary differential equations, such as those that describe the CP Model's dynamic response. In turn, Simulink® Real-Time environment converts the Simulink®-implemented model into executable code and deploys it in dedicated hardware for real-time execution. For example, in our implementation, the dedicated computer is equipped with a high performance Intel® Core™ i7 processor, which is capable of solving the differential equations of the CP Model at a rate of 5 kHz (step size of 0.0002 s). Additionally, the computer includes a data acquisition card (NI-6529, National Instruments Corp., Austin, TX) for analog-to-digital conversion of the pressure transducer's measurements and for interfacing with the breathing simulator and, in turn, with the ventilator via a digital-to-analog converter. In particular, the ASL 5000 of our setup runs in a non-feedback mode, called "flow pump mode" that ignores the pressure reading from the built-in sensor. In this mode, the piston is exclusively controlled by the flow profile commanded through the simulator's analog input port (AIN). Notice that although the default ASL 5000 configuration uses its piston-cylinder arrangement to simulate respiratory mechanics (see Section 3.2), we instead use it merely as a two-way transducer. In addition, we have incorporated a separate pressure transducer within the device casing that allows us to read the pressure at the ASL 5000 orifice, the connection point with the ventilator. The CP Model that is deployed in the dedicated computer then reads the pressure at the simulator's orifice, which now serves as the virtual patient's airway, and calculates an instantaneous flow value based on the selected model parameters (e.g., resistances, elastances). The simulated flow signal is then transmitted through the AIN to the ASL 5000 motion controller that assures that the piston follows the commanded flow. As a result, this dedicated computer and ASL 5000 arrangement constitutes the patient emulator system that can be hydraulically connected to any ventilator via a standard breathing circuit[6].

It is also worth mentioning that the choice of the patient emulator's hardware components and, particularly, the selection of the pressure transducer was done after a thorough evaluation of the sensor's performance with reference to the system's requirements. We tested three different pressure designs, as depicted in Fig. 3.6. The Validyne PS309 (Validyne Engineering, Northridge, CA) in Fig. 3.6a is a portable, completely self-contained pressure manometer. Despite the easy accessibility of such an external device, its location

---

[6] Such a system was deployed at two Philips Healthcare facilities that manufacture mechanical ventilators and is currently being used for testing purposes.

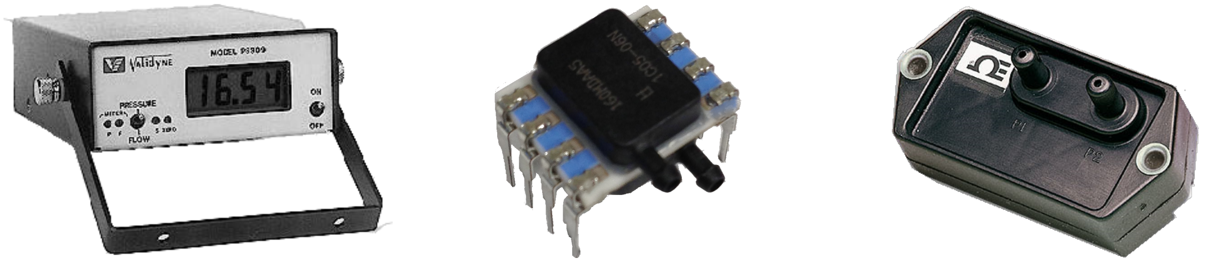

(a) Validyne PS309.
Image courtesy of Validyne Engineering.

(b) Honeywell TruStability®.
Image courtesy of Honeywell International, Inc.

(c) Omega PX140.
Image courtesy of Omega Engineering, Inc.

Fig. 3.6. Pressure transducers.

with reference to the pressure measurement point (inside the cylinder of the ASL 5000 simulator) necessitates a long connecting tube. The ensuing large hydraulic delays due to the long tubing as well as the sensor's relatively high time constant[7] (about 10 ms) rendered the Validyne sensor incompatible with our application. Delays either due to long hydraulic connections or due to the sensor's slow dynamic response are known to have detrimental effects on closed-loop systems, including our patient emulator. Accordingly, we decided to evaluate the Honeywell TruStability® (Honeywell International, Inc., Morris Plains, NJ) and Omega PX140 (Omega Engineering, Inc., Norwalk, CT) sensors (Figs. 3.6b and 3.6c respectively) which both feature a fast response with a 1 ms time constant. In addition, their small form factor allowed us to place them inside the ASL 5000 casing, thus reducing any excess tubing. The final selection of the Omega pressure sensor, which includes a hybrid integrated circuit and temperature compensation, was selected due to its more robust design and accurate pressure measurements. For example, Fig. 3.7 shows a comparison between the Honeywell TruStability® and Omega PX140 sensors in terms of noise levels (Fig. 3.7a) and dynamic responses to a step change in the pressure reading (Fig. 3.7b). It is evident that the Omega pressure transducer (blue line in both plots) has a lower measurement noise—about 0.1 cmH_2O versus about 0.2 cmH_2O of the Honeywell (red line in both plots)—and a faster response with its tracing leading in time the one from Honeywell by about 1 ms.

---

[7] The time constant of a pressure transducer indicates how fast it responds to step changes in pressure at the measurement point.

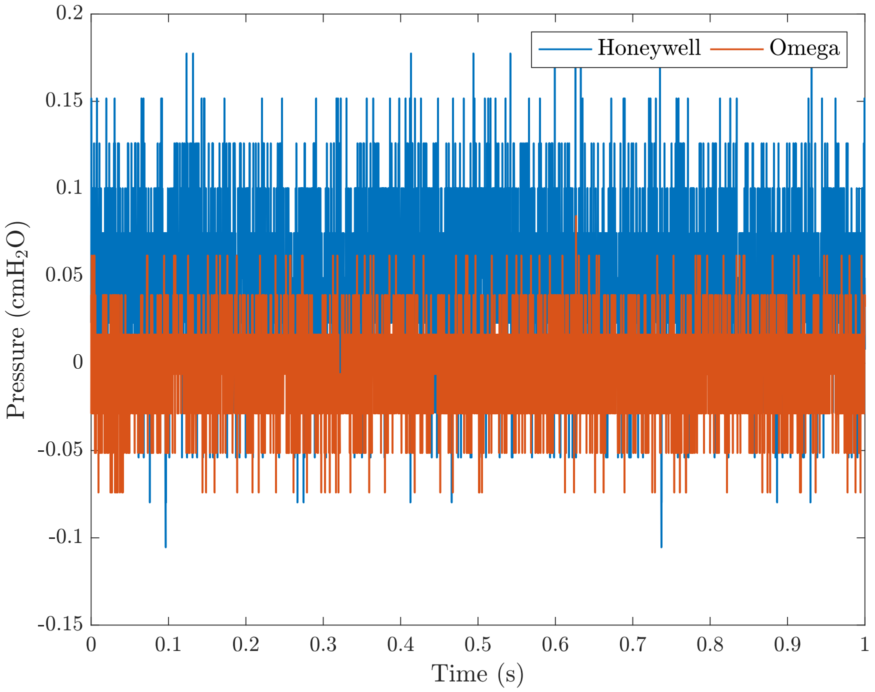

(a) Measurement noise in ambient pressure conditions.

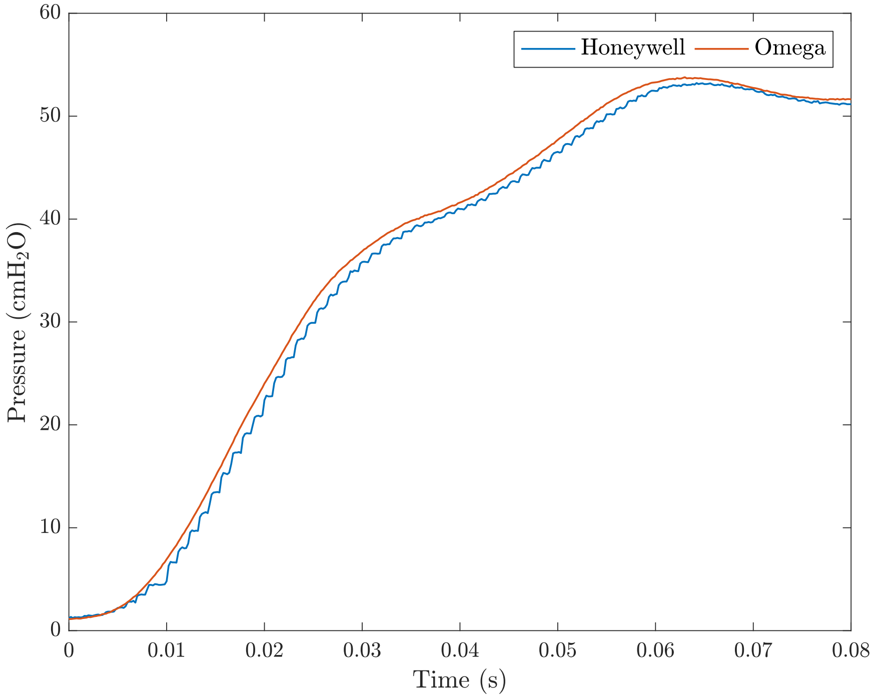

(b) Response to a step change in pressure.

Fig. 3.7. Comparison of Honeywell TruStability® and Omega PX140 pressure transducers.

3.3.2 Graphical user interface

Interaction with the CP Model engine inside the dedicated computer is accomplished by means of a custom-made graphical user interface (GUI) that runs on a host computer (e.g., the laptop in Fig. 3.4). Via the GUI, a user, like a testing engineer or a physician, can easily change parameters of the CP Model as to introduce pathological conditions, and display and log model-simulated waveform data.

Fig. 3.8 shows sample screenshots of our custom-made GUI that was developed in C# .Net programming language. It comprises six physiological system tabs corresponding to the following organ/systems: heart (Fig. 3.8a), lungs (Fig. 3.8b), circulation (Fig. 3.8c), neural feedback (Fig. 3.8d), metabolism (Fig. 3.8e), and gas exchange (Fig. 3.8f). Each physiological system tab offers a set of numeric up/down controls[8] (see the right-most two-thirds of each screenshot in Fig. 3.8) for changing parameter values, i.e., for modifying the physiology of the virtual patient or instilling specific pathologies/diseases. As explained in Chapter 2, the CP Model is a lumped-parameter model, where parameters (e.g., compliances, resistances, etc.) represent the material properties and geometries of different physiological organs/systems. While the structure of the ordinary differential equations is the same for all humans, it is the parameter values that make people differ from one another and that distinguish a healthy person from a sick one. Hence, by changing the parameters of the model, one can control its behavior without changing the model's structure. Notice some of the model parameters are constants, i.e., their values are determined as part of the model design process and cannot be changed at run-time. Others can be changed via the GUI at run-time to facilitate changes in the virtual patient's behavior, e.g., instilling a pathological condition. For example, an ARDS disease can simulated (like in the simulation studies in Section 2.5) by selecting the lungs tab (Fig. 3.8b) and accordingly modifying the compliance and unstressed volume values of lungs and chest wall.

---

[8] Here, "control" is a software design term that refers to a graphical user interface element.

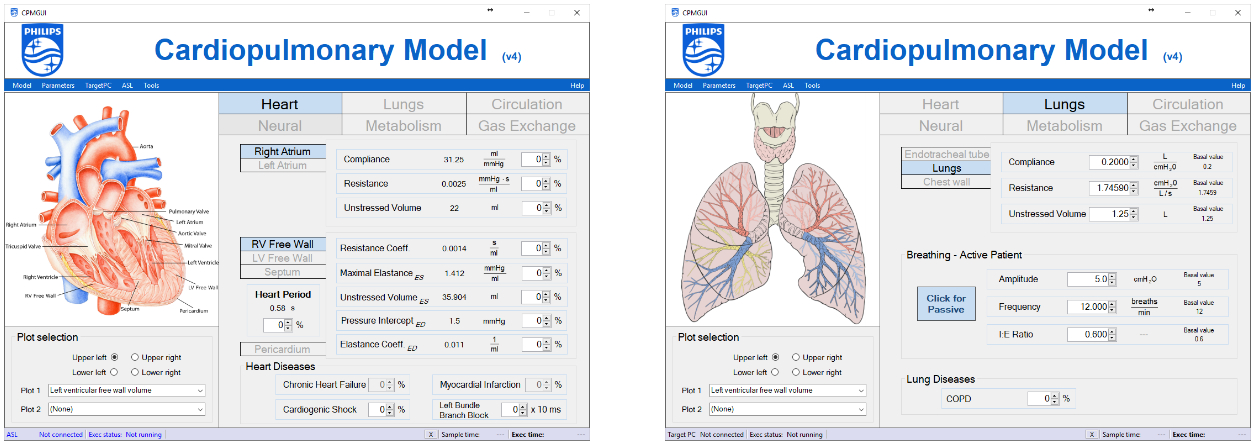
CPMGUI
PHILIPS
Cardiopulmonary Model (v4)
Model Parameters TargetPC ASL Tools Help
Heart Lungs Circulation
Neural Metabolism Gas Exchange
Plot selection
Upper left ● Upper right ○
Lower left ○ Lower right ○
Sample time: --- Exec time: ---

Right Atrium / Left Atrium
Compliance 31.25 ml/mmHg 0 %
Resistance 0.0025 mmHg · s/ml 0 %
Unstressed Volume 22 ml 0 %

RV Free Wall / LV Free Wall / Septum
Resistance Coeff. 0.0014 s/ml 0 %
Maximal Elastance $_{ES}$ 1.412 mmHg/ml 0 %
Unstressed Volume $_{ES}$ 35.904 ml 0 %
Pressure Intercept $_{ED}$ 1.5 mmHg 0 %
Elastance Coeff. $_{ED}$ 0.011 1/ml 0 %

Heart Period 0.58 s 0 %

Pericardium

Heart Diseases
Chronic Heart Failure 0 %
Myocardial Infarction 0 %
Cardiogenic Shock 0 %
Left Bundle Branch Block 0 x 10 ms

Plot 1 Left ventricular free wall volume
Plot 2 (None)

ASL Not connected Exec status: Not running

Endotracheal tube / Lungs / Chest wall
Compliance 0.2000 L/cmH$_2$0 Basal value 0.2
Resistance 1.74590 cmH$_2$0/(L/s) Basal value 1.7459
Unstressed Volume 1.25 L Basal value 1.25

Breathing - Active Patient
Click for Passive
Amplitude 5.0 cmH$_2$O Basal value 5
Frequency 12.000 breaths/min Basal value 12
I:E Ratio 0.600 --- Basal value 0.6

Lung Diseases
COPD 0 %

Plot 1 Left ventricular free wall volume
Plot 2 (None)

Target PC Not connected Exec status: Not running

(a) The heart tab.

(b) The lungs tab.

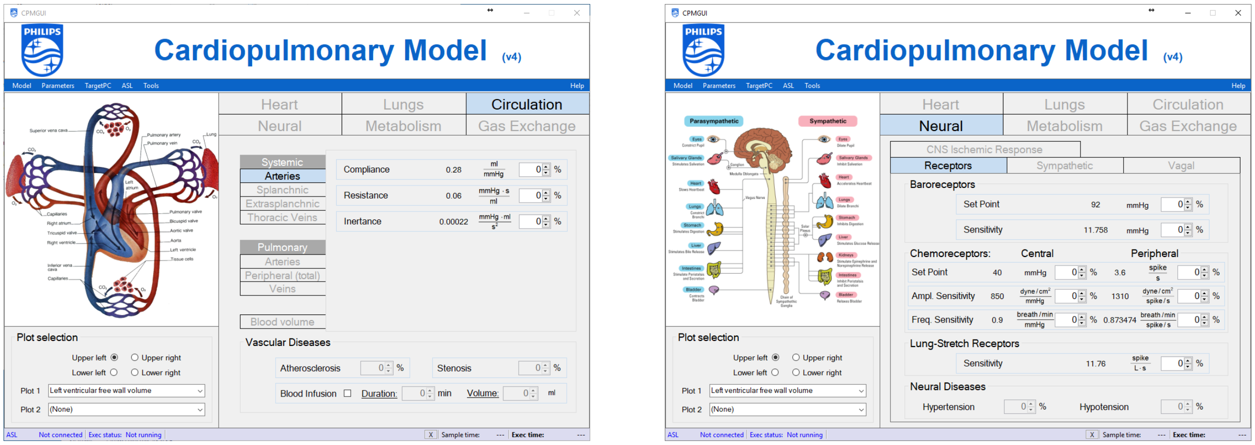
CPMGUI
PHILIPS
Cardiopulmonary Model (v4)
Model Parameters TargetPC ASL Tools Help
Heart Lungs Circulation
Neural Metabolism Gas Exchange
Parasympathetic
Sympathetic
Plot selection
Upper left ● Upper right ○
Lower left ○ Lower right ○
Sample time: --- Exec time: ---

Systemic: Arteries / Splanchnic / Extrasplanchnic / Thoracic Veins
Pulmonary: Arteries / Peripheral (total) / Veins
Blood volume

Compliance 0.28 ml/mmHg 0 %
Resistance 0.06 mmHg · s/ml 0 %
Inertance 0.00022 mmHg · ml/s^2 0 %

Vascular Diseases
Atherosclerosis 0 %
Stenosis 0 %
Blood Infusion ☐ Duration: 0 min Volume: 0 ml

Plot 1 Left ventricular free wall volume
Plot 2 (None)

ASL Not connected Exec status: Not running

CNS Ischemic Response
Receptors / Sympathetic / Vagal

Baroreceptors
Set Point 92 mmHg 0 %
Sensitivity 11.758 mmHg 0 %

Chemoreceptors:	Central				Peripheral			
Set Point	40	mmHg	0	%	3.6	spike/s	0	%
Ampl. Sensitivity	850	dyne/cm^2/mmHg	0	%	1310	dyne/cm^2/(spike/s)	0	%
Freq. Sensitivity	0.9	breath/min/mmHg	0	%	0.873474	breath/min/(spike/s)	0	%

Lung-Stretch Receptors
Sensitivity 11.76 spike/(L · s) 0 %

Neural Diseases
Hypertension 0 %
Hypotension 0 %

Plot 1 Left ventricular free wall volume
Plot 2 (None)

ASL Not connected Exec status: Not running

(c) The circulation tab.

(d) The neural tab.

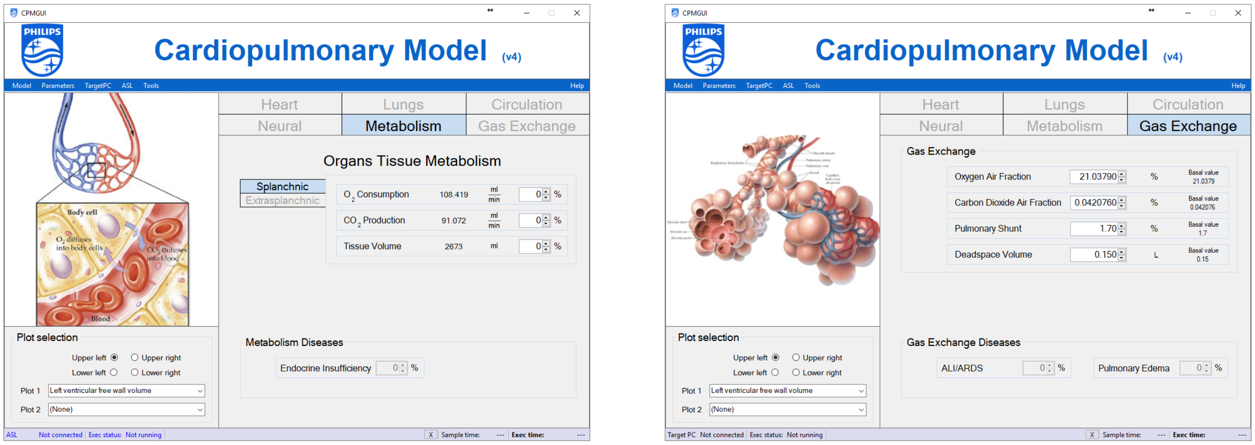
CPMGUI
PHILIPS
Cardiopulmonary Model (v4)
Model Parameters TargetPC ASL Tools Help
Heart Lungs Circulation
Neural Metabolism Gas Exchange
Body cell
O$_2$ diffuses into body cells
CO$_2$ diffuses into blood
Blood
Plot selection
Upper left ● Upper right ○
Lower left ○ Lower right ○
Sample time: --- Exec time: ---

Organs Tissue Metabolism
Splanchnic / Extrasplanchnic
O$_2$ Consumption 108.419 ml/min 0 %
CO$_2$ Production 91.072 ml/min 0 %
Tissue Volume 2673 ml 0 %

Metabolism Diseases
Endocrine Insufficiency 0 %

Plot 1 Left ventricular free wall volume
Plot 2 (None)

ASL Not connected Exec status: Not running

Gas Exchange
Oxygen Air Fraction 21.03790 % Basal value 21.0379
Carbon Dioxide Air Fraction 0.0420760 % Basal value 0.042076
Pulmonary Shunt 1.70 % Basal value 1.7
Deadspace Volume 0.150 L Basal value 0.15

Gas Exchange Diseases
ALI/ARDS 0 %
Pulmonary Edema 0 %

Plot 1 Left ventricular free wall volume
Plot 2 (None)

Target PC Not connected Exec status: Not running

(e) The metabolism tab.

(f) The gas exchange tab.

Fig. 3.8. Sample screenshots of the patient emulator's GUI depicting the different physiological system tabs.

Plotting of the model-simulated outputs can be easily performed via the GUI. The model plot window can host up to four plots, as shown in the sample screenshot of Fig. 3.9. Each plot can show one or two signals, selectable from the "Plot selection" section on the lower left of the main GUI window (see Fig. 3.8). Signals are shown in an oscilloscope-light manner, i.e., as a moving time window. The length of the displayed time window (horizontal time axis span) can be adjusted within a range of 10 to 600 seconds via the up/down control at the top of the plot window.

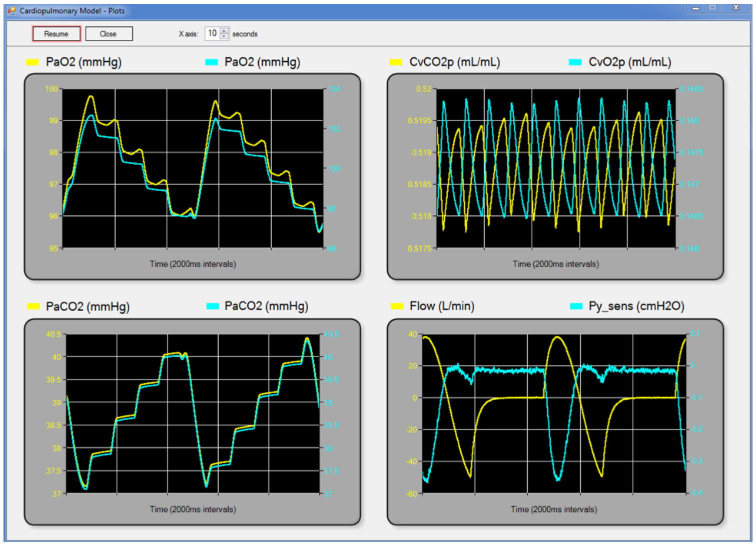
Cardiopulmonary Model - Plots
Resume
Close
PaO2 (mmHg)
PaO2 (mmHg)
100
99
98
97
96
95
104
102
100
98
96
Time (2000ms intervals)
CvCO2p (mL/mL)
CvO2p (mL/mL)
0.52
0.5195
0.519
0.5185
0.518
0.5175
0.1485
0.148
0.1475
0.147
0.1465
0.146
Time (2000ms intervals)
PaCO2 (mmHg)
PaCO2 (mmHg)
40.5
40
39.5
39
38.5
38
37.5
37
Time (2000ms intervals)
Flow (L/min)
Py_sens (cmH2O)
40
20
0
-20
-40
-60
0.1
0
-0.1
-0.2
-0.3
-0.4
Time (2000ms intervals)

X axis: 10 seconds

Fig. 3.9. Sample screenshot of the plot window of the patient emulator's GUI.

3.4 System validation

3.4.1 Standardized tests

The ISO standard 80601-2-12 [80] prescribes requirements for basic safety and essential performance of critical care ventilators. Even though such standardized tests are designed for testing critical care ventilators on isothermal test lungs[9], we decided to evaluate the behavior of the patient emulator for the settings prescribed in the ISO document for the pressure-

---

[9] Isothermal test lungs are chambers filled with copper to ensure constant temperature levels, thereby allowing a highly accurate volume measurement [81].

Table 3.1. ISO standardized tests for pressure-controlled breaths

Test #	IDV	DV	C_{rs}	R_{rs}	RR	I-time	PCV	PEEP
1	500	571	0.05	5	20	1	10	5
2	500	390	0.05	20	20	1	15	10
3	500	655	0.02	5	20	1	25	5
4	500	514	0.02	20	20	1	25	10
5	300	303	0.02	20	20	1	15	5
6	300	310	0.02	50	20	1	25	10
7	300	315	0.01	50	20	1	30	5
8	200	308	0.01	20	20	1	25	10
9	50	71	0.003	20	30	0.6	15	5
10	50	61	0.003	50	30	0.6	15	10
11	50	75	0.003	200	30	0.6	25	5
12	30	39	0.003	50	30	0.6	10	5
13	30	46	0.003	200	30	0.6	15	10
14	30	82	0.001	50	30	0.6	30	5
15	30	84	0.001	200	30	0.6	30	10
16	20	42	0.001	200	60	0.4	20	5
17	15	36	0.001	200	60	0.4	15	10
18	10	27	0.001	50	60	0.4	10	5
19	5	44	0.0005	50	60	0.4	15	10
20	5	27	0.0005	50	30	0.4	10	5
21	5	39	0.0005	200	60	0.4	15	10

IDV, intended delivered volume (ml); DV, actual delivered volume (DV); C_{rs}, respiratory system compliance (l/cmH_2O); R_{rs}, respiratory system resistance (cmH_2O·s/l); RR, respiratory rate ventilator setting (breaths/min); I-time, inspiratory time ventilator setting (s); PCV, pressure control ventilator setting (cmH_2O); PEEP, positive end-expiratory pressure (cmH_2O).

controlled breath type testing, as documented in Table 3.1. Accordingly, one should not interpret the results literally, but rather analyze the overall behavior of the patient emulator under such ventilator settings. For example, an increase in the model's respiratory system compliance is associated with a reduced delivered volume for the same level of supplied pressure (PCV level in Table 3.1). Notice also that because there was no oxygen supply to the ventilator, the tests were done with a fixed $F_{I_{O_2}}$ ventilator setting (i.e., at the normal room air level of 21%) instead of the values prescribed in the standard.

3.4.2 Comparison with experimental data

In this study, we have assessed the capability of the proposed patient emulator to simulate a typical physiological response that is observed in patients subjected to different levels of pressure support. Pressure support ventilation (PSV) is a ventilation mode that allows the patient to actively breathe and hence share the work performed on the respiratory system with the machine. Thus, appropriate selection of the PSV level can effectively load or offload the patient's respiratory muscles according to the physician's desired therapeutic path. For example, there are several clinical protocols that employ decreasing sequences of PSV levels in order to exercise the respiratory muscles and ultimately prepare the patient for liberation from the mechanical ventilator.

In the proposed experimental scenario, the patient emulator was connected to a Philips Respironics V200 ventilator (Koninklijke Philips N.V., Andover, MA), configured to provide pressure support with a triggering sensitivity of -2 cmH$_2$O and PEEP of 5 cmH$_2$O. According to the study by VandeGraaff et al. [5], we induced both positive and negative changes of the PSV level in steps of 10 cmH$_2$O, covering a range of [0–30] cmH$_2$O. In order to match the average population data from the human study in [5], a few key parameters of the CP Model were modified relative to the nominal values reported in [18]. In particular, the respiratory system resistance and compliance were set to 9 cmH$_2$O·s/l and 0.06 l/cmH$_2$O, respectively. The virtual patient's O_2 metabolic demand was reduced to about 130 ml/min in agreement with the low average consumption measured in the human study. Additionally, in order to set the $F_{I_{O_2}}$ to 35% as in [5], we assumed a higher than normal pulmonary shunt percentage and dead space volume. Finally, we adjusted the chemoreceptors' sensitivity and the basal breathing amplitude and frequency in order to achieve baseline values (at 0 $\mathrm{cmH_2O}$ PSV) of mean arterial oxygen and carbon dioxide partial pressures similar to those published in [5].

The patient emulator-predicted response to the PSV-step protocol described above is summarized in Fig. 3.10 for airway opening pressure (P_{ao}), respiratory muscle pressure (P_{mus}), and work of breathing (WOB). The results are in good agreement with several studies [5, 82, 83] that have investigated the effect of PSV on patient's effort and WOB. In short, increasing the PSV level decreases WOB and vice versa. Fig. 3.10 also reveals that the steady-state value of WOB after each PSV step is independent of whether or not we have previously applied a negative or positive change in the PSV level. A similar observation was also made by the investigators in [5] who concluded that the order of PSV change (increasing or decreasing) does not affect the patient's work.

Fig. 3.11 shows a zoomed-in view of the P_{mus} profile changes predicted by the virtual patient in response to a PSV increase from 10 to 20 $\mathrm{cmH_2O}$. It reveals two distinct rates of decrease in the amplitude: a sudden drop on the first breath right after the PSV was increased (around 19.15 min), followed by a further, but gradual, decrease throughout the subsequent breaths. The former effect is attributed to the Hering-Breuer (HB) reflex, which is an inhibitory reflex triggered to prevent overinflation of the lungs[10]. As illustrated in the left-hand side plot of Fig. 3.11, not only does the HB reflex reduce the maximal negative inspiratory pressure ($P_{mus,max}$) but it affects the duration of inspiration as well [84, 85]. For this particular case, the neural inspiratory time decreased from 1.38 s to 0.96 s. The secondary gradual decrease of the P_{mus} amplitude, on the other hand, can be ascribed to a reduced stimulation of the central and peripheral chemoreceptors. The increased ventilation, which is generated by the increased PSV level, leads to increased oxygen and reduced carbon dioxide tensions in blood. These changes in gas tensions are then sensed by the chemoreceptors that, in turn, cause the gradual reduction of $P_{mus,max}$ illustrated at the bottom right plot of Fig. 3.11 (after the 19 min mark).

---

[10] For more information about the Hering-Breuer (HB) reflex, see Section 2.2.

Table 3.2 and Fig. 3.12 show an extensive comparison between the results from the patient emulator and the human study in terms of WOB, tidal volume (V_T), respiratory rate (RR), minute ventilation (V_e), and arterial oxygen and carbon dioxide partial pressures ($P_{a_{O_2}}$ and $P_{a_{CO_2}}$ respectively). The mean and standard error of the mean values in both Table 3.2 and Fig. 3.12 are calculated across subjects (n in number) for the human study and across breaths (b in number) for the patient emulator. According to these, the emulator-predicted WOB values are within the range of the corresponding data from the human study for all four PSV levels. This indicates that the main physiological effects of PSV on patient's effort, as mediated by the HB reflex and the activation of the chemoreceptors, are well captured by the proposed patient emulator system. Furthermore, all the other physiologic variables exhibit similar trends as in [5]; as PSV increases from 0 to 30 cmH$_2$O, V_T and V_e increase, RR decreases, whereas $P_{a_{O_2}}$ and $P_{a_{CO_2}}$ remain relatively constant.

Finally, to verify the consistency of the patient emulator's response with respect to the simulation results from the software version of the CP Model in Chapter 2 (i.e., having the model run on a host computer where a simplified ventilator model is implemented), we replicated the experimental protocol reported by Dhainaut et al. [4] and presented in Section 2.5. According to that protocol, the PEEP level was first adjusted in increments of 5 cmH$_2$O, covering a range of [0–20] cmH$_2$O (PEEP$_0$, PEEP$_5$, PEEP$_{10}$, PEEP$_{15}$, and PEEP$_{20}$ respectively) and then volume expansion (VE) with plasma expanders (i.e., fluid resuscitation) was administered. Each ventilatory period lasted 20 minutes, and the hemodynamic study measurements collected within the last 10 minutes of each interval were presented in Table 2.8. Fig. 3.13 accordingly shows the predicted response of the patient emulator, in terms of cardiac index (CI), heart rate (HR), and stroke volume index (SVI), over the course of such an experimental protocol. Comparison of the emulator's steady-state response at the end of each ventilatory period with the data in Table 2.8 demonstrates the consistency between the software CP Model version and the one implemented in the emulator system.

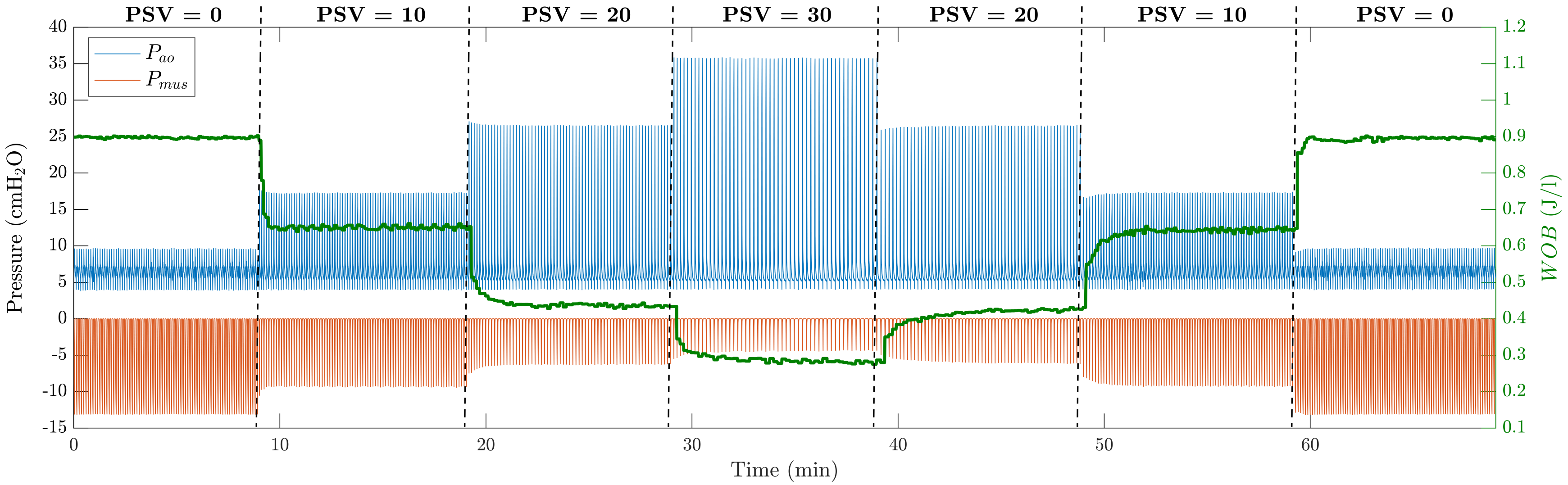

Fig. 3.10. Muscle pressure (P_{mus}, *left* axis) and work of breathing (WOB, *right* axis) of the virtual patient in response to step changes of the supplied PSV level (cmH$_2$O) as reflected in the measured airway opening pressure (P_{ao}, *left* axis).

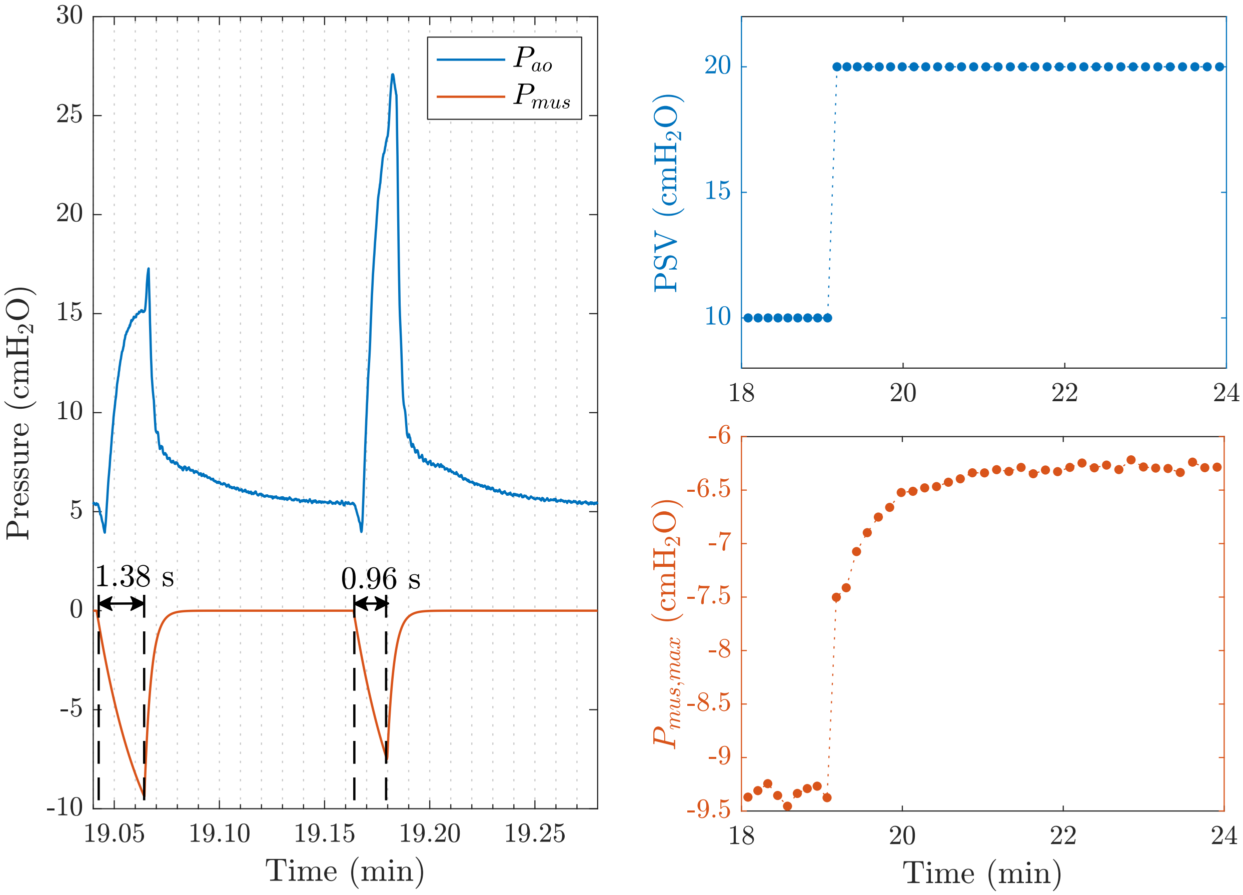

Fig. 3.11. Effect of a PSV step change (from 10 cmH$_2$O to 20 cmH$_2$O, *top right* plot) on the duration of inspiration (*left* plot) and on the amplitude of P_{mus} ($P_{mus,max}$, *bottom right* plot) as a result of the Hering-Breuer reflex and the chemoreceptors' feedback (slow decay of $P_{mus,max}$ in the *right* plot). Airway opening pressure P_{ao} is also included in the left plot for reference to the P_{mus} profile.

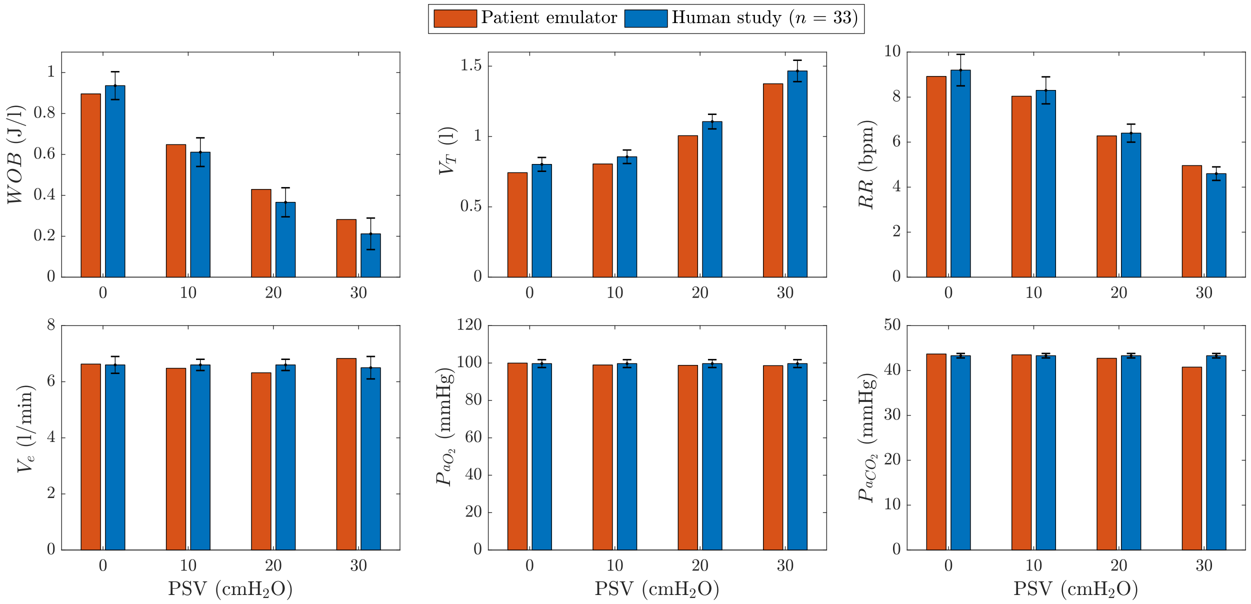

Fig. 3.12. Comparison between patient emulator (*red* bars, mean values) and experimental data from a human study involving 33 patients and reported by VandeGraaff et al. [5] (*blue* bars, mean±standard error of the mean values). WOB, work of breathing; V_T, tidal volume; RR, respiratory rate; V_e, minute ventilation; $P_{a_{O_2}}$ and $P_{a_{CO_2}}$, arterial oxygen and carbon dioxide partial pressures respectively.

Table 3.2. Comparison between patient emulator (PE) and literature data (Lit.) reported in [5]

	PSV = 0		PSV = 10		PSV = 20		PSV = 30	
Variable	PE ($b = 54$)	Lit. ($n = 33$)	PE ($b = 49$)	Lit. ($n = 33$)	PE ($b = 28$)	Lit. ($n = 33$)	PE ($b = 15$)	Lit. ($n = 23$)
WOB (J/l)	0.896 ± 0.002	0.936 ± 0.068	0.648 ± 0.006	0.611 ± 0.070	0.429 ± 0.006	0.366 ± 0.071	0.282 ± 0.004	0.212 ± 0.077
V_T (l)	0.743 ± 0.001	0.802 ± 0.049	0.805 ± 0.005	0.856 ± 0.048	1.006 ± 0.003	1.106 ± 0.052	1.375 ± 0.003	1.466 ± 0.076
RR (bpm)	8.92 ± 0.02	9.20 ± 0.70	8.04 ± 0.06	8.30 ± 0.60	6.28 ± 0.09	6.40 ± 0.40	4.96 ± 0.01	4.60 ± 0.30
V_e (l/min)	6.63 ± 0.02	6.60 ± 0.30	6.48 ± 0.07	6.60 ± 0.20	6.32 ± 0.09	6.60 ± 0.20	6.83 ± 0.02	6.50 ± 0.40
$P_{a_{O_2}}$ (mmHg)	99.97 ± 0.02	99.70 ± 2.10	98.97 ± 0.04	99.70 ± 2.10	98.77 ± 0.03	99.70 ± 2.10	98.61 ± 0.01	99.70 ± 2.10
$P_{a_{CO_2}}$ (mmHg)	43.68 ± 0.01	43.30 ± 0.50	43.50 ± 0.03	43.30 ± 0.50	42.73 ± 0.04	43.30 ± 0.50	40.76 ± 0.03	43.30 ± 0.50

Literature (Liter.) data (mean±standard error of the mean) are reported by VandeGraaff et al. [5] based on a human study involving $n = 33$ patients. Notice that not all patients were subjected to the highest level of PSV, i.e., 30 cmH_2O. Patient emulator statistical data (mean±standard deviation) are computed over segments with b number of breaths.

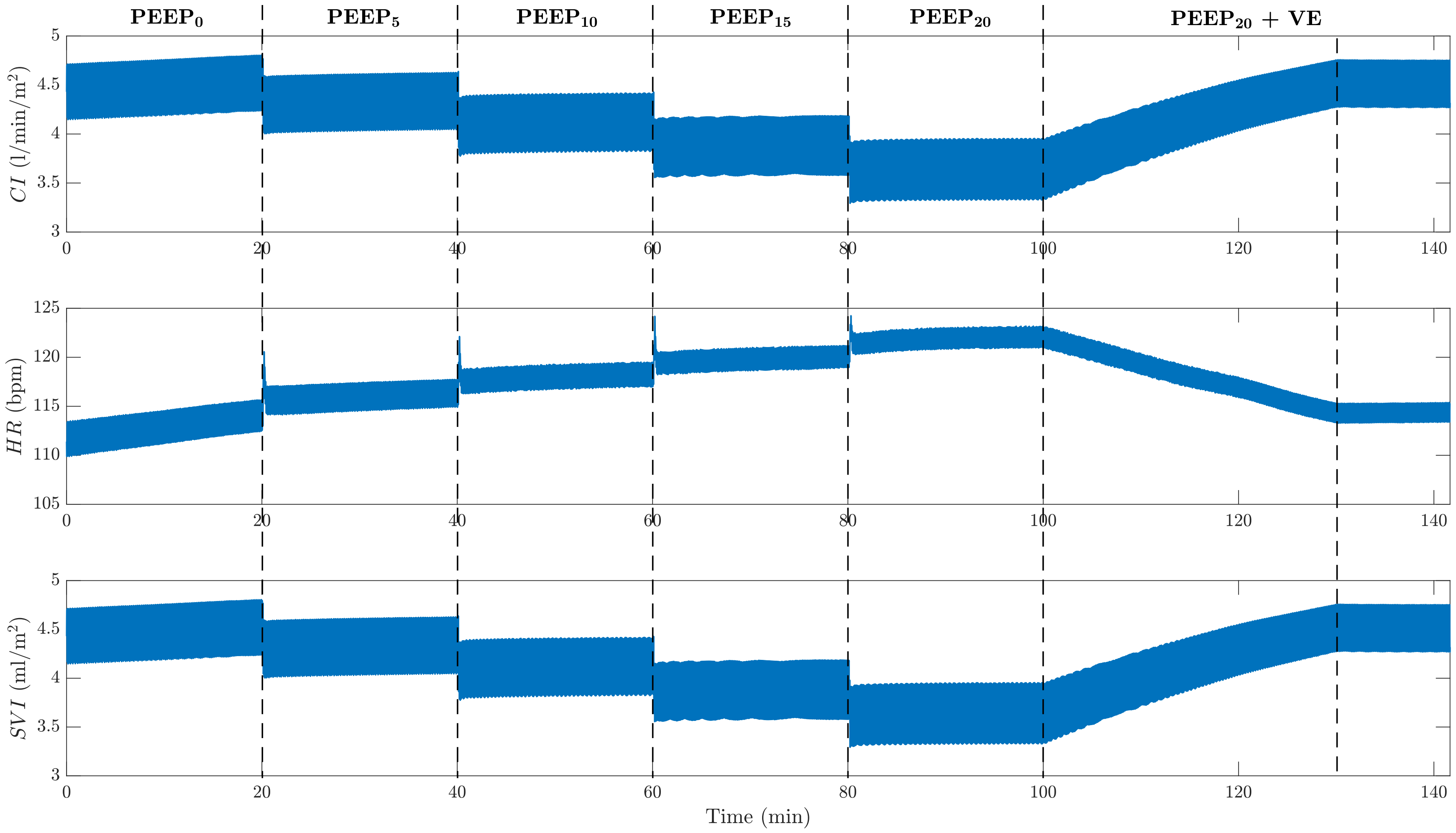

Fig. 3.13. Patient emulator-predicted data based on the human study protocol reported by Dhainaut et al. [4]. Each PEEP level is applied for a period of 20 minutes. PEEP$_x$, PEEP at x cmH_2O where x = {0, 5, 10, 15, 20}; PEEP$_{20}$ + VE, PEEP at 20 cmH_2O and blood volume expansion with 625±72 ml of plasma expanders; CI, cardiac index; HR, heart rate (bpm, beats per minute); SVI, stroke volume index. See Section 2.5 and Table 2.8 for more information.

3.5 Potential applications

The patient emulator system is a versatile device that leverages the computational power of a dedicated computer and the mathematical rigor of physiological models to emulate the behavior of a real mechanically ventilated patient. Its user friendly GUI allows for easy experimentation of different patient classes and a variety of pathological conditions. The patient emulator, hence, presents itself as a platform for research, educational, and clinical applications in addition to permitting a more efficacious testing of mechanical ventilators. First, it allows research investigators to understand physiological mechanisms, interpret experimental observations, and generate physiological hypotheses. It can also be used as a test bench for the development and validation of parameter estimation algorithms aiming to infer clinical variables and parameters noninvasively (as for example the one presented in Chapter 4). Second, its comprehensive mathematical model engine allows medical personnel to use the patient emulator system as an education tool to understand physiological cardiorespiratory interaction phenomena and as a clinical tool to formulate more personalized therapies. Lastly, such a system can potentially be suitable for testing different medical devices—besides mechanical ventilators—in-silico, before or in place of costly, time-consuming, and complicated human and animal trials.

3.6 Conclusion

In this chapter, we introduced the patient emulator system, a novel device that is based on the large-scale integrated mathematical model of the cardiopulmonary system presented in Chapter 2. Despite the system's plethora of potential applications, as summarized in the previous section, we focused on investigating its effectiveness for testing mechanical ventilation therapies as it represents a clear improvement as compared with the commercially available simple breathing simulators.

The proposed patient emulator was demonstrated under a realistic clinical scenario, where the level of PSV provided by the ventilator is changed in a step-wise fashion to induce variations in patient's respiratory effort. Such a physiologic response is driven by mechanisms that are primarily respiratory-related, like the HB reflex, and by mechanisms that depend on complex interactions between the cardiovascular and respiratory systems, like the chemoreflex. This clinical scenario, hence, clearly demonstrates the importance of using an integrated model of the cardiorespiratory system when one wants to simulate patients under mechanical ventilation. We also illustrated the consistency of the patient emulator system with respect to the software version of the CP Model as per Chapter 2. In particular, we replicated a "PEEP titration" procedure (i.e., gradually increasing the level of PEEP), typically used on ARDS subjects for determining the optimal level of PEEP that promotes lung recruitment and facilitates arterial blood oxygenation. The results of this study demonstrated the equivalence of the two model implementations. Last but not least, with the "PEEP titration" study, we evaluated another important mechanism of patient-ventilator interaction, i.e., the effect of PEEP on the cardiac function (e.g., cardiac index), which is of paramount importance in mechanically ventilated patients.

Despite these promising results, our validation presents some limitations. For instance, the comparison with human data was performed in terms of steady-state values only. Due to lack of available data in the literature, we did not carry out any validation on the transient dynamic response. Therefore, additional studies are envisioned to further extend the validation of the proposed patient emulator system and promote its use as a valid tool for testing mechanical ventilation therapies.

Chapter 4

Cardiovascular system identification

4.1 Introduction

System identification has recently drawn great attention, particularly in fields of engineering where mathematical models are employed to describe the dynamics of physical systems. It is considered the counterpart of modeling by first principles (or forward modeling [86]) that was used in Chapter 2 for the development of the cardiopulmonary model. Forward modeling determines, based on physical laws and the structure of the system under consideration, a set of mathematical equations that describe the system's dynamics. These dynamic equations essentially contain *variables*, which are physical quantities that vary with time and can potentially be measured, and *parameters*, which are elements that depend on the geometry and material properties of the physical system. Most of the times, though, the structure of the system of interest is not readily apparent to an external observer. Furthermore, practical difficulties in assessing the physical attributes (i.e., geometry and material property) of different parts of the system render the quantification of the system parameters virtually infeasible. System identification techniques lend themselves to addressing such issues. In fact, the primary objective of system identification is to obtain from experimental data a mathematical model that characterizes the dynamic response of the system under investigation. System identification techniques practically find the order of such a model and determine the corresponding model coefficients, which are respectively associated with the structure and the physical attributes of the real system.

Fig. 4.1 shows a schematic diagram of a dynamic system that is excited by an input signal $u(t)$ and, in turn, generates an output $y(t)$. Notice that although Fig. 4.1 schematically represents a single-input single-output (SISO) system, physical systems may have multiple excitation signals and more than one outputs—the number of system outputs is practically determined by the number of sensors installed on the real physical system.

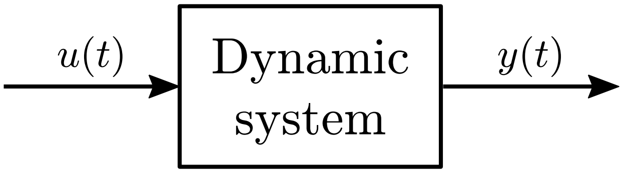

Fig. 4.1. A schematic block diagram of a dynamic system that is excited by input $u(t)$ and generates output $y(t)$.

A dynamic system of order n is commonly modeled via two mathematically equivalent representations: 1) a nth-order *differential equation* that maps the dynamics of the input signals to those of the outputs, or 2) a set of n coupled first-order differential equations that combines input, output, and state variables and is commonly referred to as the system's *state-space representation.* Assuming a multiple-input multiple-output linear time-invariant system of order n with m inputs and q outputs, the nth-order differential equation is defined as

$$\begin{aligned}\alpha_n \frac{d^n\mathbf{y}(t)}{dt^n} + \alpha_{n-1}\frac{d^{n-1}\mathbf{y}(t)}{dt^{n-1}} + \ldots + \alpha_2\frac{d^2\mathbf{y}(t)}{dt^2} + \alpha_1\frac{d\mathbf{y}(t)}{dt} + \alpha_0\mathbf{y}(t) = \\ \beta_n\frac{d^n\mathbf{u}(t)}{dt^n} + \beta_{n-1}\frac{d^{n-1}\mathbf{u}(t)}{dt^{n-1}} + \ldots + \beta_2\frac{d^2\mathbf{u}(t)}{dt^2} + \beta_1\frac{d\mathbf{u}(t)}{dt} + \beta_0\mathbf{u}(t),\end{aligned} \tag{4.1}$$

where $\mathbf{u} \in \mathbb{R}^{m\text{x}1}$ is the input vector, $\mathbf{y} \in \mathbb{R}^{q\text{x}1}$ is the output vector, and α_i and β_j are constant matrices. The equivalent continuous-time state-space representation is

$$\dot{\mathbf{x}}(t) = A\mathbf{x}(t) + B\mathbf{u}(t) \tag{4.2a}$$

$$\mathbf{y}(t) = C\mathbf{x}(t) + D\mathbf{u}(t), \tag{4.2b}$$

where $A \in \mathbb{R}^{nxn}$ is the system matrix, $B \in \mathbb{R}^{nxm}$ is the input matrix, $C \in \mathbb{R}^{qxn}$ is the output matrix, and $D \in \mathbb{R}^{qxm}$ is the direct influence matrix (all matrices are constant with time since the system is assumed to be time-invariant). (4.2a) is the *state equation*, while (4.2b) is called the *output (or observation) equation.* Even though (4.2), and correspondingly (4.1), refer to the deterministic case of a system's representation as it is derived, for instance, by modeling by first principles, in practical scenarios process and measurement noises corrupt (4.2a) and (4.2b) respectively, owing to the presence of unmodeled phenomena, disturbances, and noise in the sensors.

Physical systems are typically associated with their continuous-time dynamic responses represented by either (4.1) or (4.2). However, most contemporary data processing algorithms, such as system identification techniques, operate in digital platforms, where physical signals are recorded via data acquisition devices, i.e., analog-to-digital converters. As a result, most of the work presented in this chapter is focused on discrete-time models which are suitable for digital implementation. In that regard, the discrete-time counterpart of (4.1) is a nth-order difference equation defined as

$$\begin{aligned}\bar{a}_n\mathbf{y}[k-n] + \bar{a}_{n-1}\mathbf{y}[k-n-1] + \ldots + \bar{a}_2\mathbf{y}[k-2] + \bar{a}_1\mathbf{y}[k-1] + \bar{a}_0\mathbf{y}[k] = \\ \bar{b}_n\mathbf{u}[k-n] + \bar{b}_{n-1}\mathbf{u}[k-n-1] + \ldots + \bar{b}_2\mathbf{u}[k-2] + \bar{b}_1\mathbf{u}[k-1] + \bar{b}_0\mathbf{u}[k],\end{aligned} \tag{4.3}$$

where $\bar{a}_i$ and $\bar{b}_j$ are constant matrices as well. Such a discrete-time input-output mapping—that is, the output at every time step k is a linear combination of past input and output values—is known in the literature as an autoregressive model with exogenous input (ARX model). It is typically introduced as:

$$\begin{aligned}\mathbf{y}[k] &= a_1\mathbf{y}[k-1] + a_2\mathbf{y}[k-2] + \ldots + a_n\mathbf{y}[k-n] + \\ &\qquad b_0\mathbf{u}[k] + b_1\mathbf{u}[k-1] + b_2\mathbf{u}[k-2] + \ldots + b_n\mathbf{u}[k-n] + w[k] \\ &= \sum_{i=1}^{n} a_i\mathbf{y}[k-i] + \sum_{j=0}^{n} b_j\mathbf{u}[k-j] + w[k]. \end{aligned} \tag{4.4}$$

The matrix coefficients in the ARX model of (4.4) can be readily derived from those in (4.3) according to the following equations: $a_i = -(\bar{a}_0)^{-1}\bar{a}_i$ and $b_j = (\bar{a}_0)^{-1}\bar{b}_j$ for $i = 1, \ldots, n$ and $j = 0, \ldots, n$. Notice also that (4.4) now includes a noise term $w[k]$, thereby representing the stochastic form of an ARX model.

The discrete-time linear time-invariant state-space model is accordingly defined as:

$$\mathbf{x}[k+1] = A_d\mathbf{x}[k] + B_d\mathbf{u}[k] + \mathbf{w}_p[k] \tag{4.5a}$$

$$\mathbf{y}[k] = C_d\mathbf{x}[k] + D_d\mathbf{u}[k] + \mathbf{w}_m[k], \tag{4.5b}$$

where $A_d \in \mathbb{R}^{n\text{x}n}$, $B_d \in \mathbb{R}^{n\text{x}m}$, $C_d \in \mathbb{R}^{q\text{x}n}$, and $D_d \in \mathbb{R}^{q\text{x}m}$ are the discrete-time system, input, output, and direct influence matrices, respectively. $\mathbf{w}_p \in \mathbb{R}^{n\text{x}1}$ and $\mathbf{w}_m \in \mathbb{R}^{q\text{x}1}$ represent the process (or state) and output noises, respectively. Process noise typically indicates the presence of system dynamics that have not been included in the model. Despite the best of our efforts to accurately model the most prevalent dynamic characteristics of the real physical system, simplifications made either consciously or due to insufficient knowledge of the system will eventually lead to the existence of unmodeled phenomena. On the other hand, the output noise term includes any measurement noise in the sensors along with any potential environmental disturbance affecting the system (e.g., electrical interference). Finally, it is worth pointing that under the zero-order hold assumption for the analog-to-digital conversion (assuming T_s is the sampling period), the relationship between discrete- (4.5) and continuous-time (4.2) state-space matrices is described by the following equations:

$A_d = e^{A T_s}$, $B_d = B \int_0^{T_s} e^{A\xi} d\xi$, $C_d = C$, and $D_d = D$.

4.1.1 System identification and parameter estimation

As mentioned earlier, system identification algorithms aim to find from experimental data a mathematical model that describes the dynamics of the system of interest. For example, Fig. 4.2 schematically shows the identification process for a state-space identification technique; it accepts discrete-time input and output sequences ($\{u[k]\}$ and $\{y[k]\}$ respectively), which are measured and collected from the system under investigation (see Fig. 4.1), and then determines a state-space representation of the physical system, in terms of a set of A_d, B_d, C_d, and D_d matrices. The main advantage of system identification lies in the fact that the order of the system is not necessary to be known a priori. Identification methods determine the dimensions of the system matrix A_d which are, in turn, indicative of the system's order. This feature is also the primary difference with the field of parameter estimation, which shares the same objective as system identification. In particular, parameter estimation techniques operate with the underlying assumption that the order of the system is known prior to the algorithmic execution. Determining the system's order requires the knowledge of the system's structure along with the physical phenomena that dictate its dynamic response. With such an understanding, the system's differential (4.1) or difference (4.3) form can then be cast, allowing for parameter estimation algorithms to estimate, as the name suggests, the coefficients (parameters[1]) of these dynamic equations.

Nevertheless, the primary advantage of parameter estimation techniques—provided that the system's dynamic model can be determined a priori—pertains to their capability in estimating the coefficients of nonlinear models. In such a case, one can represent the model's dynamics in a differential (4.1), or difference (4.3), form with nonlinear-in-variables terms,

---

[1] Note that the coefficients of the differential and difference forms are not necessarily directly associated with the system's parameters, i.e., elements that depend on system's geometry and material properties. Such coefficients could be a nonlinear combination of different parameters, as well as of the sampling time in the case of the discrete-time difference equations.

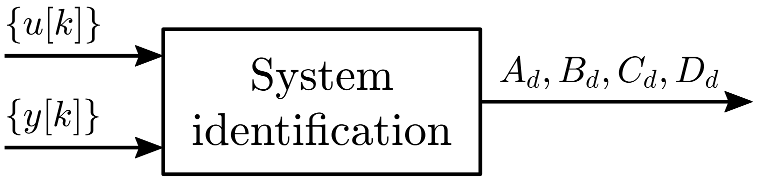

Fig. 4.2. A schematic diagram of a state-space identification technique. $u[k]$, input sequence; $y[k]$, output sequence; A_d, B_d, C_d, and D_d, matrices of discrete-time state-space model.

such as, for example, a flow-squared term if we were to model a flow-dependent resistance[2]. Estimation of the coefficients of such nonlinear terms does not bear any difference as compared to their linear counterparts; that is, any estimation algorithm can be readily applied, with no additional modifications, on the model's nonlinear dynamic equation and hence estimate the coefficients of both linear and nonlinear terms.

In conclusion, state-space identification is typically preferred in cases where there is insufficient knowledge of the system's underlying dynamics[3]. In such cases, state-space identification techniques are employed to determine the system's order, and hence structure, via the information embedded in the measured input and output experimental data. As mentioned above, state-space techniques have been developed with the inherent assumption of a linear system model. It is, nevertheless, worth pointing out that most systems tend to behave linearly in a limited range operation. As such, state-space identification schemes become a powerful tool in finding the best linear approximation of a model that optimally describes the system's dynamic response. On the other hand, parameter estimation techniques are utilized when the model's dynamic equations can be specified a priori, whether such equations contain linear- or nonlinear-in-variables terms. Estimation algorithms are then capable of finding the model's coefficients, which are, in turn, related to the system's physical attributes.

---

[2] The constitutive equation of a linear resistance is: $P_1(t) - P_2(t) = R \cdot \dot{V}(t)$, where P_1 and P_2 are the upstream and downstream pressures respectively and $\dot{V}$ is the flow over the constant-valued resistance R. If we were to model a flow-dependent resistance value, i.e., $R(\dot{V}) = k_1 \cdot \dot{V} + k_2$, the constitutive equation is then formulated as: $P_1(t) - P_2(t) = k_1 \cdot \dot{V}^2(t) + k_2 \cdot \dot{V}(t)$, where $k_1 \cdot \dot{V}^2(t)$ is the nonlinear-in-variable term.

[3] Note that state-space identification, via estimation of the system's state vector, is also a critical component in state-feedback controllers where the knowledge of the state is necessary in closing the loop.

4.2 The cardiovascular system

The human cardiovascular (CV) system is typically viewed as a transport system and is considered an indispensable element for the proper function of body organs. Its primary function is the delivery of nutrients, like oxygen (O_2), to the various body tissues, while guaranteeing the removal of waste products, such as carbon dioxide (CO_2), of the tissue metabolic activity. The cardiovascular system (Fig. 4.3) consists of three main components, which are connected in a series configuration: the heart and the systemic and pulmonary circulations. Each of the two circulatory subsystems comprises three distinct, in terms of material properties and structure, vascular elements; namely, the arteries, the peripheral circulation (including the capillaries), and the veins [87]. Systemic arteries carry the oxygen-rich blood to the capillary level of the various body organs, where tissue gas exchange takes place. That is, O_2 is absorbed by the tissues which, in turn, release CO_2 into the bloodstream of the systemic capillaries. The deoxygenated blood is then transported back to the heart via the venous circulation and subsequently propagated into the pulmonary circulation for the alveolar gas exchange. In particular, the capillaries of the pulmonary circulatory system are in direct contact with the lung alveoli so that O_2 and CO_2 can be exchanged between blood and air (i.e., the carbon dioxide in the deoxygenated blood of the pulmonary capillaries is exchanged for oxygen in the alveoli).

4.2.1 The heart as a source

Movement of blood through the entire vascular system cannot occur passively without any energy expenditure. The heart hence serves as the primary source of energy within the human cardiovascular system by propelling blood into both systemic and pulmonary circulations. As explained in Chapter 2, the heart pumps blood by means of the contractile activity of the two ventricles[4]. Practically, the cyclic electrical stimulation of the ventricular myocardium, which

---

[4] A schematic representation of the anatomy of the heart is shown in Fig. 2.2.

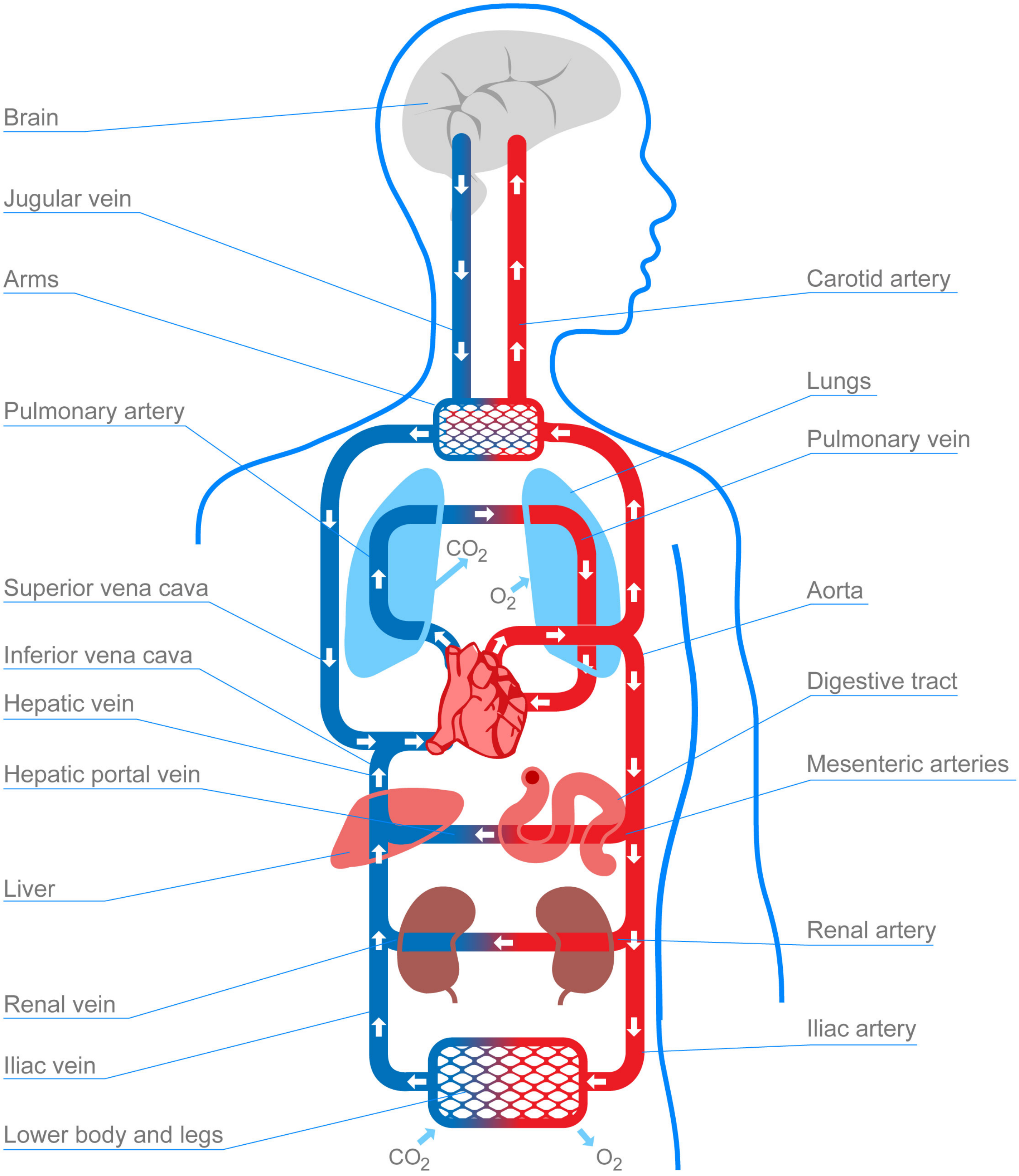
Brain
Jugular vein
Arms
Carotid artery
Lungs
Pulmonary artery
Pulmonary vein
CO_2
O_2
Superior vena cava
Aorta
Inferior vena cava
Digestive tract
Hepatic vein
Mesenteric arteries
Hepatic portal vein
Liver
Renal artery
Renal vein
Iliac artery
Iliac vein
Lower body and legs
CO_2
O_2

Fig. 4.3. A schematic representation of the human cardiovascular system. Red lines indicate vessels that transfer oxygenated blood (e.g., arteries and arterioles), whereas blue lines are vessels with deoxygenated blood (e.g., veins). Magenta areas represent the vascular beds involved in either alveolar or tissue gas exchange (capillaries). Image distributed under a CC BY-SA 3.0 license.

triggers the cardiac contraction, is responsible for generating adequate levels of pressure to drive the flow of blood through the circulatory system. Left ventricular activity determines systemic blood flow, whereas the right ventricle pumps blood into the pulmonary circulation. In that sense, the heart ought to be considered a *pressure source* which generates, via its periodic contraction, the pressures inside the two ventricles.

Despite such a physiologic understanding of the nature of cardiac function, an external observer, who views the heart from the aortic (or pulmonary) root, can indistinguishably assume that the output of the heart's pumping action could either be a pressure or a flow signal. For example, Fig. 4.4 shows pressure and blood flow waveforms at the aortic root level (P_{sa} and $Q_{lv,o}$, respectively) in addition to the ventricular pressure (P_{lv}) generated by ventricular contraction (all signals are simulated by the CP Model introduced in Chapter 2). Clearly, P_{lv} is the source that drives $Q_{lv,o}$ and hence induces changes in P_{sa}. However, one can realistically consider that the excitation, which propagates the blood and engenders the dynamics of the systemic circulation, can equally be produced by either P_{sa} or $Q_{lv,o}$ since both are defined at the beginning of the arterial vascular tree. Moreover, one can also argue that the closure of the aortic valve during diastole practically dissociates P_{lv} from the circulatory dynamics, thus making P_{lv} incompatible as the system's source during the diastolic phase[5]. It is hence reasonable to associate either P_{sa} or $Q_{lv,o}$ as the driving source of the systemic bloodstream. The choice between P_{sa} or $Q_{lv,o}$ is up to the investigator's discretion and the particular modeling assumptions, as we will explain in Section 4.3.

4.2.2 The systemic circulation as a dynamic system

The systemic circulation, as previously mentioned, comprises three major components: the arteries, the peripheral circulation (or microcirculation), and the veins. The division of vessels within the circulatory tree into these three categories is based on their distinct functional

---

[5] It is important to note that there exist significant difficulties—both practically and clinically—in getting access to the ventricular cavity without major complications on cardiac function. This, in fact, prohibits measurement of ventricular pressures in clinical practice.

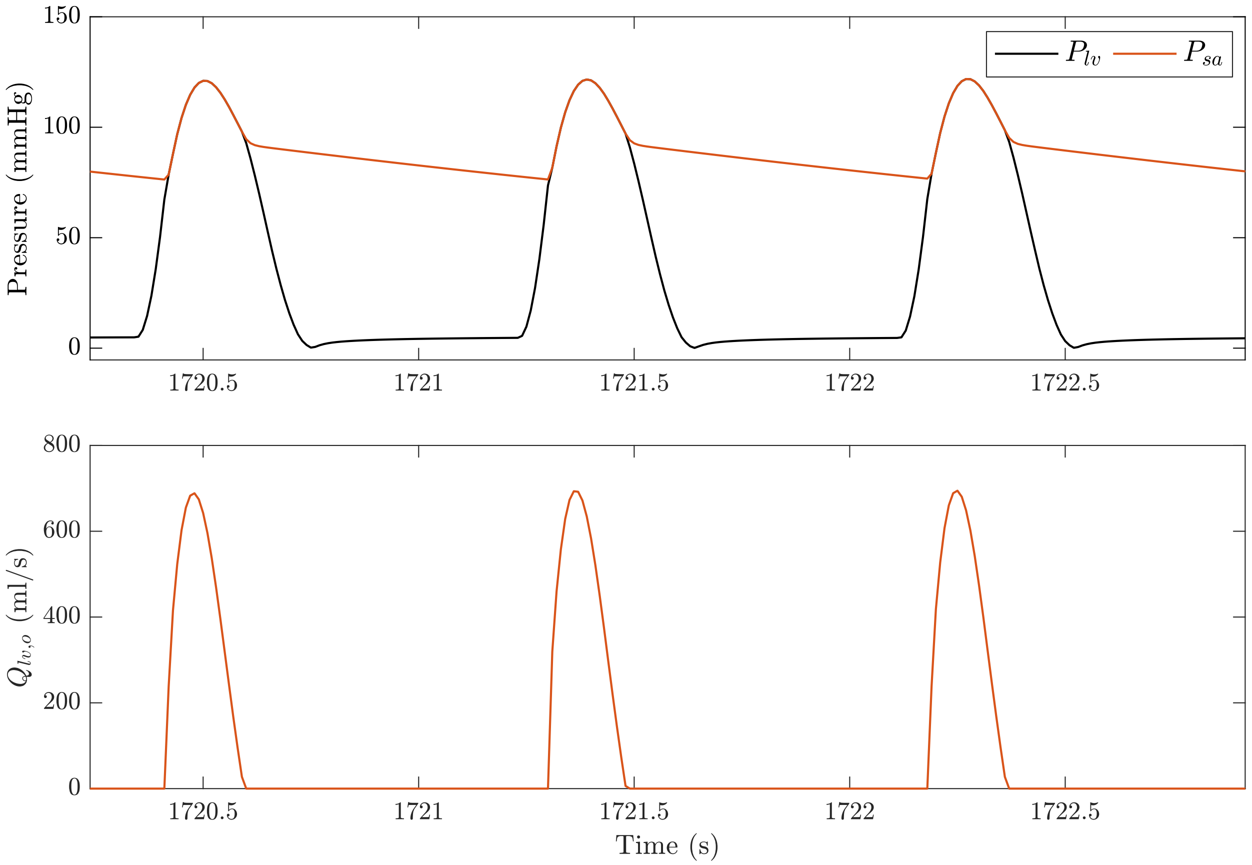

Fig. 4.4. Pressure and flow waveforms simulated by the CP Model over three cardiac cycles. P_{lv}, left ventricular pressure (*top* plot, *black* line); P_{sa}, systemic aortic pressure (*top* plot, *red* line); $Q_{lv,o}$, left ventricular output blood flow (*bottom* plot, *red* line).

role in blood transport and gas exchange. Such functional differences, in turn, determine the structure and mechanical properties of each vascular component [87]. For instance, arteries have a high composition of elastin fibers which are easily stretched. The high elasticity of the arterial vessels significantly contributes to the aortic pressure pulse dampening and subsequently to the distribution of blood to the various body organs[6]. On the other hand, veins are primarily composed of collagen fibers, which have high resistance to stretching. This particular composition allows the venous circulation to hold a large portion of the total blood volume—for this reason, veins are referred to as the capacitance vessels. Lastly, in the peripheral circulation, the pre-capillary arteriolar bed consists of a dense network of smooth muscle cells, whereas the capillaries include only a thin layer of endothelial cells that permits the exchange of gases with the surrounding tissues. The smooth muscle of the arteriolar compartment is highly innervated via the autonomic nervous system's sympathetic pathways. These efferent signals are responsible for constricting or dilating the arteriolar vessels, thereby regulating the level of arterial blood pressure and the amount of blood flow within the body organs.

---

[6] Note that arterial elasticity is a crucial element of cardiovascular function. Firstly, it dampens the pressure pulse during contraction and, secondly, it contributes to blood propagation in diastole when the aortic valve is closed. Practically, the arterial tree assures a continual flow of blood toward the peripheral circulation during the entire heart beat, whether heart is actually pumping (systole, open aortic valve) or not (diastole, closed aortic valve).

It is apparent that the systemic circulation is a complex system whose dynamic behavior does not depends only on the pumping action of the heart but also on changes in the mechanical properties of the vasculature. For example, aging leads to changes in the composition of arteries, thus resulting in arterial stiffening and increased blood pressure [88, 89]. On the contrary, infectious diseases, like sepsis, induce vascular inflammation, which results in peripheral vasodilation—particularly in the systemic arteriolar level—and hence in hypotension [90]. Accordingly, the systemic circulatory system, as any other dynamic system, can be defined mathematically via its input-output relationship; that is, the system's output is dependent upon the dynamics of the input signal as well as those of the system itself. A simplified version of the systemic circulation of Fig. 4.3 is depicted in Fig. 4.5a. The output of the heart, and hence the input (forcing function) to the circulatory system[7], is represented by either the aortic blood pressure (P_{sa} or ABP) or the ventricular output flow ($Q_{lv,o}$). Anatomically, the systemic circulation terminates at the right side of the heart, and in particular at the right atrium. Hence, one can reasonably assume that the output of the corresponding dynamic system is the right atrial pressure (P_{ra}), which is clinically approximated by the central venous pressure (CVP) waveform. Following the schematic representation of a dynamic system introduced in Section 4.1, Fig. 4.5b shows the input-output block diagram of the circulatory system.

---

[7] Although the term "circulatory system" physiologically refers to both pulmonary and systemic circulations, we will henceforth use it as a reference to the systemic circulation and thus the terms "circulatory system" and "systemic circulation" will be used interchangeably.

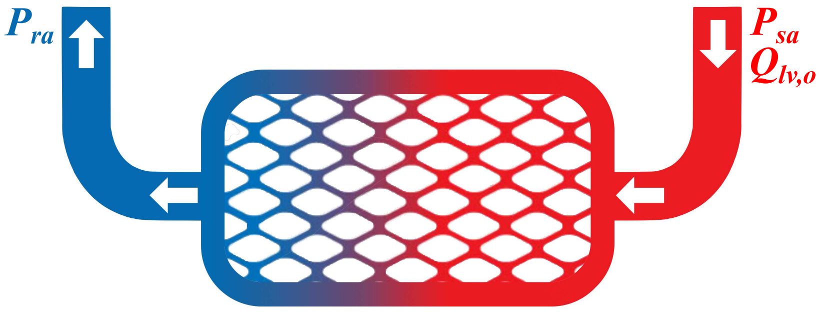

(a) A simplified representation.

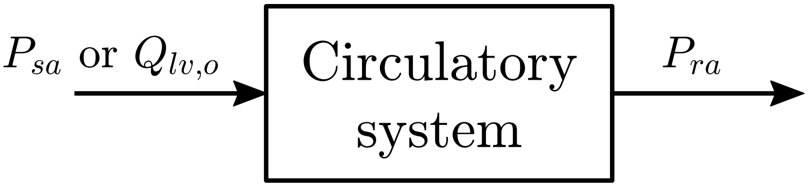

(b) A block-diagram representation.

Fig. 4.5. Representations of the systemic circulation. The coloring scheme in Fig. 4.5a follows that of Fig. 4.3. Note that Fig. 4.5a follows the clinically accepted convention for the arterial compartment (i.e., input) being on the right-hand side, whereas Fig. 4.5b adheres to the engineering community's approach where the input is placed on the left-hand side of the schematic. P_{sa}, systemic aortic pressure; $Q_{lv,o}$, left ventricular output blood flow; P_{ra}, right atrial pressure (or central venous pressure).

4.3 Mathematical models of systemic circulation

Mathematical models of the human physiology offer remarkable insights in describing and elucidating the dynamics of the cardiopulmonary system, as clearly demonstrated by our analysis in Chapter 2. Inevitably, the systemic circulation, as a major component of the cardiopulmonary system, has drawn special attention by the research community—particularly since its dynamics profoundly affect the circulation of blood between the heart and the various body organs. Translating such dynamics into mathematical equations dates back to 1878 and the work by Moens [91] and Korteweg [92] who studied and modeled the propagation of the pressure pulse inside the arterial tree; they formulated, for instance, the well-known Moens-Korteweg relationship between the wave propagation velocity within a vascular compartment and the elastic modulus of the vascular wall [93]. Thereafter, the research focus naturally broadened out to the development of physiological models that aim to describe the dynamic response of the entire circulatory system. Various mathematical models have since been proposed; from the work by Frank [94], who introduced the concept of "windkessel" (or elastic reservoir), to the analog electrical model of the systemic arterial tree from Westerhof et al. [95]. The pioneering work by these two investigators essentially established two distinct families of circulatory models; namely, the lumped- and the distributed-parameter models.

4.3.1 Lumped-parameter models

Lumped-parameter models are formally defined as systems with lumped-parameter elements. Under such a definition, one considers that the system of interest can be divided into regions whose geometry and material properties are assumed to be locally uniform. Hence, a lumped-parameter model consists of 1) parameters that are lumped in space and 2) variables which, at a given spatial point, represent the variables in the near vicinity of that point. Such variables are functions of time only and are thus described by ordinary differential equations with respect to time. It is also worth pointing out that lumped-parameter models are fundamental components of both parameter estimation and system identification algorithms. The equations introduced in Section 4.1 (see (4.1)–(4.5)) implicitly assumed a lumped-parameter system, whose parameters or structure are to be assessed by a parameter estimation or an identification method, respectively.

One of such lumped-parameter models is the Windkessel model. The Windkessel model, as first proposed by Frank [94], was the result of the effort to simplify the complex nature of the circulatory system in order to describe the load imposed by the latter on the heart. To this end, many assumptions had to be made; the most important of these was related to the fact that the concepts of wave reflection and pulse wave propagation were neglected. Implicitly, Frank [94] assumed that pulse wave velocity was infinite[8] and thus no wave reflections could occur. More specifically, he suggested that the elastic arteries behave like an elastic reservoir which, in turn, serves a resistive conduit representing the microcirculation (peripheral circulation). That is, a Windkessel model, as per Frank [94], is a combination of a compliance element followed by a hydraulic resistor, as depicted in the electrical analog of Fig. 4.6. The compliance C_t reflects the total compliance of all arteries[9], whereas R_t is the equivalent summed resistance of all peripheral vessels, such as arterioles and capillaries—accordingly, the original Windkessel model is typically referred to as a two-element Windkessel model. Despite the aforementioned simplifying modeling assumptions, the two-element Windkessel model was capable of reproducing the low-frequency dynamics of the arterial tree, including the mean and pulse[10] pressures [96]. These values were considered to be of great significance in assessing the clinical status of the cardiovascular system. As a result, the Windkessel model gained great traction by both research and clinical communities primarily due to its simple mathematical form and its direct clinical interpretability.

---

[8] The assumption of an infinite pulse wave velocity practically means that the pressure pulse is able to travel instantly through the entire systemic circulation. Consequently, the same pressure waveform is assumed to be observed at any point along the arterial tree.

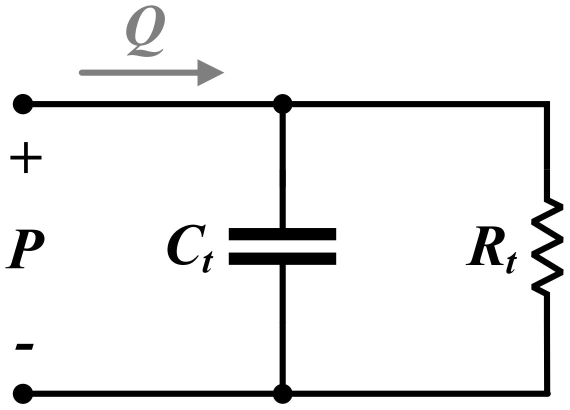

Fig. 4.6. Electrical analog of the two-element Windkessel model of the systemic circulation. P, arterial pressure; Q, arterial blood flow; C_t, total arterial compliance; R_t, peripheral (or terminal) resistance.

As mentioned above, the purpose for the development of the Windkessel model was to analyze the load imposed on the heart. For this reason, the pressure (P) and flow (Q) variables

---

[9] Note that due to the assumption of an infinite pulse wave velocity, all arteries are considered to attain the same pressure simultaneously. Hence, they can be thought as being in a parallel arrangement.

[10] Pulse pressure is defined as the difference between the maximum (systolic) and the minimum (diastolic) arterial pressure values within a heart beat. For example, the systolic P_{sa} value in Fig. 4.4 is about 121 mmHg, whereas the diastolic value is 76 mmHg. Hence, pulse pressure is equal to $121 - 76 = 45$ mmHg.

in Fig. 4.6 were initially considered to be the aortic pressure (P_{sa}) and the left ventricular output flow ($Q_{lv,o}$), respectively (as per Fig. 4.5). Nevertheless, in the electrical analog of Fig. 4.6, we used the generic P and Q variable labels because such a lumped-parameter model can be applied to explain the low-frequency dynamics of any arterial segment in addition to the aorta. Further, notice the absence of CVP (or P_{ra}) in Fig. 4.6. As explained earlier (see Fig. 4.5a), the veins are anatomically located after the peripheral circulation and thus CVP is expected to be the pressure downstream of R_t. However, a few reasons can justify the decision by Frank [94] to ignore the central venous pressure in the Windkessel model. First and foremost, CVP values are notably lower than the corresponding ABP signal. Hence, one can reasonably assume, without significant model prediction errors[11], that CVP is approximately zero with respect to the arterial pressure. Second, technical difficulties in venous-side catheterization along with high infection risks render the measurement of CVP not readily available in both clinical and experimental settings. Third, central venous pressure is a low-power signal and thus easily corrupted by additive measurement noise; that is, the CVP signal has a low signal-to-noise ratio. Finally, physiological phenomena, such as the contraction of skeletal muscles that propels venous blood toward the heart as well as the right atrial contractile activity, are associated with the presence of additional disturbances in the CVP waveform. Such disturbances complicate the dissociation of the actual circulatory system dynamics from the effects of these physiological reflex mechanisms. Consequently, based on these reasons, it is sensible for one to assume that the effect of CVP on circulatory dynamics is negligible, especially when analyzing the response of simple models, such as the Windkessel model. Additionally, in Section 4.5.1 we will demonstrate that, even from a system identification point of view, the use of CVP as a signal additional to regular ABP monitoring is not sufficient to provide a more accurate and detailed description of the systemic circulation dynamics.

Since the time of the work by Frank [94], the advancements in computing technologies have greatly facilitated the analysis of the circulatory system's frequency response (i.e., impedance) [97]. This, in turn, lead to the expansion of the original Windkessel model and to the development of derivative models, known as Windkessel-type models. In fact, such newly developed models were designed to provide a more accurate representation of the circulatory load on the heart by adding additional elements to the original two-element Windkessel model. For example, the three- and four-element Windkessel models are among the most popular ones and are depicted in Fig. 4.7; they were proposed by Westerhof et al. [98] and Stergiopulos et al. [96], respectively. R_t and C_t in Fig. 4.7 are defined as in the two-element model of Fig. 4.6. On the other hand, R_c and L_c represent the circulatory system's characteristic (or proximal) impedance which describes the system's frequency response at high frequencies. Despite the differences among these three Windkessel-type models, it is important to note that all of them exhibit a homogeneous response[12] which is characterized by an exponential decay with the same time constant τ, equal to $R_t\,C_t$. The time constant is practically the main determinant for the system's low-frequency dynamics that were well captured by the two-element Windkessel model [99, 100, 101, 102]. This is the reason why the development of the new models focused on better replicating the high-frequency components of the circulatory system's impedance (i.e., load on the heart) via the addition of R_c and L_c that were not part of the original model. Multiple studies [96, 97, 98] have since demonstrated that such three- and four-element Windkessel models can more accurately represent the dynamics of the systemic arterial tree.

---

[11] Recall that the goal of *forward modeling* is to replicate the dynamic response of the system under investigation.

Windkessel-type models also served as the basis for more elaborate circulatory models, like the one included in the CP Model of Chapter 2. Besides our group [18, 19], several other investigators [29, 30, 33, 37, 48, 103, 104] have developed mechanistic physiological models of the circulatory system. Even though their purpose was to understand and explain the complex dynamics and inter-connections of the entire human cardiopulmonary system, they further illustrate the remarkable importance of the seminal work by Frank [94] and his

---

[12] Homogeneous response is the system's response when input is zero.

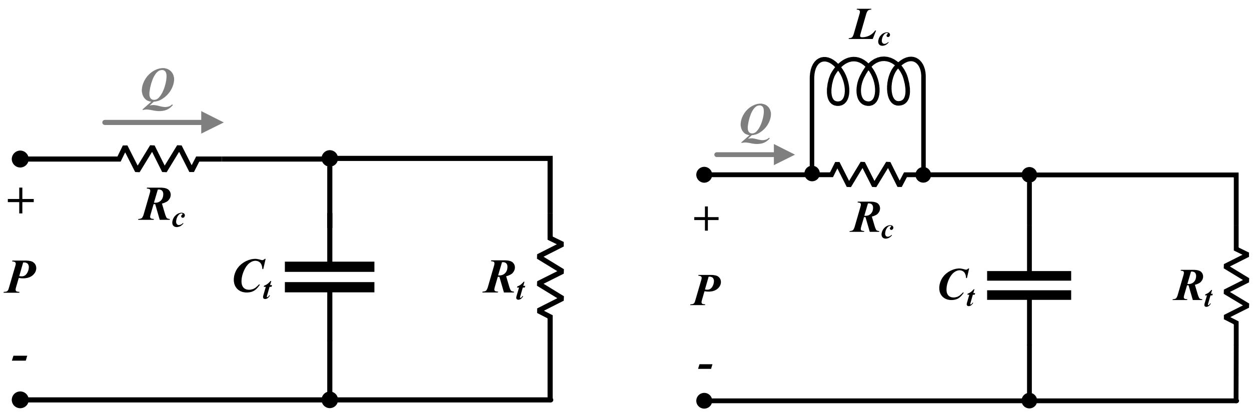

(a) Three-element model.

(b) Four-element model.

Fig. 4.7. Electrical analogs of Windkessel-type models. P, systemic arterial pressure; Q, blood flow; R_c, characteristic resistance; L_c, characteristic inertance; C_t, total arterial compliance; R_t, peripheral (or terminal) resistance.

original Windkessel model.

4.3.2 Distributed-parameter models

Distributed-parameter models, on the other hand, include variables that are continuous functions of not just time but also of space; that is, their dynamic responses change with respect to both temporal and spatial locations. Hence, distributed-parameter models are described by partial differential equations (PDEs). More specifically, such models comprise infinitesimally small—in space—elements which are necessary in order to replicate the distributed nature of the system's attributes (i.e., geometry and material properties) throughout the system's medium. The dynamic behavior of each infinitesimally small element is characterized by a set of PDEs that depend on the properties of the specific element as well as the dynamics of both preceding and succeeding elements. Inevitably, distributed-parameter models are more complicated than their lumped counterparts, although more accurate in their representation of the dynamics of the real physical system under investigation. Moreover, the complexity in their mathematical formulation via partial differential equations and the distributed parameter nature preclude the development of parameter estimation and system identification methods that would obtain from experimental data a distributed-parameter model. As a result, distributed models are primarily used for *forward modeling* schemes, where the objective is to generate synthetic (simulated) data that offer a better representation of the system's true dynamics and the underlying physical phenomena.

In fact, distributed-parameter models of the systemic arterial tree provide great insight into the circulatory system's dynamics. These models allow the study of pressure wave propagation[13] and the analysis of wave reflections along the arterial circulation. Such distributed models are also capable of simulating pressure and flow profiles at different locations of the arterial tree (e.g., at the aorta and the radial and femoral arteries). Multiple experimental studies [105, 106, 107, 108] have demonstrated that physiological phenomena, such as wave reflections and arterial viscoelasticity, induce profound variations in the pressure and flow waveforms at different points of the circulatory system. Therefore, it is of significant importance if we are able to replicate the physiological dynamics of the arterial system via the use of a distributed-parameter model.

Westerhof et al. [95] was the first to propose a distributed model of the systemic circulation. Due to the limited availability of digital computers at that time, the model by Westerhof et al. [95] (Fig. 4.8a) was comprised of analog circuit components, like resistors, capacitors, and inductors, arranged in such a way to mirror the structure of the systemic arterial tree. Subsequently, the advances in computing technologies allowed the research community to digitally program the PDEs of distributed-parameter models. For example, Avolio [109] proposed a model that was based on the transmission line theory, a well-known area in communications where distributed models are used for describing the transmission of digital information via alternating current. On the other hand, the distributed model by Stergiopulos et al. [6] was derived according to the one-dimensional blood flow equations, describing the conservation of mass (4.6) and momentum (4.7) for each of the 55 arterial

---

[13] Note that analysis of pressure wave propagation implicitly indicates that pulse wave velocity is finite, in contrast to Windkessel models that assume, as explained earlier, an infinite wave velocity.

segments shown scematically in Fig. 4.8b[14]:

$$\frac{\partial A}{\partial t} + \frac{\partial Q}{\partial x} = 0 \tag{4.6}$$

$$\frac{\partial Q}{\partial t} + \frac{\partial}{\partial x}\left(\frac{Q^2}{A}\right) = -\frac{A}{\rho}\frac{\partial P}{\partial x} + \frac{2\pi r \tau_w}{\rho}, \tag{4.7}$$

where Q is the blood flow through the vascular segment, P, A and r are the pressure, cross-sectional area and radius of the vascular segment respectively, ρ is the viscosity of blood, and τ_w is the shear stress of the vascular wall.

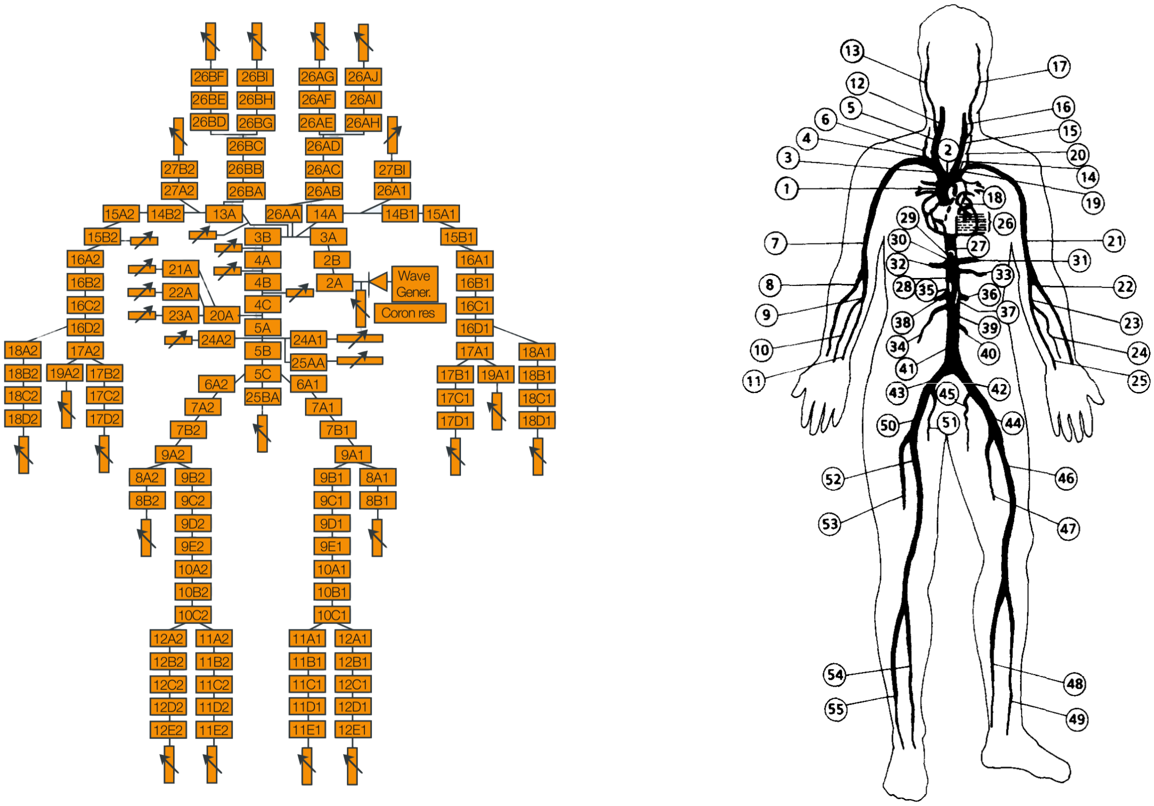
26BF
26BI
26AG
26AJ
26BE
26BH
26AF
26AI
26BD
26BG
26AE
26AH
26BC
26AD
27B2
26BB
26AC
27BI
27A2
26BA
26AB
26A1
15A2
14B2
13A
26AA
14A
14B1
15A1
15B2
3B
3A
15B1
16A2
21A
4A
2B
16A1
16B2
22A
4B
2A
Wave Gener.
16B1
16C2
23A
20A
4C
Coron res
16C1
16D2
5A
16D1
18A2
17A2
24A2
24A1
17A1
18A1
18B2
19A2
17B2
5B
25AA
17B1
19A1
18B1
18C2
17C2
5C
17C1
18C1
18D2
17D2
6A2
25BA
6A1
17D1
18D1
7A2
7A1
7B2
7B1
9A2
9A1
8A2
9B2
9B1
8A1
8B2
9C2
9C1
8B1
9D2
9D1
9E2
9E1
10A2
10A1
10B2
10B1
10C2
10C1
12A2
11A2
11A1
12A1
12B2
11B2
11B1
12B1
12C2
11C2
11C1
12C1
12D2
11D2
11D1
12D1
12E2
11E2
11E1
12E1
13
12
5
6
4
3
1
2
17
16
15
20
14
19
18
29
26
30
27
21
32
31
33
28
35
36
22
7
8
9
10
11
38
37
39
34
40
41
23
24
25
43
45
42
50
51
44
52
46
53
47
54
55
48
49

(a) The analog electrical model proposed by Westerhof et al. [95].

(b) The human arterial model proposed by Stergiopulos et al. [6].

Fig. 4.8. Schematic representations of two distributed-element models of the systemic arterial tree.

Fig. 4.9 shows blood flow and pressure waveforms at two different locations of the ar-

---

[14] The one-dimensional conservation of mass and momentum equations used by Stergiopulos et al. [6] are simplified forms of the general equations developed by Navier and Stokes that describe the motion of a viscous fluid—such equations are also known as Navier-Stokes equations.

terial tree: the ascending aorta[15] and the femoral artery. They are simulated from the distributed-parameter model by Stergiopulos et al. [6]. As anticipated, there are marked differences between the simulated waveforms from these two arterial segments due to the finite wave velocity and wave reflections along the arterial system model. Further, such model-predicted spatial differences in blood flows and pressures were shown to in good agreement with experimental data [6]. For these reasons, we deemed necessary to implement the distributed model[16] by Stergiopulos et al. [6] in order to generate high-fidelity simulated data for evaluating our proposed estimation technique (see Section 4.6.2).

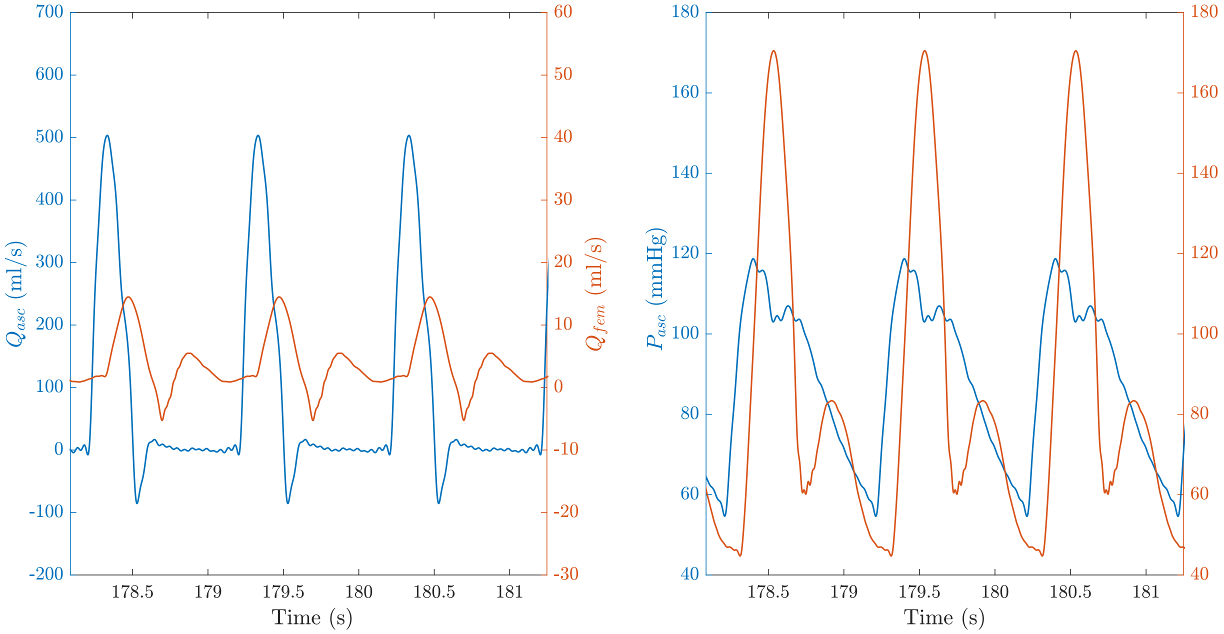

Fig. 4.9. Sample pressure and flow waveforms simulated from the distributed arterial model by Stergiopulos et al. [6] over three cardiac cycles. Q_{asc} (*left* plot, left vertical axis) and P_{asc} (*right* plot, left vertical axis) are the ascending aortic blood flow and pressure, respectively. Q_{fem} (*left* plot, right vertical axis) and P_{fem} (*right* plot, right vertical axis) are the femoral blood flow and pressure, respectively. Note that the two axes in the left plot are on different scales, whereas the ones in the right plot have the same limits.

---

[15] Note that the ascending aorta is the same anatomical location as the aortic root. Thus, the CP Model-predicted $Q_{lv,o}$ and P_{sa} of Fig. 4.4 are the lumped-parameter counterparts of the ascending aortic flow and pressure profiles in Fig. 4.9.

[16] The development of the distributed-parameter model of the arterial tree was done according to the work presented in [110].

4.4 Cardiac output assessment

Cardiac output (CO) describes the amount of blood pumped by the heart per minute of time and it is formally defined as the product between heart rate (HR) and stroke volume (SV), $CO = HR{\cdot}SV$[17]. In practical terms, CO depends on a combination of factors, affecting both cardiac and circulatory functions. For instance, autonomic innervation regulates the firing frequency of the sinoatrial node, thereby directly altering heart rate. Moreover, sympathetic efferent fibers affect myocardial contraction (inotropy), effectively influencing the pumping efficiency of the heart. Lastly, the autonomic nervous system modulates arterial vasodilation and vasoconstriction which, in turn, change the systemic arterial load on the heart (the higher the circulatory load, the lower the pumping efficiency of the heart). It is therefore reasonable that cardiac output is considered the most reliable clinical indicator of cardiac performance.

Beyond the aforementioned reasons, assessment of cardiac output is of paramount importance for hospitalized patients, whether mechanically ventilated or not. For example, an acute drop in arterial blood pressure (i.e., acute hypotension), referred to as shock, is a frequent clinical symptom in intensive care units. However, its underlying root cause is not readily apparent by solely relying on blood pressure monitoring. In particular, a circulatory shock can be categorized into the following four types, based on the underlying pathological condition [111]: 1) *distributive* shock, when blood distribution is impaired either due to an infectious disease (subcategorized as septic shock), like a virus, or due to noninfectious inflammatory conditions (subcategorized as non-septic shock), like burns, 2) *cardiogenic* shock, when the heart's pumping action is impaired, like in the case of myocardial infarction, 3) *hypovolemic* shock, when there is blood loss in the circulation and blood volume is reduced, like during bleeding conditions (subcategorized as hemorrhagic hypovolemic shock), and 4) *obstructive* shock, when the pulmonary circulation is obstructed, like in pulmonary embolism.

---

[17] In equation $CO = HR \cdot SV$, stroke volume typically refers to the volume of blood pumped into the systemic circulation by the *left ventricle*. Notice, however, that even though left and right ventricular stroke volumes may differ in transient conditions, like, for example, during a breathing cycle (see Fig. 2.9), mass balance dictates that in steady-state conditions the outputs of the two ventricles ought to be the same.

Even though the above pathological conditions are all manifested by hypotension, each one of them is related to different attributes in the function of the cardiovascular system. For instance, both hypovolemic and septic shocks are associated with low SV values (hence, low pressure) and a high HR. However, the reason for the reduced cardiac stroke volumes pertains to different factors. On one hand, blood loss during a hypovolemic shock leads to a reduction in cardiac preload and thus to reduced stroke volumes according to the Frank-Starling mechanism. Peripheral resistance, though, remains at nominal levels[18]. On the other hand, a septic shock, typically caused by an infectious disease, is linked to a reduction in peripheral resistance due to the disease-induced peripheral vasodilation. Blood distribution is thus impaired, leading to reduced venous return and hence stroke volume. Undoubtedly, distinguishing the underlying cause of a shock is critical to the patient's survival because different therapeutic interventions are required for each specific root cause. For example, as briefly explained in Chapter 2, fluid resuscitation is typically considered as a means to restore CO even though it may not always be the appropriate action. It is beneficial only to truly hypovolemic patients, but it can have adverse consequences in those who are not hypovolemic, potentially causing congestive heart failure.

To this end, knowledge of the direction of change (trend) in cardiac output, in addition to the routine blood pressure monitoring, would allow the evaluation of the patient's clinical condition (i.e., determining the type of shock) and the prediction of their response to potential interventions. In mechanically assisted patients, evaluation of cardiac output is equally important. As demonstrated by both experimental and simulation studies in Chapter 2, mechanical heart-lung interactions have a significant effect on cardiac function. Therefore, assessment of cardiac output prior to a ventilatory intervention can help determine any ensuing detrimental effects on cardiac function.

---

[18] Recall the meaning of peripheral resistance in the Windkessel model proposed by Frank [94] and shown in Fig. 4.6.

4.4.1 Current clinical methods

Invasive techniques

Until recently, measurement[19] of cardiac output in the clinical setting has mostly relied on invasive techniques. Two of the most commonly used invasive methods are 1) the direct Fick method and 2) the thermodilution method [112]. Their invasive nature pertains to the fact that both require pulmonary artery catheterization, which has been linked to major complications, such as pulmonary artery perforation, pulmonary infarction, and thromboembolism.

The Fick method[20], which is considered the "gold standard" approach to assess cardiac output [113], is based on the principle that each body organ consumes a certain amount of oxygen per unit of time. By substituting the notion of a single organ with the function of the entire human body, we can then evaluate the total oxygen consumption (VO_2). Specifically, conservation of mass dictates that, in steady-state conditions, the total oxygen consumption is equal to the product of cardiac output (i.e., the volume of blood per unit of time) and the O_2 concentration difference between arterial ($C_{a_{O_2}}$) and mixed venous ($C_{v_{O_2}}$) blood; namely, $VO_2 = CO \cdot (C_{a_{O_2}} - C_{v_{O_2}})$. $C_{a_{O_2}}$ and $C_{v_{O_2}}$ practically represent the amount of oxygen before and after its uptake by the body tissues (tissue gas exchange), respectively. That is, the arteriovenous oxygen difference ($C_{a_{O_2}} - C_{v_{O_2}}$) indicates the amount of oxygen consumed by the tissues of the entire human body. It is typically determined by gas analysis on blood samples from a systemic and a pulmonary arterial line catheter. Note that a pulmonary artery, rather than a venous, catheter is necessary to compute $C_{v_{O_2}}$. In such a way, we can evaluate the oxygen consumption from both upper and lower body parts, whose deoxygenated blood returns to the right atrium via the superior and inferior venae cavae, respectively[21]. Consequently, one can readily use the Fick equation and compute a cardiac output value [114], provided that, besides the arteriovenous oxygen difference, the total body O_2 consumption is also measured. However, VO_2 measurement is technically demanding, especially at the bedside. It requires spirometry, an elaborate measurement method, which limits the direct use of the Fick method for CO computation in clinical practice [115]. Nevertheless, if the direction of change in cardiac output is only of interest (rather than its actual value), the Fick equation can be used without requiring a VO_2 measurement. Under the assumption that VO_2 remains relatively constant[22], one can associate the arteriovenous oxygen difference, measured by gas analysis from arterial and mixed venous blood, with a relative cardiac output value that is able to track changes in the actual CO.

---

[19] Note that the word "measurement" is used loosely in this particular context. Most of the presented techniques do not measure cardiac output directly. Instead, they measure a quantity that is related to cardiac output and can then be used to provide a cardiac output value.

[20] The Fick method is named after Adolf Eugen Fick who conceptualized the technique in 1870.

[21] Despite potential errors in computing the arteriovenous oxygen difference, some investigators do use intravenous cannulation to assess $C_{v_{O_2}}$ due to its less invasive and potentially less harmful nature.

Thermodilution[23], on the other hand, uses a special triple-lumen pulmonary artery catheter, commonly referred to as Swan-Ganz catheter. Since the catheter's introduction in 1971 [117], the thermodilution method has been extensively used to measure cardiac output despite the skepticism about its accuracy, the ensuing cardiovascular complications, and the need of skilled personnel for inserting the catheter [118]. As its name conveys, the thermodilution method computes cardiac output by measuring change in temperature via a thermistor located at the distal tip of the catheter inside the pulmonary artery. In particular, the operator injects, through the catheter, a bolus of cold or warm indicator into the right ventricle. Mixing of the indicator with blood changes the temperature of the intraventricular blood, which is, in turn, pumped into the pulmonary artery. Temperature change is then recorded as the blood passes over the thermistor and the measured temperature time profile is used to determine a cardiac output value. Specifically, the area under the temperature-time curve is inversely proportional to the flow rate (i.e., cardiac output) in the pulmonary artery. The accuracy of the thermodilution method depends on multiple factors, such as the position of the catheter, the volume and temperature of the indicator, the patient's body position, as well as the phase in the respiratory cycle at which the injection is administered

---

[22] This assumption will be invalid if tissue metabolism, and hence oxygen consumption, is altered, like in cases of fever or excessive work of breathing.

[23] The thermodilution method was originally proposed by Fegler [116].

[119, 120]. Thus, in clinical practice, particular attention has to be paid on the reliability of thermodilution-based cardiac output measurements which, even under ideal circumstances, may have a 10% error [121]. To minimize potential measurement errors, it is advised to perform more than one injections—typically three—and then average their values, a process that complicates even further the overall method.

Lastly, it is worth mentioning the ultrasonic flowmeter, a highly invasive technique that is rarely used in clinical applications. Because the flowmeter is placed around the aorta, such a method requires an incision into the pleural space of the chest (thoracotomy) in order to gain access to the heart and the aorta. This surgical procedure is prone to major complications, thereby limiting the use of the ultrasonic flowmeter solely to experimental studies. Nevertheless, this method provides a real-time waveform of aortic volumetric blood flow, thus making it the most accurate way to assess cardiac output at every single heart beat[24].

Minimally invasive and noninvasive techniques

The adverse consequences associated with the invasive nature of pulmonary artery catheterization prompted the development of techniques that would assess cardiac output in a minimally invasive or even noninvasive way [122, 123]. For example, pulse contour and trans-esophageal Doppler devices are minimally invasive methods, whereas partial carbon dioxide rebreathing and transthoracic Doppler are completely noninvasive techniques.

Doppler-based methods, whether transesophageal or transthoracic, employ ultrasound imaging and the Doppler's principle to measure an instantaneous blood flow velocity ($v(t)$) on the descending aorta. Since Doppler ultrasound gives flow velocity, computation of volumetric flow, and therefore of stroke volume, requires the knowledge of the cross-sectional area (A) of the aorta. That is, $SV = A \int_{t_o}^{t_e} v(t)\,dt$, where t_o and t_e are the time instances of the onset and end of a heart beat, respectively. The aortic cross-section area is typically derived from published nomograms based on age, sex, weight, and height. It can be also directly measured via pulsed ultrasound, if such modality is available at the bedside [124]. Notice, however, that ultrasound methods assume a cylindrical aorta, an assumption that can potentially lead to errors in the computed stroke volume. Even though both methods are based on the same working principle, transesophageal and transthoracic Doppler devices differ on their respective implementation. On one hand, flow velocity from a transesophageal probe is measured via the catheter inserted into the patient's esophagus. This is a minimally invasive procedure which offers cardiac output monitoring as long as the catheter remains inside the esophagus. On the other hand, a transthoracic Doppler probe is placed externally on the thorax and hence is completely noninvasive. However, because placement of such a probe on the thorax requires a human operator, a transthoracic device provides intermittent cardiac output measurements. Nevertheless, both transesophageal or transthoracic techniques require an expensive external apparatus for the analysis of the ultrasound images and expert personnel for the accurate placement of the probe, whether inside the esophagus or on the patient's chest[25].

---

[24] Assuming, as previously mentioned, that $Q_{lv,o}$ is the aortic (or left ventricular) output flow, then a beat-by-beat stroke volume can be computed as: $SV = \int_{t_o}^{t_e} Q_{lv,o}(t)\,dt$, where t_o and t_e are the time instances of the onset and end of a heart beat, respectively. Then, the formula $CO = SV \cdot HR$ can be readily applied.

Partial carbon dioxide rebreathing is another noninvasive approach to assess cardiac output. It requires, however, an adjustable dead space[26] component that is attached to the patient's breathing circuit [126], thus making the technique applicable only to mechanically ventilated patients. Its operation is practically based on the Fick principle for the CO_2 mass balance. Similar to the invasive O_2 Fick method, cardiac output can also be computed using the total carbon dioxide production (VCO_2) and the corresponding arterial and mixed venous CO_2 concentrations, i.e., $CO = \dfrac{VCO_2}{Cv_{CO_2} - Ca_{CO_2}}$ (note that Cv_{CO_2} is greater than Ca_{CO_2}). VCO_2 is measured via volumetric capnography[27], Ca_{CO_2} is approximated by the

---

[25] Note that placement of the probe is typically considered the primary reason for the low accuracy of ultrasound methods, as reported by multiple clinical studies [125].

[26] Dead space is the volume of inhaled air that does not participate in gas exchange.

[27] Capnography is a technique for analyzing and monitoring the concentration of CO_2 in air during breathing.

CO_2 concentration in the exhaled air at the end of every breathing cycle (end-tidal CO_2), while the airway dead space component is employed for estimating the C_{vCO_2} through partial breathing of the exhaled air [127]. Hence, cardiac output can only be assessed intermittently, whenever partial rebreathing is performed. Despite the fact that the partial CO_2 rebreathing method has shown reasonable accuracy as compared to invasively measured cardiac output values acquired via thermodilution [118], the requirement of mechanical ventilation has limited its use in the clinic.

Finally, pulse contour methods provide cardiac output values by analyzing the time profile of arterial blood pressure measured via an arterial line catheter (typically placed in a femoral or radial artery). The reason why such methods are categorized as minimally invasive pertains to the fact that (systemic) arterial catheterization is routinely used for continuous hemodynamic monitoring in most intensive care units, especially in critically ill patients. In addition, it is important to note that, in contrast to pulmonary artery catheterization, arterial catheterization has not been associated with significant cardiovascular complications. Measurement of cardiac output based on a pulse contour method was first proposed by Warner et al. [128], but it was the work by Wesseling et al. [129] that described a clinically usable technique. In particular, Wesseling et al. [129] used the transmission line theory and suggested that stroke volume is proportional to the area under the systolic portion of the arterial pressure (P) curve and inversely proportional to the characteristic impedance (Z_c) of the arterial tree. Namely, $SV = \frac{1}{Z_c} \int_{t_{os}}^{t_{es}} P(t)\, dt$, where t_{os} and t_{es} are the time instances of the onset and end of systole, respectively. Based on transmission line theory, the characteristic impedance[28] is the impedance of an infinitely long transmission line that does not generate any reflected waves—this is equivalent to the assumption of an infinite pulse wave velocity used for the development of Windkessel-type models. To overcome the presence of wave reflections in practical applications, Wesseling et al. [129] suggested the use of correction factors, computed from pressure waveform analysis, to replace the unknown arterial characteristic impedance, thereby allowing beat-by-beat computation of stroke volume and hence cardiac output. The main advantage of pulse contour methods in providing continuous cardiac output measurements without additional instrumentation—besides the arterial line—sparked the interest of the clinical community. Nevertheless, it was later indicated that bedside calibration is indeed necessary for improved measurement accuracy, particularly if absolute, rather than relative, cardiac output readings are of interest.

---

[28] As introduced by the three- and four-element Windkessel models in Fig. 4.7, characteristic impedance is also associated with the system's impedance at high frequencies.

4.4.2 Model-based estimation methods

Another promising family of methods to assess cardiac output involves the use of parameter estimation, or system identification, algorithms. As explained in Section 4.1, these algorithms are developed based on lumped-parameter models of the system under investigation, cast either in an input-output (e.g., differential (4.1) or difference (4.4) forms) or in a state-space (4.5) representation. However, when applied to the systemic arterial system, most of such estimation techniques are based on the simplistic Windkessel-type models (see Figs. 4.6 and 4.7) due to the following reasons [130]: 1) the limited number of unknown parameters to be estimated, 2) the physiological and clinical interpretability with respect to the models' dynamic response and parameters, and 3) the models' widespread acceptance by the medical community.

Model-based estimation methods typically rely on the dynamics of arterial pressure (e.g., peak-to-peak amplitude and diastolic decay) and thus necessitate the use of a continuous pressure signal acquired via an arterial line catheter. As mentioned above, arterial catheterization is routinely used in intensive care units. As such, these estimation techniques are categorized as part of the minimally invasive approaches for cardiac output assessment. Despite, however, their direct clinical interpretability and applicability, estimation methods face a significant challenge; namely, cardiac output, the unknown quantity to be estimated, is directly related to the aortic blood flow $Q_{lv,o}$[24], the forcing function of the systemic circulation (recall the schematic representations of Fig. 4.5). If we represent, for instance, the systemic arterial tree as a two-element Windkessel model, as per Fig. 4.6, with $Q = Q_{lv,o}$ being the circulatory system's input, then the arterial pressure ($P = P_{sa}$) can be considered the system's response (output). Hence, the time profile of P is described by the following differential equation:

$$\frac{dP(t)}{dt} = \frac{Q(t)}{C_t} - \frac{P(t)}{R_t\,C_t}, \tag{4.8}$$

where R_t and C_t are the peripheral (or terminal) resistance and total arterial compliance, respectively. By examining (4.8), it becomes apparent that the P is the only measurable variable. The system's input, Q, along with the system's parameters, R_t and C_t, are unknown elements. Undoubtedly, the task of estimating any quantity, whether that being the cardiac output (i.e., blood flow, Q) or the system's mechanical properties (i.e., model parameters), constitutes an ill-posed problem due to the lack of adequate information, in terms of measurable elements.

To overcome such an underdetermined nature of the estimation problem at hand and make it somewhat feasible[29], past researchers [7, 131, 132, 133, 134, 135] have relied on two main assumptions on the aortic blood flow profile.

1. According to the first assumption, the heart's pumping action is a *periodic impulse flow generator* which, at the nth heart beat, ejects a total volume of blood equal to stroke volume, SV_n. Thus, $Q_{lv,o}$ can be depicted as an impulse train function with the amplitude of each Dirac delta function being equal to SV_n, i.e., $Q_{lv,o}(t) = \sum_n \mathrm{SV}_n \cdot \delta(t - t_n)$, where t_n is the time instance of the nth Dirac delta function. For example, the left-hand side plot of Fig. 4.10 shows such an impulse train $Q_{lv,o}$ function over three cardiac cycles (three Dirac delta functions). Note that each SV_n value is equal to about 79 ml—a value that is within the normal physiological range observed in healthy subjects. The right-hand side plot of Fig. 4.10 accordingly shows the pressure waveform simulated by a two-element Windkessel model, whose response is described

---

[29] As we will see later, the notion of "somewhat feasible" refers to the fact that even when the proposed assumptions are satisfied, only a relative cardiac output value can be derived.

by (4.8), for $R_t = 1.15$ mmHg·s/ml and $C_t = 1.50$ ml/mmHg[30].

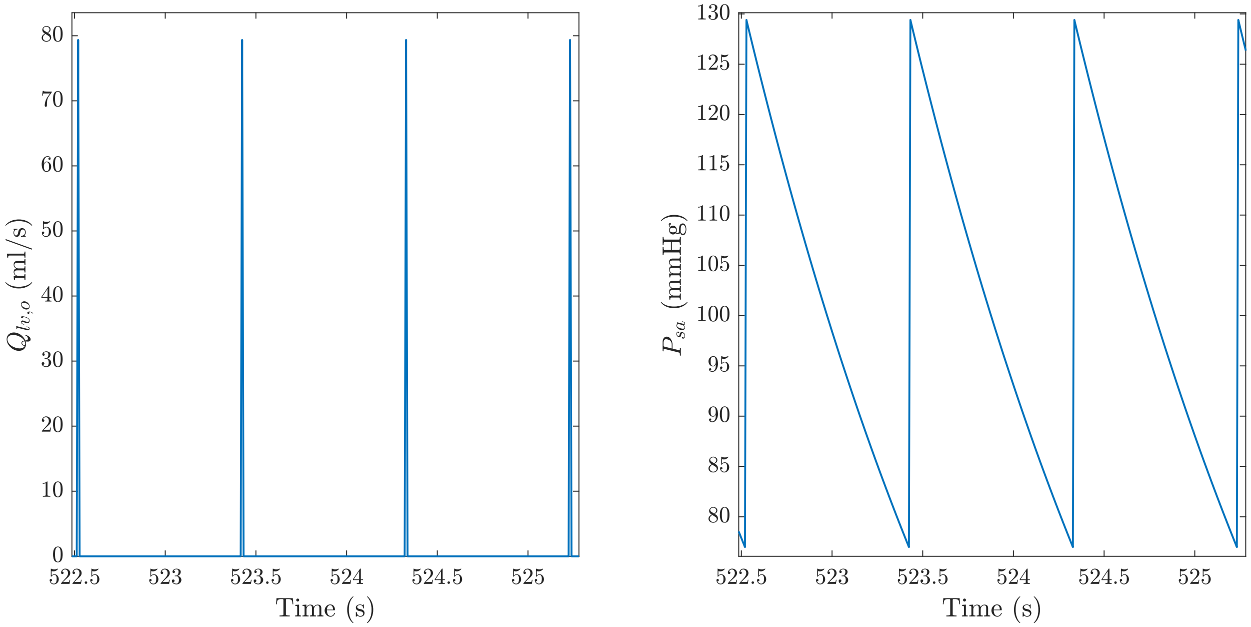

Fig. 4.10. Sample pressure and flow waveforms simulated from a two-element Windkessel model over three cardiac cycles. $Q_{lv,o}$, left ventricular output blood flow (*left* plot); P_{sa}, systemic arterial pressure (*right* plot).

Under the impulse flow assumption, (4.8) can be solved as:

$$\begin{aligned}
&\frac{dP(t)}{dt} \cdot e^{t/R_t C_t} + \frac{P(t)}{R_t C_t} \cdot e^{t/R_t C_t} = \frac{Q(t)}{C_t} \cdot e^{t/R_t C_t} \\
&\Rightarrow \int_{t_n^-}^{t} \frac{d}{d\xi}\left(P(\xi) \cdot e^{\xi/R_t C_t}\right) d\xi = \int_{t_n^-}^{t} \frac{Q(\xi)}{C_t} \cdot e^{\xi/R_t C_t} d\xi \\
&\Rightarrow P(t) \cdot e^{t/R_t C_t} - P(t_n^-) \cdot e^{t_n/R_t C_t} = \int_{t_n^-}^{t_n^+} \frac{Q(\xi)}{C_t} \cdot e^{\xi/R_t C_t} d\xi + \underbrace{\int_{t_n^+}^{t} \frac{Q(\xi)}{C_t} \cdot e^{\xi/R_t C_t} d\xi}_{0} \\
&\Rightarrow P(t) \cdot e^{t/R_t C_t} = \int_{t_n^-}^{t_n^+} \frac{SV_n \delta(\xi - t_n)}{C_t} \cdot e^{\xi/R_t C_t} d\xi + P(t_n^-) \cdot e^{t_n/R_t C_t} \\
&\Rightarrow P(t) = \left(\frac{SV_n}{C_t} \cdot \int_{t_n^-}^{t_n^+} \delta(\xi - t_n) \cdot e^{\xi/R_t C_t} d\xi + P(t_n^-) \cdot e^{t_n/R_t C_t}\right) \cdot e^{-t/R_t C_t} \\
&\Rightarrow P(t) = \left(\frac{SV_n}{C_t} + P(t_n^-)\right) \cdot e^{-(t-t_n)/R_t C_t}, \qquad (4.9)
\end{aligned}$$

---

[30] The values of peripheral resistance, R_t, and total arterial compliance, C_t, are taken from Segers et al. [136] and represent parameters from subjects with normal blood pressure values (normotensive).

where t_n^- and t_n^+ are infinitesimal time instances before and after the onset, t_n, of the Dirac delta function, respectively and time t spans the interval between two consecutive delta functions. Notice that (4.9) demonstrates that the response of a Windkessel model has indeed an exponential nature with time constant equal to $R_t\,C_t$, thereby supporting our comments in Section 4.3.1.

Accordingly, if we evaluate the pressure output at t_n^+, (4.9) becomes:

$$\begin{aligned} P(t_n^+) &= \left(\frac{SV_n}{C_t} + P(t_n^-)\right) \cdot e^{-(t_n - t_n)/R_t\,C_t} \\ \Rightarrow P(t_n^+) &= \frac{SV_n}{C_t} + P(t_n^-) \\ \Rightarrow PP_n \triangleq P(t_n^+) - P(t_n^-) &= \frac{SV_n}{C_t}, \end{aligned} \tag{4.10}$$

where the difference, $P(t_n^+) - P(t_n^-)$, is defined as the pulse pressure (PP_n) at $t = t_n$ (i.e., the difference between systolic and diastolic values). The simulation results in Fig. 4.10 agree with the mathematical derivation in (4.10); namely, the pulse pressure of the P_{sa} waveform is $129.4 - 76.98 = 52.42$ mmHg, which is approximately equal to $\frac{SV_n}{C_t} = \frac{79}{1.5} = 52.67$ mmHg[31]. So, the assumption of impulsive cardiac pumping action establishes a direct relationship between pulse pressure and stroke volume. That is, beat-to-beat stroke volume, SV_n, is directly proportional to both pulse pressure, PP_n, and the total arterial compliance, C_t.

2. The second assumption claims that the *aortic blood flow during diastole is zero.* Notice that such consideration is part of the first assumption as well, because the impulsive cardiac function implicitly assumes that diastolic blood flow is zero (see Fig. 4.10). Nevertheless, this second assumption can also be used independently. In particular, if $Q(t) = 0$ for $t \in [t_0, t)$, it can be derived from (4.8) that the system's homogeneous

---

[31] The small difference in the two values pertains to the fact that the simulated response in Fig. 4.10 is derived from a discrete-time Windkessel model (difference form) rather than a continuous-time one as per the ODE in (4.9).

response is expressed by an exponential decay of the form

$$P(t) = P(t_0) \cdot e^{-(t-t_0)/R_t C_t}, \tag{4.11}$$

where $P(t_0)$ is the pressure at $t = t_0$ (i.e., onset of diastolic phase at which blood flow becomes zero). Further, notice that in the case of the impulse train blood flow, (4.11) is equivalent to (4.9) with $P(t_0) = \dfrac{SV_n}{C_t} + P(t_n^-)$. Hence, under the second assumption and since arterial pressure is a measurable quantity, one can readily extract the circulatory system's time constant. However, it is not feasible to independently assess R_t and C_t.

Early model-based methods to estimate cardiac output using arterial blood pressure measurements were developed based on the first assumption [131, 132]. Particularly, such methods relied on the fact that stroke volume is directly proportional to pulse pressure (4.10). Despite that assessment of arterial compliance, C_t, was not possible (it is still not easily measured), Erlanger and Hooker [131] proposed the use of pulse pressure as a surrogate of stroke volume by realizing that $SV \propto PP \Rightarrow CO \propto PP \cdot HR$, where HR is the heart (or pulse) rate. Therefore, they were able to compute a relative cardiac output value, $CO_{rel} = k \cdot PP \cdot HR$, where k is an unknown proportionality factor—under the impulsive cardiac function assumption, k is equal to C_t. Later, Liljestrand and Zander [132] suggested an improvement on the relative cardiac output computation by taking into consideration that the arterial compliance (i.e., k) is not constant but varies as a function of arterial pressure (nonlinear compliance). Hence, according to Liljestrand and Zander [132], CO_{rel} can be computed as: $CO_{rel} = \dfrac{k_1}{P_{sys} + P_{dias}} \cdot PP \cdot HR$, where k_1 is a different proportionality constant, and P_{sys} and P_{dias} are the systolic and diastolic values of arterial pressure, respectively. Clearly, the approach by Liljestrand and Zander [132] established a heuristic method to account for the physiologically varying nature of C_t (and thus of k in the original equation) in an effort to provide better estimates of CO_{rel}.

Even though such estimation methods were not designed to provide absolute cardiac output values, assessment of a relative cardiac output proved to be equally important in clinical practice. A relative value can track changes in the actual quantity; that is, it is expected that CO_{rel} can follow changes in the true CO value, provided that the proportionality factor remains constant with respect to the underlying physiological reasons that caused such a CO change. Tracking changes in the cardiovascular system's function and mechanical properties is of paramount clinical importance, especially in intensive care units with hemodynamically unstable patients. Such a clinical significance of such an information maintained the interest of the research community toward a more accurate and robust estimation of relative cardiac output values.

The more recent model-based estimation methods by Bourgeois et al. [133], Mukkamala et al. [7], and Parlikar et al. [135] utilize either just the second assumption or a combination of both in order to find a relative cardiac output. Bourgeois et al. [133] proposed a two-step approach by considering only the second assumption (that is, assuming that blood flow is zero during diastole): 1) a time constant value would first be estimated during the diastolic phase of the cardiac cycle, and 2) a relative stroke volume value would then be computed by considering that, during systole, portion of the blood volume pumped by the heart is stored in the elastic arterial vessels (arterial compliance) while the rest is being propagated into the peripheral circulation (peripheral resistance). Bourgeois et al. [133] validated their method on central aortic (e.g., ascending or descending aortic) pressure waveforms, whose diastolic phase is known to resemble an exponential decay. Aortic pressure, though, is rarely measured at the beside due to the risk of formation of blood clots, hence making this technique not clinically applicable.

To overcome such a limitation and be able to use arterial pressure waveforms (instead of central aortic), Mukkamala et al. [7] proposed a more sophisticated method to estimate the system's time constant by combining the impulsive cardiac function assumption with a novel exponential fitting approach. In particular, they suggested that, as we explained in Section 4.3, the complexity of the arterial tree renders the effects of wave reflections on pressure and flow waveforms quite significant. Consequently, they asserted that simple fitting methods, such as that in [133], would fail to find a reasonable (and accurate) time constant value due to the fact that the typically measured femoral and radial pressure signals do not exhibit a discernible exponential decay (compare, for example, P_{asc} and P_{fem} in the right-hand side plot of Fig. 4.9). According to their method, the high complexity of the arterial system can be modeled by an nth-order ARX model, like in (4.4), where blood flow Q is the system's input and arterial pressure P is the corresponding output. That is,

$$P[k] = \sum_{i=1}^{n} a_i P[k-i] + \sum_{j=0}^{n} b_j Q[k-j] + w[k], \tag{4.12}$$

where w is the residual unmeasured error, and a_i and b_j are constant scalar coefficients that are related to the system's mechanical properties. Notice that the output coefficients a_i are also associated with the poles of the system's transfer function that characterize its dynamic response[32]. For instance, the differential equation describing the function of the two-element first-order Windkessel model in (4.8) can be written in an equivalent ARX form as follows (using the first-order Taylor approximation for the derivative term and assuming T_s is the sampling period):

$$\begin{aligned} \frac{P[k]-P[k-1]}{T_s} &= \frac{Q[k-1]}{C_t} - \frac{P[k-1]}{R_t\,C_t} \\ \Rightarrow P[k] &= \left(1 - \frac{T_s}{R_t\,C_t}\right) P[k-1] + \frac{T_s}{C_t} Q[k-1]. \end{aligned} \tag{4.13}$$

---

[32] The transfer function can be derived by taking the Z-transform of the system's n^{th}-order discrete-time state-space representation in (4.5). It can then be shown that the poles of the discrete-time transfer function are the same as the eigenvalues, $\lambda_{d,i}\,(i = \{1,\ldots,n\})$, of the system matrix A_d. Each eigenvalue $\lambda_{d,i}$ (or pole) is associated with a component of the system's homogeneous response, $\mathbf{y}_h[k] = \sum_{i=1}^{n} \mathbf{c}_{d,i} \cdot \lambda_{d,i}^{k}$. It is worth mentioning that the discrete-time eigenvalues are related to their continuous-time counterparts, $\lambda_{c,i}$, according to the formula: $\lambda_{d,i} = e^{\lambda_{c,i}\cdot T_s}$, where T_s is the sampling period. Hence, the system's continuous-time homogeneous response is: $\mathbf{y}_h(t) = \sum_{i=1}^{n} \mathbf{c}_{c,i} \cdot e^{\lambda_{c,i}\cdot t}$, since $t = k \cdot T_s$. Accordingly, any real eigenvalue $\lambda_{c,i}$ would represent a pure exponential response with time constant equal to the reciprocal of that eigenvalue, i.e., $\tau_i = 1/\lambda_{c,i}$ (if the eigenvalues have negative real parts, then the response will be stable).

Comparing (4.13) with (4.12), we realize that $a_1 = 1 - \frac{T_s}{R_t\,C_t}$, $b_0 = 0$, [33] and $b_1 = \frac{T_s}{C_t}$. Notice that $1 - \frac{T_s}{R_t\,C_t}$ is the first-order Taylor expansion of the exponential function $e^{-T_s/(R_t\,C_t)}$. This indicates that without any simplifying approximations $a_1 = e^{-T_s/(R_t\,C_t)}$, thereby illustrating that the discrete-time response of the two-element Windkessel model is indeed characterized by the same time constant, $\tau = R_t\,C_t$, as its continuous-time counterpart.

Ideally, if both P and Q waveforms are known, one can easily estimate the coefficients of the ARX model in (4.12) and correspondingly assess the system's dynamic response. In practice, though, blood flow Q is unknown. Mukkamala et al. [7] addressed this issue with the following proposition. As per our first assumption, they assumed that blood flow is a train of Dirac delta functions. However, they did not follow the typical consideration for the delta functions' amplitudes (i.e., equal to SV) but they rather assumed that each impulsive heart beat has an amplitude equal to the corresponding pulse pressure value. Such a consideration is supported by two mathematical aspects. 1) Under the impulsive cardiac function, PP is proportional to SV within a scaling factor equal to the inverse of the total arterial compliance; namely, $PP = \frac{SV}{C_t}$. 2) As seen in (4.9) and (4.11), the amplitude of an impulse forcing function does not affect the time constant of the ensuing exponential decay, but only the decay's initial condition ($P(t_0)$ in (4.11)). Thus, since estimation of the system's time constant is what Mukkamala et al. [7] were after, the amplitude of each impulsive heart beat in the blood flow impulse train is not expected to have an impact on time constant estimation.

As such, Fig. 4.11 represents, in a schematic way, the estimation method proposed by Mukkamala et al. [7], which can be summarized as follows:

1. Assume that the system's input (u) is an impulse train whose Dirac delta functions have amplitudes equal to each heart beat's pulse pressure, PP_n. Following the Windkessel model concept, the system's output is considered to be the measured arterial blood

---

[33] The direct influence term, b_0, is zero because the two-element Windkessel is a strictly proper system, whose transfer function has more poles than zeros.

pressure, P.

2. Estimate, via least squares, an ARX model using input, u, and output, P, data over a segment that spans multiple heart beat—notice that, for illustration purposes, Fig. 4.11 shows only three cardiac cycles. It is important to note that the proposed estimation scheme does not require the order of the ARX model to be selected a priori. Instead, it determines the model order by minimizing the minimum description length criterion[34]. Essentially, such a criterion provides a way to optimally find the model that has the best trade-off between output prediction error (goodness of fit) and model complexity with respect to the number of estimated parameters (the higher the model order, the higher the number of parameters to be estimated).

3. Evaluate the impulse response of the estimated ARX model and estimate the time constant from the ensuing exponential decay[35].

According to Mukkamala et al. [7], the time constant estimated by their proposed method corresponds to the time constant, $R_t C_t$, of a Windkessel model. This is despite the fact that the optimal ARX model is typically of order higher than first due to the complexity of the arterial tree and the presence of wave reflections. Such a consideration is attributed to the experimental evidence that the Windkessel model can capture the low-frequency dynamics of the arterial tree, as mentioned earlier. Low-frequency dynamics are associated with the system's eigenvalue with the slowest exponential decay (i.e., high time constant value). Hence, it is reasonable that Mukkamala et al. [7] conjectured that the estimated time constant (assessed after the estimated model's high-frequency dynamics have vanished) is theoretically equivalent to that of a Windkessel model.

---

[34] The minimum description length criterion introduced by Rissanen [137] defines a value for each model under consideration based on the formula: $N \cdot \log(SSR/N) + p \cdot \log(N)$, where N is the number of samples in the segment, SSR is the sum of squared residuals between measured and model-predicted outputs, and p is the model order. SSR determines the model's goodness of fit, whereas p indicates the model complexity.

[35] Typically, the exponential decay of a system's impulse response is characterized by the time constant of the largest eigenvalue, whose exponential component has the slowest decay and thus dominates the response after the high frequency dynamics (associated with small eigenvalues) have vanished.

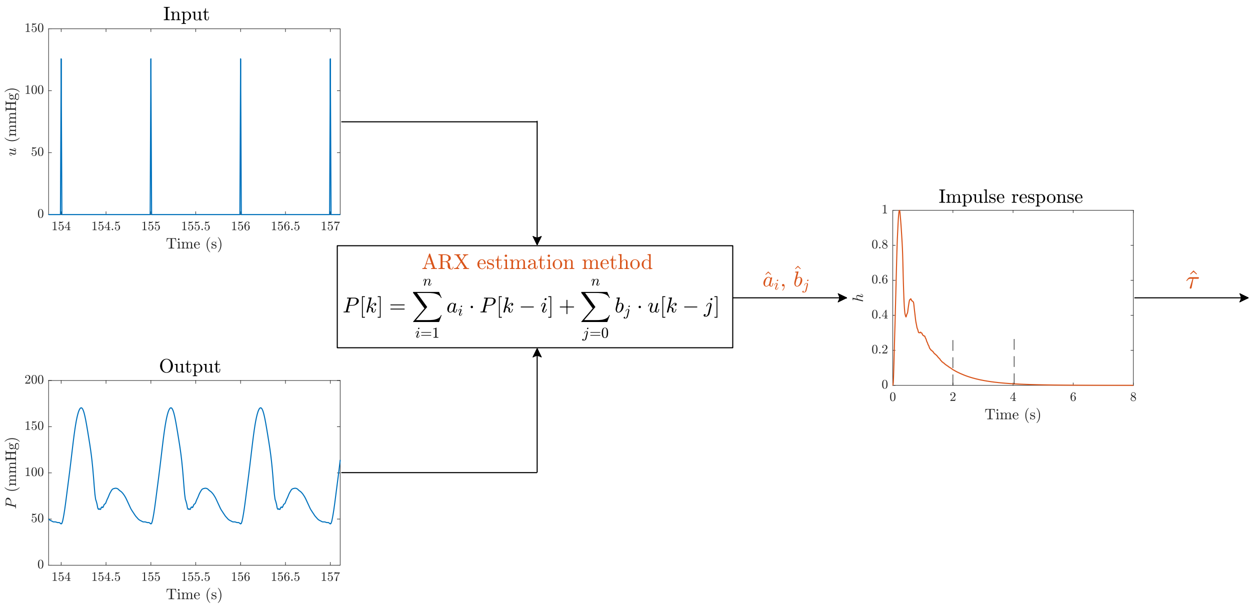
Input
u (mmHg)
150
100
50
0
154
154.5
155
155.5
156
156.5
157
Time (s)
Output
P (mmHg)
200
150
100
50
0
154
154.5
155
155.5
156
156.5
157
Time (s)
ARX estimation method
$P[k] = \sum_{i=1}^{n} a_i \cdot P[k-i] + \sum_{j=0}^{n} b_j \cdot u[k-j]$
$\hat{a}_i, \hat{b}_j$
Impulse response
h
1
0.8
0.6
0.4
0.2
0
0
2
4
6
8
Time (s)
$\hat{\tau}$

Fig. 4.11. A schematic representation of the estimation method proposed by Mukkamala et al. [7]. u, impulse train input; P, systemic arterial pressure (system's output); $\hat{a}_i$ and $\hat{b}_j$, estimates of the optimal ARX model; $\hat{\tau}$, estimated time constant.

Finally, after such a time constant is estimated, a relative cardiac output value can be computed using the formula: $CO_{rel} = \frac{\bar{P}}{\hat{\tau}}$, where $\bar{P}$ is the average arterial pressure over a segment of data and $\hat{\tau}$ is the estimated time constant. This formula is derived by taking the summation of (4.13) over a segment with $N+1$ data samples:

$$
\begin{aligned}
&\sum_{k=1}^{N} P[k] = \sum_{k=1}^{N} \left[\left(1 - \frac{T_s}{R_t\, C_t}\right) P[k-1] + \frac{T_s}{C_t} Q[k-1] \right] \\
\Rightarrow &\sum_{k=1}^{N} P[k] - \sum_{k=1}^{N} P[k-1] = \frac{T_s}{C_t} \sum_{k=1}^{N} Q[k-1] - \frac{T_s}{R_t\, C_t} \sum_{k=1}^{N} P[k-1] \\
\Rightarrow &\underbrace{P[N] - P[0]}_{0} = \frac{T_s}{C_t} \sum_{k=1}^{N} Q[k-1] - \frac{T_s}{R_t\, C_t} \sum_{k=1}^{N} P[k-1] \\
\Rightarrow &\sum_{k=1}^{N} Q[k-1] = \frac{1}{R_t} \sum_{k=1}^{N} P[k-1], \qquad (4.14)
\end{aligned}
$$

where we have hypothesized that at steady-state conditions $P[0] = P[N]$. Notice that we implicitly assumed that the segment under consideration does not contain partial heart beats, meaning that $k = 0$ and $k = N$ respectively correspond to the first sample of the first heart beat and the last sample of the last heart beat within the segment. By dividing (4.14) by N, we get:

$$\begin{aligned}\frac{\sum_{k=1}^{N} Q[k-1]}{N} &= \frac{1}{R_t}\frac{\sum_{k=1}^{N} P[k-1]}{N} \\ \Rightarrow CO &= \frac{1}{R_t}\bar{P}, \end{aligned} \tag{4.15}$$

since CO can also be seen as the average flow over a time interval[36]. Because we can only estimate the system's time constant, $\tau = R_t\, C_t$, we divide (4.15) by C_t to get:

$$\begin{aligned}\frac{CO}{C_t} &= \frac{1}{R_t\, C_t}\bar{P} \\ \Rightarrow \frac{CO}{C_t} &= \frac{1}{\tau}\bar{P} = CO_{rel}. \end{aligned} \tag{4.16}$$

According to (4.16), we can appreciate that the relative cardiac output (CO_{rel}) computed by taking the ratio of $\bar{P}$ over τ is related to the true CO value within a scaling factor equal to the inverse of the total arterial compliance, C_t. Thus, if C_t remains constant throughout the course of the experimental studies, CO_{rel} will accurately track changes in the true CO. It is worth pointing out that if continuous monitoring of the true cardiac output is of interest, the estimated CO_{rel} can be *calibrated* with respect to techniques that measure cardiac output intermittently, such as thermodilution—if available—or transthoracic Doppler ultrasound [138].

Lastly, the estimation method proposed by Parlikar et al. [135] was based on a beat-to-beat averaged Windkessel model that accounts for both inter- and intra-beat variability in the arterial pressure waveform. Inter-beat variability refers to pressure dynamics within a heart beat, such as pressure peak-to-peak amplitude (pulse pressure) and diastolic decay, whereas intra-beat variability represents the pressure difference at the onset of consecutive heart beats, attributed to changes in patient's hemodynamic status. According to Parlikar et al. [135], the differential equation of (4.8) can be averaged by integration over the nth heart beat that spans of period of T_n seconds:

---

[36] From a continuous-time perspective, we have defined $CO = SV \cdot HR$. But, $SV = \int_0^T Q(t)dt$ and $HR = 1/T$, if, for instance, T is the duration of a heart beat. Then, $CO = \int_0^T Q(t)dt/T = \bar{Q}$, where $\bar{Q}$ is the average flow.

$$\begin{aligned}
&\int_0^{T_n} \frac{dP(t)}{dt}dt = \frac{1}{C_t}\int_0^{T_n} Q(t)dt - \frac{1}{R_t\,C_t}\int_0^{T_n} P(t)dt \\
&\Rightarrow P(T_n) - P(0) = \frac{1}{C_t}SV_n - \frac{1}{R_t\,C_t}\int_0^{T_n} P(t)dt \\
&\Rightarrow \frac{P(T_n) - P(0)}{T_n} = \frac{1}{T_n}\frac{SV_n}{C_t} - \frac{1}{R_t\,C_t}\underbrace{\frac{\int_0^{T_n} P(t)dt}{T_n}}_{\bar{P}_n} \\
&\Rightarrow \frac{\Delta P_n}{T_n} = \frac{1}{T_n}\frac{SV_n}{C_t} - \frac{1}{\tau}\bar{P}_n, \qquad (4.17)
\end{aligned}$$

where SV_n and $\bar{P}_n$ respectively are the stroke volume pumped by the heart and the average arterial pressure over the nth cardiac cycle, and ΔP_n is the pressure difference at the onsets of two consecutive heart beats. Notice that Parlikar et al. [135] introduced the inter-beat variability concept by relaxing the typical assumption of the circulatory system being at steady state, whereby arterial pressure returns to its initial value at the end of every heart beat. Combining (4.17) with the impulse train blood flow assumption, which expresses pulse pressure of the nth cardiac cycle as $PP_n = \dfrac{SV_n}{C_t}$, we get

$$\frac{\Delta P_n}{T_n} = \frac{1}{T_n}PP_n - \frac{1}{\tau}\bar{P}_n. \qquad (4.18)$$

ΔP_n, T_n, $\bar{P}_n$, and PP_n can be readily obtained from the measured arterial pressure waveform. Hence, the only unknown in (4.18) is the time constant τ, which can be estimated in a least squares sense over a window where it is assumed to be constant or slowly varying. Then, a cardiac output value can be evaluated by (4.17) as the mean blood flow, CO_n, over the nth heart beat:

$$CO_n = \frac{SV_n}{T_n} = C_t\left(\frac{\Delta P_n}{T_n} + \frac{\bar{P}_n}{\tau}\right). \qquad (4.19)$$

Since C_t is unknown, Parlikar et al. [135] proposed the use of $\left(\frac{\Delta P_n}{T_n} + \frac{\bar{P}_n}{\tau}\right)$ as a relative cardiac output value that is related to the true CO_n within a scaling factor equal to the inverse of the total arterial compliance[37].

Limitations

As mentioned above, the two main assumptions used by most current estimation methods to make the circulatory system identification task somewhat feasible rely on Windkessel-type models, whether on a two- (Fig. 4.6), a three- (Fig. 4.7a), or a four-element (Fig. 4.7b) model. Such models assume an infinite pulse wave velocity and thus are not able to replicate the complex dynamics of the systemic arterial tree, such as the wave propagation delay and wave reflections. Nevertheless, it has been shown [107] that in the ascending aorta and central arteries (e.g., thoracic and abdominal aorta), the blood flow during diastole can be adequately approximated as zero, likely due to the fact that wave reflections (from peripheral circulation) and re-reflections (from the closed aortic valve) are effectively cancelling one another. Consequently, estimation techniques that use central aortic pressure waveforms and estimate the circulatory system's time constant have proved to be quite accurate. It is worth pointing out, though, that in a clinical setting, pressure manometry is rarely performed at these vessels due to high risk of catheter-associated complications, like blood clots. As a result, clinical pressure monitoring is typically conducted on either femoral or radial arteries. However, the flow profile at these arterial segments significantly deviates from the zero value assumption. This phenomenon is primarily attributed to the wave reflections that are generated by the closely located peripheral vessels, thereby presenting a major challenge for current estimation approaches that are based on Windkessel-type models and end up using femoral or radial pressure waveforms to estimate the circulatory system's time constant.

---

[37] Notice the difference between the formula (4.19) suggested by Parlikar et al. [135] and the one in (4.16) which is typically used. The absence of the term $\Delta P_n/T_n$ in (4.16) is ascribed to the steady-state condition that the circulatory system is assumed to be in.

4.5 Proposed approach

4.5.1 A feasibility study with central venous pressure

It is clear from our discussion in previous sections that monitoring of physiological variables at the bedside can offer significant advances in the diagnosis and tracking of cardiovascular diseases. Undoubtedly, arterial blood pressure (ABP) is the most commonly measured variable due to its profound importance in monitoring the status of the cardiovascular system. In addition to ABP, central venous pressure (CVP) is another variable that is often measured in critical care units. It is considered a close proxy of right atrial pressure (P_{ra}) and thus typically used by the medical community as an indirect index of cardiac preload[38]. Even though studies [139] have shown that CVP poorly correlates with such index and despite the adverse consequences of venous catheterization [140], CVP monitoring can still offer an indication of the interaction between cardiac function and circulatory system [141], as portrayed by the well-known Frank-Starling curves. In addition, although CVP is, from a dynamic point of view, less rich as a signal compared to ABP, it still contains physiological information on the dynamics of the circulatory system. Therefore, we want to investigate the potential benefits of using both ABP and CVP signals for the identification of the circulatory system. The analysis is conducted in two parts: 1) we analyze the identifiability of the circulatory system's state-space representation by considering the theoretical concepts of controllability[39] and observability[40] and 2) we evaluate the performance of a state-space identification technique on simulated data with and without the influence of noise.

---

[38] As explained in Chapter 2, ventricular preload describes the level of stretching in cardiac myocytes, therefore indicating the pumping capacity of the ventricle. Myocardial stretching is a function of end-diastolic ventricular volume. However, ventricular volumes are not easily measured in clinical scenarios. As a result, end-diastolic ventricular pressure, which is approximately equal to atrial pressure at the end of diastole, is typically used as a surrogate of ventricular preload.

[39] Controllability is a property of a state-space model for which there exists input $u(t)$ that can transfer any initial state $x(t_0)$ to any final state $x(t_1)$ in a finite time.

[40] Observability is a property of a state-space model for which the knowledge of input, $u(t)$, and output, $y(t)$, for $t \in [t_0, t_1]$ (t_1 finite) suffices to uniquely determine any unknown initial state, $x(t_0)$.

Simplified systemic circulation model

To simplify the analysis, we propose a simplified version of the systemic circulation model presented in Chapter 2 as part of the cardiopulmonary model. In particular, we lump the two parallel compartments, representing the splanchnic and extra-splanchnic circulations (see Fig. 2.2), into a single one and accordingly compute the equivalent values for the hydraulic resistances and compliances. The derived fourth-order model is shown in Fig. 4.12. As analyzed in Section 4.2.2 and illustrated in Fig. 4.5, we assume that ABP, measured in the aorta and denoted as P_{sa}, is the driving pressure source and P_{ra} is the right atrial pressure (CVP signal) and the output of the system. The nodes P_{sp} and P_{sv} represent the pressures in the systemic peripheral and venous circulations respectively.

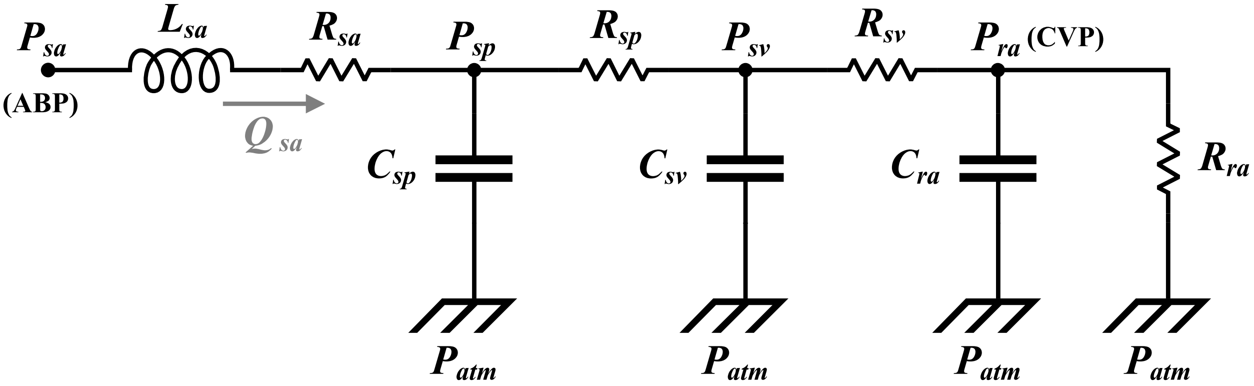

Fig. 4.12. Electrical diagram of the simplified fourth-order model of the systemic circulation system. ABP, arterial blood pressure; CVP, central venous pressure; P, pressure; Q, blood flow; R, resistance; L, inertance; C, compliance. Subscripts: sa, systemic arteries; sp, systemic peripheral circulation; sv, systemic veins; ra, right atrium. P_{atm} is the atmospheric pressure which is assumed equal to zero.

The simplified model of Fig. 4.12 has the following limitations. First, it does not account for the contractions of the right atrium and right ventricle. Hence, the dynamics owing to any of these phenomena, which profoundly affect a clinically measured CVP waveform, are absent in the simulated P_{ra} signal. Second, atmospheric pressure is the common reference pressure for all pressure nodes. Thus, the effect of pleural pressure on CVP, which as described in Chapter 2 is quite significant, is herein assumed to be negligible. Third, the function of the atrioventricular valve is not appropriately considered. To be specific, R_{ra} effectively represents the resistance of the tricuspid valve that opens and closes based on the pressure difference between the right atrium and the right ventricle. However, with this model, we assume that the valve is always in an open state with flow exiting the high pressure point, P_{ra}, towards the atmospheric downstream pressure. Mitigation of this limitation can be ensured by splitting the identification into two portions; one made of segments when the tricuspid valve is open, the other when it is closed. Nevertheless, for our study, such a complication is not deemed necessary. In fact, it will be shown later that the identifiability of the system in Fig. 4.12 is independent of the value of R_{ra}.

The continuous-time state-space representation, as in (4.2), of the simplified model in Fig. 4.12 is derived by considering Q_{sa}, P_{sp}, P_{sv}, and P_{ra} are the states of the system:

$$\begin{bmatrix} \dot{Q}_{sa} \\ \dot{P}_{sp} \\ \dot{P}_{sv} \\ \dot{P}_{ra} \end{bmatrix} = \begin{bmatrix} -\dfrac{R_{sa}}{L_{sa}} & -\dfrac{1}{L_{sa}} & 0 & 0 \\ \dfrac{1}{C_{sp}} & -\dfrac{1}{R_{sp}\,C_{sp}} & \dfrac{1}{R_{sp}\,C_{sp}} & 0 \\ 0 & \dfrac{1}{R_{sp}\,C_{sv}} & -\dfrac{R_{sp}+R_{sv}}{R_{sp}\,R_{sv}\,C_{sv}} & \dfrac{1}{R_{sv}\,C_{sv}} \\ 0 & 0 & \dfrac{1}{R_{sv}\,C_{ra}} & -\dfrac{R_{sv}+R_{ra}}{R_{sv}\,R_{ra}\,C_{ra}} \end{bmatrix} \cdot \begin{bmatrix} Q_{sa} \\ P_{sp} \\ P_{sv} \\ P_{ra} \end{bmatrix} + \begin{bmatrix} \dfrac{1}{L_{sa}} \\ 0 \\ 0 \\ 0 \end{bmatrix} \cdot P_{sa} \tag{4.20a}$$

$$P_{ra} = \begin{bmatrix} 0 & 0 & 0 & 1 \end{bmatrix} \cdot \begin{bmatrix} Q_{sa} \\ P_{sp} \\ P_{sv} \\ P_{ra} \end{bmatrix} + 0 \cdot P_{sa}. \tag{4.20b}$$

The values of the parameters in (4.20) are computed based on the ones reported by Albanese et al. [18]: $L_{sa} = 0.220 \cdot 10^{-4}$ mmHg·s^2/ml, $R_{sa} = 0.0600$, $R_{sp} = 0.595$, $R_{sv} = 0.0112$, $R_{ra} = 0.0250$ mmHg·s/ml, and $C_{sp} = 3.72$, $C_{sv} = 77.8$, $C_{ra} = 31.3$ ml/mmHg. The eigenvalues (or poles of the system's transfer function) of the continuous-time A matrix in (4.20), which will be used for evaluation of the identification performance, are $\lambda_{1,2,3,4} = -0.31039$, -4.9570, -5.0481, -268.17. Thus, the corresponding time constants (in seconds) are equal to $\tau_{1,2,3,4} = -1/\lambda_{1,2,3,4} = 3.22180$, 0.20173, 0.19810, 0.0037290.

The reason why we are interested in the eigenvalues of the A matrix is attributed to the fact that a state-space model is unique within a similarity transformation[41]. It is then usual that, in state-space identification, the identified model will not necessarily be in the same coordinate frame as the original system. Thus, a common and convenient way of judging the identified model is via eigenvalue analysis, since the eigenvalues of the system matrix A are invariant under similarity transformation.

Theoretical considerations

Identifiability of state-space models is determined by the rank of the controllability and observability matrices. Full-rank matrices signify that all states of the system are controllable and observable and thus the corresponding model can be identified. Because (4.20) is a SISO model, both controllability and observability matrices are square. Hence, they will have full rank if and only if their determinant is non-zero, regardless of the magnitude. For the model in (4.20), the determinants of the continuous-time controllability and observability matrices $\mathcal{Q}$ and $\mathcal{O}$ are given by

$$\det(\mathcal{Q}) = \det\left(\left[B \; AB \; A^2B \; A^3B\right]\right) = \frac{1}{L_{sa}^4 R_{sp}^2 \, R_{sv} \, C_{sp}^3 \, C_{sv}^2 \, C_{ra}} \tag{4.21}$$

$$\det(\mathcal{O}) = \det\left(\left[C^T \; (CA)^T \; (CA^2)^T \; (CA^3)^T\right]^T\right) = \frac{1}{R_{sp}^2 \, R_{sv}^3 \, C_{sp} \, C_{sv}^2 \, C_{ra}^3}. \tag{4.22}$$

It is apparent that for any finite values of the parameters, the determinants in (4.21) and (4.22) are non-zero. We can then infer that the assumed model is controllable and observable. Hence, all states can be identified using input and output data, provided that the input is sufficiently rich to excite the system's dynamics. Besides, based on (4.21) and (4.22), we observe that the identifiability of the system does not depend on the right atrial resistance, R_{ra}, since the determinants are invariant of its value.

---

[41] A similarity transformation is considered when the state $x(t)$ of the state-space model in (4.2) gets multiplied by a nonsingular matrix $T \in \mathbb{R}^{nxn}$, i.e., $z(t) = Tx(t)$. The corresponding state-space model describes the same input-output pair via a different state $z(t)$ and new state matrices, $T^{-1}AT$, $T^{-1}B$, CT, D.

Numerical simulations

For the simulation studies, we use the novel and robust-to-noise observer Kalman filter identification with deterministic projection (OKID/DP) algorithm proposed by Vicario et al. [142]. Such a non-parametric state-space system identification technique is preferred over parameter estimation methods, because it is designed to optimally assess the system's order without any prior knowledge of its actual structure. Instead of estimating the parameters of an a priori assumed model, identifiability is then evaluated based on whether the correct order of the system is identified and how precisely its eigenvalues are estimated. This is important, as in practical scenarios noise may significantly affect the dynamics associated with some of the eigenvalues and make their estimates highly uncertain. To this end, we use Monte-Carlo (MC) numerical simulations to take into account noise in the data and assess the system's identifiability under varying levels of noise. Additionally, note that most identification techniques, like the one adopted here (OKID/DP), are formulated for implementation in a digital machine and thus they identify a discrete-time state-space model. Nevertheless, under the standard zero-order-hold assumption, the identified discrete-time model can be readily converted into its continuous-time counterpart in (4.20).

Specifically, we want to verify via numerical simulations whether OKID/DP can correctly identify the fourth-order model depicted in Fig. 4.12 and represented by the state-space form in (4.20). The ABP waveform generated by the comprehensive cardiopulmonary model of Chapter 2 is taken as the input signal and the output CVP pressure is then simulated via the model in (4.20). A segment, for instance, of the simulated ABP and CVP signals is illustrated in Fig. 4.13. Subsequently, such input and output data are passed on to the OKID/DP algorithm. Like any state-space identification method, a key step in OKID/DP is the singular value decomposition (SVD) of a data matrix. The number of non-zero singular values indicates the order of the model whose A, B, C, and D matrices the algorithm would then identify. In more practical terms, the presence of a noticeable gap between two groups of singular values (e.g., zero and non-zero) in the SVD plot demonstrates that the identification algorithm is able to determine, from the available data, that the system is of order equal to the number of singular values before such a gap. It is worth mentioning that the algorithmic performance with regards to the true model will be assessed, as described earlier, via the eigenvalues of the system matrix A.

Deterministic case When noise-free simulated input and output data are used in OKID/DP, the singular value plot (blue dots in Fig. 4.14) shows a significant gap between the fourth and fifth singular values. Note that the small singular values are in magnitude very close to zero (within Matlab's working precision). As predicted by the theoretical indicators and shown in Fig. 4.14, the fourth-order model is correctly identified since the eigenvalues of the identified A matrix closely match the true ones.

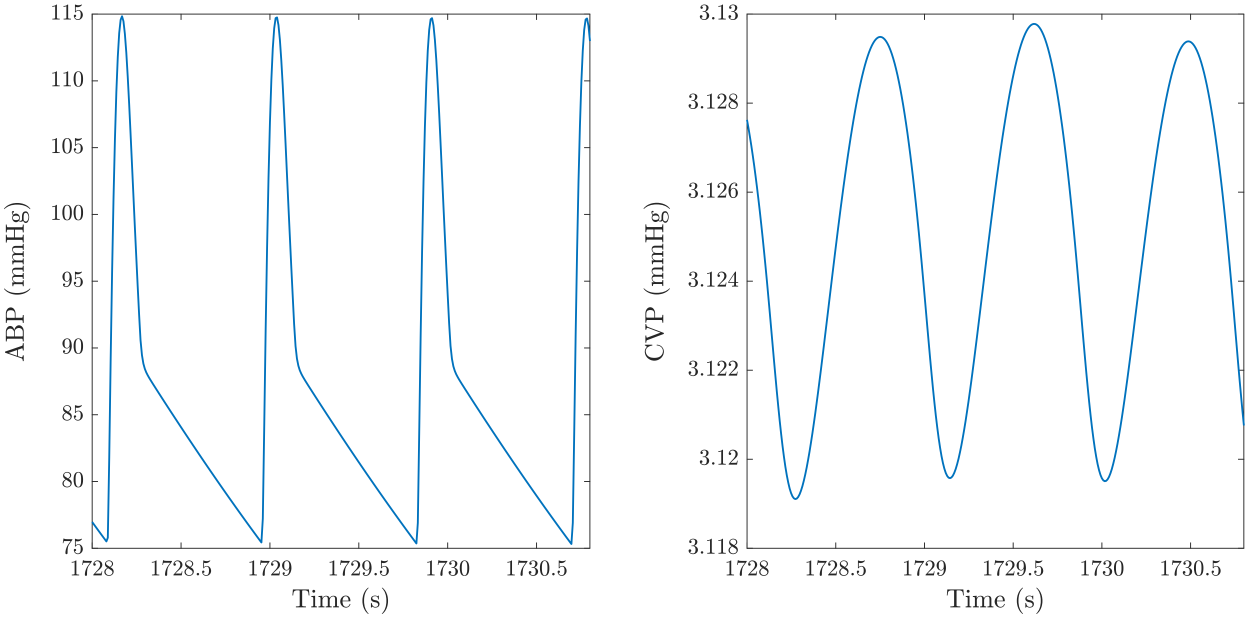

Fig. 4.13. Sample ABP (*left* plot) and CVP (*right* plot) waveforms simulated under noise-free conditions from the fourth-order model presented in Fig. 4.12 and described in (4.20).

Stochastic case In the stochastic case, zero-mean Gaussian-distributed random noise is added to corrupt both input and output data before they are passed on to OKID/DP. The standard deviation (SD) of input and output noise is chosen proportional to the SD of the corresponding uncorrupted signal. We thus intend to keep the signal-to-noise ratios of both

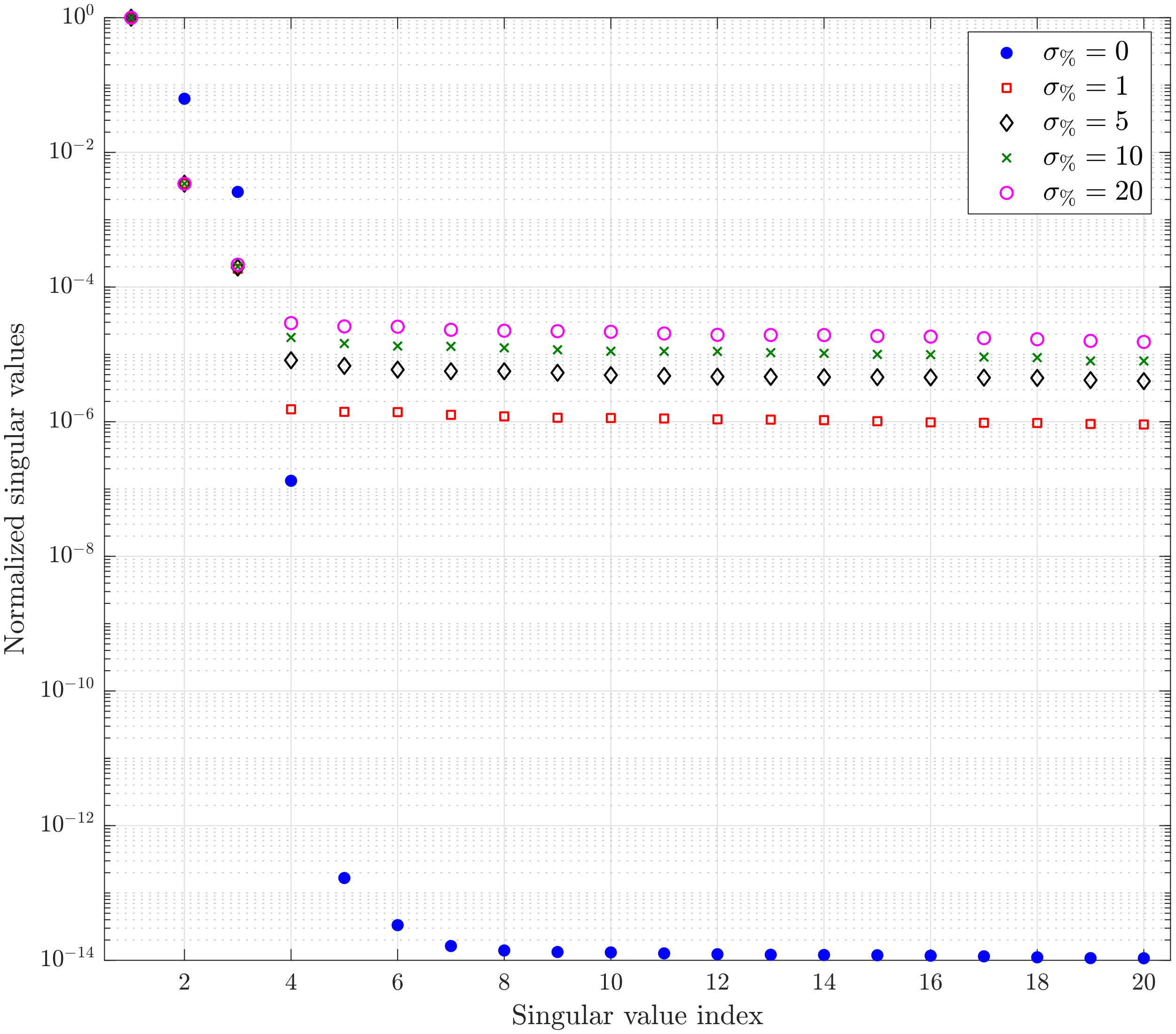

Fig. 4.14. Singular value plot of OKID/DP for the noise-free ($\sigma_\% = 0$) and noisy data with levels of noise standard deviation $\sigma_\% = 1, 5, 10, 20$. Notice that the number of non-zero—with reference to the noise level corrupting the data—singular values indicates the order of the model.

input and output data at relatively the same levels, while we analyze the effects of noise with its standard deviation ($\sigma_\%$) ranging from 1% up to 20% of the original signal's SD.

For instance, Fig. 4.14 compares the singular value plot for $\sigma_\% = 1$ (red squares) with the one of the deterministic case (blue dots). It is apparent that even such a relative small noise level renders the model not fully identifiable as the fourth singular value can no longer be distinguished from the rest. This phenomenon can also be conjectured from the deterministic case (blue dots) since the first three singular values are dominant relative to the fourth one, whose value is considerably smaller. Similar conclusion can be inferred from a theoretical perspective as the time constant associated with the smallest eigenvalue λ_4 is significantly smaller (at least two orders of magnitude) than the other three. As a consequence, the corresponding dynamics decay very fast and they are difficult to be identified. Further, mathematical derivation shows that the fourth and smallest eigenvalue is associated with blood inertance. Simplification of the model shown in Fig. 4.12 by removing the inertance L_{sa} and assuming that the differential pressure across the resistive element R_{sa} is equal to $P_{sa} - P_{sp}$ eliminates the above-unidentified eigenvalue with the fastest response. The remaining eigenvalues of this simplified third-order model, i.e., $\lambda_{1,2,3} = -0.31028$, -4.9106, -5.0105, are minimally affected as compared with those of the fourth-order model. Hence, since noise is always present in real-case scenarios, we can conclude that inertial effects of the blood, which are predominant in the aorta, cannot be effectively determined by using only ABP and CVP signals.

Moreover, Fig. 4.14 clearly illustrates that as the noise level increases, the gap between the non-zero singular values and the ones that are supposed to be zero reduces. For $\sigma_{\%} = 20$ (magenta circles), for instance, the singular value plot suggests that the gap is minimal and the order of the identified model can be anything between first and third. Essentially, the singular value plot does not provide any clear indication that the dynamics of the system could be generated by a model of an order higher than one.

To further illustrate this point, we execute MC simulations in order to assess the precision of the estimated eigenvalues in the presence of random noise in the input-output data generated by the fourth-order model. For each run, we get singular value plots similar to the ones in Fig. 4.14 and we pick only the three largest singular values, as the fourth eigenvalue is clearly obscured by the noise. Table 4.1 shows the eigenvalues of the 3x3 A matrix in terms of mean and standard deviation of the results from 100 runs for each noise level. It is evident that the dynamics of λ_1 are dominant in the noisy simulated data as the SD of

λ_1 estimate is, in relative terms, one order of magnitude smaller than the SD of λ_2 and λ_3 estimates. Similar conclusion was drawn from Fig. 4.14, where the small separation gap between the zero and non-zero singular values confirmed the difficulty in identifying a model of an order higher than one.

Table 4.1. Eigenvalue comparison between true and identified A matrices

	λ_1		λ_2		λ_3	
Noise level ($\sigma_{\%}$)	Mean	SD	Mean	SD	Mean	SD
(True)	(−0.31028)	—	(−4.9572)	—	(−5.0479)	—
1%	−0.31048	0.00128	−4.7740	0.18477	−5.2455	0.20456
5%	−0.30778	0.00579	−4.7553	0.32977	−5.2563	0.41156
10%	−0.29773	0.01101	−4.8096	0.27239	−5.0834	0.39558
20%	−0.26423	0.01827	−4.6777	0.18347	−4.6899	0.20720

Mean and standard deviation (SD) of the estimated A matrix's eigenvalues have been computed from 100 Monte-Carlo simulations for each noise level.

In conclusion, the results of this study suggest that the use of CVP as a signal additional to regular ABP monitoring is not sufficient to provide a more accurate and detailed description of the circulatory system. Even from data numerically generated from a simplified fourth-order model of the systemic circulation, part of its dynamics is not correctly (if at all) identified under the influence of input and output noise. Moreover, the simulations showed that, even if it were possible to measure the ABP in the aorta, where the inertial effects of the blood flow are the highest, the dynamics attributed to the inertance could be extracted only in the ideal case of noise-free data. The presence of noise renders the corresponding eigenvalue completely unidentifiable. Finally, noise in the data considerably narrows the gap in the singular value plot that is necessary to distinguish between zero and non-zero singular values. Even third- or second-order models are not easily, or accurately, identified as illustrated by the ambiguous separation in the singular value plot and by the relatively large SD of the λ_2 and λ_3 estimates.

4.5.2 Proposed estimation algorithm

The feasibility study, delineated above, clearly demonstrated that even under ideal and simplified conditions (i.e., a simplified fourth-order model of the systemic circulation, no effects of atrial or ventricular contraction on central venous pressure), the dynamics of the CVP waveform are not adequate in providing a more detailed description of the circulatory system (i.e., a model with order higher than first). Accordingly, our efforts focused on estimation techniques that would only use the ubiquitously monitored arterial (femoral or radial) blood pressure.

Similar to the model-based techniques analyzed in Section 4.4.2, the proposed cardiac output estimation method is designed according to the typical consideration that blood flow is the forcing function (input) to the arterial tree, which, in turn, generates the measured arterial blood pressure waveform. On the contrary, though, to most existing estimation methods that are based on the impulsive cardiac function assumption, we instead intend to use more appropriate physiological assumptions on the shape of the circulatory system's forcing function. Formulation of such assumptions requires a thorough understanding of the complex dynamics of the arterial circulation (e.g., wave reflections phenomena) as well as a substantial exposure to real-time pressure and flow waveform data. However, an extensive collection of such data is an enormously challenging task due to the invasiveness of a continuous and real-time measurement of blood flow[42]. Hence, one way to acquire such hemodynamic data is by creating a high-fidelity in-silico model of the arterial tree. This model ought to be able to generate realistic synthetic data, reflecting physiological phenomena observed in the measured arterial blood pressure under different clinical conditions (i.e., different arterial material properties).

To this end, we developed a high-order distributive model of the arterial system based on the work reported in [6] and briefly introduced in Section 4.3.2 (see Fig. 4.8b). A sample of

---

[42] Notice that blood flow waveforms can be continually collected only via an ultrasonic flowmeter placed around the vessel of interest. As explained earlier, such a measuring method is highly invasive and thus rarely used.

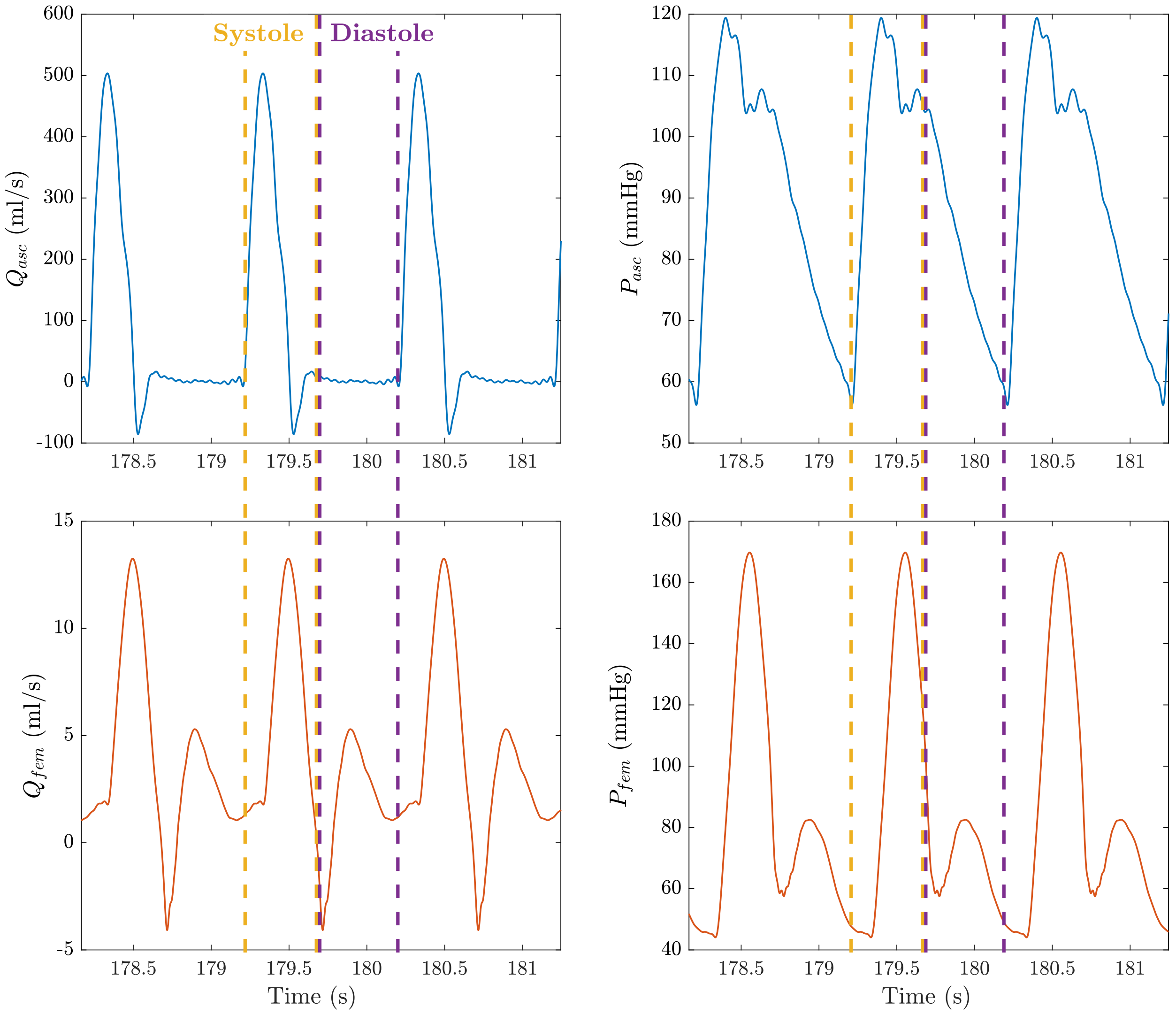

Fig. 4.15. Sample pressure and flow waveforms simulated from the distributed arterial model by Stergiopulos et al. [6] over three cardiac cycles. Q_{asc} (*top left* plot) and P_{asc} (*top right* plot) are the ascending aortic blood flow and pressure, respectively. Q_{fem} (*bottom left* plot) and P_{fem} (*bottom right* plot) are the femoral blood flow and pressure, respectively. The yellow and purple vertical lines respectively indicate the systolic and diastolic portions of the second cardiac cycle.

the simulation results from the distributive model is displayed in Fig. 4.15, where flow and pressure waveforms in the ascending aorta and femoral artery are compared[43]. As reported in literature studies [143, 144] and evident from the simulated waveforms in Fig. 4.15, the femoral flow shows prominent swings in the diastolic phase, whereas, at the same time, the ascending aortic flow is very close to zero because of the closed aortic valve (i.e., no cardiac pumping activity). As a consequence, the diastolic profile of the pressure at the ascending aorta follows an exponential trajectory [99, 100, 101, 102]. On the contrary, femoral pressure is clearly disturbed from the wave reflections and no clear exponential decay is discernible during diastole. Hence, estimation algorithms that use femoral arterial pressure but rely on the diastolic exponential decay assumption are expected to have poor performance, in terms of their accuracy in estimating the circulatory system's time constant. It is also worth noting the delay on the foot of the waves[44] between the femoral artery and the ascending aorta—compare, for instance, the two waveforms at the time instance of the onset of positive blood flow in the ascending aorta (marked by the first yellow line). This is a characteristic feature of a physiological phenomenon according to which the pressure wave travels through the arterial system at a certain finite wave velocity that depends on the elasticity, thickness, and radius of the arterial vessels as well as the density of the blood [145].

---

[43] Note that the model-predicted variables in Fig. 4.15 are the same as those in Fig. 4.9. Nevertheless, they are presented again here in reference to the development process of the estimation algorithm.

Moreover, the physiological contractile behavior of the heart results in blood flow profiles that do not arbitrarily change over the systolic portion of a cardiac cycle; they typically monotonically increase in early systole, following the cardiac contraction (ventricular depolarization), then monotonically decrease in late systole during cardiac muscle relaxation (ventricular repolarization) [87]. It is therefore expected that the profile of blood flows in systole can be satisfactorily parametrized via a piecewise quadratic function. For example, Fig. 4.16 shows the blood flow in ascending aorta (Q_{asc}) and femoral artery (Q_{fem}) over a single cardiac cycle—they are simulated, as before, from the distributed arterial model by Stergiopulos et al. [6]. Both blood flow waveforms have been superposed with piecewise quadratic functions (black dashed lines in Fig. 4.16) that are described based on the actual waveform's onset (t_o), peak (t_p), and return (t_r) time instances[45]. In particular, a generic piecewise quadratic flow profile (Q) is defined by the following the equations:

---

[44] We define the foot of the pressure wave in a beat-by-beat fashion as the point of the pressure waveform with the lowest value at every heart beat. This typically precedes the steeper upward pressure slope associated with the systolic phase of cardiac function.

$$Q(t) = \begin{cases} -\dfrac{Q_p - Q_o}{(t_p - t_o)^2} \cdot (t - t_o)^2 + \dfrac{2 \cdot (Q_p - Q_o)}{t_p - t_o} \cdot (t - t_o) + Q_o, & t \in [t_o, t_p) \\ \dfrac{Q_o - Q_p}{(t_r - t_p)^2} \cdot (t - t_p)^2 + Q_p, & t \in [t_p, t_r] \end{cases} \tag{4.23}$$

where Q_p is the maximum flow value at $t = t_p$ and Q_o is the flow value at the beat onset, t_o.

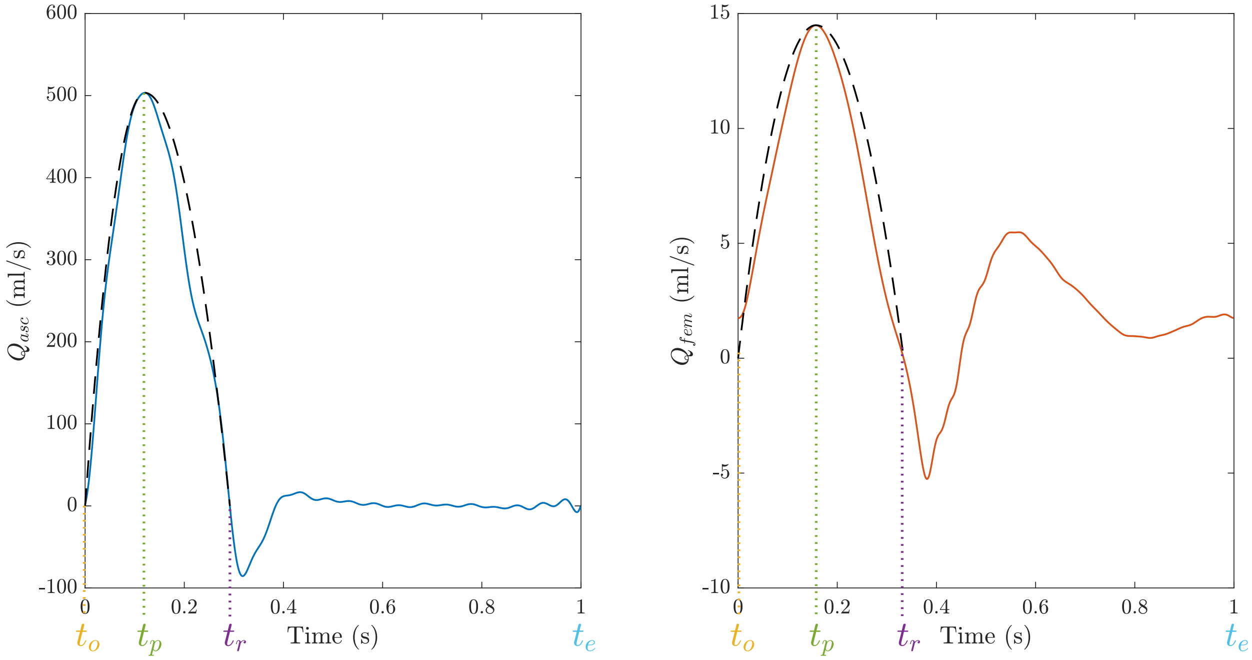

Fig. 4.16. Sample ascending aortic (Q_{asc}, *left* plot) and femoral (Q_{fem}, *right* plot) flow waveforms simulated from the distributed arterial model by Stergiopulos et al. [6] over a single cardiac cycle. The black dashed lines on both plots represent piecewise quadratic profiles derived from parametrization of the corresponding flow waveforms during systole. Notice that the time axis is normalized with respect to the beginning of the heart beat. t_o, t_p, and t_r are the onset, peak, and return time instances of the piecewise quadratic functions respectively and t_e represents the end of the heart beat.

Notice that we introduce the concept of flow parametrization during systole only (see (4.23) and Fig. 4.16). As shown above, wave reflections are prominent in femoral artery during the diastolic phase[46]. Consequently, parametrization of the flow profile in diastole cannot be generally performed, with the only exception being at the aorta where flow is close to zero. In addition, the absence of wave reflections on systolic flow and pressure waveforms allows us to assume that the dynamics of the arterial tree during systole can be adequately described by Windkessel-type models (i.e., first- or second-order models) [143].

---

[45] Such time instances are defined with respect to the systolic portion of blood flow, i.e., t_o indicates the beginning of systole, t_p corresponds to the maximum systolic flow, and t_r represents the time instance when backward flow starts.

As schematically represented in Fig. 4.17, the proposed estimation algorithm follows the overall scheme introduced by Mukkamala et al. [7], whereby a series of cardiac cycles are utilized as inputs to the estimation algorithm (signals u and P in Fig. 4.17) and the arterial system's time constant ($\hat{\tau}$) is then estimated from the impulse response of the optimal ARX model. However, the proposed algorithm differs from that in [7] because it accounts for the aforementioned two physiological considerations; namely, 1) the parameterization of blood flow profile during systole with a piecewise quadratic function and 2) the absence of wave reflections in systole allowing the system to be described by low-order models. More specifically and in reference to Fig. 4.17, the algorithm can be summarized as follows:

- Construct many sets of onset (t_o), peak (t_p), and return (t_r) time instances, defined with respect to the foot (onset) of the arterial pressure waveform, P.
- For each set, generate a quadratic piecewise quadratic waveform corresponding to the systolic portion of every heart beat in the data segment[47].
- For each piecewise quadratic input waveform, construct the corresponding least squares (LS) problem using only the systolic portions of input and output waveforms (notice the thick u and P lines in Fig. 4.17).
- Solve each LS problem to estimate the coefficients ($\bar{a}_i$ and $\bar{b}_j$) of a low-order autore-

---

[46] In fact, wave reflections are prominent in diastole not only in femoral artery but in all small arteries, such as radial and brachiocephalic arteries.

[47] Note that estimation of the system's time constant is independent of the amplitude of the system's input and thus we set the latter equal to pulse pressure, as per Mukkamala et al. [7].

gressive model with exogenous inputs (ARX).

- For each ARX model (and, correspondingly, for each piecewise quadratic input), compute the sum of squared residuals (SSR) between the model-predicted output and system's true output signal (i.e., measured arterial pressure P).
- Select the ARX model (optimal ARX model with coefficients $\hat{a}_i$ and $\hat{b}_j$) that attains the minimum SSR among all LS solutions.
- Compute an estimated time constant ($\hat{\tau}$) from the optimal ARX model's impulse response.
- Repeat the same procedure progressively for all segments in the dataset.

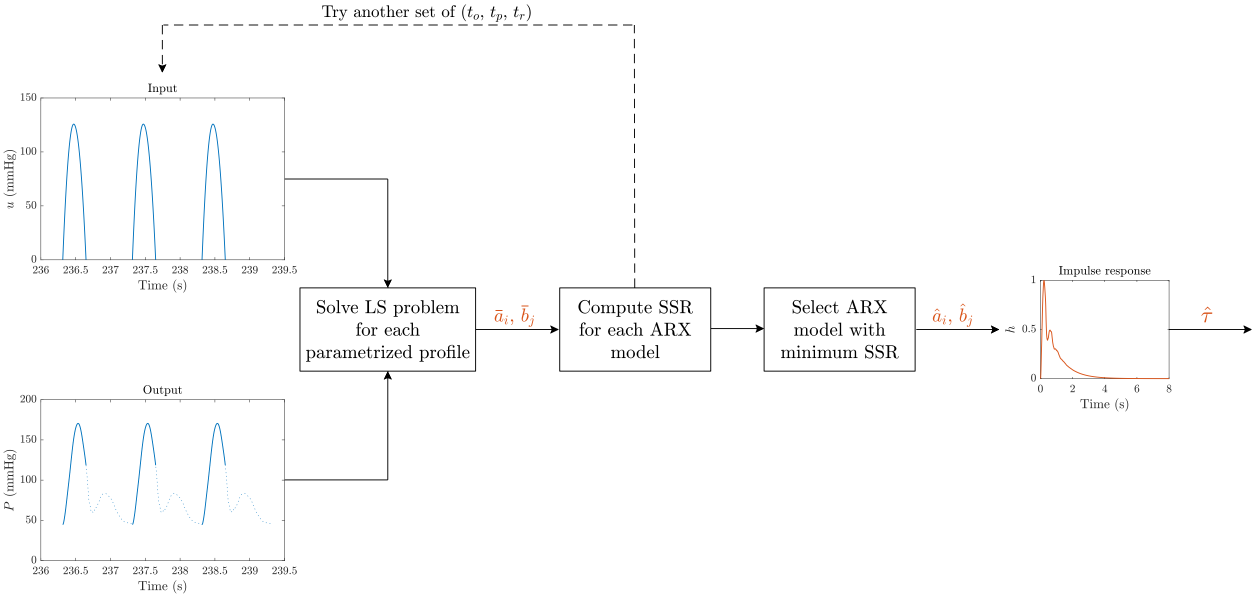
Try another set of (t_o, t_p, t_r)
Input
u (mmHg)
150
100
50
0
236
236.5
237
237.5
238
238.5
239
239.5
Time (s)
Output
P (mmHg)
200
150
100
50
0
Solve LS problem for each parametrized profile
$\bar{a}_i$, $\bar{b}_j$
Compute SSR for each ARX model
Select ARX model with minimum SSR
$\hat{a}_i$, $\hat{b}_j$
Impulse response
h
1
0.5
0
2
4
6
8
Time (s)
$\hat{\tau}$

Fig. 4.17. Schematic diagram of the proposed estimation algorithm. u, piecewise quadratic input based on the selected onset (t_o), peak (t_p), and return (t_r) time instances; P, systemic arterial pressure (system's output); $\bar{a}_i$ and $\bar{b}_j$, estimates of ARX model for each flow profile; $\hat{a}_i$ and $\hat{b}_j$, estimates of the optimal ARX model (with minimum SSR); $\hat{\tau}$, estimated time constant of optimal ARX model; LS, least squares; SSR, sum of squared residuals.

4.6 Algorithm validation

An indispensable component in the development of any parameter estimation, or system identification, algorithm pertains to its validation against synthetic (simulated) and experimental datasets. Validation with synthetic data generated via simulations from an in-silico mathematical model is a fundamental step before any clinical validation. In-silico simulations provide significant advantages over human (or animal) studies. 1) They offer a controlled "environment" that permits the generation of data under various clinical conditions, attained by selecting specific sets of model parameters (e.g., a decrease in arterial compliance would represent the hemodynamic response of elderly hypertensive patients). Such an environment also allows easy reproducibility of the simulated experimental conditions, a critical component for algorithmic validation and comparison with existing techniques. 2) The direct interpretability of the model-simulated data, in reference to the associated model parameters, allows researchers to draw conclusions with respect to potential limitations and, eventually, to the clinical applicability of the estimation algorithm at hand.

For these reasons, we herein focus on evaluating the performance of the proposed estimation algorithm under two distinct types of simulation studies: 1) studies with data from a lumped-parameter Windkessel-type model and 2) studies with data from a distributed-parameter model. It is important to point out that despite both studies are performed on synthetic data, the use of a distributed-parameter model presents three challenges to the estimation method:

1. The distributed model used for data generation is a high-order model with nonlinear parameters. The estimation algorithm, on the other hand, assumes a linear low-order lumped-parameter model. Such a disparity between the model for data generation and the one used for estimation, typically referred to as *modeling error*, resembles real experimental conditions, since the human arterial tree is undoubtedly a highly

nonlinear system[48].

2. Simulated pressure and flow waveforms from a distributed model exhibit *realistic dynamics* that include physiological characteristics, such as finite wave velocity and wave reflections, typically observed in experimentally collected data.

3. The distributed model comprises *multiple arterial segments*. This allows us to test the parameter estimation method on waveforms from different locations of the arterial tree, as if we were collecting data from different arteries. For example, we can evaluate the algorithmic performance on data representing the dynamics in the aorta (e.g., ascending or descending aorta) or in the femoral artery. We could also be able to investigate whether the location of the arterial line (femoral versus radial artery) can affect the estimation results. Femoral catheterization was traditionally preferred for pressure monitoring but recently radial pressure manometry is gaining wider acceptance due to fewer complications associated with it [146].

The algorithmic performance will be assessed with regard to the true model parameters, selected for the generation of the synthetic data, as well as in comparison to the method proposed by Mukkamala et al. [7], which is considered a novel and promising model-based cardiac output estimation algorithm.

4.6.1 Simulation studies on Windkessel-type models

As opposed to a distributed model, Windkessel-type models (such as the two-, three-, and four-element Windkessel models introduced in Section 4.3.1 or even the systemic circulation component of the CP Model in Chapter 2, which comprises Windkessel-type subcomponents) are rather simple low-order lumped-parameter models. Nevertheless, they present themselves as a necessary first step to evaluate the estimation algorithm on simplistic simulated data, where modeling errors and high-order nonlinear dynamics are neglected.

---

[48] Notice that this type of error is different than the frequently considered measurement error due to noise corrupting the sensors. In particular, modeling error refers to the process noise term w_p in (4.5a), whereas measurement (or output) error is related to the term w_m in (4.5b).

For the present simulation studies, we will generate synthetic data from the two-element Windkessel model of Fig. 4.6 using as its forcing function the blood flow waveform predicted by the CP Model in Chapter 2. For example, Fig. 4.18 shows the flow waveform (Q) predicted by the CP Model and herein used as the input function of the two-element Windkessel model. The pressure waveform (P) is the corresponding output signal simulated by the Windkessel model. It is worth mentioning that with such a selection of the model for data generation and the type of forcing function, we want to evaluate the estimation algorithm with respect to the following aspects. 1) The two-element Windkessel model is a simple lumped-parameter model that abides by the underlying limitation of estimation methods according to which they are only able to estimate parameters of lumped models (e.g., ARX model). 2) The selected blood flow profile has a parabolic shape during systole and a zero value during diastole. Even though this decision may seem to work better for our proposed method (Mukkamala et al. [7] assume a pulse train input function), it is worth pointing out the algorithm by Mukkamala et al. [7] is considered a more sophisticated exponential fitting method and thus it primarily relies on the zero flow assumption during diastole.

As mentioned earlier, simulation studies offer the possibility to generate data from specific sets of parameter values allowing us to simulate different pathological conditions. Such sets of parameter values can also be applied sequentially in the data generation process, thereby allowing the evaluation of the estimation algorithm's ability to track changes in the model parameters. Accordingly, the dataset to be used herein for the simulation studies includes changes in both parameters, R_t and C_t, of the two-element Windkessel model such that we induce changes in the system's time constant (the quantity we want to estimate). Fig. 4.19 then shows the main pressure features—namely, pulse (PP, red dots in upper plot) and mean ($\bar{P}$, blue dots in upper plot) pressures calculated in a beat-by-beat fashion—over the entire

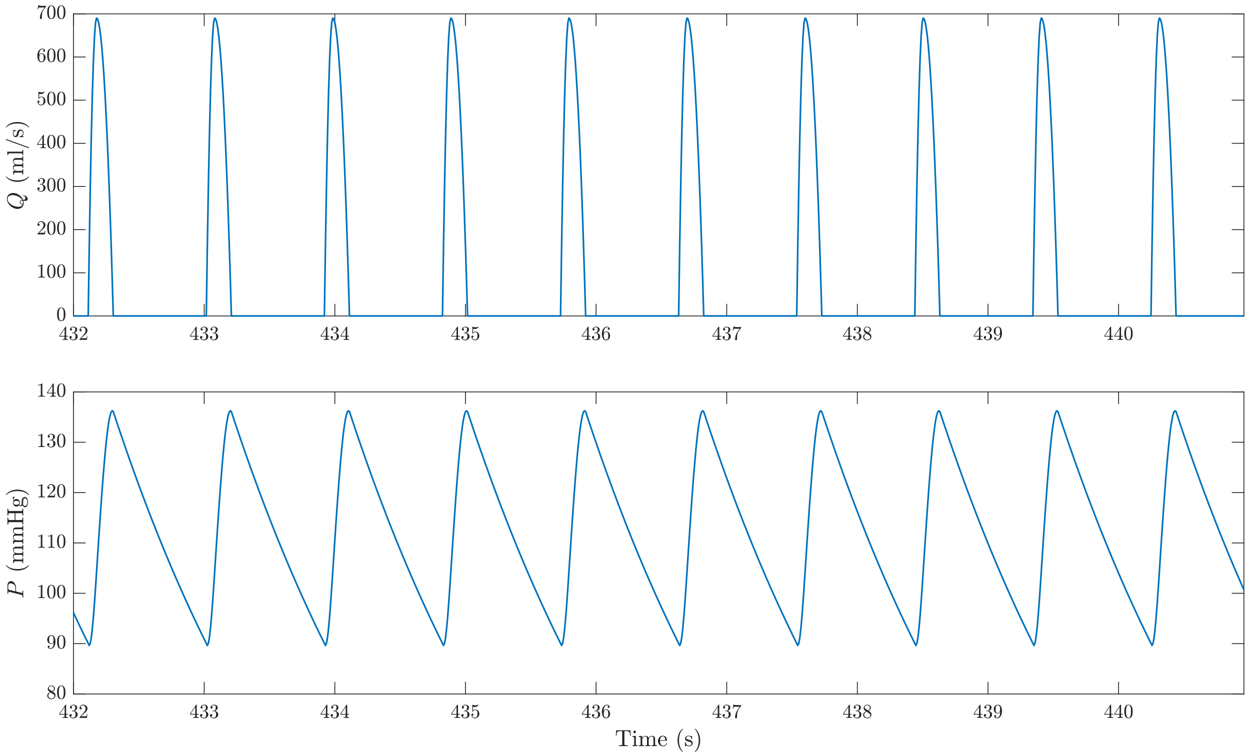

Fig. 4.18. Sample flow (Q, *top* plot) and pressure (P, *bottom* plot) waveforms generated by the two-element Windkessel model. Q is used as input to the model and P is the corresponding simulated output.

simulated dataset of length equal to about 8100 s (or 135 min)[49]. Fig. 4.19 also illustrates the induced changes in R_t and C_t values along with the corresponding time constant (τ). The nominal parameter set at the beginning of the dataset (i.e., $R_t = 1.15$ mmHg·s/ml and $C_t = 1.50$ ml/mmHg; hence, $\tau = 1.725$ s) was selected based on the values reported by Segers et al. [136] for normotensive subjects. Subsequently, we cycle through increases and decreases (each by 50% with respect to the nominal value), first in the compliance (see red line in middle plot of Fig. 4.19) and then in the resistance (see blue line in middle plot of Fig. 4.19). As expected, a change in compliance induces a similar-in-direction change in pulse pressure. The same behavior is observed between changes in resistance and in mean pressure.

---

[49] We omit to present the actual pressure and flow waveforms in Fig. 4.19 due to the minimal visual information that is provided over such a long dataset.

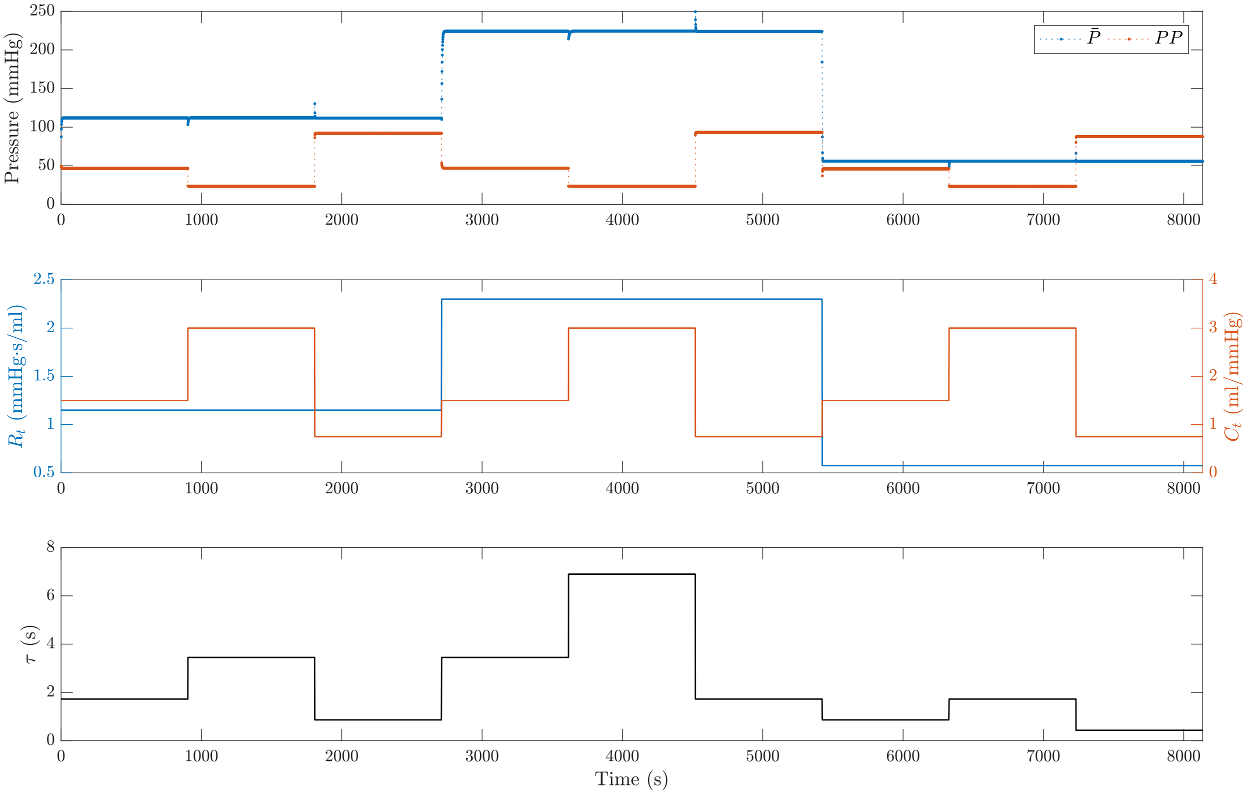

Fig. 4.19. Pressure features and model parameters of the dataset used for the simulation studies on a two-element Windkessel model. $\bar{P}$ and PP (*upper* plot), beat-by-beat mean and pulse pressures, respectively; R_t and C_t (*middle* plot), peripheral resistance and total arterial compliance of the two-element Windkessel model, respectively; τ (*lower* plot), time constant (equal to $R_t\,C_t$).

Deterministic case

We first evaluate the proposed estimation algorithm under noise-free (deterministic) conditions, i.e., with no additive noise in the model-generated pressure waveform which is the single input to the estimation routine. Fig. 4.20 compares the time constant estimated from the proposed algorithm ($\hat{\tau}_{prop}$, blue crosshairs) with its true value (τ_{true}, black line) and the one estimated from the method by Mukkamala et al. [7] ($\hat{\tau}_{muk}$, red stars). Notice that the sporadic nature of the estimates is attributed to the fact that the two methods do not operate in a beat-by-beat fashion. Instead, as explained in Section 4.5.2, they analyze an interval of data that spans multiple heart beats. For the present simulation studies, we follow the convention in [7] and select the interval to be of length equal to 6 minutes. The estimation results in Fig. 4.20 clearly illustrate that both methods are able to perfectly estimate the time constant, apart from the intervals that include the transition points. This latter observation is expected since the transition intervals include data segments generated under different model parameters[50].

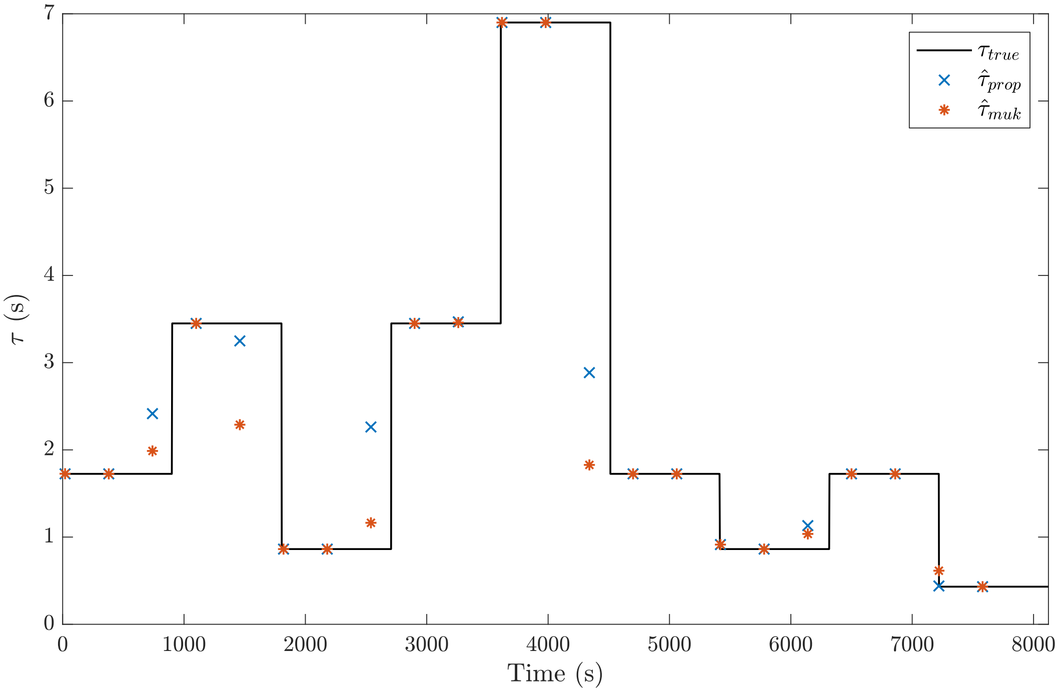

Fig. 4.20. Comparison of the estimated time constant values from *noise-free* data simulated by the two-element Windkessel model. τ_{true}, true time constant value; $\hat{\tau}_{prop}$, estimated time constant from the proposed algorithm; $\hat{\tau}_{muk}$, estimated time constant from the algorithm by Mukkamala et al. [7].

Fig. 4.21 shows a sample segment of three cardiac cycles for comparison of the optimal piecewise quadratic function (Q_{prop}, red dashed line in right plot) found by the proposed algorithm with the true flow (Q, blue line in right plot), which was used as forcing function to generate the data. In addition, the noise-free model-simulated pressure waveform (P, left plot) is also depicted in Fig. 4.21. It is important to note that the depicted flow waveforms have been normalized with respect to their maximum value[51]. Nevertheless, the shape of the optimal Q_{prop} shows excellent agreement with that of the true flow profile, indicating that the algorithm has determined the correct set of onset, peak, and return time instances.

---

[50] Notice also that the change in parameter values is instantaneous and quite significant, thereby creating an additional challenge to the estimation.

[51] As described in Section 4.5.2, the amplitude of the flow profile, although unknown, does not affect the estimation of the time constant.

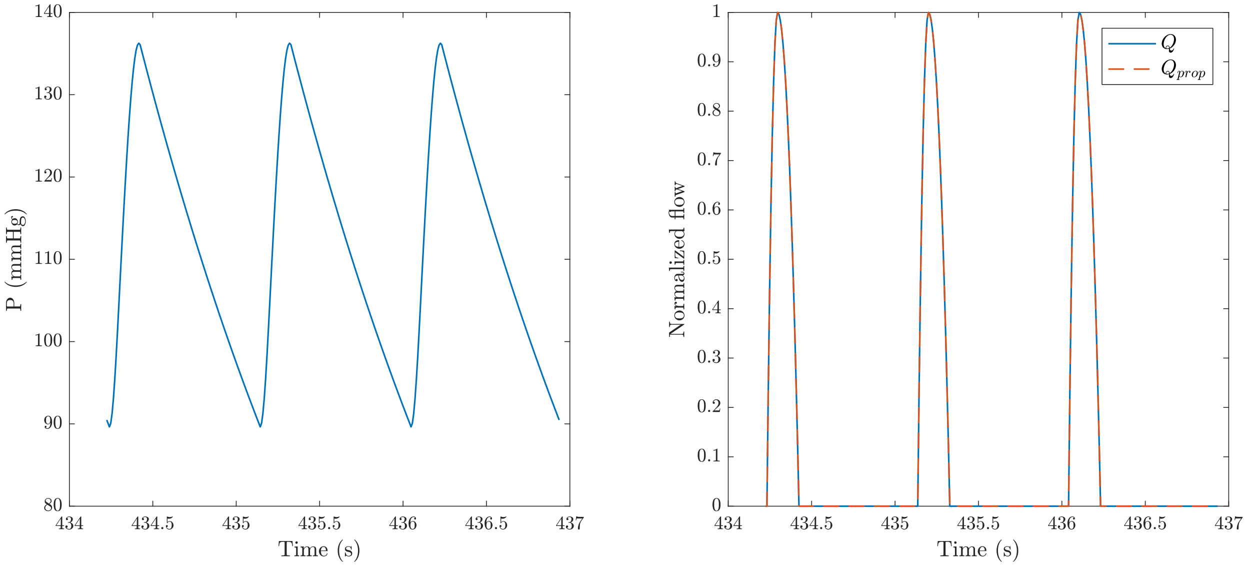

Fig. 4.21. A sample segment of three cardiac cycles showing the *noise-free* pressure waveform (P, *left* plot), the true flow signal (Q, *blue* line in *right* plot), and the optimal piecewise quadratic function (Q_{prop}, *red* dashed line in *right* plot) found by the proposed estimation algorithm. Notice that the flow waveforms are normalized with respect to their maximum values.

Stochastic case

Subsequently, we evaluate the performance of the algorithm under noisy (stochastic) conditions, where the model-simulated pressure waveform is corrupted by gaussian distributed white noise with zero mean and standard deviation equal to 0.1, 0.2, and 0.5 mmHg. Such noise levels are typically observed in experimentally measured arterial blood pressure signals. Similar to the noise-free case, For each of the three noise levels, Fig. 4.22 then shows the values of time constant as estimated from our proposed method ($\hat{\tau}_{prop}$, blue crosshairs) and from Mukkamala et al. [7] ($\hat{\tau}_{muk}$, red stars) and compares them with their true value (τ_{true}, black line). Accordingly, Fig. 4.23 displays the optimal piecewise quadratic function (Q_{prop}, red dashed line in right plot) found by the proposed method.

It is evident from Fig. 4.22 that, as per our earlier analysis, the algorithm by Mukkamala et al. [7] is quite robust to noise when the zero diastolic flow assumption is met, like in the present simulation data. Intuitively thinking, exponential fitting on the pressure diastolic decay via a least squares method is optimal when pressure is corrupted by zero-mean white gaussian noise, as done herein. Since the algorithm by Mukkamala et al. [7] is considered an improved exponential pressure fitting technique that uses a least squares method to estimate an nth-order ARX model, it is thus expected to have such a good accuracy of the time constant estimates even when used on noisy data.

On the other hand, our proposed algorithm is slightly more susceptible to estimation errors when measurement noise corrupts the pressure signal. This issue is exemplified in the case of 0.5 mmHg noise standard deviation and especially when pulse pressure attains its lowest value, equal to about 22 mmHg (see, for example, in Fig. 4.22c around 1000 and 4000 s, and before 7000 s time marks). Such a pulse pressure value is, however, abnormally low since a resting pulse pressure in healthy adults is about 30–40 mmHg, with a value below 25 mmHg indicating congestive heart failure. In addition, we notice that for the same low pulse pressure value, a high mean pressure yields worse estimation results. For instance, the proposed estimation algorithm returns abnormally high time constant values (truncated in Fig. 4.22c) for the simulated data around the 4000 s time mark that show a very high mean pressure (about 220 mmHg) with the lowest pulse pressure value. Even the estimates from the method by Mukkamala et al. [7] illustrate a lower accuracy as compared with those in the rest of the dataset. However, it is worth mentioning that even severe hypertensive patients do not reach such high values of arterial pressures [147]. Based on these two observations, we can hence conjecture that the algorithmic performance may degrade in extreme pathological conditions—although the cases shown here can be reasonably conveyed as unrealistic.

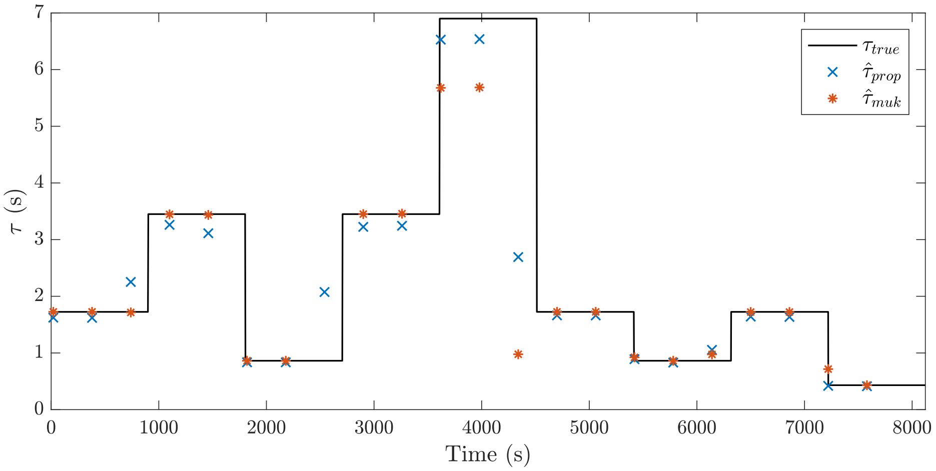

(a) Results on simulated data with 0.1 mmHg noise standard deviation.

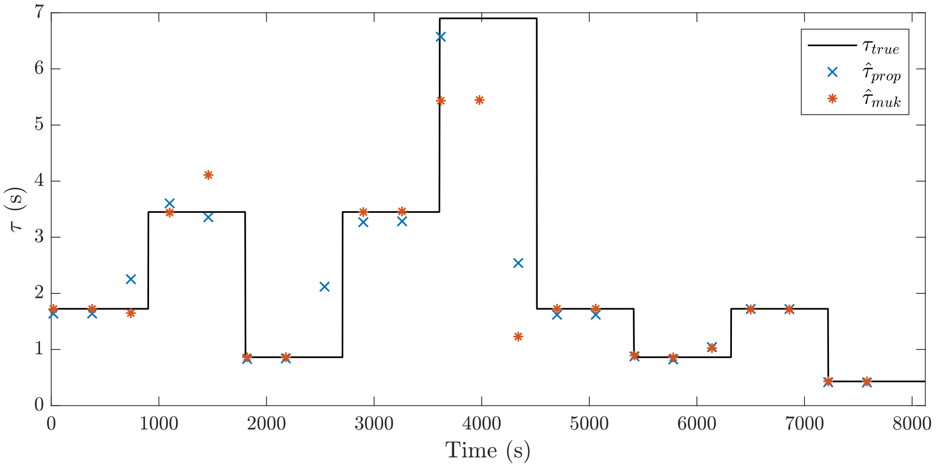

(b) Results on simulated data with 0.2 mmHg noise standard deviation.

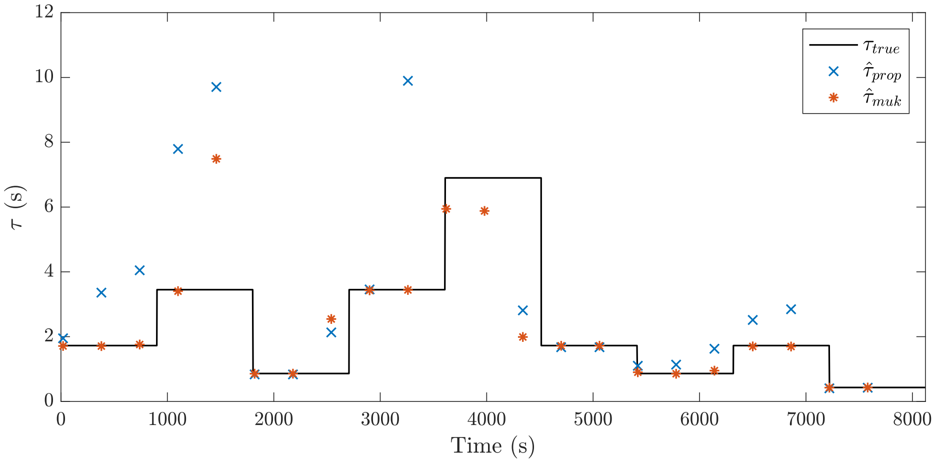

(c) Results on simulated data with 0.5 mmHg noise standard deviation.

Fig. 4.22. Comparison of the estimated time constant values from simulated pressure data corrupted by different levels of gaussian distributed white *noise*. Missing entries have abnormally high values. See Fig. 4.20 legend for explanation of symbols.

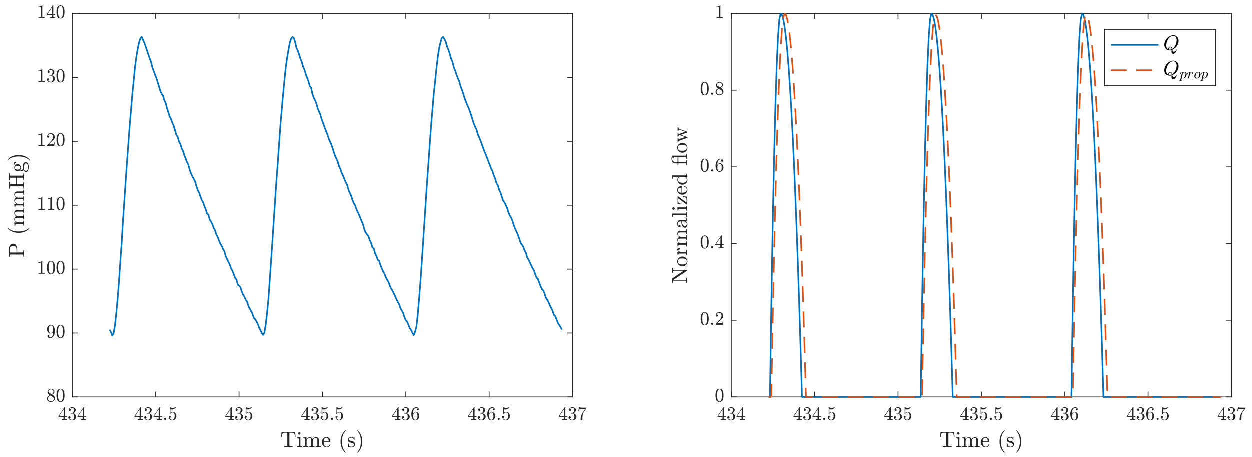

(a) Results on simulated data with 0.1 mmHg noise standard deviation.

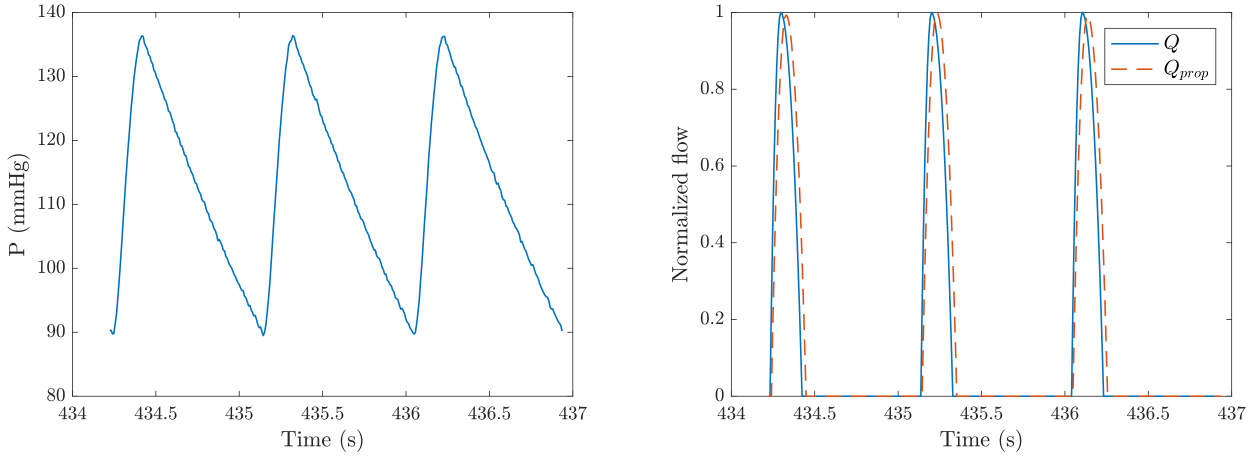

(b) Results on simulated data with 0.2 mmHg noise standard deviation.

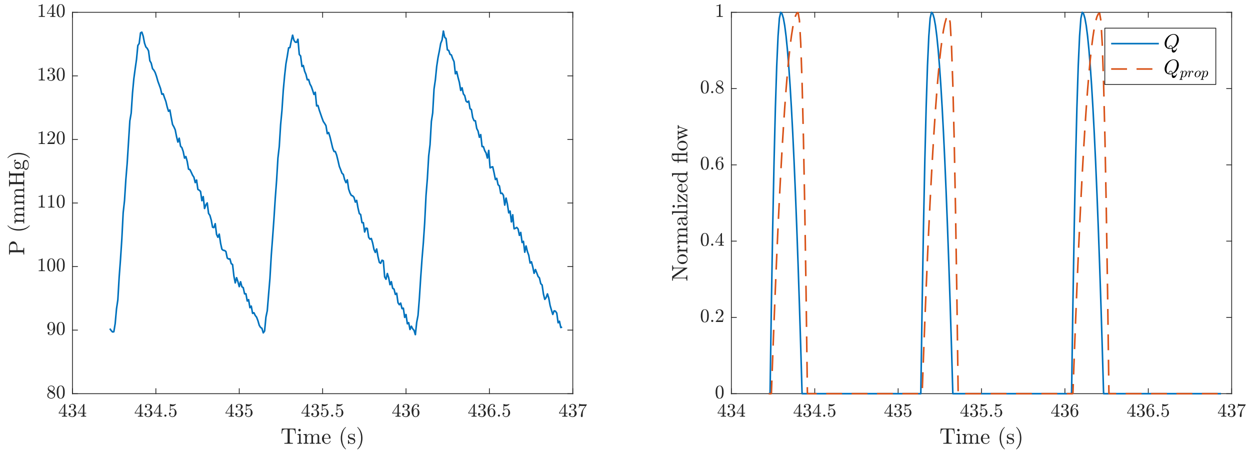

(c) Results on simulated data with 0.5 mmHg noise standard deviation.

Fig. 4.23. A sample segment of three cardiac cycles showing the optimal piecewise quadratic function (Q_{prop}, *right* plot) found by the proposed estimation algorithm on simulated pressure data corrupted by different levels of gaussian distributed white *noise*. See Fig. 4.21 legend for explanation of symbols.

4.6.2 Simulation studies on a distributed systemic arterial model

As explained thoroughly at the beginning of the current section, simulation studies on data generated by a distributed model is of particular importance for algorithmic evaluation due to the realistic dynamics that such data can portray. To this end, we will use the distributed model that we developed based on the work by Stergiopulos et al. [6] and introduced in Section 4.3.2. In contrast, though, to the simulation studies on a Windkessel model (Section 4.6.1), we will herein only focus on changes in peripheral resistance. As contemplated by multiple investigators [7, 133, 134, 148, 149, 150], the arterial compliance can be approximated as constant over a wide pressure range and it is hence expected to exhibit minimal changes during a patient's hospitalization period.

It is important to note that a distributed-parameter model, like the one by Stergiopulos et al. [6], requires a set of boundary conditions to be cast, both at the first and terminal nodes of the model (i.e., proximal and distal ends of the arterial tree, respectively). Anatomically, the first node of the model is part of the aortic root segment, while the terminal nodes represent the systemic circulation's peripheral vessels. It thus reasonable to prescribe the aortic blood flow (as dictated by the heart's pumping action) as the proximal boundary condition, whereas the impedance at the distal end of each terminal arterial segment ought to characterize the dynamics of the peripheral vessels and microcirculation. As such, Stergiopulos et al. [6] proposed the use of three-element Windkessel models (see Fig. 4.7a) as the terminal impedance of the distributed model's terminal segments, thereby representing both resistive and compliant effects of the vessels beyond the termination points (i.e., microcirculation). Consequently, in the present study, we will simulate changes in peripheral resistance by increasing or decreasing the respective resistance, R_t, of all terminal three-element Windkessel models. In particular, we induce changes in R_t with steps of 25% of their nominal values, first by increasing them to 125%, 150%, and 175%, and finally lowering them to 125% of their initial values (each step change in R_t was maintained over a duration of 10 minutes). That is, if $R_{t,nom}$ represents a nominal peripheral resistance value at the beginning of the study, the actual R_t value over the course of this case simulation study will be: $R_t = [1.25, 1.5, 1.75, 1.25] \cdot R_{t,nom}$. For example, Fig. 4.24 shows how such changes in R_t affect the ascending aortic pressure waveform (P_{asc}), in terms of mean ($\bar{P}$) and pulse (PP) pressure values. Even though we only considered changes in the resistive properties of the terminal impedances—changes in $\bar{P}$ are thus expected—, we notice that pulse pressure of P_{asc} is also influenced. This is a consequence of the varying levels of wave reflections, whose magnitude is known to be affected by the terminal boundary conditions (i.e., peripheral vessels in the arterial tree). Notice that ascending aortic blood flow (Q_{ac}) is unaffected because it is the model's forcing function (proximal boundary condition) and thus imposed by us—we herein assume a constant cardiac activity.

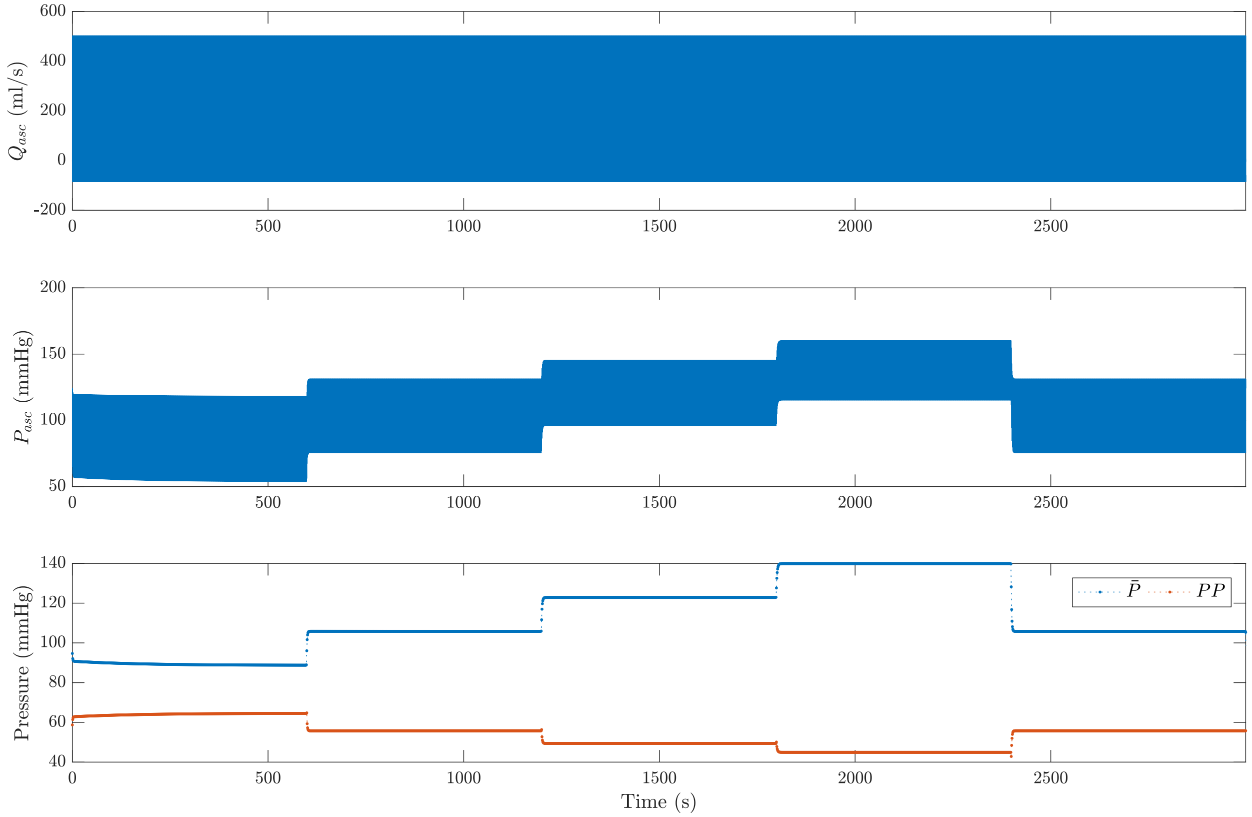

Fig. 4.24. Ascending aortic flow (Q_{asc}, *upper* plot) and pressure (P_{asc}, *middle* plot) waveforms simulated from the distributed-parameter model by Stergiopulos et al. [6]. $\bar{P}$ and PP (*lower* plot), beat-by-beat mean and pulse pressures, respectively.

Ascending aorta

We will first evaluate the proposed algorithm on synthetic data from the ascending aortic model segment (see Fig. 4.24). As detailed in Fig. 4.15, the ascending aortic flow is approximately zero during diastole and thus P_{asc} decays exponentially. Such a physiological behavior resembles the dynamics of Windkessel-type models[52], like the two-element Windkessel model used for the simulation studies in Section 4.6.1, thus making the estimation of the system's time constant readily available by fitting the pressure exponential decay during diastole. Having this observation in mind, we will then consider as the system's "true" time constant the value estimated from the exponential diastolic decay of the ascending aortic pressure waveform. For example, Fig. 4.25 shows the exponential fitting function P_f on the diastolic part of P_{asc} during the segment of the simulated data in Fig. 4.24, where parameters are at their nominal levels. The time constant of such a decay is, hence: $\tau = 1/1.288 = 0.78$ s.

Fig. 4.26 compares the estimation results from our proposed estimation algorithm ($\hat{\tau}_{prop}$, *left* column) and the algorithm by Mukkamala et al. [7] ($\hat{\tau}_{muk}$, *right* column). As in Section 4.6.1, we evaluated the algorithmic performance under different levels—in terms of the noise standard deviation (σ)—of additive zero-mean gaussian white noise corrupting the pressure waveform; namely, $\sigma = 0$ for noise-free conditions (deterministic case, *first* row in Fig. 4.26) and $\sigma = 0.1$, 0.2, and 0.5 mmHg for the stochastic case (*second*, *third*, and *fourth* rows in Fig. 4.26 respectively). It is important to point out that, as mention earlier, such type of noise is treated as measurement noise and is not related to disturbances from unmodeled phenomena. However, in the simulation studies analyzed herein, the discrepancy between the model for data generation (i.e., distributed-parameter model) and the model considered in the estimation routine (i.e., lumped-parameter ARX model) gives rise to unmodeled dynamics (i.e., dynamics that cannot be explained by the estimated model). Undoubtedly, such a phenomenon is present when estimation algorithms are applied on experimental data, thus

---

[52] Recall that Windkessel-type models were developed precisely for detailing the load of the arterial tree on the heart as portrayed in the pressure and flow waveforms at the aortic root level.

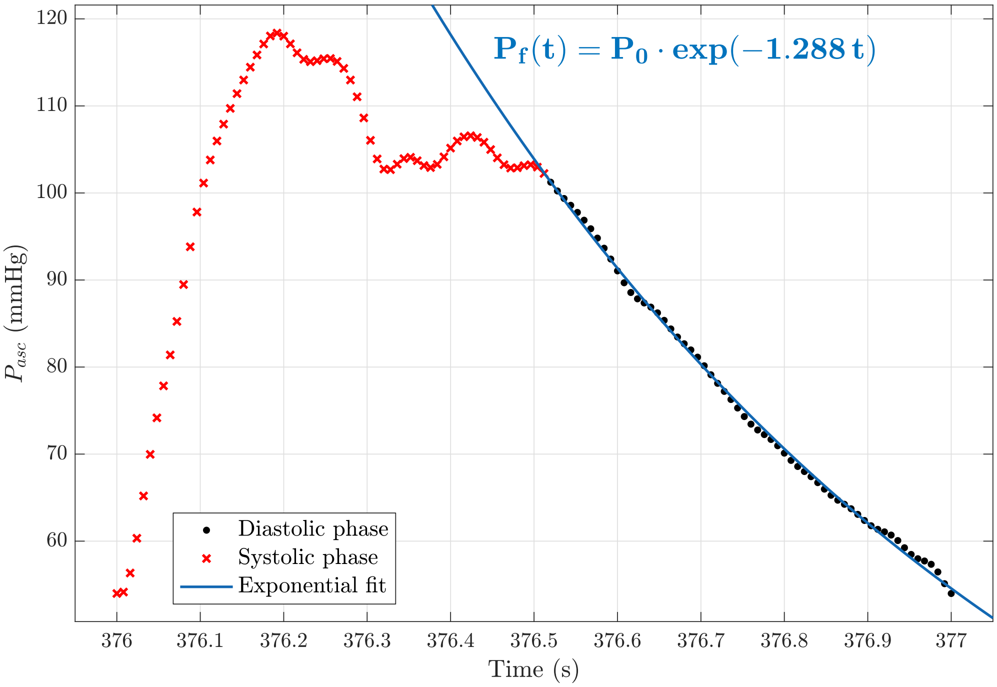

Fig. 4.25. Exponential fitting on the diastolic part of the ascending aortic pressure (P_{asc}) simulated from the distributed-parameter model by Stergiopulos et al. [6]. P_f, exponential fitting function; P_0, initial value of exponential function (not meaningful in this case).

making the simulation studies on distributed model-generated data an essential component if one wants to complete a thorough evaluation of any potential estimation algorithm, prior to using experimental data.

A quick examination of the data in Fig. 4.26 reveals that the estimates from the algorithm by Mukkamala et al. [7] attain values closer to the system's "true" time constants (*black* dots in all plots of Fig. 4.26) as computed by fitting an exponential function on the diastolic pressure decay for every beat in the dataset. In addition, Mukkamala et al. [7] algorithm maintains its robustness to additive white noise, consistent with our conclusion from the simulation studies on lumped-parameter data (see Fig. 4.22). On the other hand, our proposed technique seems to be prone to some errors when additive noise is corrupting the pressure waveform, particularly when the 6-minute segment under investigation contains data generated from different model parameters, i.e., different time constants, and noise has a standard deviation of $\sigma = 0.5$ mmHg (see dashed encircled estimates in bottom left plot of Fig. 4.26). Further, our algorithm's estimates ($\hat{\tau}_{prop}$) obtain lower values as compared with the system's "true" time constants. Notice, however, that despite such an estimation error in absolute terms, the percent change in $\hat{\tau}_{prop}$ for each step change in the model's peripheral resistances is relatively consistent with the change in τ_{true}. Particularly, in the $\sigma = 0.1$ mmHg noisy case (second row in Fig. 4.26), $\hat{\tau}_{prop}$ progressively increases from 0.37 s to 0.43, 0.53, and 0.62 s and finally decreases to 0.43 s. In relative terms, with reference to the initial $\hat{\tau}_{prop}$ of 0.37 s, the percent change in $\hat{\tau}_{prop}$ is: 16%, 43%, 68%, and finally 16% (compare that with the change in τ_{true} of 25%, 50%, 75%, and back to 25%). In contrast, $\hat{\tau}_{muk}$ values respectively change from 0.87 s to 1.3, 1.8, 2.3 s and then back to 1.3 s, which correspond to a relative percent change of 49%, 108%, 164%, and finally 49%. Such an outcome is of particular significance since the final output of algorithms that aim to estimate the circulatory system's time constant is a relative cardiac output value. As mentioned in Section 4.4.2, such algorithms rely on an accurate time constant estimation in order to infer cardiac output within a proportionality constant equal to the inverse of the total arterial compliance (4.16). It is hence apparent that even though $\hat{\tau}_{prop}$ is erroneous in absolute terms with respect to the model's "true" time constant, our proposed estimation scheme seems to be advantageous as compared to the one by Mukkamala et al. [7] because the change in $\hat{\tau}_{prop}$ is relatively consistent with the change in τ_{true}.

Finally, Fig. 4.27 shows the optimal piecewise quadratic function (Q_{prop}, red dashed line in right plot) found by the proposed method for the three noise-corrupted cases, i.e., $\sigma = 0.1$, 0.2, and 0.5 mmHg (from top to bottom). As anticipated from the estimation results on lumped-parameter data, increasing the noise level leads to slightly skewed optimal flow profiles. This outcome is attributed to the fact that the onset, peak, and return indices of the piecewise quadratic function depend on the pressure onset, which is affected by the additive noise. Nevertheless, one can appreciate the relatively good performance of the algorithm to approximate the system's true blood flow Q.

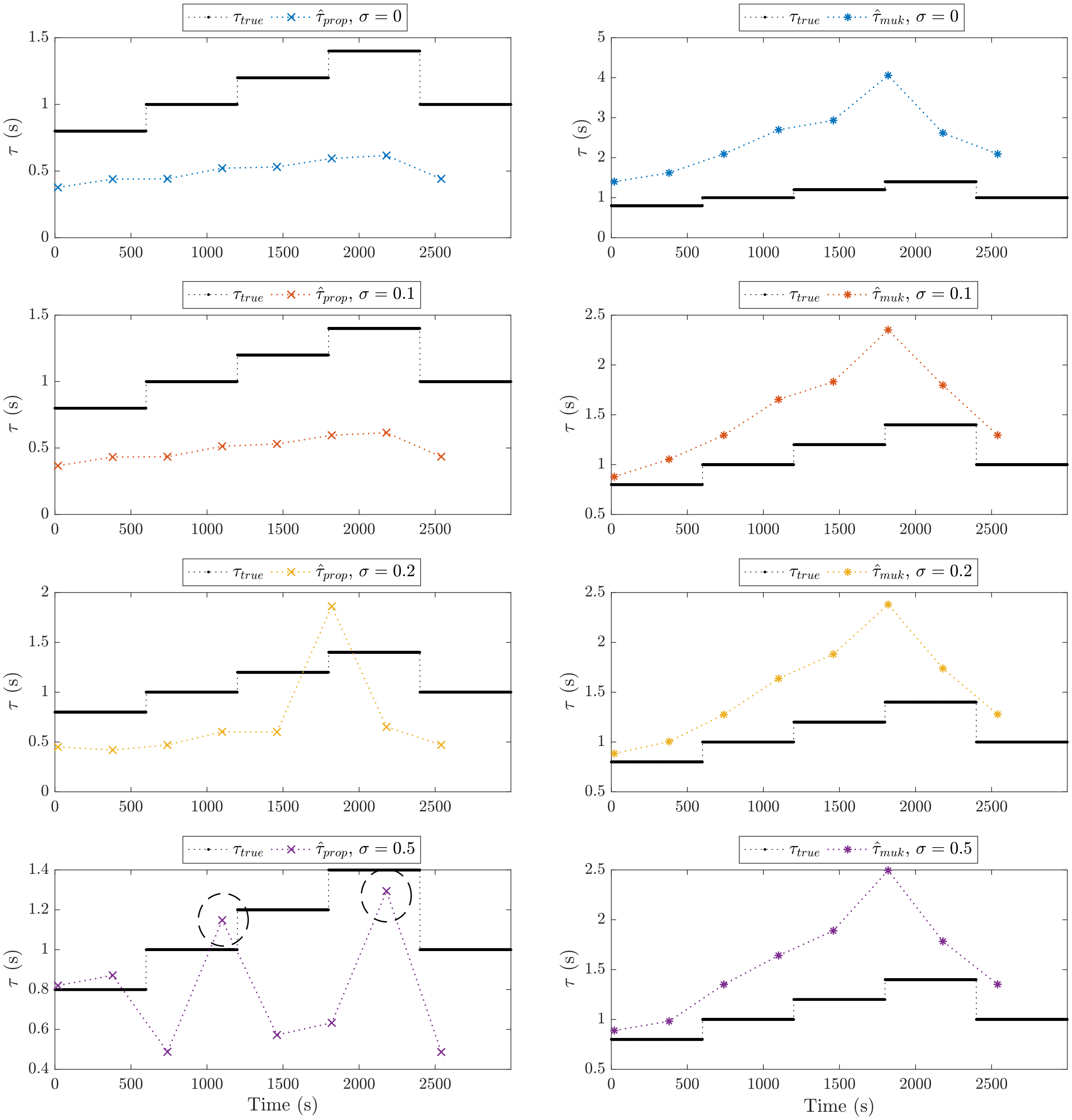

Fig. 4.26. Comparison of the estimated time constant values from *ascending aortic* synthetic data with different levels of additive white noise. τ_{true} (*blank* dots), true time constant value; $\hat{\tau}_{prop}$ (*crosshairs* in left column), estimated time constant from the proposed algorithm; $\hat{\tau}_{muk}$ (*stars* in right column), estimated time constant from the algorithm by Mukkamala et al. [7]; σ, standard deviation (in mmHg) of additive gaussian zero-mean white noise. Dashed encircled estimates indicate segments containing data generated from different model parameters, i.e., different time constants.

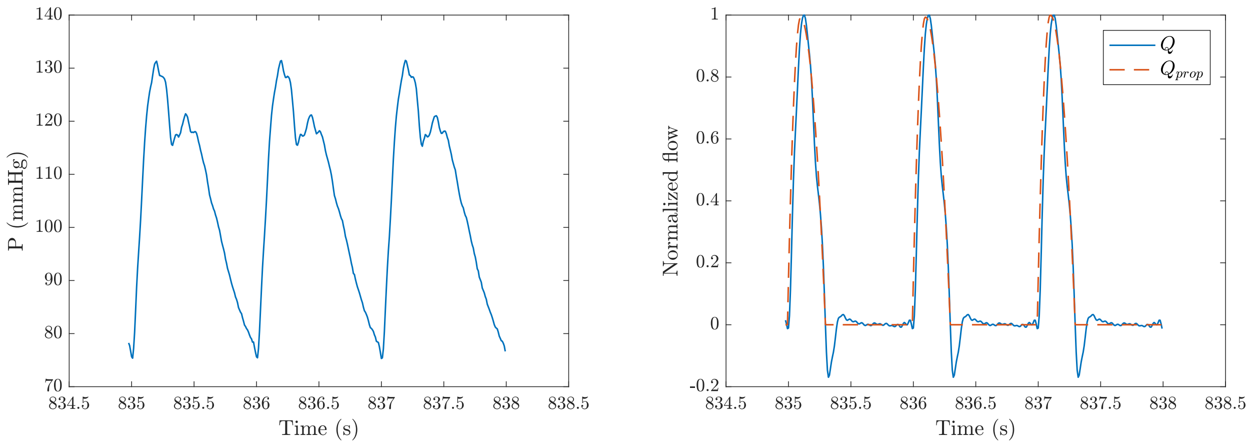

(a) Results on simulated data with 0.1 mmHg noise standard deviation.

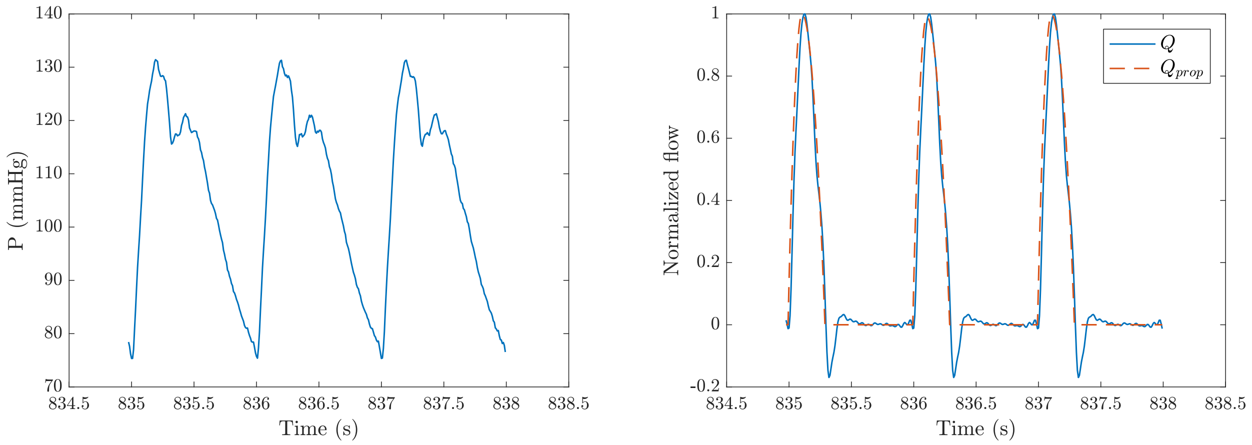

(b) Results on simulated data with 0.2 mmHg noise standard deviation.

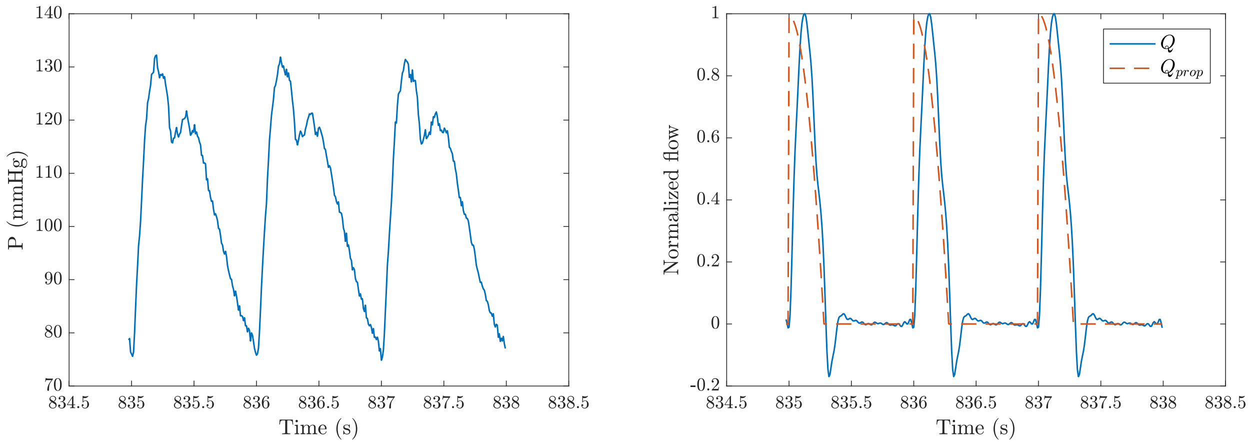

(c) Results on simulated data with 0.5 mmHg noise standard deviation.

Fig. 4.27. A sample segment of three cardiac cycles showing the optimal piecewise quadratic function (Q_{prop}, *right* plot) found by the proposed estimation algorithm on synthetic *ascending aortic* pressure data corrupted by different levels of gaussian distributed white noise. $P = P_{asc}$ (*left* column), ascending aortic pressure; Q (*right* column), normalized ascending aortic flow.

Deep femoral artery

In this section, we investigate the performance of the proposed algorithm on data from the deep femoral model segment. As opposed to the waveforms from the ascending aortic segment, analyzed in the previous section, deep femoral pressure and flow waveforms are affected by wave reflections, similar to those observed in the femoral artery (see, for example, Fig. 4.15). The reason, though, that we focused on data simulated from the deep femoral segment of the distributed model, instead of using the femoral artery waveforms, is twofold: 1) Anatomically, the deep femoral artery originates from the same location as the femoral artery; that is, from the iliac artery. Hence, experimental flow and pressure waveforms from these two arteries are expected to have relatively similar dynamic characteristics. 2) Stergiopulos et al. [6] modeled the deep femoral artery as a terminal segment of the distributed model via a lumped-parameter Windkessel model (distal boundary condition). As a consequence, we know precisely the values of the terminal resistance and compliance that contribute to the time constant to be estimated. It is important to reiterate, however, that even though the deep femoral arterial segment has been modeled via a three-element Windkessel model, its pressure waveform does not exhibit an exponential decay during diastole, as evidently shown in Fig. 4.28 for a segment of the dataset considered in the present study. Fig. 4.29 then summarizes the main features of the deep femoral pressure waveform (i.e., mean and pulse pressures in upper plot of Fig. 4.29) along with the true time constant (lower plot of Fig. 4.29) over the entire dataset. Even though we only induced changes in terminal resistance, it is noticeable that pulse pressure was also affected, a clear indication of the wave reflection phenomena influencing the deep femoral waveforms[53].

Similar to how we analyzed the results on the ascending aortic waveforms, Fig. 4.30 shows the estimated time constant values from our proposed algorithm ($\hat{\tau}_{prop}$) and from the algorithm by Mukkamala et al. [7] ($\hat{\tau}_{muk}$) and compares them with the true value (τ_{true}). Then,

---

[53] Compare such an observation with Fig. 4.19, which depicts the dataset used for the simulated studies on Windkessel model-generated data, and notice that a change in R_t of the Windkessel model did not affect the ensuing pulse pressure (see, for instance, around the 2800 s time mark when R_t is increased).

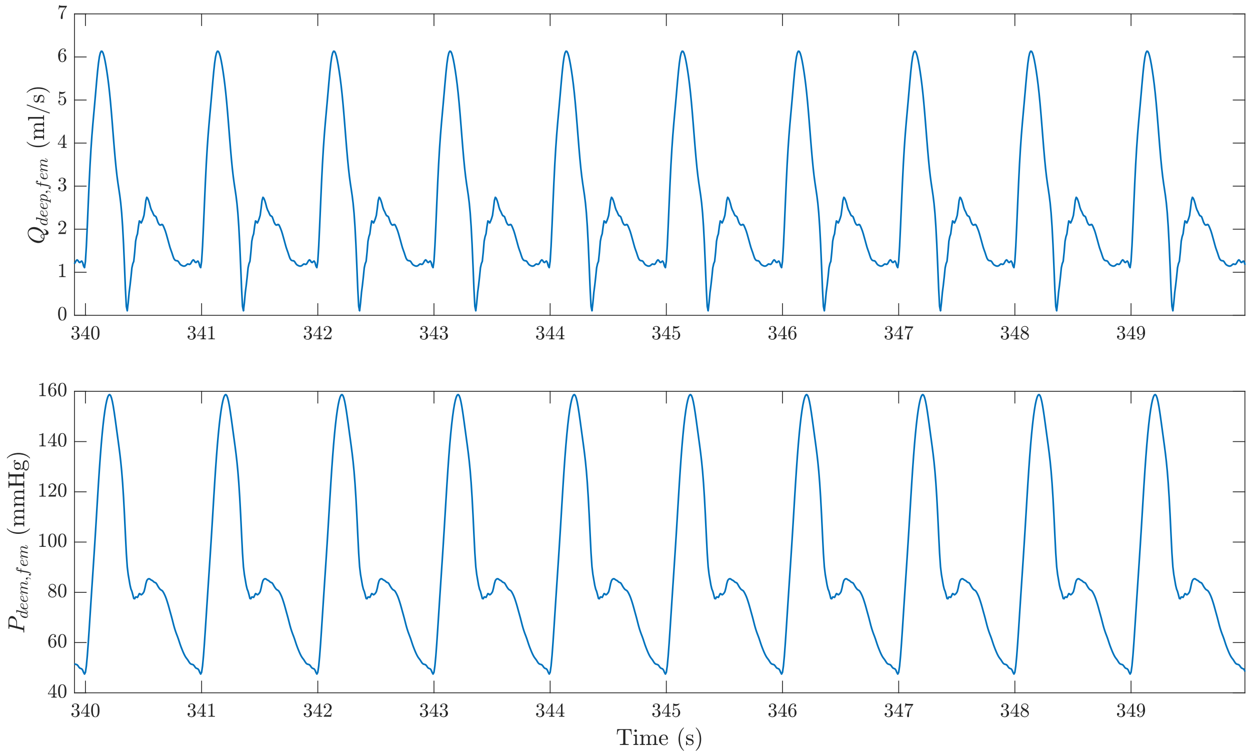

Fig. 4.28. Sample deep femoral flow ($Q_{deep,fem}$, *top* plot) and pressure ($P_{deep,fem}$, *bottom* plot) waveforms generated from the distributed model by Stergiopulos et al. [6].

Fig. 4.31 depicts the optimal piecewise quadratic function (Q_{prop}) found by the proposed estimation scheme. Clearly, our method is able to get more accurate estimation results for all levels of additive white noise, except for some instances, like the two unreasonably high estimates in the noise-free case, that require further investigation. Remarkable is also the fact that despite the marked difference in the underlying model dynamics, the time constant estimates by Mukkamala et al. [7] exhibit a minor change in value as compared with those from the ascending aortic case (e.g., the estimated values on the first data segment are around 1 s for both ascending aortic and deep femoral cases). On the contrary, though, to the observations from Fig. 4.26, the estimates from both algorithms show a relative change with respect to their initial values similar to the change observed in τ_{true} after each step change in terminal resistance (i.e., 25%, 50%, 75%, and back to 25%). For example, in the $\sigma = 0.1$ mmHg noisy case (second row in Fig. 4.30), we get the following results: $\hat{\tau}_{prop} = 0.14$, 0.18, 0.22, 0.25, and 0.18 s (that is, 28%, 57%, 78%, and 28% increase of the initial value)

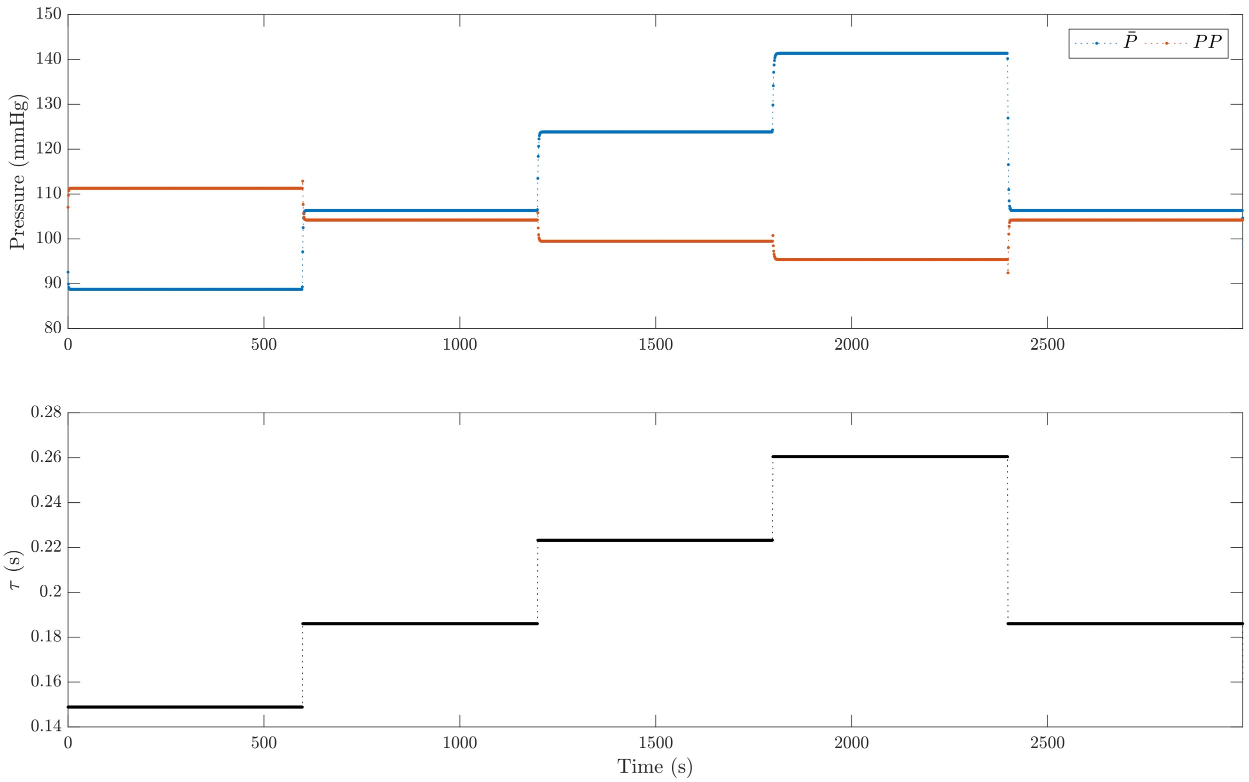

Fig. 4.29. Pressure features ($\bar{P}$ and PP, beat-by-beat mean and pulse pressures, respectively) and time constant ($\tau = R_t\, C_t$, *lower* plot) of the terminal three-element Windkessel model at the terminal node of the *deep femoral* arterial segment of the distributed model by Stergiopulos et al. [6].

and $\hat{\tau}_{muk} = 0.91$, 1.08, 1.31, 1.52, and 1.08 s (that is, 19%, 44%, 67%, and 19% increase of the initial value)

4.7 Conclusion and future work

In this chapter, we first introduced the concepts of system identification and parameter estimation and briefly described how such algorithms can be applied on assessing the structure and parameters of a dynamic system of interest. We then explained the function of the cardiovascular system by considering the heart as a source and the systemic circulation as a dynamic system. Accordingly, we discussed the efforts of the research community to model the complex dynamics of the arterial tree either via lumped-parameter or distributed-parameter modeling techniques. Before delineated our proposed model-based algorithm to estimate the arterial tree's time constant from arterial blood pressure measurements, we deemed necessary to summarize the current clinical methods and the existing model-based techniques for cardiac output assessment and highlight their limitations. Finally, we evaluated the performance of the proposed estimation scheme via simulation studies on data generated from either a lumped or a distributed model of the systemic arterial tree. The validation showed the potential of such an algorithm but also revealed some of its limitations. Particularly, the estimation results from the proposed method seemed to be less robust during abrupt changes in the underlying model parameters (e.g., a change in peripheral resistance). Nevertheless, we believe that such sudden changes in the mechanical properties of the arterial tree are unrealistic and we, instead, expect them to happen gradually over a period of time. It is hence desirable to extend our validation process on datasets with gradual changes in the model parameters and evaluate the algorithm's estimation results under such a more physiological hemodynamic response. In addition, it is also necessary to assess the effect of the duration of the data segment under consideration on the algorithm's performance. We herein assumed a duration of 6 minutes for the data segment that the algorithm will process to infer an estimated time constant. Besides any clinical considerations on the necessity of having shorter segments, it is also worth analyzing the effect of the segment's duration when noise levels are increasing. In terms of noise, precise evaluation of its impact on estimation results needs to be conducted via Monte-Carlo simulations. Finally, adoption of any newly proposed algorithm requires its validation on experimental data collected from human or animal studies. This is undoubtedly the ultimate and most crucial step for assessing the algorithm's clinical applicability and potential impact. It is worth pointing out that the nonlinear nature of the cardiopulmonary system and the occurrence of unforeseeable events may lead to suboptimal experimental conditions, compromising the quality of the collected data. Nevertheless, the necessity of experimental validation is indisputable and it is of high priority in our future work.

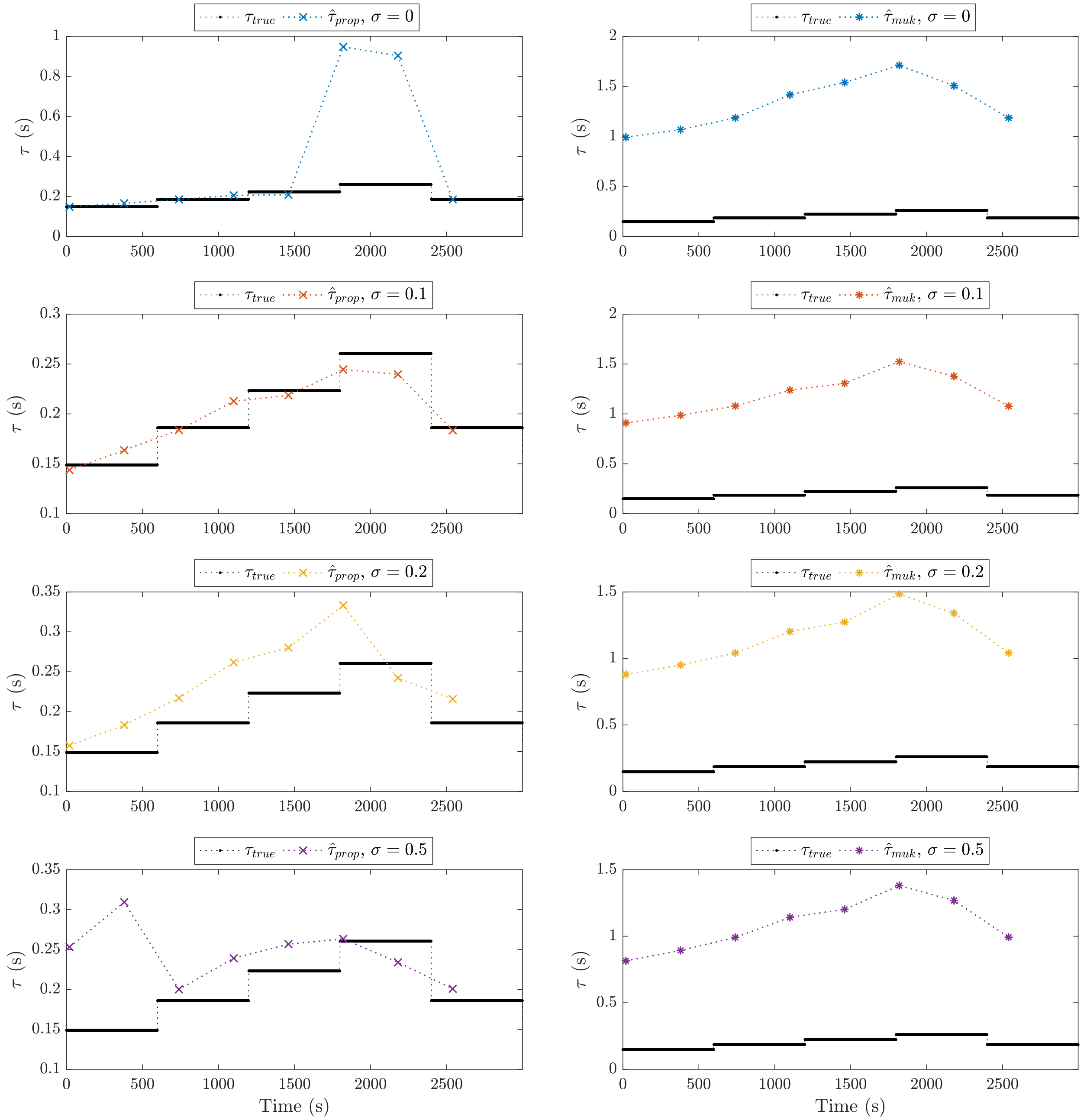

Fig. 4.30. Comparison of the estimated time constant values from *deep femoral* synthetic data with different levels of additive white noise. τ_{true} (*blank* dots), true time constant value; $\hat{\tau}_{prop}$ (*crosshairs* in left column), estimated time constant from the proposed algorithm; $\hat{\tau}_{muk}$ (*stars* in right column), estimated time constant from the algorithm by Mukkamala et al. [7]; σ, standard deviation (in mmHg) of additive gaussian zero-mean white noise.

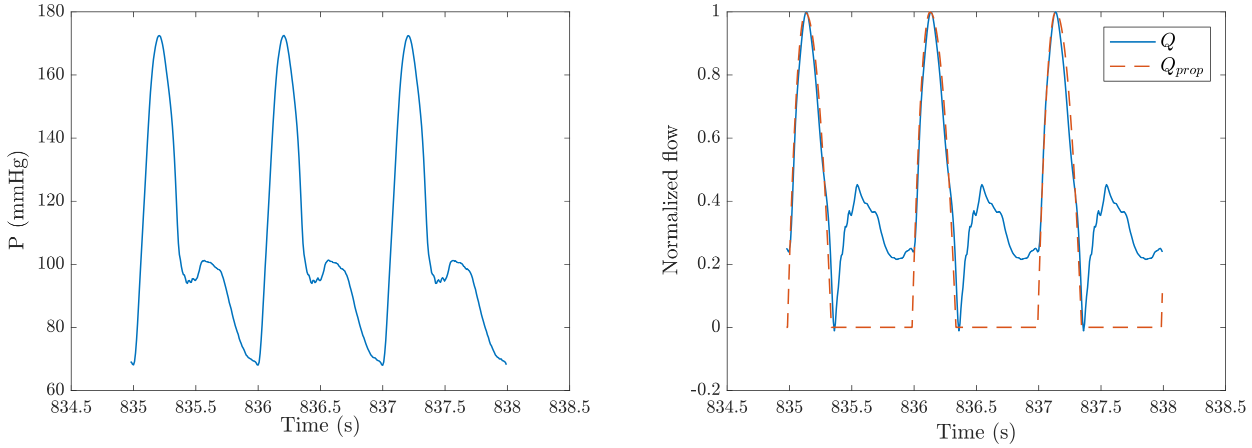

(a) Results on simulated data with 0.1 mmHg noise standard deviation.

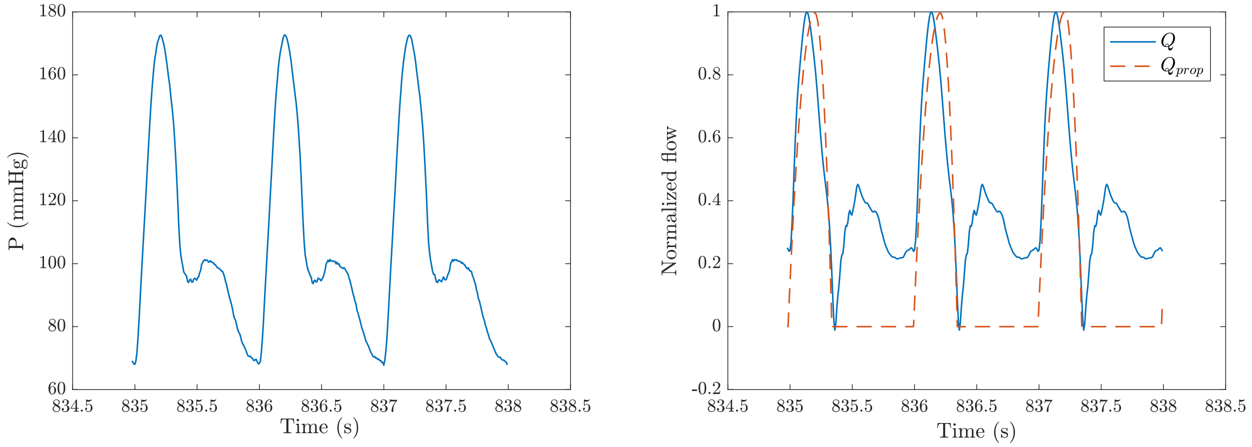

(b) Results on simulated data with 0.2 mmHg noise standard deviation.

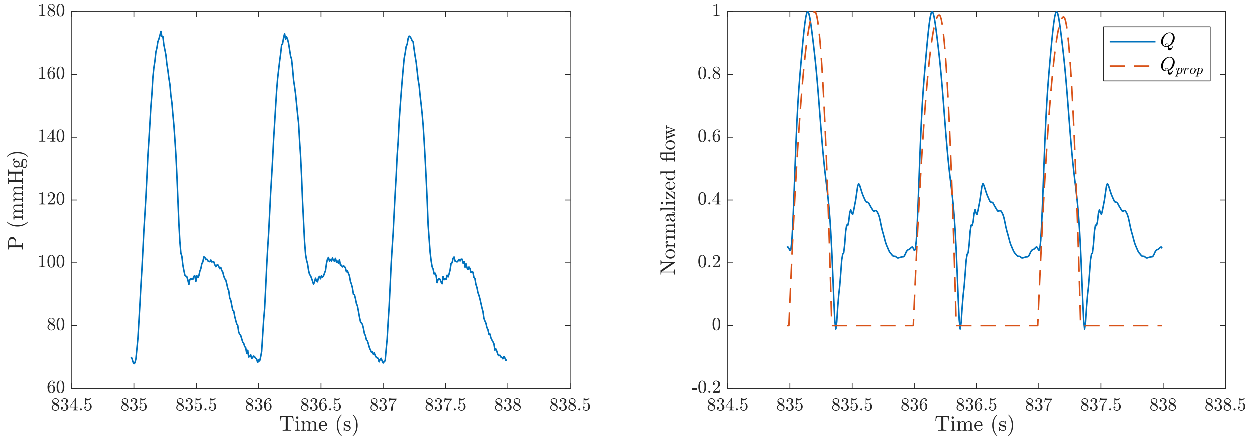

(c) Results on simulated data with 0.5 mmHg noise standard deviation.

Fig. 4.31. A sample segment of three cardiac cycles showing the optimal piecewise quadratic function (Q_{prop}, *right* plot) found by the proposed estimation algorithm on synthetic *deep femoral* pressure data corrupted by different levels of gaussian distributed white noise. $P = P_{deep,fem}$ (*left* column), deep femoral pressure; Q (*right* column), normalized deep femoral flow.

Chapter 5

Summary and future research

In this thesis, we introduced a set of tools that could become the foundation of future developments in patient-tailored critical care medicine. They could also lead to major improvements in the design phase of medical devices such as mechanical ventilators—the specific case presented herein. To this end, we leveraged the power of mathematical models in order to describe and analyze physiological heart-lung interaction phenomena and to propose a model-based parameter estimation technique to infer the function and properties of the cardiovascular system.

In particular, in *Chapter 2*, we proposed a series of improvements on a previously developed cardiopulmonary model to better replicate the heart-lung interaction mechanisms typically observed in mechanical ventilation conditions. As such, we appended the pericardial membrane and interventricular septum and we modified the pulmonary circulation model to account for the compression of the pulmonary peripheral vessels from lung inflation; hence, the modified cardiopulmonary model (CP Model). We compared this newly proposed modified model with the original model in normoxic, hypercapnic, and hypoxic conditions and we validated its response against literature data collected under mechanical ventilation conditions. Finally, we used simulations from the modified model to: 1) analyze heart-lung interaction phenomena during two common clinical interventions, i.e., mechanical ventilation and fluid resuscitation, and 2) provide physiological explanations to a few contradicting experimental results regarding the effects of PEEP on right ventricular function and on the position of the interventricular septum. All these simulation studies provided further credence to the capability of the model in describing the underlying mechanisms of cardiorespiratory interactions.

We then presented the patient emulator system *(Chapter 3)*, a novel device that is based on the proposed modified cardiopulmonary model. The novelty of this system is the fact that it includes a piston-cylinder configuration which allows the software-implemented virtual patient (i.e., the modified model of Chapter 1) to interface with a physical ventilator. Hence, the patient emulator is capable to reliably and correctly reproduce the physiological cardiorespiratory interaction mechanisms that are of profound importance in mechanically ventilated patients. It is then possible for one to use the proposed patient emulator to: 1) quantitatively test and compare mechanical ventilation therapies in a well-controlled experimental environment, and 2) assess therapeutic outcomes for different cardiorespiratory pathologies based on to the virtual patient's health progression—a clear advancement from the current state-of-art devices, such as the mechanical (e.g., bellows-type) systems and the simple model-based breathing simulators. In that regard, we demonstrated a test case scenario where we simulated a realistic pressure support ventilation step protocol and showed good agreement between the emulator-simulated response and averaged experimental data from human subjects.

Lastly, in *Chapter 4*, we first summarized and described the most commonly used devices to assess cardiac output in a clinical setting. We then detailed existing *model-based* algorithms for cardiac output estimation along with their limitations. Accordingly, we proposed a novel *model-based* technique to estimate two clinically important attributes of the cardiovascular system, namely the cardiac output and the arterial tree's time constant. Although an absolute cardiac output estimate is practically not feasible, we described the clinical importance of providing *relative* cardiac output values. Such values are expected to be proportional to the true cardiac output and hence follow any changes in the true value. This is particularly important for hemodynamic unstable patients whose cardiovascular function needs to be monitored when external interventions (e.g., fluid resuscitation) are considered and unforeseen cardiac complications need to be avoided. Finally, we evaluated the performance of the proposed estimation scheme on realistic synthetic data generated from a distributed-parameter model of the systemic circulation.

5.1 Future research

The solutions proposed and developed in this thesis constitute a small step toward improving the current standard of medical care and enhancing the clinical decision-making process. Although we primarily focused on mechanical ventilation therapy, the mathematical frameworks, on which the proposed solutions are based, can be applicable to other areas of therapeutic care, such as fluid management, anesthesia, and drug infusion.

In particular, we envision the combination of forward modeling approaches and of estimation techniques (inverse modeling) into a single platform that would allow the development of patient-tailored therapies across the continuum of care (operating room, ICU, general ward, home). The solutions for critical care management, including decision support tools for clinical interventions (e.g., fluid management and PEEP titration) and optimal closed-loop strategies for bedside medical devices (e.g., mechanical ventilators), are of paramount importance in improving medical practice. As such, potential future research can be summarized via the block diagram presented in Fig. 5.1 and previously introduced in Chapter 1 as part of our vision. Fig. 5.1 schematically shows how the current standard of care (blue and orange boxes) can be enhanced by the solutions presented in this thesis (green boxes). In a typical clinical setting, attending physicians interact with medical devices, such as a mechanical ventilator and an infusion pump, in a purely empirical and heuristic way. That is, before considering any intervention or therapeutic path, medical personnel assess the health status of each patient by primarily relying on their knowledge and personal clinical experience for the interpretation of the physiological data from the bedside clinical instrumentation. However, such an empirical assessment provides an insufficient image of the patient's true condition, primarily due to the following two factors: 1) the low specificity of the data that are typically monitored in the ICU, and 2) the data overload problem. Most of the bedside physiological data offer limited information about the patient's underlying condition, unless some highly invasive interventions (e.g., pulmonary artery catheterization) are considered. For example, hypotension can be easily determined via the ubiquitous blood pressure monitoring. However, as illustrated in Section 2.5, hypotension is a clinical manifestation of more than a single pathology. It can be linked to either a cardiac complication (e.g., low cardiac output), a vascular disease (e.g., sepsis), or blood loss (hypovolemia). Crucially, though, each of these pathological conditions requires a different treatment; volume expansion, for instance, is only beneficial to those patients who are truly in hypovolemic state. It is then evident that by relying only on pressure monitoring, the hypotensive patient's true pathology cannot be effectively determined unless additional, highly invasive, techniques are employed, such as the pulmonary artery catheterization for the measurement of cardiac output. In addition to this difficulty in measuring quantities that are essential for inferring the patient's true condition, physicians have to deal with the problem of data overload, particularly when it comes to multi-bed care units. Every day, attending physicians have to oversee a large number of critical care patients. Furthermore, for each patient, there is a plethora of signals and vital signs being displayed at the bedside monitoring devices. As a result, these two factors add further burden on the clinicians' daily load and may hamper the correct interpretation of the available physiological data during the short time window of the decision-making process. It is also important to note that attaining a more accurate health status assessment is not necessarily correlated with the number of clinical data being collected; it is rather the relevance between the measured variables and the patient's pathology that matters the most. For example, in the hypotension case presented above, collecting additional pressure waveforms (e.g., arterial and venous pressures) will not provide additional information about the cardiovascular status of the patient. On the contrary, it is the monitoring of specific variables, such as the cardiac output, that would ultimately provide a more accurate image of the patient's true condition.

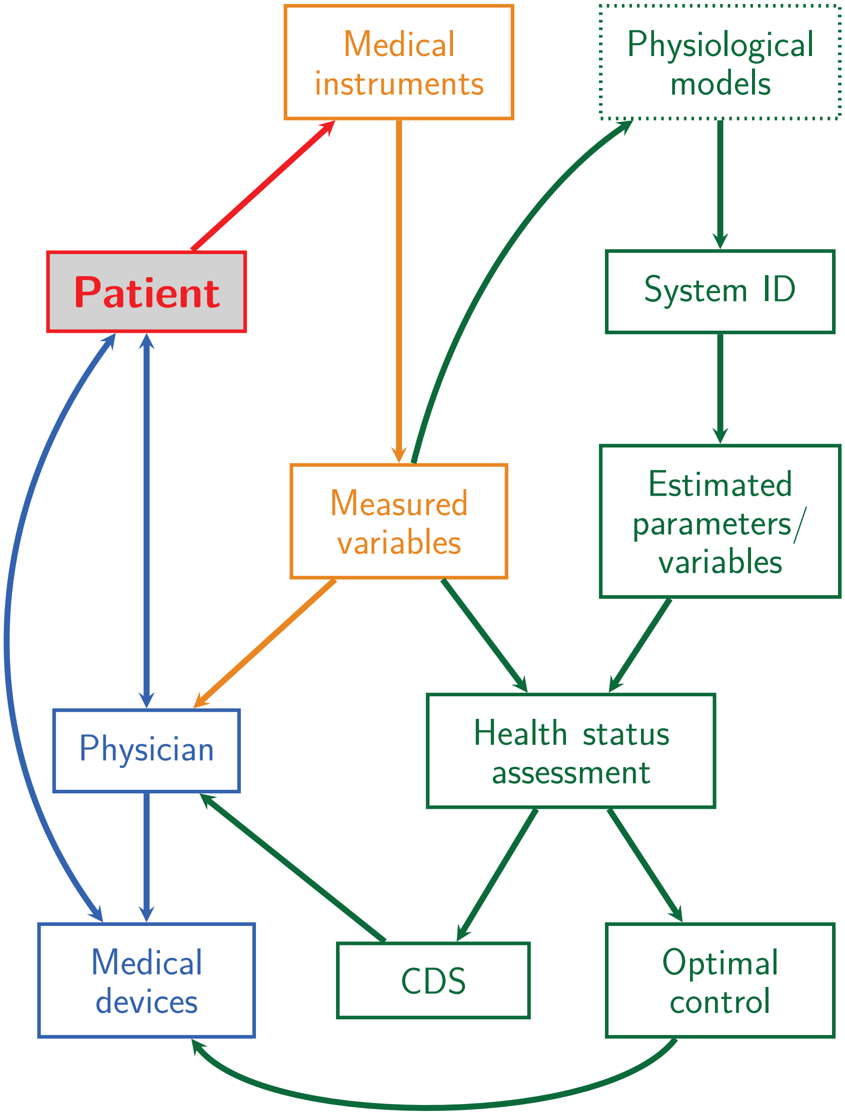
Medical instruments
Physiological models
Patient
System ID
Measured variables
Estimated parameters/ variables
Physician
Health status assessment
Medical devices
CDS
Optimal control

Fig. 5.1. A high-level schematic representation of potential future research based on the work presented in this thesis (*green* boxes). System ID, system identification; CDS, clinical decision support.

One way to mitigate the aforementioned two problems is by enhancing the clinical decision-making process via the development of clinical decision support (CDS) tools. In that regard and as illustrated in Fig. 5.1 (green boxes), forward modeling techniques offer significant benefits. Physiology-based mathematical models, such as the cardiopulmonary model introduced in *Chapter 2*, can provide a holistic understanding of the function of the human body, including the effects of the neural feedback mechanisms and of the mechanical heart-lung interactions. As a result, model-based computer simulations can provide an efficient quantitative tool to analyze cardiopulmonary dynamics. Using such simulations, medical personnel can conduct virtual physiological experiments, investigate different clinical scenarios, and assess the outcomes of specific treatments based on the virtual patient's health progression.

Despite these advantages in performing in-silico physiological experiments, there are certain limitations with our modified CP Model. In particular, such a model is purely deterministic in nature since model parameters are deterministic quantities. In other words, the user (e.g., a clinician) can only select a specific set of parameter values that would, in turn, result in a specific trajectory in the model-simulated variables, such as the pressures and flows in the model's cardiovascular component. Typically, such a set of model parameters would be selected so that it represents average values for a particular patient class of interest, such an ARDS patient. Consequently, the model's dynamic response, as described via the model outputs, would replicate features that are typical to the average patient class data. It is then apparent that a probabilistic framework to simulating the model outputs can offer substantial benefits and improvements to clinical decision support. Describing the model parameters via probability density functions over the parameter space would allow the physicians to utilize the fact that certain values of a parameter are more (or less) likely than others, based on previous studies or knowledge. The model outputs can then be represented as stochastic processes rather than deterministic time-dependent variables. The inherent capability of stochastic processes to be associated with probability density functions will render the possibility to simulate the health progression of the entire patient class instead of just of a single subject. This will practically allow the physicians to promptly examine the effects of a specific treatment for the entire class of interest (even for marginal patient cases within each class) without having to rerun the simulations with different parameter sets from the same class.

Aside from the probabilistic simulation framework, the modified CP Model can be further expanded, with respect to the version presented in Chapter 2, by adding the following components: 1) long-term humoral regulation (e.g., renin-angiotensin-aldosterone system), 2) fluid filtration in the lungs, and 3) a renal component for describing the acid-base and fluid balance in the human body. All these additional model subsystems are expected to improve the model's overall response under certain disease states and clinical interventions. For example, in ARDS patients, the increased permeability of the pulmonary vascular wall allows fluid to seep into the alveolar compartments, thereby affecting lung fluid filtration. On the other hand, regulation of body fluids by the kidneys can be of paramount importance during fluid resuscitation scenarios, when fluids are administered to the patient in an effort to improve their cardiovascular status.

The patient emulator system of *Chapter 3* is as another useful tool for enhancing clinical decision making. Not only does it provide a physical device on which clinicians can examine the effects of different device settings and therapeutic paths, but it can also be used by medical device companies for verification and validation of their new products, such as mechanical ventilators. Thus, upgrading the patient emulator system in terms of hardware components can address certain limitations of the current implementation and enhance its value in testing and developing new medical devices. We envision the following improvements:

1. Gas mixing inside the emulator's piston-cylinder arrangement, according to the model-predicted oxygen and carbon dioxide fractions in expired air, would be a highly desirable upgrade. Currently, the ventilator's gas fraction settings and sensors are not interfaced with the model's parameters and variables; for example, a change in the ventilator's $F_{I_{O_2}}$ setting is not sensed by the model, unless a corresponding change in the respective model parameter is made. In addition, gas mixing will also allow test-

ing of respiratory devices that monitor end-tidal CO_2, another critical and universally used vital sign for ventilated patients.

2. A more sophisticated hardware interface between model and ventilator, i.e., improving or replacing the piston-cylinder arrangement, can also be considered. This is expected to enhance the system's closed-loop response, which currently relies on the piston-cylinder's default hardware controller.

Lastly, the concepts and theoretical frameworks of parameter estimation, or system identification, are at the core of the development of personalized clinical decision support tools and optimal closed-loop strategies, as per Fig. 5.1. The importance of such techniques lies in the fact that they can turn a generalized model into a patient-specific one, which is then able to accurately replicate the dynamic behavior of the patient at hand. For example, continual cardiovascular system identification could enable monitoring of the effects of a specific ventilation or fluid therapy (e.g., change of ventilator settings or administration of fluids) on the particular patient under treatment. As analyzed in *Chapter 4*, our efforts focused on classic (or Fisherian) estimation approaches, in which the parameters to be estimated are assumed deterministic and the only information available to the algorithm is the measurement data from the bedside monitoring devices. Future work can then be extended into probabilistic (or Bayesian) approaches. These assume that a priori information about the unknown parameters is available in the form of probability density functions. Such information is typically generated from population studies and, if appropriately selected, can practically constrain the feasible parameter space and appreciably enhance the estimation accuracy.

Moreover, parameter estimation algorithms can also be applied for different body organs, such as the respiratory (see earlier work by our group [32, 151, 152, 153]) and renal systems. Combining the estimation results from different physiological subsystems (e.g., cardiovascular and respiratory) would allow us to develop feedback control strategies that optimally alter ventilator settings, or fluid administration rates, while taking into consideration the specific patient's particular clinical condition. The optimality of such control strategies is greatly associated with the fact that the selected therapeutic path may have opposite effects on different organs. As shown, for instance, in the simulation studies in *Chapter 2*, PEEP application may improve ventilation and gas exchange, but it may also induce detrimental effects on cardiac performance. We can, hence, envision the use of optimal control strategies that regulate the level of PEEP while monitoring its influence on the particular patient's cardiac function.

Complementary to the aforementioned model-based estimation approaches (whether classic or Bayesian), data mining (or machine learning) methods can also be incorporated into the health status assessment component (see Fig. 5.1). Although not mentioned in this thesis, machine learning offers significant advantages over model-based methods, particularly with respect to disease detection and patient class classification. For example, we can consider running classification algorithms to specify the class of the patient at hand before applying Bayesian estimation which would then utilize the a priori information of the classified patient class. Furthermore, data mining techniques can be developed to take advantage of non-physiologic data, such as the information stored in the patient's electronic medical records (EMR), drug types, and administration rates, as well as different waveform features that can be associated to the patient's health condition.

Bibliography

[1] K. Kyhl, K. A. Ahtarovski, K. Iversen, C. Thomsen, N. Vejlstrup, T. Engstrøm, and P. L. Madsen, "The decrease of cardiac chamber volumes and output during positive-pressure ventilation," *American Journal of Physiology-Heart and Circulatory Physiology*, vol. 305, no. 7, pp. H1004–H1009, 2013.

[2] A. Vieillard-Baron, K. Chergui, R. Augarde, S. Prin, B. Page, A. Beauchet, and F. Jardin, "Cyclic changes in arterial pulse during respiratory support revisited by Doppler echocardiography," *American Journal of Respiratory and Critical Care Medicine*, vol. 168, no. 6 I, pp. 671–676, 2003.

[3] F. Michard and J.-L. Teboul, "Using heart-lung interactions to assess fluid responsiveness during mechanical ventilation," *Critical Care*, vol. 4, pp. 282–289, 2000.

[4] J. F. Dhainaut, J. Y. Devaux, J. F. Monsallier, F. Brunet, D. Villemant, and M. F. Huyghebaert, "Mechanisms of decreased left ventricular preload during continuous positive pressure ventilation in ARDS," *Chest*, vol. 90, no. 1, pp. 74–80, 1986.

[5] W. B. Van de Graaff, K. Gordey, S. E. Dornseif, D. J. Dries, B. S. Kleinman, P. Kumar, and M. Mathru, "Pressure support. Changes in ventilatory pattern and components of the work of breathing," *Chest*, vol. 100, no. 4, pp. 1082–1089, 1991.

[6] N. Stergiopulos, D. F. Young, and T. R. Rogge, "Computer simulation of arterial flow with applications to arterial and aortic stenoses," *Journal of Biomechanics*, vol. 25, no. 12, pp. 1477–1488, 1992.

[7] R. Mukkamala, A. T. Reisner, H. M. Hojman, R. G. Mark, and R. J. Cohen, "Continuous cardiac output monitoring by peripheral blood pressure waveform analysis," *IEEE Transactions on Biomedical Engineering*, vol. 53, no. 3, pp. 459–467, 2006.

[8] R. Schmitz, M. Lantin, and A. White, "Future Needs in Pulmonary and Critical Care Medicine," Abt Associates Inc., Tech. Rep., 1998.

[9] H. Wunsch, D. C. Angus, D. A. Harrison, W. T. Linde-Zwirble, and K. M. Rowan, "Comparison of medical admissions to intensive care units in the United States and United Kingdom," *American Journal of Respiratory and Critical Care Medicine*, vol. 183, no. 12, pp. 1666–1673, 2011.

[10] H. Wunsch, J. Wagner, M. Herlim, D. H. Chong, A. A. Kramer, and S. D. Halpern, "ICU occupancy and mechanical ventilator use in the United States," *Critical Care Medicine*, vol. 41, no. 12, pp. 2712–2719, 2013.

[11] F. Lellouche, P. A. Bouchard, S. Simard, E. L'Her, and M. Wysocki, "Evaluation of fully automated ventilation: a randomized controlled study in post-cardiac surgery patients," *Intensive Care Medicine*, vol. 39, no. 3, pp. 463–471, 2013.

[12] M. L. Barrett, M. W. Smith, A. Elixhauser, L. S. Honigman, and J. M. Pines, "Utilization of Intensive Care Services, 2011," Healthcare Cost and Utilization Project, Tech. Rep., 2014.

[13] N. A. Halpern and S. M. Pastores, "Critical care medicine in the United States 2000 –2005: An analysis of bed numbers, occupancy rates, payer mix, and costs," *Critical Care Medicine*, vol. 38, no. 1, pp. 65–71, 2010.

[14] M. R. Baldwin, H. Wunsch, P. A. Reyfman, W. R. Narain, C. D. Blinderman, N. W. Schluger, M. C. Reid, M. S. Maurer, N. Goldstein, D. J. Lederer, and P. Bach, "High burden of palliative needs among older intensive care unit survivors transferred to post-Acute care facilities," *Annals of the American Thoracic Society*, vol. 10, no. 5, pp. 458–465, 2013.

[15] E. Damuth, J. A. Mitchell, J. L. Bartock, B. W. Roberts, and S. Trzeciak, "Long-term survival of critically ill patients treated with prolonged mechanical ventilation: a systematic review and meta-analysis," *The Lancet Respiratory Medicine*, vol. 3, no. 7, pp. 544–553, 2015.

[16] A. Aitawa, "Mechanical Ventilators Market 2013-2020," iHealthcareAnalyst, Inc., Tech. Rep., 2016.

[17] R. M. Kacmarek, "The mechanical ventilator: past, present, and future," *Respiratory Care*, vol. 56, no. 8, pp. 1170–1180, 2011.

[18] A. Albanese, L. Cheng, M. Ursino, and N. W. Chbat, "An integrated mathematical model of the human cardiopulmonary system: model development," *American Journal of Physiology-Heart and Circulatory Physiology*, vol. 310, no. 7, pp. H899–H921, 2016.

[19] L. Cheng, A. Albanese, M. Ursino, and N. W. Chbat, "An integrated mathematical model of the human cardiopulmonary system: model validation under hypercapnia and hypoxia." *American Journal of Physiology-Heart and Circulatory Physiology*, vol. 310, no. 7, pp. H922–H937, 2016.

[20] M. McGregor, "Pulsus paradoxus," *New England Journal of Medicine*, vol. 301, no. 9, pp. 480–482, 1979.

[21] S. M. Scharf, R. Brown, N. Saunders, and L. H. Green, "Hemodynamic effects of

positive-pressure inflation," *Journal of Applied Physiology*, vol. 49, no. 1, pp. 124–131, 1980.

[22] B. C. Morgan, W. E. Martin, T. F. Hornbein, E. W. Crawford, and W. G. Guntheroth, "Hemodynamic effects of intermittent positive pressure Respiration," *Anesthesiology*, vol. 27, no. 5, pp. 584–590, 1966.

[23] A. Roos, L. J. Thomas, E. L. Nagel, and D. C. Prommas, "Pulmonary vascular resistance as determined by lung inflation and vascular pressures," *Journal of Applied Physiology*, vol. 16, no. 1, pp. 77–84, 1961.

[24] F. Michard, "Changes in arterial pressure during mechanical ventilation," *Anesthesiology*, vol. 103, no. 2, pp. 419–428, 2005.

[25] S. W. Patterson, H. Piper, and E. H. Starling, "The regulation of the heart beat," *The Journal of Physiology*, vol. 48, no. 6, pp. 465–513, 1914.

[26] NIH NHLBI, "NIH NHLBI ARDS clinical network mechanical ventilation protocol summary," 2008.

[27] The ARDS Definition Task Force, "Acute respiratory distress syndrome the berlin definition," *JAMA*, vol. 307, no. 23, pp. 2526–2533, 2012.

[28] J. C. Richard, S. M. Maggiore, B. Jonson, J. Mancebo, F. Lemaire, and L. Brochard, "Influence of tidal volume on alveolar recruitment: Respective role of PEEP and a recruitment maneuver," *American Journal of Respiratory and Critical Care Medicine*, vol. 163, no. 7, pp. 1609–1613, 2001.

[29] L. Cheng, O. Ivanova, H.-H. Fan, and M. C. Khoo, "An integrative model of respiratory and cardiovascular control in sleep-disordered breathing," *Respiratory Physiology & Neurobiology*, vol. 174, no. 1, pp. 4–28, 2010.

[30] K. Lu, J. W. Clark, F. H. Ghorbel, D. L. Ware, and A. Bidani, "A human cardiopulmonary system model applied to the analysis of the Valsalva maneuver," *American Journal of Physiology-Heart and Circulatory Physiology*, vol. 281, no. 6, pp. H2661–H2679, 2001.

[31] M. R. Pinsky, "Hemodynamic effects of ventilation and ventilatory maneuvers," in *Respiratory-Circulatory Interactions in Health and Disease*, S. M. Scharf, M. R. Pinsky, and S. Magder, Eds. New York, NY: Marcel Dekker, 2001, ch. 8, pp. 183–218.

[32] F. Vicario, A. Albanese, N. Karamolegkos, D. Wang, A. Seiver, and N. Chbat, "Noninvasive estimation of respiratory mechanics in spontaneously breathing ventilated patients: a constrained optimization approach," *IEEE Transactions on Biomedical Engineering*, vol. 63, no. 4, pp. 775–787, 2016.

[33] M. Ursino, "Interaction between carotid baroregulation and the pulsating heart:

a mathematical model," *American Journal of Physiology-Heart and Circulatory Physiology*, vol. 275, no. 5, pp. H1733–H1747, 1998.

[34] D. C. Chung, S. C. Niranjan, J. W. Clark, A. Bidani, W. E. Johnston, J. B. Zwischenberger, and D. L. Traber, "A dynamic model of ventricular interaction and pericardial influence," *The American Journal of Physiology*, vol. 272, no. 6 Pt 2, pp. H2942–H2962, 1997.

[35] M. Takata and J. L. Robotham, "Mechanical heart-pericardium-lung interactions," in *Respiratory-Circulatory Interactions in Health and Disease*, S. M. Scharf, M. R. Pinsky, and S. Magder, Eds. New York, NY: Marcel Dekker, 2001, ch. 10, pp. 257–278.

[36] C. Luo, D. L. Ware, J. B. Zwischenberger, and J. W. Clark, "Using a human cardiopulmonary model to study and predict normal and diseased ventricular mechanics, septal interaction, and atrio-ventricular blood flow patterns," *Cardiovascular Engineering*, vol. 7, no. 1, pp. 17–31, 2007.

[37] M. Ursino and E. Magosso, "Acute cardiovascular response to isocapnic hypoxia. I. A mathematical model," *American Journal of Physiology-Heart and Circulatory Physiology*, vol. 279, no. 1, pp. H149–H165, 2000.

[38] J. A. Goldstein, J. S. Tweddell, B. Barzilai, Y. Yagi, A. S. Jaffe, and J. L. Cox, "Hemodynamic effects of atrial interaction," *Coronary Artery Disease*, vol. 4, no. 6, 1993.

[39] E. L. Boulpaep, "The heart as a pump," in *Medical Physiology*, 2nd ed., W. F. Boron and E. L. Boulpaep, Eds. Philadelphia: Saunders Elsevier, 2009, ch. 22, pp. 529–553.

[40] A. A. Bove and W. P. Santamore, "Ventricular interdependence," *Progress in Cardiovascular Diseases*, vol. 23, no. 5, pp. 365–388, 1981.

[41] S. Permutt, B. Bromberger-Barnea, and H. Bane, "Alveolar pressure, pulmonary venous pressure, and the vascular waterfall," *Respiration*, vol. 19, no. 4, pp. 239–260, 1962.

[42] J. L. Whittenberger, M. McGregor, E. Berglund, and H. G. Borst, "Influence of state of inflation of the lung on pulmonary vascular resistance," *Journal of Applied Physiology*, vol. 15, no. 5, pp. 878–82, 1960.

[43] A. Maceira, S. Prasad, M. Khan, and D. Pennell, "Normalized left ventricular systolic and diastolic function by steady state free precession cardiovascular magnetic resonance," *Journal of Cardiovascular Magnetic Resonance*, vol. 8, no. 3, pp. 417–426, 2006.

[44] Edwards Lifesciences LLC, "Normal Hemodynamic Parameters and Laboratory," 2009.

[45] A. M. Maceira, S. K. Prasad, M. Khan, and D. J. Pennell, “Reference right ventricular systolic and diastolic function normalized to age, gender and body surface area from steady-state free precession cardiovascular magnetic resonance,” *European Heart Journal*, vol. 27, no. 23, pp. 2879–2888, 2006.

[46] W. W. Chen, H. Gao, X. Y. Luo, and N. A. Hill, “Study of cardiovascular function using a coupled left ventricle and systemic circulation model,” *Journal of Biomechanics*, vol. 49, no. 12, pp. 2445–2454, 2016.

[47] J. Ruskin, R. J. Bache, J. C. Rembert, and J. C. Greenfield, “Pressure-flow studies in man: effect of respiration on left ventricular stroke volume,” *Circulation*, vol. 48, no. 1, pp. 79–85, 1973.

[48] R. L. Hester, A. J. Brown, L. Husband, R. Iliescu, D. Pruett, R. Summers, and T. G. Coleman, “HumMod: a modeling environment for the simulation of integrative human physiology,” *Frontiers in Physiology*, vol. 2, p. 12, 2011.

[49] R. L. Summers, K. R. Ward, T. Witten, V. A. Convertino, K. L. Ryan, T. G. Coleman, and R. L. Hester, “Validation of a computational platform for the analysis of the physiologic mechanisms of a human experimental model of hemorrhage,” *Resuscitation*, vol. 80, no. 12, pp. 1405–1410, 2009.

[50] P. M. Suter, H. B. Fairley, and M. D. Isenberg, “Optimum end-expiratory airway pressure in patients with acute pulmonary failure,” *New England Journal of Medicine*, vol. 292, no. 6, pp. 284–289, 1975.

[51] J. F. Dhainaut, B. Schlemmer, J. F. Monsallier, V. Fourestie, and A. Carli, “Behavior of the right ventricle following PEEP in patients with mild and severe ARDS,” *Am Rev Respir Dis*, vol. 129, p. A99, 1984.

[52] M. R. Pinsky, “Heart-lung interactions,” *Current Opinion in Critical Care*, vol. 13, pp. 528–531, 2007.

[53] F. Jardin, J. C. Farcot, P. Guéret, J. F. Prost, Y. Ozier, and J. P. Bourdarias, “Echocardiographic evaluation of ventricles during continuous positive airway pressure breathing,” *Journal of Applied Physiology*, vol. 56, no. 3, pp. 619–627, 1984.

[54] G. Huemer, N. Kolve, A. Kurz, and M. Zimpfer, “Influence of positive end-expiratory pressure on right and left ventricular performance assessed by doppler two-dimensional echocardiography,” *Chest*, vol. 106, no. 1, pp. 67–73, 1994.

[55] F. Jardin, J.-C. Farcot, L. Boisante, N. Curien, A. Margairaz, and J.-P. Bourdarias, “Influence of positive end-expiratory pressure on left ventricular performance,” *New England Journal of Medicine*, vol. 304, no. 7, pp. 387–392, 1981.

[56] R. A. Perschau, C. J. Pepine, W. W. Nichols, and J. B. Downs, “Instantaneous blood

flow responses to positive end-expiratory pressure with spontaneous ventilation," *Circulation*, vol. 59, no. 6, pp. 1312–1318, 1979.

[57] L. Gattinoni, P. Pelosi, P. M. Suter, A. Pedoto, P. Vercesi, and A. Lissoni, "Acute respiratory distress syndrome caused by pulmonary and extrapulmonary disease different syndromes?" *American Journal of Respiratory and Critical Care Medicine*, vol. 158, no. 1, pp. 3–11, 1998.

[58] F. Jardin, B. Genevray, D. Brun-Ney, and J.-P. Bourdarias, "Influence of lung and chest wall compliances on transmission of airway pressure to the pleural space in critically ill patients," *Chest*, vol. 88, no. 5, pp. 653–658, 1985.

[59] A. Vieillard-Baron and F. Jardin, "Why protect the right ventricle in patients with acute respiratory distress syndrome?" *Current Opinion in Critical Care*, vol. 9, no. 1, pp. 15–21, 2003.

[60] J. R. Mitchell, W. A. Whitelaw, R. Sas, E. R. Smith, J. V. Tyberg, and I. Belenkie, "RV filling modulates LV function by direct ventricular interaction during mechanical ventilation," *American Journal of Physiology-Heart and Circulatory Physiology*, vol. 289, no. 2, pp. H549–H557, 2005.

[61] A. R. Vest and F. J. Heupler, "Afterload," in *Cardiovascular Hemodynamics: An Introductory Guide*, S. Anwaruddin, J. M. Martin, J. C. Stephens, and A. T. Askari, Eds. Totowa, NJ: Humana Press, 2013, ch. 2, pp. 29–51.

[62] F. Michard, D. Chemla, C. Richard, M. Wysocki, M. R. Pinsky, Y. Lecarpentier, and J.-L. Teboul, "Clinical use of respiratory changes in arterial pulse pressure to monitor the hemodynamic effects of PEEP," *American Journal of Respiratory and Critical Care Medicine*, vol. 159, pp. 935–939, 1999.

[63] P. E. Marik, R. Cavallazzi, T. Vasu, and A. Hirani, "Dynamic changes in arterial waveform derived variables and fluid responsiveness in mechanically ventilated patients: A systematic review of the literature," *Critical Care Medicine*, vol. 37, no. 9, pp. 2642–2647, 2009.

[64] F. Michard, S. Boussat, D. Chemla, N. Anguel, A. Mercat, Y. Lecarpentier, C. Richard, M. R. Pinsky, and J. L. Teboul, "Relation between respiratory changes in arterial pulse pressure and fluid responsiveness in septic patients with acute circulatory failure," *American Journal of Respiratory and Critical Care Medicine*, vol. 162, no. 1, pp. 134–138, 2000.

[65] J. C. Kubitz, T. Annecke, G. I. Kemming, S. Forkl, N. Kronas, A. E. Goetz, and D. A. Reuter, "The influence of positive end-expiratory pressure on stroke volume variation and central blood volume during open and closed chest conditions," *European Journal of Cardio-thoracic Surgery*, vol. 30, no. 1, pp. 90–95, 2006.

[66] S. a. Glantz, G. a. Misbach, W. Y. Moores, D. G. Mathey, J. Lekven, D. F. Stowe, W. W. Parmley, and J. V. Tyberg, “The pericardium substantially affects the left ventricular diastolic pressure-volume relationship in the dog,” *Circulation Research*, vol. 42, no. 3, pp. 433–441, 1978.

[67] O. M. Hess, V. Bhargava, J. Ross, and R. Shabetai, “The role of the pericardium in interactions between the cardiac chambers,” *American Heart Journal*, vol. 106, no. 6, pp. 1377–1383, 1983.

[68] V. M. Ranieri, N. T. Eissa, C. Corbeil, M. Chassé, J. Braidy, N. Matar, and J. Milic-Emili, “Effects of positive end-expiratory pressure on alveolar recruitment and gas exchange in patients with the adult respiratory distress syndrome,” *American Review of Respiratory Disease*, vol. 144, no. 3, pp. 544–551, 1991.

[69] G. Mols, H.-J. Priebe, and J. Guttmann, “Alveolar recruitment in acute lung injury,” *British Journal of Anaesthesia*, vol. 96, no. 96, pp. 156–66, 2006.

[70] D. Burkhoff, M. W. Kronenberg, D. T. Yue, W. L. Maughan, W. C. Hunter, and K. Sagawa, “Quantitative comparison of canine right and left ventricular isovolumic pressure waves,” *American Journal of Physiology-Heart and Circulatory Physiology*, vol. 253, no. 2, pp. H475–H479, 1987.

[71] G. F. Ellinger, F. Gillick, B. R. Boone, and W. Chamberlain, “Electrokymographic studies of asynchronism of ejection from the ventricles: Normal subjects and patients with bundle branch block,” *American Heart Journal*, vol. 35, no. 6, pp. 971–979, 1948.

[72] A. A. Luisada and F. G. Fleischner, “Temporal relation between contraction of right and left sides of the normal human heart,” *Experimental Biology and Medicine*, vol. 66, no. 2, pp. 436–440, 1947.

[73] H. E. Fessler, R. G. Brower, R. A. Wise, and S. Permutt, “Effects of positive end-expiratory pressure on the canine venous return curve,” *American Review of Respiratory Disease*, vol. 146, no. 1, pp. 4–10, 1992.

[74] M. Takata and J. L. Robotham, “Effects of inspiratory diaphragmatic descent on inferior vena caval venous return,” *Journal of Applied Physiology*, vol. 72, no. 2, pp. 597–607, 1992.

[75] M. R. Pinsky, “Cardiovascular issues in respiratory care,” *Chest*, vol. 128, no. 5, pp. 592S–597S, 2005.

[76] J. a. Madden, C. a. Dawson, and D. R. Harder, “Hypoxia-induced activation in small isolated pulmonary arteries from the cat,” *Journal of applied physiology (Bethesda, Md. : 1985)*, vol. 59, no. 1, pp. 113–118, 1985.

[77] R. L. Chatburn, “Classification of ventilator modes: update and proposal for imple-

mentation," *Respiratory care*, vol. 52, no. 3, pp. 301–323, 2007.

[78] R. Sternberg and H. Sahebjami, "Hemodynamic and oxygen transport characteristics of common ventilatory modes," *Chest*, vol. 105, no. 6, pp. 1798–1803, 1994.

[79] N. Ambrosino and A. Rossi, "Proportional assist ventilation (PAV): a significant advance or a futile struggle between logic and practice?" *Thorax*, vol. 57, no. 3, pp. 272–276, 2002.

[80] *Medical electrical equipment - Part 2-12: Particular requirements for basic safety and essential performance of critical care ventilators*, International standard ISO 80601-2-12, 2011.

[81] D. W. Hill and V. Moore, "The action of adiabatic effects on the compliance of an artificial thorax," *British Journal of Anaesthesia*, vol. 37, no. 1, pp. 19–22, 1965.

[82] Y. Yamada, M. Shigeta, K. Suwa, and K. Hanaoka, "Respiratory muscle pressure analysis in pressure-support ventilation," *Journal of Applied Physiology*, vol. 77, no. 5, pp. 2237–2243, 1994.

[83] M. J. Banner, R. R. Kirby, and A. J. Layon, "Decreasing imposed work of the breathing apparatus to zero using pressure-support ventilation," *Critical Care Medicine*, vol. 21, no. 9, pp. 1333–1338, 1993.

[84] J. Breuer, "Self-steering of respiration through the nervus vagus," in *Ciba Foundation Symposium on Breathing: Hering-Breuer Centenary Symposium*, R. Porter, Ed. London: Churchill, J. & A., 1868, pp. 365–394.

[85] E. Hering, "Self-steering of respiration through the nervus vagus," in *Ciba Foundation Symposium on Breathing: Hering-Breuer Centenary Symposium*, R. Porter, Ed. London: Churchill, J. & A., 1868, pp. 359–364.

[86] J. H. T. Bates, *Lung Mechanics: An Inverse Modeling Approach*, 1st ed. Cambridge, UK: Cambridge University Press, 2009.

[87] R. E. Klabunde, *Cardiovascular Physiology Concepts*, 2nd ed. Athens, Ohio: Lippincott Williams & Wilkins, 2012.

[88] G. F. Mitchell, H. Parise, E. J. Benjamin, M. G. Larson, M. J. Keyes, J. A. Vita, R. S. Vasan, and D. Levy, "Changes in arterial stiffness and wave reflection with advancing age in healthy men and women: the Framingham Heart Study," *Hypertension*, vol. 43, no. 6, pp. 1239–1245, 2004.

[89] Z. Sun, "Aging, arterial stiffness, and hypertension," *Hypertension*, vol. 65, no. 2, pp. 252–256, 2015.

[90] B. Tavernier, O. Makhotine, G. Lebuffe, J. Dupont, and P. Scherpereel, "Systolic pres-

sure variation as a guide to fluid therapy in patients with sepsis-induced hypotension," *Anesthesiology*, vol. 89, no. 6, pp. 1313–1321, 1998.

[91] A. I. Moens, *Die Pulscurve.* Leiden, E. J. Brill, 1878.

[92] D. J. Korteweg, "Ueber die fortpflanzungsgeschwindigkeit des schalles in elastischen röhren," *Annalen der Physik*, vol. 241, no. 12, pp. 525–542, 1878.

[93] T. Kenner, "Arterial blood pressure and its measurement," *Basic Research in Cardiology*, vol. 83, no. 2, pp. 107–121, 1988.

[94] O. Frank, "Die grundform des arteriellen pulses," *Zeitschrift für Biologie*, vol. 37, pp. 483–526, 1899.

[95] N. Westerhof, F. Bosman, C. J. De Vries, and A. Noordergraaf, "Analog studies of the human systemic arterial tree," *Journal of Biomechanics*, vol. 2, no. 2, pp. 121–143, 1969.

[96] N. Stergiopulos, B. E. Westerhof, and N. Westerhof, "Total arterial inertance as the fourth element of the windkessel model," *American Journal of Physiology-Heart and Circulatory Physiology*, vol. 276, no. 1, pp. H81–88, 1999.

[97] N. Westerhof, J. W. Lankhaar, and B. E. Westerhof, "The arterial windkessel," *Medical and Biological Engineering and Computing*, vol. 47, pp. 131–141, 2009.

[98] N. Westerhof, G. Elzinga, and P. Sipkema, "An artificial arterial system for pumping hearts," *Journal of Applied Physiology*, vol. 31, no. 5, pp. 776–781, 1971.

[99] O. S. Randall, M. D. Esler, R. V. Calfee, G. F. Bulloch, A. S. Maisel, and B. Culp, "Arterial compliance in hypertension," *Australian and New Zealand Journal of Medicine*, vol. 6, pp. 49–59, 1976.

[100] P. Sipkema, N. Westerhof, and O. S. Randall, "The arterial system characterised in the time domain," *Cardiovascular Research*, vol. 14, no. 5, pp. 270–279, 1980.

[101] N. Stergiopulos, J. J. Meister, and N. Westerhof, "Simple and accurate way for estimating total and segmental arterial compliance: The pulse pressure method," *Annals of Biomedical Engineering*, vol. 22, no. 4, pp. 392–397, 1994.

[102] M. W. Mohiuddin, G. A. Laine, and C. M. Quick, "Increase in pulse wavelength causes the systemic arterial tree to degenerate into a classical windkessel," *American Journal of Physiology-Heart and Circulatory Physiology*, vol. 293, no. 2, pp. H1164–H1171, 2007.

[103] A. Guyton, "Systems analysis of arterial pressure regulation and hypertension," *Annals of Biomedical Engineering*, vol. 1, pp. 254–281, 1972.

[104] C. H. Liu, S. C. Niranjan, J. W. Clark, K. Y. San, J. B. Zwischenberger, and A. Bidani, “Airway mechanics, gas exchange, and blood flow in a nonlinear model of the normal human lung,” *Journal of applied physiology*, vol. 84, no. 4, pp. 1447–69, 1998.

[105] M. F. O’Rourke and F. Pressure, “Pressure and flow waves in systemic arteries and the anatomical design of the arterial system,” *Journal of Applied Physiology*, vol. 23, no. 2, pp. 139–49, 1967.

[106] M. F. O’Rourke and M. G. Taylor, “Input impedance of the systemic circulation,” *Circulation Research*, vol. 20, no. 4, pp. 365–380, 1967.

[107] C. J. Mills, I. T. Gabe, J. H. Gault, D. T. Mason, J. Ross, E. Braunwald, and J. P. Shillingford, “Pressure-flow relationships and vascular impedance in man,” *Cardiovascular Research*, vol. 4, no. 4, pp. 405–417, 1970.

[108] M. Karamanoglu, M. F. O’Rourke, M. F, A. P. Avolio, and R. P. Kelly, “An analysis of the relationship between central aortic and peripheral upper limb pressure waves in man,” *European Heart Journal*, vol. 14, pp. 160–167, 1993.

[109] A. P. Avolio, “Multi-branched model of the human arterial system,” *Medical & Biological Engineering & Computing*, vol. 18, no. 6, pp. 709–718, 1980.

[110] N. Stergiopulos, “Computer simulation of arterial blood flow,” Ph.D. Thesis, Iowa State University, 1990.

[111] J.-L. Vincent and D. De Backer, “Circulatory Shock,” *New England Journal of Medicine*, vol. 369, no. 18, pp. 1726–1734, 2013.

[112] J. Huygh, Y. Peeters, J. Bernards, and M. L. N. G. Malbrain, “Hemodynamic monitoring in the critically ill: an overview of current cardiac output monitoring methods,” *F1000Research*, vol. 5, 2016.

[113] D. M. Linton and D. Gilon, “Advances in noninvasive cardiac output monitoring,” *Annals of Cardiac Anaesthesia*, vol. 5, no. 2, pp. 141–8, 2002.

[114] W. A. Baxley, J. B. Cavender, and J. Knoblock, “Continuous cardiac output monitoring by the Fick method,” *Catheterization and Cardiovascular Diagnosis*, vol. 28, no. 1, pp. 89–92, 1993.

[115] M. M. Hoeper, R. Maier, J. Tongers, J. Niedermeyer, J. M. Hohlfeld, M. Hamm, and H. Fabel, “Determination of cardiac output by the Fick method, thermodilution, and acetylene rebreathing in pulmonary hypertension,” *American Journal of Respiratory and Critical Care Medicine*, vol. 160, no. 2, pp. 535–541, 1999.

[116] G. Fegler, “Measurement of cardiac output in anaesthetized animals by a thermodilution method,” *Quarterly Journal of Experimental Physiology and Cognate Medical*

Sciences, vol. 39, no. 3, pp. 153–164, 1954.

[117] W. Ganz, R. Donoso, H. S. Marcus, J. S. Forrester, and H. J. Swan, "A new technique for measurement of cardiac output by thermodilution in man," *The American Journal of Cardiology*, vol. 27, no. 4, pp. 392–396, 1971.

[118] M. Lee, G. F. Curley, M. Mustard, and C. D. Mazer, "The Swan-Ganz catheter remains a critically important component of monitoring in cardiovascular critical care," *Canadian Journal of Cardiology*, vol. 33, no. 1, pp. 142–147, 2017.

[119] T. Nishikawa and S. Dohi, "Errors in the measurement of cardiac output by thermodilution," *Canadian Journal of Anaesthesia*, vol. 40, no. 2, pp. 142–53, 1993.

[120] A. Gawlinski, "Measuring cardiac output: intermittent bolus thermodilution method," *Care Nurse*, vol. 24, no. 5, pp. 74–79, 2004.

[121] F. A. Moore, J. B. Haenel, and E. E. Moore, "Alternatives to Swan-Ganz cardiac output monitoring," *Surgical Clinics of North America*, vol. 71, no. 4, pp. 699–721, 1991.

[122] D. J. Funk, E. W. Moretti, and T. J. Gan, "Minimally invasive cardiac output monitoring in the perioperative setting," *Anesthesia and Analgesia*, vol. 108, no. 3, pp. 887–897, 2009.

[123] J. Pugsley and A. B. Lerner, "Cardiac output monitoring: is there a gold standard and how do the newer technologies compare?" *Seminars in Cardiothoracic and Vascular Anesthesia*, vol. 14, no. 4, pp. 274–282, 2010.

[124] L. L. Huntsman, D. K. Stewart, S. R. Barnes, S. B. Franklin, J. S. Colocousis, and E. A. Hessel, "Noninvasive Doppler determination of cardiac output in man. Clinical validation," *Circulation*, vol. 67, no. 3, pp. 593–602, 1983.

[125] P. J. Peyton and S. W. Chong, "Minimally invasive measurement of cardiac output during surgery and critical care," *Anesthesiology*, vol. 113, no. 5, pp. 1220–1235, 2010.

[126] D. G. Haryadi, J. a. Orr, K. Kuck, S. McJames, and D. R. Westenskow, "Partial CO2 rebreathing indirect Fick technique for non-invasive measurement of cardiac output," *Journal of Clinical Monitoring and Computing*, vol. 16, no. 5-6, pp. 361–74, 2000.

[127] M. B. Jaffe, "Partial CO2 rebreathing cardiac output – operating principles of the NICO™ system," *Journal of Clinical Monitoring and Computing*, vol. 15, no. 6, pp. 387–401, 1999.

[128] H. R. Warner, H. J. C. Swan, D. C. Connolly, R. G. Tompkins, and E. H. Wood, "Quantitation of beat-to-beat changes in stroke volume from the aortic pulse contour in man," *Journal of Applied Physiology*, vol. 5, no. 9, pp. 495–507, 1953.

[129] K. H. Wesseling, B. de Wit, J. A. P. Weber, and N. Smith, “A simple device for the continuous measurement of cardiac output,” *Advances in Cardiovascular Physics: Cardiovascular Engineering*, vol. 5, no. 2, pp. 16–52, 1983.

[130] C. M. Quick, W. L. Young, and a. Noordergraaf, “Infinite number of solutions to the hemodynamic inverse problem,” *American journal of Physiology-Heart and circulatory physiology*, vol. 280, no. 4, pp. H1472–H1479, 2001.

[131] J. Erlanger and D. R. Hooker, “An experimental study of blood-pressure and of pulse-pressure in man,” *Johns Hopkins Hospital Reports*, vol. 12, pp. 145–378, 1904.

[132] G. Liljestrand and E. Zander, “Vergleichende bestimmungen des minutenvolumens des herzens beim menschen mittels der stickoxydulmethode und durch blutdruckmessung,” *Zeitschrift für die gesamte experimentelle Medizin*, vol. 59, no. 1, pp. 105–122, 1928.

[133] M. J. Bourgeois, B. K. Gilbert, G. Von Bernuth, and E. H. Wood, “Continuous determination of beat to beat stroke volume from aortic pressure pulses in the dog,” *Circulation Research*, vol. 39, no. 1, pp. 15–24, 1976.

[134] Z. Lu and R. Mukkamala, “Continuous cardiac output monitoring in humans by invasive and noninvasive peripheral blood pressure waveform analysis,” *Journal of Applied Physiology*, vol. 101, no. 2, pp. 598–608, 2006.

[135] T. Parlikar, T. Heldt, G. Ranade, and G. Verghese, “Model-based estimation of cardiac output and total peripheral resistance,” in *2007 Computers in Cardiology*. IEEE, 2007, pp. 379–382.

[136] P. Segers, N. Stergiopulos, and N. Westerhof, “Quantification of the contribution of cardiac and arterial remodeling to hypertension,” *Hypertension*, vol. 36, no. 5, pp. 760–765, 2000.

[137] J. Rissanen, “Modeling by shortest data description,” *Automatica*, vol. 14, no. 5, pp. 465–471, 1978.

[138] J. Sun, A. Reisner, M. Saeed, and R. Mark, “Estimating cardiac output from arterial blood pressure waveforms: a critical evaluation using the MIMIC II database,” in *Computers in Cardiology, 2005*. Lyon: IEEE, 2005, pp. 295–298.

[139] T. Smith, R. M. Grounds, and A. Rhodes, “Central venous pressure: uses and limitations,” in *Functional Hemodynamic Monitoring*, ser. Update in Intensive Care and Emergency Medicine, M. Pinsky and D. Payen, Eds. Springer Berlin Heidelberg, 2005, vol. 42, ch. 8, pp. 99–110.

[140] J. a. L. Pittman, J. S. Ping, and J. B. Mark, “Arterial and central venous pressure monitoring,” *Anesthesiology Clinics*, vol. 42, no. 1, pp. 717–735, 2006.

[141] S. Magder, “The use of central venous pressure in critically ill patients,” in *Functional*

Hemodynamic Monitoring, ser. Update in Intensive Care and Emergency Medicine, M. Pinsky and D. Payen, Eds. Springer Berlin Heidelberg, 2005, vol. 42, ch. 24, pp. 299–311.

[142] F. Vicario, M. Q. Phan, R. Betti, and R. W. Longman, "OKID via output residuals: A Converter from stochastic to deterministic system identification," *Journal of Guidance, Control, and Dynamics*, vol. 40, no. 12, pp. 3226–3238, 2017.

[143] M. F. O'Rourke, *Arterial function in health and disease*, 1st ed. Churchill Livingstone, 1982.

[144] M. F. O'Rourke and T. Yaginuma, "Wave reflections and the arterial pulse," *Archives of internal medicine*, vol. 144, no. 2, pp. 366–371, 1984.

[145] N. Westerhof, N. Stergiopulos, and M. I. M. Noble, *Snapshots of hemodynamics: an aid for clinical research and graduate education.* New York: Springer, 2010.

[146] T. G. Schaufele, J.-P. Grunebaum, and B. Lippe, "Radial access versus conventional femoral puncture: outcome and resource effectiveness in a daily routine: the raptor trial," *Circulation*, vol. 120, pp. 2152–2161, 2009.

[147] P. K. Whelton, R. M. Carey, W. S. Aronow, D. E. Casey, K. J. Collins, C. Dennison Himmelfarb, S. M. DePalma, S. Gidding, K. A. Jamerson, D. W. Jones, E. J. MacLaughlin, P. Muntner, B. Ovbiagele, S. C. Smith, C. C. Spencer, R. S. Stafford, S. J. Taler, R. J. Thomas, K. A. Williams, J. D. Williamson, and J. T. Wright, "2017 ACC/AHA/AAPA/ABC/ACPM/AGS/APhA/ASH/ASPC/NMA/PCNA guideline for the prevention, detection, evaluation, and management of high blood pressure in adults," *Hypertension*, p. HYP.0000000000000065, 2017.

[148] J. J. Osborn, J. A. Russell, J. Beaumont, P. de Lanerolle, B. McChesney, and F. Garfield, "The measurement of relative stroke volume from aortic pulse contour of pulse pressure," *Vascular Diseases*, vol. 5, no. 3, pp. 165–77, 1968.

[149] P. Hallock and I. C. Benson, "Studies on the elastic properties of human isolated aorta," *The Journal of Clinical Investigation*, vol. 16, no. 4, pp. 595–602, 1937.

[150] M. J. Bourgeois, B. K. Gilbert, D. E. Donald, and E. H. Wood, "Characteristics of aortic diastolic pressure decay with application to the continuous monitoring of changes in peripheral vascular resistance," *Circulation Research*, vol. 35, no. 1, pp. 56–66, 1974.

[151] A. Albanese, N. Karamolegkos, S. W. Haider, A. Seiver, and N. W. Chbat, "Real-time noninvasive estimation of intrapleural pressure in mechanically ventilated patients: A feasibility study," in *2013 35th Annual International Conference of the IEEE Engineering in Medicine and Biology Society (EMBC).* Osaka: IEEE, jul 2013, pp. 5211–5215.

[152] F. Vicario, R. Buizza, W. A. Truschel, and N. W. Chbat, “Noninvasive estimation of alveolar pressure,” in *2016 38th Annual International Conference of the IEEE Engineering in Medicine and Biology Society (EMBC)*. Orlando, FL: IEEE, 2016, pp. 2721–2724.

[153] F. Vicario, A. Albanese, D. Wang, N. Karamolegkos, and N. W. Chbat, *Simultaneous Parameter and Input Estimation of a Respiratory Mechanics Model.* Cham: Springer International Publishing, 2017, pp. 235–247.

Appendix

The equations describing the pulmonary circulation model of Section 2.3.3 are obtained by applying the conservation of mass (continuity equation) and momentum (compatibility equation) laws on the electrical analog in Fig. 2.3.

$$C_{pa} \cdot \frac{d(P_{pa} - P_{pl})}{dt} = Q_{rv,o} - Q_{pa} \tag{A1}$$

$$V_{pa} = C_{pa} \cdot (P_{pa} - P_{pl}) + V_{u,pa} \tag{A2}$$

$$L_{pa} \cdot \frac{dQ_{pa}}{dt} = P_{pa} - P_{pal} - R_{sa} \cdot Q_{pa} \tag{A3}$$

$$C_{pal} \cdot \frac{d(P_{pal} - P_{pl})}{dt} = Q_{pa} - (Q_{pal} + Q_{ps}) \tag{A4}$$

$$Q_{pp,tot} = Q_{pal} + Q_{ps} = \frac{Q_{pal}}{1 - sh} \tag{A5}$$

$$Q_{pal} = \frac{P_{pal} - P_{pc}}{R_{pal}} \tag{A6}$$

$$V_{pal} = C_{pal} \cdot (P_{pal} - P_{pl}) + V_{u,pal} \tag{A7}$$

$$C_{pc} \cdot \frac{d(P_{pc} - P_A)}{dt} = Q_{pal} - Q_{pc} \tag{A8}$$

$$Q_{pc} = \frac{P_{pc} - P_{pv}}{R_{pc}} \tag{A9}$$

$$V_{pc} = C_{pc} \cdot (P_{pc} - P_A) + V_{u,pc} \tag{A10}$$

$$C_{pv} \cdot \frac{d(P_{pv} - P_{pl})}{dt} = Q_{ps} + Q_{pc} - Q_{pv} \tag{A11}$$

$$Q_{ps} = \frac{sh}{1 - sh} \cdot Q_{pal} \tag{A12}$$

$$Q_{pv} = \frac{P_{pv} - P_{la}}{R_{pv}} \tag{A13}$$

$$V_{pv} = C_{pv} \cdot (P_{pv} - P_{pl}) + V_{u,pv} \tag{A14}$$

Derivation of (2.10) from (2.9) is based on the following two assumptions:

1. $R_{pp,tot}$ is the total resistance of the pulmonary peripheral circulation, i.e., the equivalent resistance of the electrical circuit between P_{pal} and P_{pv} in Fig. 2.3, at steady-state

conditions and at a nominal functional residual capacity, FRC_{nom},

$$R_{pp,tot} = \frac{R_{ps} \cdot (R_{pc} + P_{pal}(V_A = FRC_{nom}))}{R_{ps} + R_{pc} + P_{pal}(V_A = FRC_{nom})}. \tag{A15}$$

2. Similar to the model by Lu et al. [30], the resistance R_{pc} does not change with respect to V_A. Its value is considered equal to R_{pal} when alveolar volume is equal to FRC_{nom},

$$R_{pc} = R_{pal}(V_A = FRC_{nom}). \tag{A16}$$

Consequently, at steady-state conditions when $V_A = FRC_{nom}$,

$$\begin{aligned} \frac{Q_{pal}}{Q_{ps}} = \frac{1 - sh}{sh} \Rightarrow R_{ps} &= \frac{1 - sh}{sh} \cdot (R_{pal}(V_A = FRC_{nom}) + R_{pc}) \\ &= \frac{2 \cdot (1 - sh) \cdot R_{pal}(V_A = FRC_{nom})}{sh}. \end{aligned} \tag{A17}$$

Hence, (A15) becomes:

$$R_{pp,tot} = 2 \cdot (1 - sh) \cdot R_{pal}(V_A = FRC_{nom}). \tag{A18}$$

Using the definition for R_{pal} (2.9), (A18) gives us the constant, but unknown, quantity $R_{pal,0}$ as:

$$R_{pal,0} = \frac{R_{pp,tot}}{2 \cdot (1 - sh)} \cdot \left(\frac{V_{A,max}}{FRC_{nom}}\right)^2. \tag{A19}$$

Then,

$$R_{pal} = \frac{R_{pp,tot}}{2 \cdot (1 - sh)} \cdot \left(\frac{V_A}{FRC_{nom}}\right)^2 \tag{A20}$$

$$R_{pc} = \frac{R_{pp,tot}}{2 \cdot (1 - sh)}. \tag{A21}$$

Notice that the shunt resistance R_{ps} does not need to be explicitly specified because the flow over the pulmonary shunts, Q_{ps}, is replaced by Q_{pal} according to (A12).